

Biologically Inspired Microstructured and Nanostructured Polymeric Biomaterials

Mohamed H. Ramadan

Carnegie Mellon University

Department of Chemistry

Advisor:

Prof. Newell R. Washburn

August 2015

In partial fulfillment of the requirements for the degree of Ph.D. in Chemistry

Dedication

To the best educators, care takers and role models. To my parents goes everything that I am, everything that I was and everything that I will ever be.

Preface

The precise designs of nature have inspired scientists for centuries to find solutions for complex problems. By studying natural biological systems, scientists are able to identify patterns, sequences and draw conclusions in order to propose possible solutions. The interplay between chemistry and structure is a common theme in all biological systems. This interplay is often responsible for the function of a given system, for any alterations to this balance leads to undesirable result, namely, systemic malfunction. While chemists have taken advantage of biological systems, nature does not provide answers to every problem or error. Hence, the field of biomaterials combines the beauty of natural design and function with the versatility of chemistry, in the context of this thesis, polymer chemistry. Using elements from nature, polymer chemists are able to modify, functionalize and enhance the function of synthetic systems and offer solutions to complex problems in the biomedical and diagnostic fields.

The focus of this thesis centers on the microfabrication of biologically inspired polymeric biomaterials. While the scope of the thesis is broad in the nature of applications considered, given the versatility of the systems developed, the main context or target application remains in the biomedical and diagnostic applications and the intersection of these two domains. The main theme and focus of this thesis is to tailor the chemistry of the system and control the microarchitecture to address relevant biomedical problems. The systems reported here target complex, yet common problems in the field such as: protein fouling on medical devices and diagnostic assays, tissue engineering scaffolding, drug delivery and wet tissue adhesives. Gaining insight into the problems from readily available biological systems, solutions are proposed using modified polymers for promising

biomaterials-based approaches. With special emphasis on tailoring the microarchitecture to specific functions, synthesis, characterization and subsequent microfabrication and testing are reported.

Keeping the common theme of controlling the basic polymer chemistry of the system combined with careful microstructure design to address the final application, the thesis is divided into 6 chapters that are grouped to highlight various aspects of the intended applications. Chapters 2-4, address the issue of protein fouling onto medical devices and diagnostic assays. Chapter 5 addresses the microfabrication of tissue engineering scaffolds and drug delivery vehicles. Finally, chapter 6 deals with developing pressure-sensitive wet tissue adhesives.

In chapter 2, titled: **Reducing Protein Adsorption with Polymer-grafted Hyaluronic Acid Coatings**, a novel antifouling coating system based on a thermoresponsive hyaluronic acid polymer hybrid is reported. These materials are designed, synthesized and characterized to possess reversible coating and adhesive properties at relevant physiological temperatures, presenting a nonfouling, hydrophilic layer to the solution. A comparison of the antifouling profile of hyaluronic acid to that of similar polysaccharides, namely dextran, alginate and carboxymethyl cellulose, is performed in chapter 3 under the title: **Polymer-grafted Polysaccharide Coatings for Reduced Blood Protein Adsorption**. A very promising application of such coatings is then designed to enhance detection accuracy and precision of clinically relevant diagnostic methods, namely enzyme-linked immunosorbent assay (ELISA), which is introduced in chapter 4, titled: **Non-Fouling Hyaluronic Acid Coatings for Improved Sandwich ELISA Measurements in Plasma Mixtures**. Chapter 5, entitled **Microfabricated and**

Nanofabricated Hyaluronic Acid Constructs: Design and Applications, deals with microfabrication of tissue engineering scaffolds using a novel modified rapid prototyping method for 3D printing of modified hydrogels. Moreover, the potential of micro needles arrays (MNAs) in treating relevant disorders is also investigated. The final chapter of this thesis, Chapter 6: **Microfabricated Gecko-inspired Microfibers for Enhanced Wet Tissue Adhesion**, explores the wet adhesive properties of mussel-inspired wet adhesives coatings of gecko-inspired polyurethane microfibers.

Acknowledgments

"Praise to God, who has guided us to this; and we would never have been guided if God had not guided us." *A`rāf` 7:43*

I would like to thank my advisor Prof. Newell Washburn for the support and help he offered me for the past 5 years both academically and personally. Working under his supervision has always been a pleasing and nourishing experience. I am particularly grateful for his constant help, accommodation and understanding every time the situation became harder than expected. I always felt respected, protected and appreciated.

My many thanks also extend to my committee members Prof. Krzysztof Matyjaszewski, Prof. Carmel Majidi, Prof. Marcel Bruchez, Prof. Danith Ly and Prof. Adam Fienberg, for accepting to be on my committee and for all the helpful questions, advice and useful discussions we have had.

I would like to express my thanks to everybody in the Chemistry program, my colleagues and my collaborators. Also, the administrative staff have always been pleasant and understanding. Special thanks go to Rea for our many open conversations and her accommodation. Brenda has been very nice in helping me through my health issues and went out of her way to offer assistance. Sara and Valerie have always been there when I needed them, with a smile on their faces no matter how busy they were. To Tim go special thanks for his help and explanations throughout my complicated funding situations. The store room staff and security officers Rayan, Paul, Mark, Mike, Dana and Charles were very nice and helpful at all times. I would like to extend my special thanks to Prof. Gloria Silva for her very valuable advice and understanding early on during my PhD journey, for that I am ever grateful.

To the Washburn group members, past and present, go my many thanks as well. Particularly Joe, Allison, Hoyung and Chetali for being such good colleagues and friends. Our many discussions and conversations have helped me both personally and professionally.

My sincere thanks go to my family. My father, mother, brothers (Mahmoud, Mostafa, Mumen) and my sister Mona for the enormous support, prayers and help throughout my PhD career.

My gratitude cannot be complete without acknowledging my beloved fiancé, Sara, for being there since my first day at CMU. Her enormous encouragement, constant believe and trust in me have kept me going so far. Her understanding and unconditional love during the time of stress have enabled me to focus on my research. From the bottom of my heart, I thank her very much.

My work at Carnegie Mellon wouldn't have been possible without the generous scholarship I received from the Libyan government. I also would like to thank the Canadian Bauru for International Education (CBIE) for their constant support and professionalism even during the worst times of turmoil and hurdles in Libya.

Table of Contents

Preface.....	iv
Acknowledgments	vii
Chapter 1 : Introduction	1
1.1. Microfabrication of polymeric biomaterials	16
1.1.1. Porosity control	17
1.1.2. Three dimensional architecture control:	20
Chapter 2 : Reducing protein adsorption with polymer-grafted hyaluronic acid coatings	42
2.1. Abstract	43
2.2. Introduction	44
2.3. Experimental Section	49
2.3.1. Materials.....	49
2.3.2. Synthesis of the homopolymer of PMEO₂MA by ATRP.	49
2.3.3. Modification of PMEO₂MA with amine group.....	50
2.3.4. Synthesis of HA-PMEO₂MA conjugates.	50
2.3.5. ¹H NMR characterization.....	51
2.3.6. Gel Permeation Chromatography (GPC).....	51
2.3.7. Dynamic light scattering (DLS).....	51
2.3.8. Tapping mode atomic force microscopy (AFM).....	51
2.3.9. Water contact angle measurements for modified HA films.	52

2.3.10. Quartz Crystal Microbalance (QCM-D) analysis.....	52
2.3.11. Biolayer Interferometry (BLI) analysis.	53
2.4. Results and discussion.....	55
2.4.1. HA Modification.	55
2.4.2. Proposed structure of coating.....	56
2.4.3. Dynamic Light Scattering.	57
2.4.4. Atomic Force Microscopy (AFM) Analysis.....	58
2.4.5. Water contact angle.....	60
2.4.6. Biolayer Interferometry (BLI) Analysis.....	60
2.4.7. Quartz Crystal Microbalance with Dissipation Monitoring (QCM-D)....	65
2.4.8. Coatings on complex objects.....	67
2.5. Conclusion.....	68
Chapter 3 : Polymer-grafted polysaccharide coatings for reduced blood protein adsorption	77
3.3. Experimental Section	88
3.3.1. Materials.....	88
3.3.2. Synthesis of the homopolymer of PMEO ₂ MA by ATRP.	89
3.3.3. Modification of PMEO ₂ MA with amine group.....	89
3.3.4. Synthesis of polysaccharide-PMEO ₂ MA conjugates.....	90
4.3.5. ¹ H NMR characterization.....	90

4.3.6. Gel Permeation Chromatography (GPC).....	91
4.3.7. Dynamic light scattering (DLS).....	91
4.3.8. Tapping mode atomic force microscopy (AFM).....	91
4.3.9. Water contact angle measurements for modified polysaccharide films...	92
3.4. Results and discussion.....	92
3.4.1. Polysaccharides Modification.....	92
3.4.2. Dynamic Light Scattering.....	93
3.4.4. Atomic Force Microscopy (AFM) Analysis.....	95
3.4.5. Water contact angle.....	97
3.4.6. Biolayer Interferometry (BLI) Analysis.....	99
3.5. Conclusions	103
Chapter 4 : Non-Fouling Hyaluronic Acid Coatings for Improved Sandwich ELISA Measurements in Plasma Mixtures	113
4.1. ABSTRACT:.....	114
4.2. Introduction	115
4.3. Methods	118
4.4. Results and Discussion	120
Chapter 5 : Microfabricated and Nanofabricated Hyaluronic Acid Constructs: Design and Applications	136
5.1. Introduction	137

5.1. 3D Printing of Complex Biological Structures by Freeform Reversible Embedding of Suspended Hydrogels.....	142
5.1.1. Materials and Methods	145
5.1.2. Results and Discussion	153
5.2. Therapeutic intradermal delivery of tumor necrosis factor-alpha antibodies using tip-loaded dissolvable microneedle arrays.....	171
5.2.1. Abstract	171
5.2.2. Introduction	172
5.2.3. Materials and Methods	175
5.2.4. Results and Discussions.....	184
5.2.4. Conclusion	197
5.2.5. Acknowledgments.....	198
5.3. Supporting Figures.....	211
Chapter 6 : Microfabricated Gecko-inspired Fibers for Enhanced Wet Tissue Adhesion	216
6.1. Abstract	217
6.2. Introduction	218
6.3. Experimental.....	223
6.3.1. Materials.....	223
6.3.2. Synthesis of DMA Monomer	223

6.3.3. Synthesis of DMA Copolymer	225
6.3.4. Coatings of gecko-microfibers	227
6.3.5. Indentation adhesion test	227
6.3.6. Extraction of DMA Copolymer and Analysis by UV-Vis	228
6.3.7. Adhesion and Compression Tests	229
6.3.8. GPC, ESI-MS, and NMR	230
6.4. Results and Discussion	230
6.4.1. Adhesion and Compression Tests	230
6.4.2. Mass Spectrometry and UV-Vis Absorbance	234
6.4.3. GPC and NMR.....	236
6.5. Conclusions	238

List of Figures

Figure 1.1 The structure of collagen ⁹	4
Figure 1.2 A view of marine mussels structure. ¹⁴	8
Figure 1.3 Simplified structure of a typical blood vessel. ²⁸	9
Figure 1.4 A schematic illustrating the composition and function of cell membrane. ³² ..	11
Figure 1.5 The chemical structure of Hyaluronic acid (HA)	15
Figure 1.6 A representation of the temporary role of TE scaffold supporting the injured tissue during as compared to that of newly-formed tissue ¹²	17
Figure 1.7 SEM micrographs a) Chitosan 50x; b) Collagen-chitosan 50x; c) Chitosan 150x; and d) Collagen-chitosan 150x. ⁶⁵	19
Figure 2.1 ¹ HNMR for HA-PMEO ₂ MA coating material.	56
Figure 2.2 Schematic of HA-PMEO ₂ MA in solution at $T < LCST$ (left) and the coating ($T > LCST$). The schematic at $T > LCST$ illustrates a potential structure that is compatible with the AFM images but is not drawn to scale.....	57
Figure 2.3 DLS data showing the distributions of diameters for HA-PMEO ₂ MA below LCST and above LCST.....	58
Figure 2.4 AFM images HA-PMEO ₂ MA materials. Images on the left show height (nm) while those on the right show cantilever deflection (nm). (A) Unmodified silica wafer surface. (B) HA-PMEO ₂ MA coatings. (C) Scratched HA-PMEO ₂ MA coatings. (D) Height profile of coating.....	59
Figure 2.5 Binding behavior of BSA and Fbg proteins (left) and unmodified HA (right) against TMS functionalized sensor tip as measured.	61

Figure 2.6 Protein adsorption profiles on PEG-modified sensor tips as measured by BLI against BSA, Fbg and IgG.	63
Figure 2.7 Protein adsorption profiles on HA-PMEO ₂ MA materials as measured using BLI. (A) Fbg. (B) BSA. IgG (C).....	64
Figure 2.8 Injection of BSA over HA-coated (HA-PMEO ₂ MA) sensors and plain silicon dioxide as indicated at 37 °C. For injection over HA-PMEO ₂ MA, the response of the negative control (water injected over HA-PMEO ₂ MA, not shown) was subtracted.	65
Figure 2.9 Confocal images of HA-PMEO ₂ MA-coated PMMA discs (A) 1x 2D view (B) 5x 2D, (C) 5x Z-stack view, (D) 4x optical view of PMMA discs after washing with cold water. Grids are 100 x 100 µm.	68
Figure 3.1 Example of multipolysaccharide-polymer hydrogel construct. ¹⁵	82
Figure 3.2 DLS data showing the distributions of diameters for (a) HA-PMEO ₂ MA, (b) Alg-PMEO ₂ MA, (c) CMD-PMEO ₂ MA and (d) CMC-PMEO ₂ MA below LCST and above LCST.....	94
Figure 3.3 AFM images of polysaccharide-PMEO ₂ MA materials in phase mode (Left) and height (Right). a) CMD-PMEO ₂ MA, b) CMC-PMEO ₂ MA, c)Alg-PMEO ₂ MA and d)HA-PMEO ₂ MA.....	97
Figure 3.4 Binding behavior of BSA and Fbg proteins (left) and unmodified HA (right) against TMS functionalized sensor tip as measured.	99
Figure 3.5 Protein adsorption profiles on PEG-modified sensor tips as measured by BLI against BSA, Fbg and IgG.	101

Figure 3.6 Protein adsorption profiles on HA-PMEO ₂ MA, Alg-PMEO ₂ MA, CMC-PMEO ₂ MA and CMD-PMEO ₂ MA materials as measured using BLI: (a) overall steps, (b) BSA association and dissociation curves and (c) polysaccharide loading curves	102
Figure 4.1 Non-Fouling Hyaluronic Acid Coatings for Improved Sandwich ELISA Measurements in Plasma Mixtures	115
Figure 4.2 Schematic of the coating and antibody immobilization process. Figure not drawn to scale.	121
Figure 4.3 Residual anti-TNF- α quantification using BLI on ForteBio: (a) real-time association vs. time for anti-TNF- α standards and (b) anti-TNF- α standards and samples binding rate vs concentration.(N=40, $r^2= 0.999$, $SD\pm 0.002411$).....	122
Figure 4.4 ELISA detection of TNF α : calibration curves of TNF- α standards for (a) commercial, non-coated microwells and (b) HA-coated microwells	123
Figure 4.5 ELISA detection of TNF- α in solutions consistent of pure TNF- α , protein mixtures of subphysiological and physiological concentrations of BSA, IgG and FbG and plasma samples (a) results from TNF- α concentration of 800 pg/mL (b) results from TNF- α concentration of 200 pg/mL (c) Results from TNF- α concentration of 50 pg/mL (d) results from TNF- α concentration of 12.5 pg/mL. All data are presented as mean \pm SD. (p<0.001).....	127
Figure 5.1 Illustration of the four types of microneedles. ⁸	140
Figure 5.2 Interpenetrating polymer networks IPNs.....	141
Figure 5.3 Mechanical properties of IPNs compared to individual networks. ^{14, 16}	142
Figure 5.4 Synthesis of HAGM	145

Figure 5.5 FRESH printing is performed by depositing a hydrogel precursor ink within thermoreversible support bath consisting of gelatin microparticles and initiating gelling in situ through one of multiple crosslinking mechanisms. (A) A schematic of the FRESH process showing the hydrogel (green) being extruded and crosslinked within the gelatin slurry support bath (yellow). The 3D object is built layer-by-layer and when completed is released by heating to 37 °C and melting the gelatin. (B) Images of the letters “CMU” FRESH printed in alginate in Times New Roman font (black) and released by melting the gelatin support (grey material in the Petri dish). (C) Representative images of gelatin particles produced by blending for 30, 75 or 120 s. (D) The mean Feret diameter of gelatin particles as a function of blending time from 30 to 120 s (N > 1000 per time point, red line is a linear fit, error bars indicate standard deviation). (E) Rheological analysis of storage (G') and loss (G'') modulus for gelatin support bath showing Bingham plastic behavior. Scale bars, (B) 1cm and (C) 1mm..... 154

Figure 5.6 Analysis of the hydrogel filaments and structures fabricated using FRESH. (A) A representative alginate filament (green) embedded within the gelatin slurry support bath (red). (B) Histogram of the diameter of isolated alginate filaments within the gelatin support bath showing a range from 160 to 260 μm . (C) A standard square lattice pattern commonly used for infill in 3D printing FRESH printed in fluorescent alginate (green) and viewed (D) top down and (E) in 3D. (F) An octagonal infill pattern FRESH printed in fluorescent alginate (green) and viewed (G) top down and (H) in 3D. (I) Example of a two material print of coaxial cylinders in red and green fluorescently labeled alginate with a continuous interface shown in top down and lateral cross-sections. (J) An example of a freeform, non-planar FRESH print of a helix shown embedded in the gelatin support bath.

(K) A zoom in of the helix demonstrating that FRESH can print in true freeform and is not limited to standard layer-by-layer planar fabrication. Scale bars, (A) 1 mm, (D, G) 500 μ m, (I) 2 mm, (J) 10 mm, and (K) 2.5 mm. 157

Figure 5.7 FRESH printing of biological structures based on 3D imaging data and functional analysis of the printed parts. (A) A model of a human femur from 3D CT imaging data is scaled down and processed into machine code for FRESH printing. (B) The femur is FRESH printed in alginate and after removal from the support bath closely resembles the model and is easily handled. (C) Uniaxial tensile testing of the printed femur demonstrates the ability to be strained up to 40% and elastically recover. (D) A model of a section of a human right coronary arterial tree from 3D MRI imaging is processed at full scale into machine code for FRESH printing. (E) An example of the arterial tree printed in alginate (black) and embedded in the gelatin slurry support bath. (F) A section of the arterial tress printed in fluorescent alginate (green) and imaged in 3D to show the hollow lumen and multiple bifurcations. (G) A zoom in of the arterial tree shows the clearly defined vessel wall <1 mm thick and well-formed lumen. (H) A darkfield image of the arterial tree mounted in a perfusion fixture to position a syringe in the root of the tree. (I) A time-lapse image of black dye perfused through the arterial tree false-colored at time points of 0 to 6 s to show flow through the lumen and not through the vessel wall. Scale bars, (B) 4 mm, (E) 10 mm, (F) 500 μ m, (G) 250 μ m, and (H, I) 500 μ m..... 160

Figure 5.8 FRESH printed scaffolds with complex internal and external architectures based on 3D imaging data from whole organs. (A) A darkfield image of an explanted embryonic chick heart. (B) A 3D image of the 5-day-old embryonic chick heart stained for fibronectin (green), nuclei (blue), and F-actin (red) and imaged with a confocal microscope.

(C) A cross-section of the 3D CAD model of the embryonic heart with complex internal trabeculation, based on the confocal imaging data. (D) A cross-section of the 3D printed heart in fluorescent alginate (green) showing recreation of the internal trabecular structure from the CAD model. The heart has been scaled up by a factor of 10 to match the resolution of the printer. (E) A darkfield image of the 3D printed heart with internal structure visible through the translucent heart wall. (F) A 3D rendering of a human brain from MRI imaging data processed for FRESH printing. (G) A zoom in of the 3D brain model showing the complex, external architecture of the white matter folds. (H) A lateral view of the brain 3D printed in alginate showing major anatomical features including the cortex and cerebellum. The brain has been scaled down to ~3 mm in length to reduce printing time and test the resolution limits of the printer. (I) A top down view of the 3D printed brain with black dye dripped on top to help visualize the white matter folds printed in high fidelity. Scale bars, (A, B) 1 mm, (D, E, H, I) 1 cm. 162

Figure 5.9 ¹HNMR 20% DM HAGM..... 165

Figure 5.10 Printed HAGM circle-threads. a) Swelling of the printed constructs leads to brittle hydrogel. b) Swollen individual threads increases feature size. Scale bar 1000 μ m 166

Figure 5.11 Sodium alginate crosslinks 167

Figure 5.12 Confocal images of printed HAGM/alginate constructs (a) circle thread view shows improved print fidelity and feature size. (b) Sharp individual non-swollen threads. (c) A printed circle shows sharp-edged hydrogel constructs. Scale bar 500 μ m..... 168

Figure 5.13 Description of the micromilling/spin-casting based fabrication approach used for creating tip-loaded dissolvable microneedle arrays. Three-steps: (a) Mechanical

micromilling of mastermolds. (b) Elastomer molding of production molds. (c) Spin-casting to localize anti-TNF- α in the apex of obelisk microneedles and fabricate tip-loaded dissolvable MNAs..... 186

Figure 5.14 Tip-loaded dissolvable MNAs created using the micromilling/spin-casting technique for intradermal delivery of anti-TNF- α . (a) ESEM images of the PMMA mastermold. Scale bars on the image of array and individual microneedle correspond to 1 mm and 100 μ m, respectively. (b) Optical microscope images of the production mold after tip loading with bioactive cargo. (c) Bright field microscope images of the tip-loaded MNAs. Scale bars on the image of array and individual microneedle correspond to 1 mm and 100 μ m, respectively. (d) Inverted fluorescence microscope image of a dissolvable MNA tip-loaded with Cy3-labeled anti-TNF- α . (e) Inverted fluorescence microscope image of the individual tip-loaded dissolvable MNAs. (f) Merged bright field and fluorescence microscope image of the tip portion of the individual microneedle. 189

Figure 5.15 TNF- α binding affinity for anti-TNF- α using biolayer interferometry. Biolayer interferometry was used to measure binding affinity of fresh or previously encapsulated anti-TNF- α with TNF- α immobilized on the sensor tip to characterize the effects of processing on antibody binding affinity. (a) Characteristic binding curves of fresh and previously encapsulated anti-TNF- α show similar binding kinetics in real time. (b) K_D values extracted from binding curves using a 1:1 binding isotherm model show slight increases in K_D for anti-TNF- α previously encapsulated in MNA ($K_D = 50.6 \pm 5.84$ pM) compared to fresh anti-TNF- α ($K_D = 9.33 \pm 3.18$ pM), corresponding to a slight decrease in binding affinity. 191

Figure 5.16 Microneedle penetration, deposition of cargo and intradermal delivery of anti-TNF- α from tip-loaded CMC-MNAs. (a) ESEM image of the microneedle arrays before application. Scale bars correspond to 100 μ m. (b) ESEM image of the microneedle arrays after 30 min of application. Scale bars correspond to 100 μ m. (c) Inverted fluorescence microscope image of Cy-3 labeled microneedle traces on living human skin explants. 4 x optical magnification. (d, e, f) Intradermal delivery of anti-TNF- α from tip-loaded CMC MNAs. 20x optical magnification. (g, h, i) Intradermal delivery of anti-TNF- α from topical application with DMSO. 20x optical magnification. (d, g) Fluorescence microscope image of the DAPI stained human skin insertion sites. (e, h) Fluorescence microscope images of the Cy3-labeled antibody cargo. (f, i) Fluorescence microscope composite images that demonstrate delivery cavities penetrating the epidermis and upper dermis, and delivery of fluorescent cargo of the microneedles.	193
Figure 5.17 Intradermal release profiles of anti-TNF- α from tip-loaded CMC-MNAs. Tip-loaded MNAs created as described above were applied to living human skin for the indicated time intervals and then removed. Targeted skin was excised and assayed for Cy3-fluorescence content by spectrofluorometry. Standard deviation values were from 6 replicates.	194
Figure 6.1 A view of marine mussels structure. ¹	219
Figure 6.2 mfp-3 chemical structure as an example of the Dopa content (highlighted in red) in the mfp family	221
Figure 6.3 ¹ HNMR spectra for DMA monomer (a) and DMA-co-MEA copolymer (b)	226
Figure 6.4 Customized underwater indentation adhesion test setup.	228

Figure 6.5 Work of adhesion and compressive modulus as a function of time.	232
Figure 6.6 Underwater maximum adhesion plot of DMA-co-MEA-coated microfibers on porcine skin tissue sample as a function of preload.	233
Figure 6.7 Underwater work of adhesion plots for DMA-co-MEA-coated microfibers as a function of contact time	234
Figure 6.8 ESI-MS of Day 0 DMA copolymer extraction.....	235
Figure 6.9 UV-Vis analysis of extraction experiments from the DMA copolymer.....	236
Figure 6.10 GPC traces for days 0, 1, 3, and 16.	237
Figure 6.11 Optical microscopy images of the poorly coated mushroom tip gecko microfibers	240

List of Schemes

Scheme 2.1 The chemical composition of HA and modification route.	55
Scheme 3.1 Synthesis of the homopolymer of PMEO ₂ MA by ATRP	92
Scheme 4.1 Chemical modification of HA yielding non-fouling HA-PMEO ₂ MA coatings	120
Scheme 5.1 HA methacrylation mechanism ⁵⁰	164
Scheme 5.2 Photo initiator Irgacure I2959 mechanism of action	165
Scheme 6.1 Reaction scheme for the synthesis of DMA and DMA-co-MEA.	225

List of Tables

Table 1.1 List of some commercially available ECM scaffold materials. ¹²	6
Table 1.2. Summary of current literature on scaffold design and fabrication techniques and their application in tissue engineering ⁵⁶	30
Table 3.1 Common polysaccharide as biomaterials	83
Table 3.2 Water contact angle measurements of polysaccharide-PEMO ₂ MA-coated surfaces	98
Table 4.1 Protein and TNF- α concentrations in the analyzed samples.	123
Table 4.2 Summary of Measured TNF- α concentration under the tested conditions and concentrations	124
Table 5.1 Summary of modification conditions	164

Chapter 1 : Introduction

The importance of biomaterials-based strategies increases every year as a critical component of a broad range of technologies. It is estimated that the total market for such technologies is growing to more than \$80 billion annually in the United States alone.¹⁻² Patients in need of such strategies suffer from injuries ranging from simple tissue damage to complete organ failure; sadly, many of the latter category die while on long transplantation waiting lists due to extreme donor shortages. While standard treatment routes such as artificial organs or systems and surgical procedures can save lives, they are often associated with other serious problems that lead to significant changes in the quality of life on the patients' side, as well as repeated procedures to treat the same condition and those that are, accidentally, caused by the treatment, not to mention the financial consequences for having long-term treatment plans for such patients.²

Tissue engineering is defined as “the application of the principles and methods of engineering and life sciences toward the fundamental understanding of structure-function relationships in normal and pathological mammalian tissue and the development of biological substitutes to restore, maintain, or improve tissue function”^{1, 3-4}. At the time that tissue engineering strategies have proven to be very successful for many applications, the relatively simple tissue architecture and cellular organization of certain systems, for example skin epidermis and corneal epithelium, make the task easier. Conversely, when designing solutions for more complex tissue organs, or more metabolically active tissues such as the liver or the heart, the need for better control over the basic cellular and vascular architecture becomes more important.²

Biomaterials are materials other than food or drugs used in therapeutic or diagnostic applications. They could also be defined as materials of biologically derived origins.⁵ Biomaterials have had a huge impact in medicine, especially in the field of drug delivery. Various biomaterials have been used for tissue engineering applications in the past two decades with varying degrees of functionalities. By combining biocompatible biomaterials with mammalian cells, antibodies, growth factors or pharmaceutical drugs, it is possible to treat some very complex conditions. Since most tissues are composed of more than one cell type and very precise and highly regular microarchitectures of these cellular and acellular components, the micro and nano scale design of the biomaterials used depends primarily on the end application. Careful examination of native tissues and the pathological conditions that affect them reveals that such complex architecture serves vital roles in the functionality of the human tissue. Therefore, regardless of the intended application, from simple coatings to more active regenerative applications, the choice of both material and the design and three dimensional microarchitecture adopted are crucial criteria and, often, native tissue systems that exists in nature are used for guidance when designing such constructs.

The extracellular matrix (ECM), which is deposited by the native cell populations in each tissue, has numerous critical functions. While in dynamic equilibrium with these populations, the ECM actively and rapidly responds to cues from the surrounding cellular microenvironment on the tissue and organ levels. The role the ECM plays in tissue regeneration is gaining more attention in recent years owing to the increased knowledge scientist are gaining about its participation and micro and macrostructure.⁶⁻⁷ Structurally, the ECM consists primarily of structure proteins that give it these unique properties that

support cells proliferation, differentiation as well as regeneration and remodeling. While the ECM is produced locally by native cellular populations, major structural proteins possess very similar basic amino acid composition regardless of the origin. The ECM central role in homeostasis, as well as responding to injury and initiating regeneration, could be attributed, to a great degree, to this similarity in the basic amino acid structure.

The most abundant structural protein within mammalian ECM is collagen, with more than 20 different types identified. It is this high concentration of the different types of collagen, as well as the interplay between its concentrations and special organization, that provides the ECM with its mechanical integrity. Hence the ECM is most responsible for mechanically supporting the growth and proliferation of local and repair cell population.⁸

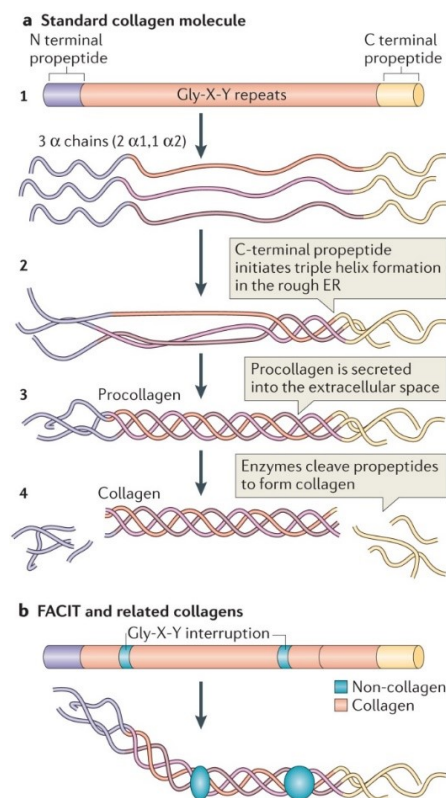


Figure 1.1 The structure of collagen⁹

Another crucial protein component of the ECM is the adhesion protein laminin. Laminin is a trimeric crosslinked polypeptide present in the basement membrane in various forms within the ECM ($\alpha 1$, $\beta 1$, $\gamma 1$) depending on the specific peptide sequences.¹⁰ Laminin plays a vital role in the formation and maintenance of vascular networks at the injury site, which makes it a very important protein to consider when examining the complex cascade of event that are triggered by an injury.¹¹

Fibronectin also exists within the ECM, both in submucosal and basement membrane structures, and performs both structural and desirable functional duties. While offering mechanical support to the ECM overall, it also contains important cell adhesion domains that aid the homing and residence of many cells types in response to injury. Functionally, the ECM is responsible for sequestering important growth factors, cytokines, hormone and signaling molecules important for tissue repair and regenerations within its structure. One important class of materials in binding to, and preserving, these growth factors at the ECM is glycosaminoglycans (GAGs).¹²

While the detailed composition of the ECM is beyond the scope of this work, it is rather important to emphasize the importance of the role the ECM plays in tissues. The ECM is a dynamic part of every tissue, the structure and composition of which changes drastically depending on, body part, age and pathological conditions. As such, ECM-based therapies are receiving more attention with the development of various products that address tissue regeneration, using native or transplanted ECM, or ECM components, across the different research and clinical phases.⁷ Table 1.1 shows some examples of commercially available ECM-based products. It is also important to use this flexibility in

combination with our knowledge about the varying roles the ECM plays and the precise and highly organized microarchitecture as a guide for future approaches.

Product	Company	Processing	Form
AlloDerm	Lifecell	Natural	Dry sheet
AlloPatch®	Lifecell	Natural	Dry sheet
CuffPatch™	Arthrotek	Cross-linked	Hydrated sheet
DurADAPT™	Pegasus Biologicals	Cross-linked	Dry sheet
Durasis®	Cook SIS	Natural	Dry sheet
Durepair®	TEI Biosciences	Natural	Dry sheet
Graft Jacket®	Wright Medical Tech	Natural	Dry sheet
Matrigel®	Corning Life Sciences.	Natural	Hydrated sheet
Oasis®	Healthpoint	Natural	Dry sheet
OrthADAPT™	Pegasus Biologicals	Natural	Dry sheet
Pelvicol®	Bard	Natural	Hydrated sheet
Peri-Guard®	Synovis Surgical	Cross-linked	Dry sheet
Permacol™	Tissue Science Laboratories	Cross-linked	Hydrated sheet
PriMatrix™	TEI Biosciences	Natural	Dry sheet
Restore™	DePuy	Natural	Dry sheet
SurgiMend™	TEI Biosciences	Natural	Dry sheet
Surgisis®	Cook SIS	Natural	Dry sheet
Stratasis®	Cook SIS	Natural	Dry sheet
Suspend™	Mentor	Natural	Dry sheet
TissueMend®	TEI Biosciences	Natural	Dry sheet
Vascu-Guard®	Synovis Surgical	Cross-linked	Dry sheet
Veritas®	Synovis Surgical	Cross-linked	Hydrated sheet
Xelma™	Molnlycke	Natural	Gel
Xenform™	TEI Biosciences	Natural	Dry sheet
Zimmer Collagen Patch®	Tissue Science Laboratories	Cross-linked	Hydrated sheet

Table 1.1 List of some commercially available ECM scaffold materials.¹²

Another example highlighting the interplay between architecture and composition in natural systems is elegantly demonstrated by marine mussels. Marine mussels live on rocky shallow shores where waves are strong, taking advantage of the abundance of nutrients and sunlight.¹³ With the aid of specialized holdfasts, called the byssus, that are actively fabricated and maintained by mussels, consuming about 12% of the total metabolic capacity of marine mussels, they are able to stick firmly onto rocky surfaces while

submerged underwater. This phenomenon has inspired much research as well as solutions for developing underwater adhesives.¹⁴⁻²¹ While there are many theories and explanations for the deteriorating adhesion of polymers underwater, mussels actually combine both the physical and the chemical aspects of the process and, once more, further highlight the importance of cooperation between the chemistry and micro architecture of tissues and organism that nature seamlessly succeeds to exhibit.

The byssus is a protein-based structure comprised of a very elegant and strict hierarchy of threads, plaques, retractor muscles, beads, stems and a root.^{14, 16} While the structure, fabrication mechanism and attachment to the living retractor muscle parts of the mussels are important aspects to the survival of mussels and the under-water adhesion sensing mechanism, the byssal plaques are solely responsible for the mussels' tenacity to various solid surfaces underwater.¹⁵⁻¹⁶ The microstructure of the plaques is precisely engineered with a very fine porous and hierarchical order. This microporous structure accommodates the distal thread core of the byssus, which consists of dense bundles of microfibers insulated by a granular matrix, and exhibits a precise pore diameter gradient ranging from 200 nm to 3 μ m near the solid surface and the thread interface respectively. This porous network, about 40% porosity, is highly interconnected and lubricated with the aids of very smooth walls and fluids and is extended to trabeculae with pore diameters of 50-500 nm and only 50 nm wall thickness.²² This highly porous microstructure of the plaques, not only permits better distribution of the microfiber bundles, but also creates a cup-like structure able to maintain an attachment angle to the solid surface and an effect similar to that of suction cups. This elegant micro organization helps adhesion protein in the tips of the microfibers find suitable spots of solid surfaces for strong adhesion.

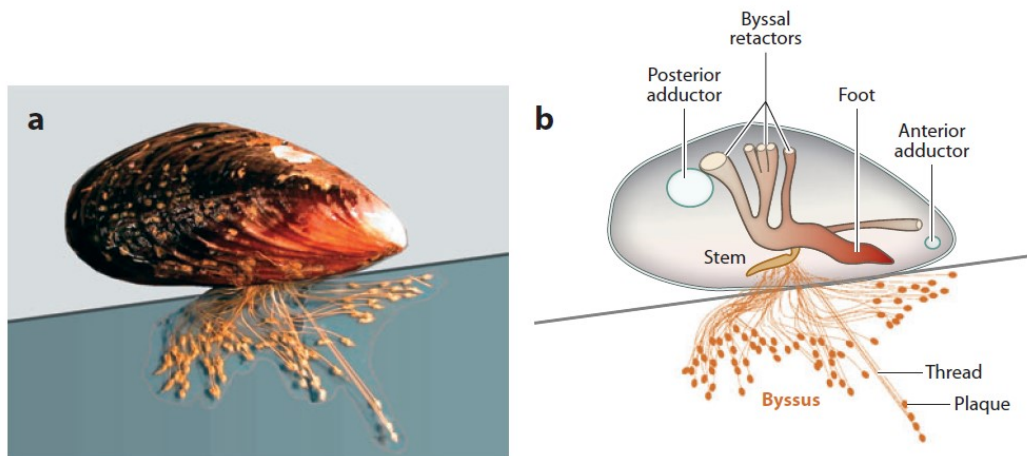


Figure 1.2 A view of marine mussels structure.¹⁴

On the molecular level, the plaque is packed with a group of 7-8 proteins that match the diversity of the microfibrillar threads. At the time the byssus is made exclusively of about 25-30 types of specialized proteins, 5 proteins exclusive to the plaque are the mussel foot protein (mfp): mfp-2, mfp-3, mfp-4, mfp-5, mfp-6.¹⁴ While the individual protein sequences for these proteins are distinctively different, one common component among all of them is the posttranslational modified amino acid 3,4-dihydroxyphenyl-L-alanine (Dopa). The molecular weights of these proteins as well as the Dopa content varies, reaching almost 40% Dopa content.^{14, 20} For decades this unique adhesion has inspired scientists to study and use these Dopa-containing polymers for various applications such as, coatings,²³⁻²⁴ synthetic medical adhesives²⁵ and sealants.²⁶⁻²⁷

While controlling the microarchitecture and bulk properties of biomaterials could afford significant advantages over other approaches, biomaterials surface properties are a crucial aspect of biomaterial design and, consequently, performance. Seeking guidance from nature, the hierarchal structure of blood vessels is a perfect example of a system where

the basic structure and function of the vessel could be dramatically compromised should the surface properties of the vessel be altered from the native state.

All blood vessels regardless of the size, location or cargo type share most characteristic properties. In general, blood vessels are consistent of three main layers: tunica intima, tunica media and tunica adventitia. Fig. 1.3 shows a simplified schematic of a typical blood vessel. Each one of these layers is comprised of a distinctive group of proteins and cells that yields the overall elasticity, which is vital for the circulation of important blood components throughout the body as well as the robustness and constant remodeling of the blood vessels.

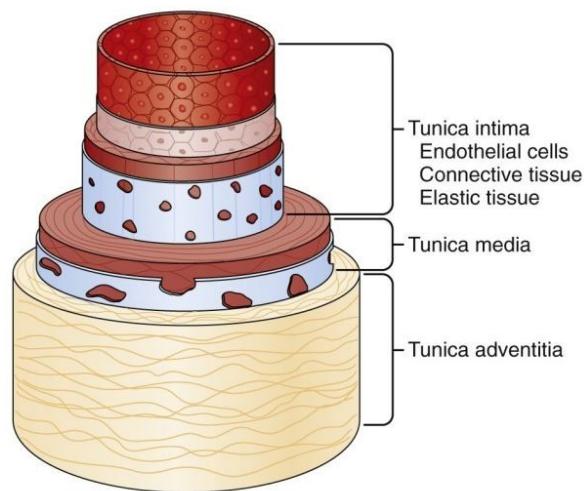


Figure 1.3 Simplified structure of a typical blood vessel.²⁸

Comprised of various structural proteins, e.g. proteoglycans, collagens (I, III, IV), laminin and fibronectin, in a highly organized microarchitecture, the media and adventitia are the most important layers, giving blood vessels their distinctive global mechanical resistance. Of great functional importance is the tunica intima, also called the lumen. In human vessels, the lumen is a very thin layer of endothelial cells that forms the inner-most

interface, i.e. in contact with biologics, of the vascular walls sitting on a very thin basal lamina layer. This layer consists of a net-like type IV collagen fibers, forming a (~70 nm) layer. The healthy lumen endothelial cells are elongated in the direction of blood flow, affording lubrication and antifouling properties to the vessels. This layer forms the biological interface between the vascular walls and the many components of the blood stream, e.g. cells, proteins, nutrients, etc, and is the main regulator of the biological processes taking place at the wall microenvironment.

While they are semipermeable membranes that regulate the transport of chemical and cellular signals between the bloodstream and the vessel, the membranes also prevent any protein or cellular adsorption on the walls of thin blood vessels.²⁸ Damage or delamination of the lumen could lead to many serious pathological conditions such as the formation of atherosclerotic plaques,²⁹⁻³⁰ Virchow's triad³¹ and, ultimately, heart failure.

Similarly, the role of the cellular membrane in the prevention of non-specific protein adsorption and cellular aggregation onto the cell surface is rather interesting. A human cell membrane is composed primarily of glycerophospholipids chains that self-assemble to form a phospholipid bilayer surrounding each individual cell as shown in Fig. 1.4. The assembly of these chains within the membrane allows for the hydrophilic heads to be pointing towards the aqueous cytoplasm and extracellular environment, while the hydrophobic chains self-assemble to form a medium for nutrients and signaling exchange. The hydrophilicity of the bilayer prevents non-specific adsorption of plasma or cytoplasm components and affords some lubricity. The other main component of the cellular membrane is the transmembrane proteins. These proteins are embedded within the cell wall

forming bridges between the intercellular component of the cell and the surrounding microenvironment at select locations of the membrane. This means that any signaling or exchange must therefore take place through these specific and selective cell membrane apparatuses, which leads to amplified and highly specific signals that guide each cell through the varying processes and pathways it undertakes. These structures are cell receptors, ion exchange channels, enzymes and anchor proteins.³²

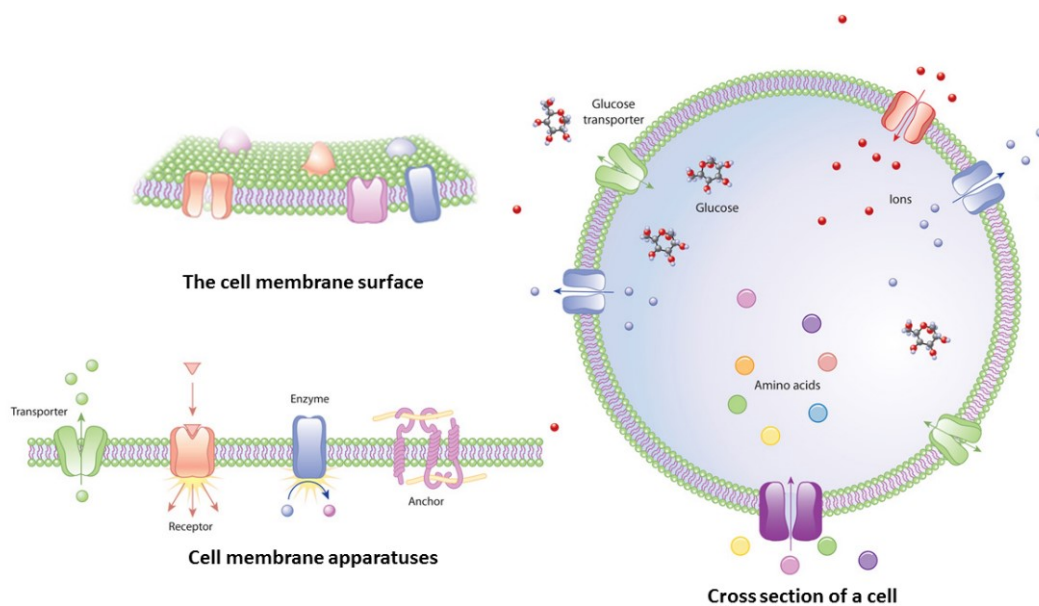


Figure 1.4 A schematic illustrating the composition and function of cell membrane.³²

Such design principles have been utilized in creating selective detection assays such as affinity-based sensors. While the mechanism of detection could vary between optical, magnetic or fluorescent singling, most of these methods share the general idea of blocking the surface with a nonfouling material that would limit non-specific adsorption. Such assays are particularly helpful when dealing with complex and clinically relevant samples such as blood or plasma. This same concept is the underlying principle behind many relevant commercial technologies such as Biacore® and VitroStelth® coatings.

These examples highlight the importance of both structure and functionality when designing biomaterials constructs. Using nature as inspiration, this work will focus on developing biomaterials solutions for tissue engineering, biomedical and diagnostics applications combining the elements learned from nature: controlling the microstructure of the constructs using modifications and microfabrication methods, as well as controlling functionality by using bioactive and biocompatible polymeric biomaterials.

When addressing complex biomaterials and tissue engineering problems, polymers offer a valuable option because they can mimic the structure and function of biopolymers. For decades, the versatility and functionalities of polymer design, as well as micro and macro architecture, has been a very attractive feature to researchers.³³ Rapid advancements in polymer chemistry, micro and macromolecular design and synthesis allow for better control over the chemical and physical interactions of various polymeric structures, which makes it possible to gain insight into the very important interfacial phenomena.³⁴ These advancements also enable a wide variety of synthetic and biomimetic polymer blocks specifically tailored towards the desired applications. This, in turn, allows for the wide adoption of polymeric systems as biomaterials components. As such, polymers, natural, synthetic and hybrid systems, have been extensively researched and used as biomaterials for many applications over the past few decades.

One of the areas that benefit the most of polymeric biomaterials is drug delivery. The careful and deliberate macromolecular design of biocompatible polymers allows for many advances in this area. A wide selection of biological cargo has been loaded into or onto polymeric vehicles either for the controlled, systemic or local, release of therapeutics

owing to better understanding of microfabrication and bioconjugation techniques. Small drug molecules, short and long peptides and proteins, as well as many growth factors and signaling molecules, have been reported to be better delivered via polymeric biomaterials.³⁵ Therefore, synthetic polymers, both hydrophilic and hydrophobic, offer solutions to complex biomaterials approaches.

Some of the most commonly investigated synthetic polymer biomaterials include the use of hydrophilic polymers. Poly (ethylene glycol) (PEG) is the most widely used hydrophilic polymer in this area due to its hydrophilicity and versatile end-group functionality, with examples of reported applications like coatings,³⁶ drug delivery³⁷ as well as tissue scaffolding.³⁸ Other hydrophilic polymer used as biomaterials include poly (vinyl alcohol) (PVA) and poly (acrylamide) (PAAm). While the use of hydrophobic polymers as biomaterials is limited by surface properties and degradation profiles, poly (α -esters) are a class of hydrophobic polymers often used as biomaterials due to their hydrolytically susceptible ester bonds.³⁹ Amphiphilic and responsive materials such as poly (N-isopropylacrylamide) (pNIPAAm) and block copolymers offer very promising solutions for more advanced biomaterial systems.^{33, 40} Biocompatibility and biodegradability are still limiting factors facing the full utilization of synthetic polymers as biomaterials. Hence, the importance of bioconjugation with biopolymers is amplified.

A myriad of bioconjugation methods are available, which allows for the facile modification and functionalization of synthetic polymers, further tailoring them to specific applications. These chemistries include PEGylation, carbodiimide, epoxide, aldehyde, active ester, radical, and hydrazide reactions.⁴¹ The conjugation of natural biopolymers

with synthetic ones increases biodegradability and allows for the use of high molecular weights, slower clearance of polymers and increased efficacy.⁴² However, some bioconjugation methods, e.g. carbodiimide, aldehyde and epoxide, are not suitable for *in situ* conjugation due to the production of cytotoxic reaction intermediates that limit cell viability. Hence, *ex situ* synthesis and extensive purification of bioconjugates is often the route of choice. To address this limitation, significant amount of work has been dedicated to developing conjugation methods more suitable for *in situ* conjugation and functionalization of polymer biomaterials. For example, addition reactions have also been utilized for *in situ* conjugation of polymers with mild, nontoxic conditions. Such reactions employ nucleophilic substituents, e.g. thiols and primary amines, in fast kinetics reactions for *in situ* and *ex situ* conjugation and crosslinking.^{41, 43} For example, Langer et al. and others, have reported the use of UV labile materials suitable for *in vivo* polymerization.⁴⁴ Moreover, the use of naturally occurring polymers is considered one of the very promising approaches.

Hyaluronic acid (HA) is a linear, viscous, naturally occurring, high molecular weight biopolymer composed of glycosaminoglycan (GAG) a copolymer of D-glucuronic acid and N-acetyl-D-glucosamine, through a β -1,4 glycosidic bond, and a β -1,3 bond that links the disaccharides units, as shown in fig. 1.5.⁴⁵⁻⁴⁹ HA is found in the human body as part of the extracellular matrix (ECM), umbilical cord, synovial fluid, the vitreous humor of the eyes and as a lubricant between the joints. The biopolymer, HA, is synthesized in the cytoplasmic surface of the plasma membrane, which is different than other GAGs and polysaccharides as they are synthesized in the Golgi apparatus.⁴⁹⁻⁵⁰

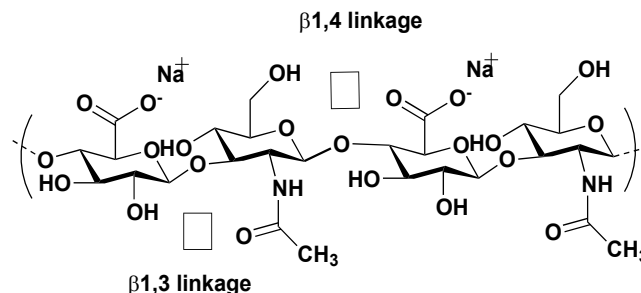


Figure 1.5 The chemical structure of Hyaluronic acid (HA)

One significant difference with PEG is the intrinsic biological activity of HA. HA is known to have anti-inflammatory activities and is recognized by cells through the cell surface receptors that promote a motile phenotype (CD44, RHAMM, ICAM-1); it is this recognition that has shown to greatly influence some biological processes such as metastasis, morphogenesis, inflammation and wound repair. Another major difference is that HA is highly degradable *in vivo* by the enzyme hyaluronidase, and the products of this degradation have been reported to influence and improve the wound healing process.⁴⁹⁻⁵¹ The high viscosity of HA offers an advantage for localization and lubrication applications. The final major difference with PEG is that while PEG can be synthesized to be reactive at one or both ends of the molecule using a broad range of reactive groups that do not cross-react with the polyether chain, most chemical functionalization strategies of HA can react at hydroxyl and carboxylic acid groups on every monomer and the residual groups on HA limit options for reactive groups.⁵²⁻⁵⁴ This provides an advantage in terms of higher reactivity of HA but also a challenge in controlling chemical functionalization, especially since site-specific functionalization of HA is essentially impossible. Soluble HA has been used in clinical applications including ocular surgery, visco-supplementation for arthritis

and wound healing. However, the relative rapid degradation and clearance *in vivo* of uncross-linked HA limit many direct clinical applications.⁵⁵

1.1. Microfabrication of polymeric biomaterials

Recent advances in microfabrication techniques have allowed for a wide range of opportunities in biomaterials. Combining successes in basic material design, chemical and physical properties with elaborate control over the underlying microarchitecture, which enables obtaining highly organized constructs able to mimic, treat and eventually replace diseased and damaged tissue organs. While utilized by many researchers to engineer 3D microarchitectures, these methods often face serious common challenges that limit their universal applicability to tissue engineering. In general, such challenges are related to interfacial cell-biomaterial interactions, porosity and efficient inter-scaffold biological mass transport, adequate vascularization, and eventually functionality of the newly forming tissue.

Much of the recent developments in microfabrication methods are aimed at addressing two main important design criteria: porosity and 3D structure. Tailoring these two criteria to the specific application in hand offers valuable tools for the success of biomaterials-based approaches. Extensive reviews of the current microfabrication methods of polymeric biomaterials are available in the literature and are outlined in table 1.2 below.⁵⁶ This section gives a brief overview of the some microfabrication techniques currently used in developing 3D biomaterials utilized for tissue engineering approaches; focus is directed to the basic principle attempting to identify patterns and common features among these techniques.

1.1.1.Porosity control

The purpose of biomaterials scaffolds is to provide temporary structural and functional support to the newly forming tissue. This dictates the need for the gradual clearance of the scaffold, followed by substitution with the new tissue. (Fig. 1.6.) The interfacial properties of the scaffold are very important, but most importantly the bulk properties are detrimental to the functionality of the new tissue. The scaffold materials must be porous enough to allow for the sufficient and active transport of nutrients and cells throughout the scaffold. This allows for cell arrangement and differentiation, ECM deposition and adequate vascularization. Moreover, the type and interconnectivity of these pores are rather important. For the newly formed tissue to be completely functional, cells, ECM and blood vessels must be homogenously distributed and supplied to all parts of the tissue. Therefore, the pores of the temporary scaffold must be highly interconnected, and much attention has been focused on this aspect of scaffold design.

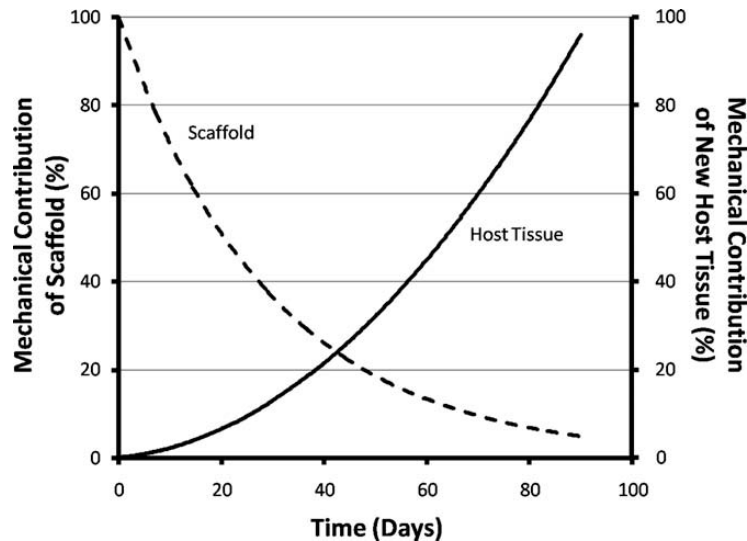


Figure 1.6 A representation of the temporary role of TE scaffold supporting the injured tissue during as compared to that of newly-formed tissue¹²

1.1.1.1.Porogen Leaching:

The final goal of porogen leaching methods is to produce biomaterials scaffolds with controlled pore size and architecture using appropriate porogen particles during the fabrication process. First, a porogen is dispersed within the polymer solution, prior to curing, at the desired concentration and density. These two parameters combined with the type and size of the used porogen will eventually determine the actual pore size and architecture. Following the uniform dispersion of porogens, the polymer scaffold is allowed to solidify to the desired 3D architecture engulfing the dispersed porogen particles within the polymer feature creating a continuous polymer-porogen network. These features are then immersed in suitable solvents that dissolve or leach the porogens away from the polymer scaffold, but do not affect the final feature size or design. Once the porogen particles are leached out, a highly porous polymeric construct is obtained.⁵⁷⁻⁵⁸

Of central importance to this method is the type of porogen used. Many different types of porogens have been reported in the literature which gives this method its versatility and wide applicability. Some of the porogen materials used include polysaccharides,⁵⁹ salts,^{57, 59-61} as well as gelatin.⁶² An added advantage is the ability to tailor the pore feature size and architecture to the desired final applications by controlling the porogen concentration, size and particle geometry.^{2, 34, 63-64}

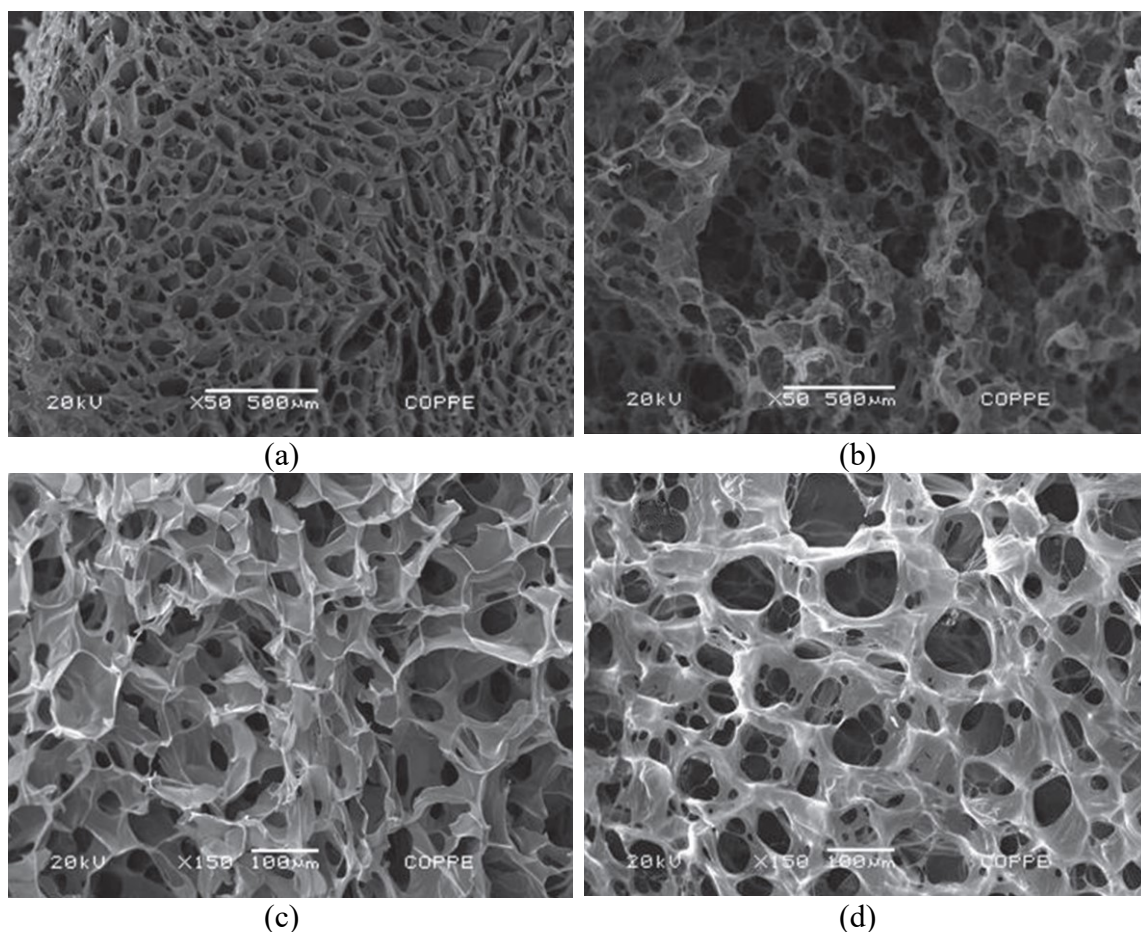


Figure 1.7 SEM micrographs a) Chitosan 50x; b) Collagen-chitosan 50x; c) Chitosan 150x; and d) Collagen-chitosan 150x.⁶⁵

1.1.1.2. Gas foaming:

Gas foaming technique is ideal for creating microporous biomaterials with controlled and uniform network of pores. Similar to salt leaching, it involves the dispersion of a gaseous phase within the polymer solution. Upon polymer solidification, the gas is then allowed to disperse out of the polymer network, which leads to the formation of highly porous microstructures. Bubbling the polymer solution with the desired gas takes place either via generating the gas bubbles *in situ*,⁶⁶ inert gas addition⁶⁷ or premixing the gas with the polymer solutions forming a dense CO₂/polymer mixture at high pressures.⁶⁸ While many groups reported the inclusion of cells within the fabricated structures, gas foaming

methods often involve harsh conditions such as the use of bubbling surfactants and dense streams of CO₂, which greatly affect cell survival.

1.1.2. Three dimensional architecture control:

Researchers have been making important strides when it comes to controlling the three dimensional architecture of biomaterials. Due to the major advances in the semiconductor industry and the ever-increasing demand on integrated circuits and like materials, the need for advanced and precise micro and nano fabrication methods becomes great. Such methods, though developed for other industrial disciplines, have been adopted, modified and utilized heavily in the field of tissue engineering. Despite the recent advances in creating micro and nano-scale biomaterials constructs, serious challenges still face such approaches. Such challenges could be technology-related, e.g. spatial and temporal control over fabricated features, or applications-relates, e.g. cell and biologics interactions and incorporation within the designed constructs. These methods include harnessing the basic material properties in conjunction with one of these basic principles: Photoillumination, micromolding, and 3D printing.

1.1.2.1. Photoillumination-based methods:

Photolithographic methods are of the most common microfabrication techniques owing to their relative simplicity and wide range of applicability. The common concept of these methods has been extensively used for protein, synthetic materials and cell-seeded materials micropatterning. Creating micropatterns via direct photopolymerization of polymers through a photomask is a common theme used in photolithographic methods. Of critical value is the 2D and 3D design of the photomask. Advances in processing and

fabrication led to significant decreases in feature sizes, which, consequently, led to more applications in tissue engineering scaffolds. These masks are composed of transparent patterns that permit light, most commonly UV light, to pass through precise channels onto the photopolymerizable polymer. As a result of illuminating the construct along the path of these patterns on the mask, the design feature is created exactly according to the predesigned mask pattern.

These methods have been employed to create constructs of various polymers, commonly with photopolymerizable acrylate groups within the polymer backbone. While straightforward, the choice of the photo initiator is key. Limiting the cytotoxicity of the construct is possible by controlling the initiator concentration and chemistry. Tailoring the four components of this process—photopolymerizable polymer, patterned photomask, initiator, and release mechanism—allows for the direct control over the final properties of the scaffold. As such, numerous reports have shown the use of many acrylate-modified polymers as hydrogel precursors fabricated using these methods. Such polymers include, but are not limited to, poly(ethyleneglycol) (PEGDA),⁶⁹ gelatin methacrylate (gelMA),⁷⁰ methacrylated hyaluronic acid (HAGM)⁷¹ and copolymers involving them. Photopatterning methods have been reported to afford hydrogels with feature sizes in the range of 100 μm .⁷²

1.1.2.2. Micromolding-based methods:

Another popular approach to microfabrication is the polymerization of prepolymers between a flat surface and an inert polymeric negative mold such as PDMS, Teflon or polyurethanes. Using micromolding methods, biomaterials constructs have been prepared

of polymers, proteins as well as cellular components. While the design and fabrication of the negative mold is key to controlling feature size and resolution, mold swelling, erosion and cross contamination are some of the limitations of micromolding. As such, constructs of feature sizes between 1 μm to over 500 μm have been reported.⁷³

Owing to their low cost, reproducibility as well as modularity, micromolds have become important parts of many microfabrication methods, which limit the need for clean room facilities and more expensive photolithographic equipment.^{2, 74} The type of materials used as micromolding precursors vary from naturally ionic crosslinkable hydrogels such as alginates,⁷⁵ methacrylated HA⁷⁶ and PEG,⁷⁷ as well as cellular-functional proteins and fibers.⁷⁸

1.1.2.3 Rapid prototyping methods

Despite the many advantages micromolding and photolithographic methods have, they are still faced by some challenges that limit their clinical applications. The ideal microfabrication methods would be low cost, precise and controlled small features size, high throughput and patient-specific. Rapid prototyping methods offer a very promising alternative to creating such constructs. Beside their high throughput automation and very precise and modular feature size and design, such approaches offer the option of creating constructs and tissue that are specifically tailored to specific patients or conditions, making their translation to the clinic feasible, while not there yet.

The basic principle that most rapid prototyping methods build upon is the use of computer-aided design (CAD) models. These designs are created individually for each construct and then fed to a computer that controls a material creator that, in turn, creates

the material in a layer-by-layer fashion. The major advantage of these methods is the ability to go to very small feature sizes while maintaining precise control over the 3D geometry. This is possible because the CAD design is sliced into very thin cross-sectional layers of the print. The material is created either via 1) layer-by-layer deposition of polymerizable material through an extruder, such is the case in printer-based methods; 2) layer-by-layer polymerization from a material reservoir, such is the case laser-based methods; 3) layer-by-layer deposition of polymer melts, such is the case in nozzle-based methods.⁷⁹

In the past 10 years, The prospects of using such precise control for the designing and creating tissue replacement constructs or even live tissue sample and organs has motivated a lot of interesting research focused on optimizing the process. Such research was to enhance extrusion mechanisms, slicing patterns and material curing methods. As such, the three main rapid prototyping could be classified according to the curing method employed. In a very general manner, these classifications are photofabrication (photopolymerizable polymer constructs), thermofabrication (curing using heat) and powder fabrication (curing of deposited powders).^{2, 80} These methods have been reported to be able to print biomaterials scaffold of various feature sizes and resolution of many materials types such as hydrogels, PEG scaffolds, PLLA, PCL. Yeong, et al. provides a valuable review of these materials.⁸¹

Technique	Porosity (%)	Pore size (μ)	Biomaterial	Comments	Cell type/tissue engineering application	Reference
Conventional techniques						
Foaming using blowing agents	–	20-1000	starch/ SEVA-C	non porous outer layer (skin)	osteosarcoma – bone tissue engineering <i>in vitro</i>	Gomes <i>et al.</i> , 2001a,b
	80	350	PLLA	Pore interconnectivity 99%	–	Lin <i>et al.</i> , 2003
Foaming using CaCO₃	81	100-1000	chitin	difficult control	–	Chow and Khor, 2000
Foaming using NH₄ HCO₃	94	100-500	PLLA	interconnected pores; moldable shapes	hepatocyte – liver tissue engineering <i>in vitro</i>	Nam <i>et al.</i> , 2000
Super-critical fluid technology (gas foaming)	93	100	PLGA	only partially interconnected pores; formation of a skin layer	–	Mooney <i>et al.</i> , 1996a
	10-30	100	PLGA	high volume of noninterconnecting micro-pores	smooth muscle – muscle tissue engineering <i>in vitro</i>	Harris <i>et al.</i> , 1998
Super-critical fluid technology (gas foaming) particulate leaching	91-95	micro 35	PLGA	low volume of noninterconnecting micro-pores	–	W hang <i>et al.</i> , 1995
		macro 200		low volume of interconnecting macro-pores		
Sintered microspheres	32-39	67–300	PLGA	interconnected pores; reverse template of trabeculae	osteoblast/fibroblast – bone tissue engineering <i>in vitro</i>	Borden <i>et al.</i> , 2002a,b, 2003
Fused salt particles solvent casting particulate leaching	97	250–425	PLA, PEGT/ PBT, PCL	improved interconnectivity compared to solvent casting particulate leaching	–	Hou <i>et al.</i> , 2003b
Fused salt particles/gas foaming particulate leaching	94	78	PLGA		–	Murphy <i>et al.</i> , 2002
Coagulation particulate leaching	92	800–1500	PLGA	large interconnections (350 μm), irregular pore morphology	–	Holy <i>et al.</i> , 1999

Technique	Porosity (%)	Pore size (μ)	Biomaterial	Comments	Cell type/tissue engineering application	Reference
	98	250–1180	PLA, PEGT/ PBT, PCL	wide range of porosities and pore size	–	Hou <i>et al.</i> , 2003a
Solvent casting particulate leaching	82–92	200	PLA/PVA	spherical pores, salt particles remain in matrix, only thin membranes or small devices	hepatocyte – liver tissue engineering <i>in vitro</i>	Mooney <i>et al.</i> , 1995
Solvent merging particulate leaching	95	250–500	PLGA	good interconnectivity	–	Liao <i>et al.</i> , 2002
Solvent casting extrusion	90	30	PLGA, PLLA	highly porous; interconnected pores; severe salt breakdown during extrusion	–	Widmer <i>et al.</i> , 1998
Solvent induced phase separation (immersion precipitation)	95	10	PU	only possible for films/tubes	–	Chen <i>et al.</i> , 1999
Emulsion freeze drying	97	200	PLGA, PEG	high volume of interconnecting micro-pores	bone tissue engineering	Whang <i>et al.</i> , 1995, 1998
TIPS	97	200	PLA, PLA/ HA	high volume of interconnecting micro-pores	–	Schugens <i>et al.</i> , 1996; Zhang and Ma, 1999a
Solid–liquid phase separation (freeze-drying)	97	500	PLA, PLLA/ PLGA, PLA/HA	1,4-dioxane, phenol, benzene, naphthalene are toxic solvents	osteosarcoma, MC3T3 – cytotoxicity test <i>in vitro</i>	Liu <i>et al.</i> , 1992; Loh <i>et al.</i> , 1996; Zhang and Ma, 1999a,b; Ma and Zhang, 2001
Liquid–liquid phase separation	–	20	pHEMA/ MMA	centrifugal casting produces porous inner layer, dense outer layer of tube	neural/spinal cord tissue engineering	Dalton <i>et al.</i> , 2002
Polymerization induced phase separated scaffolds	90	5–50	pHEMA, pHPMA	hydrogel scaffolds, mechanically weak; formed in water or acetone	ophthalmic – neural tissue engineering	Hicks <i>et al.</i> , 1999; Loh <i>et al.</i> , 2001; Hicks <i>et al.</i> , 2003;

Technique	Porosity (%)	Pore size (μ)	Biomaterial	Comments	Cell type/tissue engineering application	Reference
Textile technologies						
Nonwoven fiber	97	100–500	PGA, PLLA/PLGA	high porosity; insufficient mechanical properties	smooth muscle, endothelial, chondrocyte – muscle, blood vessel, cartilage tissue engineering <i>in vitro</i> and <i>in vivo</i> in nude mice, rabbit	Leidner <i>et al.</i> , 1983; Mikos <i>et al.</i> , 1993a; Freed <i>et al.</i> , 1994; Mooney <i>et al.</i> , 1996b
Woven fabrics	–	–	LLDPE	insufficient mechanical properties	–	Wintermantel <i>et al.</i> , 1996; Shikinami <i>et al.</i> , 1998
Fiber bonding	81	–	PGA	described process only possible for PGA-PLLA combination		Mikos <i>et al.</i> , 1993a
	–	–	PGA PLLA/PLGA	coating of fiber mesh with another polymer		Mooney <i>et al.</i> , 1996b
Nanofiber electrospinning	–	–	PCL, PU	interconnected pore structure with a high specific surface area	MSC – bone tissue engineering <i>in vitro</i>	Yoshimoto <i>et al.</i> , 2003; Kidoaki <i>et al.</i> , 2005; Matsuda <i>et al.</i> , 2005
	–	–	PEO-PCL	direct melt electrospinning technique; solventfree process	fibroblast	Dalton <i>et al.</i> , 2006
Porous membrane lamination	90	10–400	PLA, PLGA	irregular pore size, tedious procedure	–	Mikos <i>et al.</i> , 1993b
Hydrocarbon templating	88	300–1000	PLA	allows incorporation of proteins	chondrocyte – cartilage tissue engineering <i>in vitro</i>	Shastri <i>et al.</i> , 2000

Technique	Porosity (%)	Pore size (μ)	Biomaterial	Comments	Cell type/tissue engineering application	Reference
SFF techniques						
Laser and UV light sources SLA	90	200	DEF/PPF BAPO, P4HB/PHOH	100% interconnected macro-pore structure; polymers for bone, heart valve applications	–	Sodian <i>et al.</i> , 2002 ; Cooke <i>et al.</i> , 2003
	–	175–400	PEG-DMA	spatially patterned internal architectures; noninterconnecting dense pore/channel walls	MSC – bone tissue engineering <i>in vitro</i>	Mapili <i>et al.</i> , 2005
Micro SLA	–	165–650	PEG-DA	allows fabrication of complex internal features along with precise spatial distribution of biological factors	BMSC – bone tissue engineering	Lu <i>et al.</i> , 2006
SLS	–	50	PEEK/HA	low porosity primarily for drug release; PEEK/HA composite scaffolds	drug release; bone tissue engineering	Cheah <i>et al.</i> , 2002 ; Tan <i>et al.</i> , 2003
	25	30	CPP	low porosity, basic shapes	Bone tissue engineering	Porter <i>et al.</i> , 2001
	63–79	1750–2500	PCL	100% interconnected, topography optimized pore structure matching bone mechanical properties Anatomic shape	BMP-7-induced fibroblasts – bone tissue engineering <i>in vivo</i> in mouse and mini-pig	Williams <i>et al.</i> , 2005
SGC	3–10	–	vinylated polysaccharide/gelatine	noninterconnecting pores	tubular scaffolds for nerve, blood vessel tissue engineering	Matsuda and Magoshi, 2002
	–	100–500	PEG-DA	photo-patterning of single or multiple cell layers; photo-initiator concentration influences cell viability; photopolymerizing hydrogels	hepatoma cell line – liver tissue engineering <i>in vitro</i>	Liu <i>et al.</i> , 2002

Technique	Porosity (%)	Pore size (μ)	Biomaterial	Comments	Cell type/tissue engineering application	Reference
Printing Technology						
3D Printing (3DP)	60	45–150	PLA	100% interconnected macro-pore structure; irregular pore architecture; limited resolution	fibroblast, vascular smooth muscle, epithelial cells – soft tissue engineering <i>in vitro</i>	Zeltinger <i>et al.</i> , 2001
	45	1000–1600	PLGA/-TCP, HA	100% interconnected macro-pore structure containing 15- m micropores; shrinkage postsintering	bone tissue engineering <i>in vivo</i> in rabbit calvarial defect	Roy <i>et al.</i> , 2003a,b
	–	450	HA	100% interconnected macro-pore structure containing 10- to 30- m micropores; shrinkage postsintering; limited mechanical properties	bone tissue engineering	Seitz <i>et al.</i> , 2005
Cell Printing	–	350	collagen I/soy-agar gel	cells embedded in gel; 90 % cell survival; limited resolution	ovarian, endothelial, neuronal cells – cell viability <i>in vitro</i>	Boland <i>et al.</i> , 2003; Wilson <i>et al.</i> , 2003; Varghese <i>et al.</i> , 2005; Xu <i>et al.</i> , 2005
Extrusion/direct writing FDM	80	150–700	PCL	100% interconnected macro-pore structure; 200 m diameter fiber; good mechanical properties	MSC – bone tissue engineering <i>in vitro</i> and <i>in vivo</i> in rabbits	Hutmacher <i>et al.</i> , 2001 ; Zein <i>et al.</i> , 2002 ; Schantz <i>et al.</i> , 2003
	60	–	PLA	PLA degradation during processing	bone tissue engineering	Xiong <i>et al.</i> , 2001

Technique	Porosity (%)	Pore size (μ)	Biomaterial	Comments	Cell type/tissue engineering application	Reference
3DP	75	100–1000	agar, fibrin/alginate	100% interconnected macro-pore structure; 500 μm diameter fiber; only hydrogel materials investigated; room temperature fabrication	fibroblast – soft tissue engineering <i>in vitro</i>	Landers <i>et al.</i> , Landers and Mulhaupt, 2000 ; Landers <i>et al.</i> , 2002a,b
	–	200–1000	chitosan/HA	100% interconnected macro-pore structure; 200 μm diameter fiber; room temperature fabrication	osteoblast – bone tissue engineering <i>in vitro</i>	Ang <i>et al.</i> , 2002
	80	500	PCL, PEG/PCL	100% interconnected macro-pore structure; 400 μm diameter fiber	MSC – bone tissue engineering <i>in vitro</i>	Huang <i>et al.</i> , 2004
	90	100–2000	PEGT/PBT	100% interconnected macro-pore structure; 175 μm diameter fiber; good dynamic mechanical properties; anisotropic pore architectures	chondrocyte – cartilage tissue engineering <i>in vitro</i> and <i>in vivo</i> in nude mice	Woodfield <i>et al.</i> , 2004, 2005 ; Malda <i>et al.</i> , 2005 ; Miot <i>et al.</i> , 2005 ; Moroni <i>et al.</i> , 2006a,b
	62–78	100	PEGT/PBT, PBMA, PCL	100% interconnected macro-pore structure; core-shell or hollow fiber obtained via viscous encapsulation; growth factor/drug delivery	cartilage tissue engineering	Moroni <i>et al.</i> , 2006c
Direct writing	90	5–100	PAA/PEI polyelectrolyte ink	100% interconnected macro-pore structure; 1 μm diameter fiber; fiber micro-pore structure with direct writing in low pH reservoir	–	G ratson and Lewis, 2005

Technique	Porosity (%)	Pore size (μ)	Biomaterial	Comments	Cell type/tissue engineering application	Reference
Indirect SFF techniques						
Negative mold casting	–	50–800	PLA, PLA/HA, PPF/TCP	100% interconnected macro-pore structure; integration to form composite scaffolds; shrinkage after sintering; topography optimized pore structure matching bone mechanical properties; anatomic shape	biphasic scaffold for cartilage, bone tissue engineering	Taboas <i>et al.</i> , 2003 ; Schek <i>et al.</i> , 2004 ; Lin <i>et al.</i> , 2005
	50	50–400	HA (-TCP)	100% interconnected macro-pore structure; shrinkage after sintering; preferential bone growth on rough, micro-pore surface	BMC – bone tissue engineering <i>in vitro</i> and <i>in vivo</i>	Wilson <i>et al.</i> , 2004
	–	50–800	collagen I	100% interconnected vascular channels; incorporated into macro-porous, freeze-dried collagen type I	blood vessel tissue engineering	Sachlos <i>et al.</i> , 2003
Micro-robotics/MEMS						
MEMS	–	45–3000	poly(glycerol sebacate)	interconnected channels in 2D with controlled architecture	endothelial cell – vascular tissue engineering <i>in vitro</i>	Fidkowski <i>et al.</i> , 2005

Table 1.2. Summary of current literature on scaffold design and fabrication techniques and their application in tissue engineering⁵⁶

This thesis introduces novel biomaterials approaches for various therapeutic and diagnostic applications using nature as a guide and inspiration, as previously described. In chapter 2, titled: **Reducing Protein Adsorption with Polymer-grafted Hyaluronic Acid Coatings**, a novel antifouling coating system based on a thermoresponsive hyaluronic acid polymer hybrid is reported. These materials are designed, synthesized and characterized to possess reversible coating and adhesive properties at the physiological temperature of the human body, presenting a nonfouling, hydrophilic layer to the solution. A comparison of

the antifouling profile of HA to that of similar polysaccharides, namely dextran, alginate and carboxymethyl cellulose (CMC), is performed in chapter 3 under the title: **Polymer-grafted Polysaccharide Coatings for Reduced Blood Protein Adsorption**. This comparison aims to provide explanations of film formation mechanism in solution and the affect polysaccharide chemistry has on protein fouling in solution. A very promising application of such coatings is then designed to enhance detection accuracy and precision of clinically relevant diagnostic methods, namely enzyme-linked immunosorbent assay (ELISA), which is introduced in chapter 4, titled: **Non-Fouling Hyaluronic Acid Coatings for Improved Sandwich ELISA Measurements in Serum Protein Mixtures**. Chapter 5, entitled **Microfabricated and Nanofabricated Hyaluronic Acid Constructs: Design and Applications**, deals with microfabrication of tissue engineering scaffolds using a novel modified rapid prototyping method for 3D printing of modified HA. Moreover, the potential of micro needles arrays (MNAs) of HA-based antibody-conjugates in treating relevant disorders is also investigated. The final chapter of this thesis, Chapter 6: **Microfabricated Gecko-inspired Microfibers for Enhanced Wet Tissue Adhesion**, explores the wet adhesives properties of mussel-inspired wet adhesives coatings of gecko-inspired polyurethane microfibers.

References

- (1)Langer, R., Tissue engineering. *Molecular Therapy : The Journal of the American Society of Gene Therapy* **2000**, *1* (1), 12-5.
- (2)Zorlutuna, P.; Annabi, N.; Camci-Unal, G.; Nikkhah, M.; Cha, J. M.; Nichol, J. W.; Manbachi, A.; Bae, H.; Chen, S.; Khademhosseini, A., Microfabricated biomaterials for engineering 3d tissues. *Adv Mater* **2012**, *24* (14), 1782-804.
- (3)Langer, R.; Vacanti, J. P., Tissue engineering. *Science* **1993**, *260* (5110), 920-926.
- (4)Vacanti, J. P.; Langer, R., Tissue engineering: The design and fabrication of living replacement devices for surgical reconstruction and transplantation. *The Lancet* **1999**, *354*, S32-S34.
- (5)Langer, R.; Tirrell, D. A., Designing materials for biology and medicine. *Nature* **2004**, *428* (6982), 487-492.
- (6)Bissell Dm Fau - Stamatoglou, S. C.; Stamatoglou Sc Fau - Nermut, M. V.; Nermut Mv Fau - Hughes, R. C.; Hughes, R. C., Interactions of rat hepatocytes with type iv collagen, fibronectin and laminin matrices. Distinct matrix-controlled modes of attachment and spreading. (0171-9335 (Print)).
- (7)Badylak, S. F., The extracellular matrix as a scaffold for tissue reconstruction. *Seminars in Cell & Developmental Biology* **2002**, *13* (5), 377-383.
- (8)Kim, B.-S.; Mooney, D. J., Development of biocompatible synthetic extracellular matrices for tissue engineering. *Trends in Biotechnology* **1998**, *16* (5), 224-230.

- (9)Mouw, J. K.; Ou, G.; Weaver, V. M., Extracellular matrix assembly: A multiscale deconstruction. *Nat Rev Mol Cell Biol* **2014**, *15* (12), 771-785.
- (10)Timpl, R., Macromolecular organization of basement membranes. *Current Opinion in Cell Biology* **1996**, *8* (5), 618-624.
- (11)Ponce, M. L.; Nomizu, M.; Delgado, M. C.; Kuratomi, Y.; Hoffman, M. P.; Powell, S.; Yamada, Y.; Kleinman, H. K.; Malinda, K. M., Identification of endothelial cell binding sites on the laminin γ 1 chain. *Circulation Research* **1999**, *84* (6), 688-694.
- (12)Badylak, S. F.; Freytes, D. O.; Gilbert, T. W., Extracellular matrix as a biological scaffold material: Structure and function. *Acta Biomaterialia* **2009**, *5* (1), 1-13.
- (13)Hawkins, A. J. S.; Bayne, B. L., Seasonal variation in the relative utilization of carbon and nitrogen by the mussel *mytilus edulis*: Budgets, conversion efficiencies and maintenance requirements. *Mar. Ecol. Prog. Ser.* 25:181–88. *Marine Ecology - Progress Series* **1985**, *25*, 181–188.
- (14)Lee, B. P.; Messersmith, P. B.; Israelachvili, J. N.; Waite, J. H., Mussel-inspired adhesives and coatings. *Annual Review of Materials Research* **2011**, *41*, 99-132.
- (15)Waite, J. H., Mussel power. *Nature Materials* **2008**, *7*, 8-10.
- (16)Deming, T. J., Mussel byssus and biomolecular materials. *Curr. Opin. Chem. Biol.* **1999**, *3*, 100-105.
- (17)Lee, H.; Dellatore, S. M.; Miller, W. M.; Messersmith, P. B., Mussel-inspired surface chemistry for multifunctional coatings. *Science* **2007**, *318* (5849), 426-30.
- (18)Lee, H.; Lee, B. P.; Messersmith, P. B., A reversible wet/dry adhesive inspired by mussels and geckos. *Nature* **2007**, *448*, 338.

- (19)Guvendiren, M.; Messersmith, P. B.; Shull, K. R., Self-assembly and adhesion of dopa-modified methacrylic triblock hydrogels. *Biomacromolecules* **2008**, *9*, 122-128.
- (20)Lee, H.; Scherer, N. F.; Messersmith, P. B., Single-molecule mechanics of mussel adhesion. *Proc. Natl. Acad. Sci. U.S.A* **2006**, *103* (35), 12999-13003.
- (21)Yang, F.; Zhao, B., Adhesion properties of self-polymerized dopamine thin film. *The Open Surface Science Journal* **2011**, *3*, 115-122.
- (22)Tamarin A Fau - Lewis, P.; Lewis P Fau - Askey, J.; Askey, J., The structure and formation of the byssus attachment plaque in mytilus. **1976**, (0362-2525 (Print)).
- (23)Glass, P.; Chung, H.; Washburn, N. R.; Sitti, M., Enhanced reversible adhesion of dopamine methacrylamide-coated elastomer microfibrillar structures under wet conditions. *Langmuir : The ACS Journal of Surfaces and Colloids* **2009**, *25* (12), 6607-6612.
- (24)Lee, H.; Lee, B. P.; Messersmith, P. B., A reversible wet/dry adhesive inspired by mussels and geckos. *Nature* **2007**, *448* (7151), 338-341.
- (25)Brubaker, C. E.; Kissler, H.; Wang, L.-J.; Kaufman, D. B.; Messersmith, P. B., Biological performance of mussel-inspired adhesive in extrahepatic islet transplantation. *Biomaterials* **2010**, *31* (3), 420-427.
- (26)Shao, H.; Bachus, K. N.; Stewart, R. J., A water-borne adhesive modeled after the sandcastle glue of p. Californica. *Macromolecular Bioscience* **2009**, *9* (5), 464-471.
- (27)Bilic, G.; Brubaker, C.; Messersmith, P. B.; Mallik, A. S.; Quinn, T. M.; Haller, C.; Done, E.; Gucciardo, L.; Zeisberger, S. M.; Zimmermann, R., Injectable candidate sealants for fetal membrane repair: Bonding and toxicity in vitro. *American Journal of Obstetrics and Gynecology* **2010**, *202* (1), 85. e1-85. e9.

- (28)Cronenwett, J. L.; Johnston, K. W.; Rutherford, R. B., *Rutherford's vascular surgery*. Elsevier Science Health Science Division: 2010.
- (29)Galis, Z. S.; Sukhova, G. K.; Lark, M. W.; Libby, P., Increased expression of matrix metalloproteinases and matrix degrading activity in vulnerable regions of human atherosclerotic plaques. *Journal of Clinical Investigation* **1994**, *94* (6), 2493.
- (30)Wang, L.; Simon, C.; Siu, D.; Soo, Y. O.; Wong, L. K.; Leung, T. W., Abstract t p104: Remodeling of intracranial atherosclerotic plaques. *Stroke* **2015**, *46* (Suppl 1), ATP104-ATP104.
- (31)Watson, T.; Shantsila, E.; Lip, G. Y., Mechanisms of thrombogenesis in atrial fibrillation: Virchow's triad revisited. *The Lancet* **2009**, *373* (9658), 155-166.
- (32)O'Connor, C.; Adams, J. U., Essentials of cell biology. *Cambridge, MA: NPG Education* **2010**, 71-82.
- (33)Peppas, N. A.; Langer, R., New challenges in biomaterials. *Science* **1994**, *263* (5154), 1715-1720.
- (34)Peppas, N. A.; Hilt, J. Z.; Khademhosseini, A.; Langer, R., Hydrogels in biology and medicine: From molecular principles to bionanotechnology. *Advanced Materials* **2006**, *18* (11), 1345-1360.
- (35)Langer, R., New methods of drug delivery. *Science* **1990**, *249* (4976), 1527-1533.
- (36)Banerjee, I.; Pangule, R. C.; Kane, R. S., Antifouling coatings: Recent developments in the design of surfaces that prevent fouling by proteins, bacteria, and marine organisms. *Advanced Materials* **2011**, *23* (6), 690-718.
- (37)Veronese, F. M.; Pasut, G., Pegylation, successful approach to drug delivery. *Drug Discovery Today* **2005**, *10* (21), 1451-1458.

- (38)Almany, L.; Seliktar, D., Biosynthetic hydrogel scaffolds made from fibrinogen and polyethylene glycol for 3d cell cultures. *Biomaterials* **2005**, 26 (15), 2467-2477.
- (39)Nair, L. S.; Laurencin, C. T., Biodegradable polymers as biomaterials. *Progress in Polymer Science* **2007**, 32 (8), 762-798.
- (40)Duncan, R., The dawning era of polymer therapeutics. *Nature Reviews Drug Discovery* **2003**, 2 (5), 347-360.
- (41)Hermanson, B. T.; Mallia, A.; Smith, P., Academic press. *San Diego, Calif* **1996**.
- (42)Hamidi, M.; Azadi, A.; Rafiei, P., Pharmacokinetic consequences of pegylation. *Drug Delivery* **2006**, 13 (6), 399-409.
- (43)Hennink, W.; Van Nostrum, C., Novel crosslinking methods to design hydrogels. *Advanced Drug Delivery Reviews* **2012**, 64, 223-236.
- (44)Elisseeff, J.; Anseth, K.; Sims, D.; McIntosh, W.; Randolph, M.; Langer, R., Transdermal photopolymerization for minimally invasive implantation. *Proceedings of the National Academy of Sciences* **1999**, 96 (6), 3104-3107.
- (45)Sun, L. T.; Bencherif, S. A.; Gilbert, T. W.; Lotze, M. T.; Washburn, N. R., Design principles for cytokine-neutralizing gels: Cross-linking effects. *Acta Biomaterialia* **2010**, 6 (12), 4708-4715.
- (46)Garland, A.; Shen, L.; Zhu, X., Mobile precursor mediated protein adsorption on solid surfaces. *Progress in Surface Science* **2012**, 87 (1), 1-22.
- (47)Dhandayuthapani, B.; Yoshida, Y.; Maekawa, T.; Kumar, D. S., Polymeric scaffolds in tissue engineering application: A review. *International Journal of Polymer Science* **2011**, 2011.

- (48)Shi, J.; Xing, M. M.; Zhong, W., Development of hydrogels and biomimetic regulators as tissue engineering scaffolds. *Membranes* **2012**, 2 (1), 70-90.
- (49)Meyer, K.; Palmer, J. W., The polysaccharide of the vitreous humor. *Journal of Biological Chemistry* **1934**, 107 (3), 629-634.
- (50)Lapčák, L.; Lapcik, L.; De Smedt, S.; Demeester, J.; Chabreck, P., Hyaluronan: Preparation, structure, properties, and applications. *Chemical Reviews* **1998**, 98 (8), 2663-2684.
- (51)Stern, R.; Asari, A. A.; Sugahara, K. N., Hyaluronan fragments: An information-rich system. *European Journal of Cell Biology* **2006**, 85 (8), 699-715.
- (52)Kogan, G.; Šoltés, L.; Stern, R.; Gemeiner, P., Hyaluronic acid: A natural biopolymer with a broad range of biomedical and industrial applications. *Biotechnology Letters* **2007**, 29 (1), 17-25.
- (53)Schanté, C. E.; Zuber, G.; Herlin, C.; Vandamme, T. F., Chemical modifications of hyaluronic acid for the synthesis of derivatives for a broad range of biomedical applications. *Carbohydrate Polymers* **2011**, 85 (3), 469-489.
- (54)Prestwich, G. D.; Marecak, D. M.; Marecek, J. F.; Vercruysse, K. P.; Ziebell, M. R., Controlled chemical modification of hyaluronic acid: Synthesis, applications, and biodegradation of hydrazide derivatives. *Journal of Controlled Release* **1998**, 53 (1), 93-103.
- (55)Burdick, J. A.; Prestwich, G. D., Hyaluronic acid hydrogels for biomedical applications. *Advanced Materials* **2011**, 23 (12), H41-H56.
- (56)Blitterswijk, C. v., *Tissue Engineering*. 1 ed.; 2008; p 760.

- (57)Annabi, N.; Nichol Jw Fau - Zhong, X.; Zhong X Fau - Ji, C.; Ji C Fau - Koshy, S.; Koshy S Fau - Khademhosseini, A.; Khademhosseini A Fau - Dehghani, F.; Dehghani, F., Controlling the porosity and microarchitecture of hydrogels for tissue engineering. *Tissue Eng Part, B. Rev* **2011**, (1937-3376 (Electronic)).
- (58)Yang, Y.; Zhao, J.; Zhao, Y.; Wen, L.; Yuan, X.; Fan, Y., Formation of porous plga scaffolds by a combining method of thermally induced phase separation and porogen leaching. *Journal of Applied Polymer Science* **2008**, *109* (2), 1232-1241.
- (59)Horák, D.; Hlídková, H.; Hradil, J.; Lapčíková, M.; Šlouf, M., Superporous poly(2-hydroxyethyl methacrylate) based scaffolds: Preparation and characterization. *Polymer* **2008**, *49* (8), 2046-2054.
- (60)Park, J. S.; Woo, D. G.; Sun, B. K.; Chung, H.-M.; Im, S. J.; Choi, Y. M.; Park, K.; Huh, K. M.; Park, K.-H., In vitro and in vivo test of peg/pcl-based hydrogel scaffold for cell delivery application. *Journal of Controlled Release* **2007**, *124* (1–2), 51-59.
- (61)Dadsetan, M.; Hefferan, T. E.; Szatkowski, J. P.; Mishra, P. K.; Macura, S. I.; Lu, L.; Yaszemski, M. J., Effect of hydrogel porosity on marrow stromal cell phenotypic expression. *Biomaterials* **2008**, *29* (14), 2193-2202.
- (62)Salerno, A.; Guarnieri, D.; Iannone, M.; Zeppetelli, S.; Netti, P. A., Effect of micro- and macroporosity of bone tissue three-dimensional-poly(epsilon-caprolactone) scaffold on human mesenchymal stem cells invasion, proliferation, and differentiation in vitro. *Tissue Eng Part A* **2010**, *16* (8), 2661-73.
- (63)Silverstein, M. S.; Cameron, N. R.; Hillmyer, M. A., *Porous polymers*. Wiley: 2011.
- (64)Annabi, N., Porous biomaterials. In *Integrated biomaterials for biomedical technology*, John Wiley & Sons, Inc.: 2012; pp 35-65.

- (65)Fernandes, L. L.; Resende, C. X.; Tavares, D. S.; Soares, G. A.; Castro, L. O.; Granjeiro, J. M., Cytocompatibility of chitosan and collagen-chitosan scaffolds for tissue engineering. *Polímeros* **2011**, *21*, 1-6.
- (66)Barbetta, A.; Rizzitelli, G.; Bedini, R.; Pecci, R.; Dentini, M., Porous gelatin hydrogels by gas-in-liquid foam templating. *Soft Matter* **2010**, *6* (8), 1785-1792.
- (67)Barbetta, A.; Massimi, M.; Di Rosario, B.; Nardecchia, S.; De Colli, M.; Devirgiliis, L. C.; Dentini, M., Emulsion templated scaffolds that include gelatin and glycosaminoglycans. *Biomacromolecules* **2008**, *9* (10), 2844-2856.
- (68)Tai, H.; Mather, M. L.; Howard, D.; Wang, W.; White, L. J.; Crowe, J. A.; Morgan, S. P.; Chandra, A.; Williams, D. J.; Howdle, S. M., Control of pore size and structure of tissue engineering scaffolds produced by supercritical fluid processing. *Eur Cell Mater* **2007**, *14*, 64-77.
- (69)Burdick, J. A.; Anseth, K. S., Photoencapsulation of osteoblasts in injectable rgd-modified peg hydrogels for bone tissue engineering. *Biomaterials* **2002**, *23* (22), 4315-4323.
- (70)Bae, H.; Ahari, A. F.; Shin, H.; Nichol, J. W.; Hutson, C. B.; Masaeli, M.; Kim, S.-H.; Aubin, H.; Yamanlar, S.; Khademhosseini, A., Cell-laden microengineered pullulan methacrylate hydrogels promote cell proliferation and 3d cluster formation. *Soft Matter* **2011**, *7* (5), 1903-1911.
- (71)Gerecht, S.; Burdick, J. A.; Ferreira, L. S.; Townsend, S. A.; Langer, R.; Vunjak-Novakovic, G., Hyaluronic acid hydrogel for controlled self-renewal and differentiation of human embryonic stem cells. *Proceedings of the National Academy of Sciences* **2007**, *104* (27), 11298-11303.

- (72)Liu Tsang, V.; Bhatia, S. N., Three-dimensional tissue fabrication. *Advanced Drug Delivery Reviews* **2004**, *56* (11), 1635-1647.
- (73)Rivest, C.; Morrison, D.; Ni, B.; Rubin, J.; Yadav, V.; Mahdavi, A.; Karp, J.; Khademhosseini, A., Microscale hydrogels for medicine and biology: Synthesis, characteristics and applications. *Journal of Mechanics of Materials and Structures* **2007**, *2* (6), 1103-1119.
- (74)Oh, J. K.; Drumright, R.; Siegwart, D. J.; Matyjaszewski, K., The development of microgels/nanogels for drug delivery applications. *Progress in Polymer Science* **2008**, *33* (4), 448-477.
- (75)Agarwal, A.; Farouz, Y.; Nesmith, A. P.; Deravi, L. F.; McCain, M. L.; Parker, K. K., Micropatterning alginate substrates for in vitro cardiovascular muscle on a chip. *Advanced Functional Materials* **2013**, *23* (30), 3738-3746.
- (76)Khademhosseini, A.; Eng, G.; Yeh, J.; Fukuda, J.; Blumling, J.; Langer, R.; Burdick, J. A., Micromolding of photocrosslinkable hyaluronic acid for cell encapsulation and entrapment. *Journal of Biomedical Materials Research Part A* **2006**, *79* (3), 522-532.
- (77)Shim, H.-W.; Lee, J.-H.; Hwang, T.-S.; Rhee, Y. W.; Bae, Y. M.; Choi, J. S.; Han, J.; Lee, C.-S., Patterning of proteins and cells on functionalized surfaces prepared by polyelectrolyte multilayers and micromolding in capillaries. *Biosensors and Bioelectronics* **2007**, *22* (12), 3188-3195.
- (78)Feinberg, A. W.; Parker, K. K., Surface-initiated assembly of protein nanofabrics. *Nano letters* **2010**, *10* (6), 2184-2191.

- (79) Billiet, T.; Vandenhaute, M.; Schelfhout, J.; Van Vlierberghe, S.; Dubruel, P., A review of trends and limitations in hydrogel-rapid prototyping for tissue engineering. *Biomaterials* **2012**, *33* (26), 6020-6041.
- (80) Peltola, S. M.; Melchels, F. P.; Grijpma, D. W.; Kellomäki, M., A review of rapid prototyping techniques for tissue engineering purposes. *Annals of Medicine* **2008**, *40* (4), 268-280.
- (81) Yeong, W.-Y.; Chua, C.-K.; Leong, K.-F.; Chandrasekaran, M., Rapid prototyping in tissue engineering: Challenges and potential. *Trends in Biotechnology* **2004**, *22* (12), 643-652.

Chapter 2 : Reducing protein adsorption with polymer-grafted hyaluronic acid coatings

2.1. Abstract

We report a thermoresponsive chemical modification strategy of hyaluronic acid (HA) for coating onto a broad range of biomaterials without relying on chemical functionalization of the surface. Poly(di(ethylene glycol) methyl ether methacrylate) (PMEO₂MA), a polymer with a lower critical solution temperature of 26 °C in water, was grafted onto HA to allow facile formation of biopolymer coatings. While the mechanism for film formation appears to involve a complex combination of homogeneous nucleation followed by heterogeneous film growth, we demonstrate that it resulted in hydrophilic coatings that significantly reduce protein adsorption despite the high fraction of hydrophobic (PMEO₂MA). Structural characterization was performed using atomic force microscopy (AFM), which showed the formation of a dense, continuous coating based on 200 nm domains that were stable in protein solutions for at least 15 days. The coatings had a water contact angle of 16°, suggesting the formation of hydrophilic but not fully wetting films. Quartz crystal microbalance with dissipation monitoring (QCM-D) as well as a bio-layer interferometry (BLI) techniques were used to measure adsorption of bovine serum albumin (BSA), fibrinogen (Fbg) and human immunoglobulin (IgG), with results indicating that HA-PMEO₂MA-coated surfaces effectively inhibited adsorption of all three serum proteins. These results are consistent with previous studies demonstrating that this degree of hydrophilicity is sufficient to generate an effectively non-fouling surface and suggest that segregation during the solubility transition resulted in a surface that presented the HA component of the hybrid biopolymer. We conclude that PMEO₂MA-grafted HA is

a versatile platform for the passivation of hydrophobic biomaterial surfaces without need for substrate functionalization.

2.2. Introduction

Adsorption of serum proteins onto the surfaces of implanted biomaterials initiates a cascade of biological events that can lead to deleterious host responses, often resulting in formation of a fibrous capsule or the development of chronic inflammation. The Vroman effect describes the time-dependent microenvironment surrounding the implant characterized by complex dynamics of protein binding and denaturation resulting in formation of a coating that presents cell adhesion peptides or epitopes that activate immune responses.¹⁻² Within seconds of implantation, smaller, abundant proteins, such as albumin, adsorb onto nonpolar surfaces due to their high concentration and rapid diffusion in blood. Subsequently, surface rearrangement takes place via desorption of the hydrophilic, low molecular weight proteins and the adsorption of higher molecular weight proteins, such as fibrinogen, on the surface. This process leads to changes of the construct surface properties that can provoke intense host responses despite the biocompatibility of the construct. Being in an aqueous environment, protein adsorption on nonpolar surfaces leads conformational changes and the exposure of once shielded hydrophobic groups. Upon denaturation, protein epitopes can be presented to the microenvironment causing activation of the immune system, and chronic inflammation can be provoked. Preventing or minimizing protein adsorption to the surface of implants becomes an important design criterion, and strategies have focused on reducing the protein adsorption on biomaterial interfaces.¹

Numerous strategies have been developed to tune the properties of biomaterial surfaces in order to inhibit protein adsorption.²⁻⁷ One well-studied approach involves increasing the hydrophilicity of the surface through incorporation of polar and charged groups. For example, UV-light treatment of alkyl silane self-assembled monolayers was used to create a gradient in substrate oxidation that resulted in a gradient in water contact angle that ranged from 30° (hydrophilic) to 80° (hydrophobic). Following exposure to a fibronectin solution, cell adhesion and spreading decreased monotonically with water contact angle, presumably due to decreased protein adsorption.⁸ A separate study demonstrated that plasma treatment of poly(tetrafluoroethylene) surfaces could tune the water contact angle from 15-85°.⁹ This work demonstrated that water contact angles of 20-45°, which correlated with the highest concentrations of fibronectin adsorbed from serum, were optimal for promoting the adhesion of endothelial cells but surfaces with water contact angle below 20° inhibit protein adsorption due to resistance to protein adsorption.¹⁰⁻¹² However, while straightforward to perform, surface ionization using light or plasma discharge is generally a line-of-site technique, allowing for patterning using photoresist techniques but making complete passivation of complex three-dimensional objects challenging.

Steric blocking of the surface through dense grafting of poly(ethylene glycol) (PEG) is another well-established technique for reducing protein adsorption on the surface.⁴ Water-soluble PEG has established biocompatibility,^{4, 7, 13-14} and coating surfaces with it has been shown to significantly reduce protein adsorption.^{3, 15-16} Monofunctional PEG can be reacted with the surface, providing a controlled method for grafting since

unreacted PEG can be removed through washing.⁴ This technique is appropriate for surface patterning and coating complex objects^{4, 16} but requires highly reactive PEG end groups, such as silanes, or surface functionalization.

PEG-grafted polymers have been used as coatings to reduce protein adsorption in other studies relying on the polymer backbone to drive adsorption to the surface. PEG-grafted poly(L-lysine) (PLL) forms coatings on oxide surfaces, relying on the strong interactions between PLL and the oxide surface.¹⁷ For oxide surfaces with isoelectric points below 7, such as TiO₂, Nb₂O₅, and Ta₂O₅, the net negative charge of the oxide surface binds the PLL chain strongly, allowing for high grafting densities of the 2 kDa PEG chains in an adherent coating. On TiO₂, the PLL-g-PEG coating reduced fibrinogen adsorption from 559 +/- 15 ng/cm² on the oxide to 22 +/- 12 ng/cm².^{5, 18-19} For biomaterial surfaces with negative charge under physiological conditions, this approach provides a straightforward method for passivation against protein adsorption.⁵

An alternative to surface functionalization with PEG is grafting carboxymethyl dextran, a charged polysaccharide known for anticoagulant activities.²⁰ The most common protocol involves a combination of surface grafting and interchain crosslinking, resulting in the formation of a hydrogel coating with thickness *ca.* 200 nm.²¹ This has been used for designing bioanalytical interfaces, such as those used in surface plasmon resonance analysis of blood samples,²¹ where the high resistance to protein adsorption and high density of antibodies or other capture groups allows for sensitive analyte detection.²² The zwitteration of dextran is obtained through a one-pot reaction with carboxybetaine and is reported to yield good antifouling properties as well as enhanced optical transparency and

switchability.²³ However, utilization of the antifouling properties of many natural polysaccharides is challenging despite interest in these materials; several intrinsic limitations prevent their broader application in biomedical applications. QCM results show that dextran-based materials show reduced antifouling properties in contact with blood.²⁴ It was also demonstrated that the use of agarose derivatives in biosensors is challenged by nonspecific binding.²⁵ We hypothesized that HA might be an ideal candidate for formation of nonfouling coatings since it is a component of most highly hydrated tissues.

Use of controlled radical polymerization is an established method for modifying the properties of polysaccharides.²⁶⁻²⁷ In this study, hyaluronic acid (HA) was grafted with the thermoresponsive polymer poly(di(ethylene glycol) methyl ether methacrylate) (PMEO₂MA) prepared via atom transfer radical polymerization (ATRP) to make it suitable for one-step surface coating as a base for preventing protein adsorption. HA is a linear, viscous, naturally occurring, high molecular weight glycosaminoglycan (GAG) composed of a copolymer of D-glucuronic acid and N-acetyl-D-glucosamine.^{18, 28-32} Unlike dextran, HA has intrinsic anti-inflammatory activities³³ and is recognized by cells through the cell surface receptors that promote a motile phenotype (CD44, RHAMM, ICAM-1), making it a potent mediator of biological processes such as metastasis, morphogenesis, inflammation and wound repair.^{18, 28, 31-32} Chemical modification of HA through targeting the carboxylic acid groups, as well as other groups on the backbone, have been reported for various applications.³⁴⁻³⁵ The thermo-responsive behavior of the polymer can be conducted to HA by grafting the polymer to the HA backbone, similar to what was reported by Tan et al. with poly(N-isopropylacrylamide) (PNIPAM) in their preparation of HA-PNIPAM scaffolds.³⁶ Separate studies measuring the adsorption of PNIPAM on various substrates

demonstrated that hydrophobic forces keep the material bound to the substrate as long as rinse temperatures were above the LCST of the polymer.³⁷ The challenge in preparing non-fouling HA coatings based on grafts with an LCST was in providing sufficient driving force for forming a robust coating without resulting in extensive protein adsorption to the hydrophobic components of the surface.

This work presents the preparation and characterization of these materials and is organized as follows. First, coating morphologies were characterized using atomic force microscopy, and antifouling properties of coatings based on these materials were tested using novel bio-layer interferometry (BLI) using bovine serum albumin, fibrinogen and human immunoglobulin solutions. This technique, which provides similar information as surface plasmon resonance (SPR), can run multiple samples in parallel and offers significant advantages in understanding the interfacial properties of these coatings. This label-free technology allows for real-time measurement of biomolecular interactions. By analyzing the interference patterns of white light reflected from consecutive interfaces in an end-coated fiber optic, this bio-layer interferometry is able to accurately measure changes in the optical path length of the fiber and correlate this to changes in the thickness of molecules adsorbed at the solution interface with a sensitivity reported by the manufacturer of 0.1 Å. A second validation of the antifouling properties of the coatings using quartz crystal microbalance with dissipation monitoring (QCM-D) is also presented. Finally, we demonstrate coating of a two-dimensional grid suggesting this method may be a route toward surface functionalization of more complex objects.

2.3. Experimental Section

2.3.1. Materials. Di(ethylene glycol) methyl ether methacrylate (M(EO)₂MA), ethyl 2-bromo-2-methylpropionate (EBiB), 2,2'-bipyridine (bpy), Copper(I) bromide (CuBr), anisole, hexanes, ethylenediamine, triethylamine (TEA), 4-(dimethylamino)pyridine (4-DMAP), and hyaluronic acid (HA) derived from *Streptococcus equi* (ca. 1.6 MDa) were purchased from Sigma-Aldrich. Albumin from bovine serum (BSA) (>98%, received as a lyophilized powder) and fibrinogen (Fbg) from human plasma and human (IgG) were purchased from Sigma-Aldrich. Propane phosphonic acid anhydride (T3P) in 50% w/w solution in N,N-dimethylformamide was obtained from Sigma-Aldrich. Monomethoxy poly(ethylene glycol) epoxide (mPEG-epoxide) of a 10 kDa molecular weight was purchased from Creative PEGWorks and used as received.

2.3.2. Synthesis of the homopolymer of PMEO₂MA by ATRP. Synthesis of PMEO₂MA was performed as reported³⁸ with minor modifications. First bpy and CuBr (0.20 mmol and 0.12 mmol, respectively) were added to a dry 25 mL Schlenk flask. The flask was deoxygenated rapidly after adding the solids *via* four consecutive vacuum-nitrogen cycles. Anisole, M(EO)₂MA and EBiB were dried over baked 4 Å molecular sieves and degassed with nitrogen for 30 minutes prior reacting with the catalysts. Using the Schlenk techniques, 3.3 mL anisole, 4.9 mL of the monomer (M(EO)₂MA) (26.6 mmol) and 18.6 µL of EBiB (0.13 mmol) were added to the schlenk flask under nitrogen. The reaction was allowed to proceed at 60 °C using an oil bath for 6 h. The reaction was terminated by exposing it to air. The reaction mixture was then diluted in excess THF and the catalyst was removed from the mixture by passing the sample through a neutral alumina

column. The solution was then precipitated in excess hexane and the precipitate was filtered. The solid product was dried under vacuum for 6 h. Polymerization reaction kinetics were monitored by periodically withdrawing samples from the reaction mixture. Composition was validated by ^1H NMR and end group analysis indicated an M_n value of 34,000 g/mol. Gel permeation chromatography (GPC) was used to measure M_n and M_w/M_n .

2.3.3. Modification of PMEO₂MA with amine group. The procedure followed another performed by Coessens et al.³⁹ Following drying, PMEO₂MA with a terminal bromide end group was acquired. Then PMEO₂MA was dissolved in ethanol at a concentration of 50 mg/mL. PMEO₂MA solution was mixed with a 25x molar excess of ethylenediamine (EDA) and 1.2x molar excess of TEA to EDA. The mixture was allowed to react for 48 h in an oil bath at 60 °C then was precipitated into hexanes. The solid polymer was re-dissolved in Milli-Q water and dialyzed against 2,000 MWCO membrane with repeated water changes to remove unreacted reagents. Following dialysis, the sample was frozen at -80 °C and lyophilized on a Labconco Freezone Plus freeze-dry system. Products were characterized using ^1H NMR.

2.3.4. Synthesis of HA-PMEO₂MA conjugates. HA was dissolved in Milli-Q water at a concentration of 5 mg/mL. Then 20% of the carboxylic acid groups on HA were activated by 1.5x molar excess T3P. To that 4-DMAP was added to the activated HA as an acylating agent in a 2:1 ratio. To the activated HA, a 1:1 molar ratio of NH₂-PMEO₂MA was added. The reaction mixture was set at room temperature for 24 h. After 24 h the solution was diluted with water and dialyzed against a 100,000 MWCO dialysis membrane

to remove unreacted PMEO₂MA. Dialyzed samples were frozen at -80 °C and lyophilized. Then ¹H NMR characterization was carried out on the solid product to confirm HA-PMEO₂MA conjugation.

2.3.5. ¹H NMR characterization. NMR spectra were obtained using a Bruker Avance 300 MHz spectrometer. Deuterated chloroform (CDCl₃) was used as the solvent for PMEO₂MA and its derivatives. Deuterium oxide (D₂O) was used as the solvent for HA and its derivatives. All samples were prepared at a concentration of 0.5% (wt/wt).

2.3.6. Gel Permeation Chromatography (GPC). A GPC system composed of a Waters 515 HPLC Pump and Waters 2414 Refractive Index Detector using PSS columns (Styrogel 10², 10³, 10⁵ Å) in dimethylformamide (DMF) as an eluent at a flow rate of 1 mL/min at 50 °C was used. Samples were filtered over neutral alumina prior to analysis. The column system was calibrated with 12 poly(methyl methacrylate) (PMMA) standards.

2.3.7. Dynamic light scattering (DLS). Dynamic light scattering (DLS) was measured using a Zetasizer Nano from Malvern Instruments, Ltd. Samples were prepared at a 0.1% (w/w) solution, and diluted in Milli-Q water. Sphere radii were taken from an average of 3 runs.

2.3.8. Tapping mode atomic force microscopy (AFM). Experiments were carried out using a Multimode Nanoscope III system (Veeco 2 Instruments). Measurements were performed in air, using commercial silicon cantilevers with a nominal spring constant and resonance frequency respectively equal to 50 N/m and 290 kHz.

Silicon wafers with native oxide layers were cleaned with a jet of acetone, then with a jet of isopropyl alcohol, before the acetone evaporated, and blown dry with a flow of

nitrogen. All samples were drop-casted on the substrates from 1 mg/mL aqueous solutions. Casting above lower-critical solution temperature (LCST) was carried out at 37 °C in a Fisher Scientific low temperature incubator.

The HA-PMEO₂MA sample was allowed to dry on a substrate at 37 °C. Coated wafers were incubated in a 10% albumin solution for up to 15 days and then imaged to assess protein adsorption on the scratched area.

2.3.9. Water contact angle measurements for modified HA films. Water contact angle was measured for films casted on Teflon surfaces using a Ramè-Hart contact angle goniometer. A 4 mg/mL solution of HA-PMEO₂MA was prepared in pure water. The modified HA solution was drop-cast over Teflon surfaces below the LCST. The discs were then incubated at 37 °C for an hour to ensure transition, uniform and tight coating over the surface. Warm water droplets (2-15 µL) were placed over the cast film and the native substrate; images were taken 30 s post water placement. The process was repeated 10 times for each volume and average measurements were reported.

2.3.10. Quartz Crystal Microbalance (QCM-D) analysis. A Q-Sense E4 system (Biolin Scientific) was used for these measurements. Experiments were performed using 4 SiO₂ sensors (QSX 303) mounted in QFM 401 flow modules. All experiments were performed with the sensors mounted in parallel. An external digital pump (Ismatec IPC-N 4) was used to control the flow rate of the solutions, using tubing with inner diameter of 0.64 mm. An E4 Autosampler was used for liquid handling. Before each experiment, the sensors were cleaned for 10 min using a UV/Ozone ProcleanerTM (Bioforce Nanosciences) followed by immersion of the sensors in 2 wt% sodium dodecylsulfate for 30 min. The

sensors were subsequently rinsed carefully with copious amounts of deionized water, and were dried under a gentle stream of nitrogen gas. Finally, the sensors were exposed to UV/ozone for 10 min before mounting in the flow modules.⁴⁰⁻⁴⁴ After the sensors were mounted, the flow modules and tubing were filled with water and the resonance frequencies were collected at ambient temperature. The volume above the sensor is 40 μ L.

The experiments were performed as follows: the temperature was set to 15 °C, and sensors 1-3 were exposed to HA (40 μ L above sensor, 4 mg/mL), whereas sensor 4 was exposed to water at a flow rate of 100 μ L/min. Sensor 4 was further used as a positive control for BSA binding. Next, the temperature was set to 37 °C, and the resulting frequency and dissipation shifts, Δf and ΔD respectively, were recorded. Following baseline stabilization after the temperature increase, solutions of BSA, pre-heated to 37 °C, were injected to sensors 1-2 and 4, and water, as a negative control, to sensor 3. Finally, the sensors were regenerated by setting the temperature to 15 °C and rinsing with pre-cooled water to remove the HA. All results are reported for the third overtone ($n=3$), unless otherwise stated.

2.3.11. Biolayer Interferometry (BLI) analysis. A ForteBio Octet Red (Pall Life Sciences) system was used in this study. Experiments were performed in a 96-well, polypropylene, flat-bottom, black microplate (Greiner Bio-one). Experiments were performed at 37 °C for HA-PMEO₂MA samples, with the microplate shaking at 1000 rpm. The volume of the sample in each well was 230 μ L. All solutions were prepared in PBS that was filtered through a 0.2 μ m Acrodisc PTFE syringe filter. Sensor tips selected for these experiments were aminopropylsilane (APS). ForteBio sensor tips were hydrated in

PBS for a minimum of 15 minutes before beginning each experiment and the sample plate was equilibrated for 5 minutes to ensure a steady temperature. To model a moderately hydrophobic biomaterial surface, APS tips were reacted with a (3-glycidyloxypropyl)trimethoxysilane ($\geq 98\%$, Aldrich) in a 25 min loading step during the ForteBio experiments. Data analysis was performed on the ForteBio data analysis software.

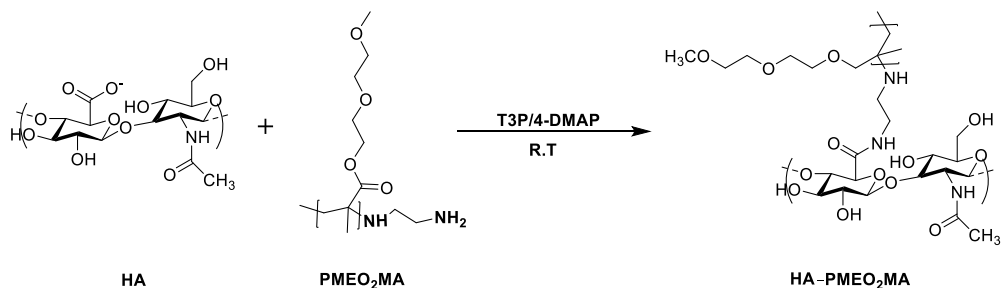
2.3.11.1. Control experiments with unmodified HA. Control experiments were run against unmodified HA to ensure that the polymer had no affinity to the trimethoxysilane sensor surface. APS sensor tips were submerged in a 0.5% (v/v) solution of (3-glycidyloxypropyl)trimethoxysilane in water, with a pH adjusted to 4.3 with 0.1% (v/v) aqueous acetic acid solution for 25 minutes. The sensor tips were then submerged in a well containing PBS for 60 s to rinse off any unreacted material. Tips were then moved to wells containing a 2.5 mg/mL solution of unmodified HA in PBS, and submerged for 10 minutes.

2.3.11.2. Control experiments with PEG. Monomethoxy poly(ethylene glycol) epoxide (mPEG-epoxide) of a 10 kDa molecular weight was purchased from Creative PEGWorks, and was used as received. A 0.5% (w/w) solution of the epoxide in water adjusted to a pH of 3.5 with a 0.1% (v/v) aqueous acetic acid solution was prepared. The APS sensor tips were submerged in a solution of mPEG-epoxide in a loading step that lasted 30 minutes. Real-time loading of the epoxide was monitored by surface thickness changes as monitored by the ForteBio software. Following loading, the sensor tip was rinsed for 60 s in PBS to remove any unreacted PEG. Functionalized sensor tips were then exposed to wells containing 0.1 mg/mL solutions of IgG, Fbg and BSA for 10 minutes.

2.3.11.3. Modified HA. Lyophilized HA-PMEO₂MA was dissolved in PBS, and was kept below its LCST before the experiment began. Sample plates were prepared with 0.2, 0.1, 0.05, 0.025, 0.0125 mg/mL concentrations of proteins BSA, Fbg and IgG. Modified HA concentrations were kept at 0.240 mg/mL for all experiments.

The experiment was performed as follows: (1) 60 s baseline in PBS, (2) 25 min loading in epoxysilane, (3) 60 s wash in PBS, (4) 20 min loading to modified HA, (5) 60 s rinse in PBS, (6) 60 s baseline in PBS, (7) 10 min association to protein, and (8) 10 min dissociation in PBS.

2.4. Results and discussion



Scheme 2.1 The chemical composition of HA and modification route.

2.4.1. HA Modification. HA was modified with PMEO₂MA, as shown in Scheme 1, by grafting the thermoresponsive polymer PMEO₂MA onto HA to prepare HA-PMEO₂MA. PMEO₂MA is a biocompatible thermoresponsive polymer whose lower critical solution temperature (LCST) can be tailored to temperatures in the range of 26-52 °C depending on the number of ethylene oxide repeat units on the side chains.³⁸ Once the LCST was exceeded, the polymer precipitated from solution, as the hydrophobic interaction within the polymer chains overcome those of the hydrophilic interactions between the polymer and the solvent, transitions from coil to globule and anchor the HA

to surrounding surfaces.⁴⁵ This drove physical adsorption of the polymer to the surface of the substrate, binding HA to the surface with it. We hypothesized that this process would result in presentation of the hydrophilic HA from the surface of the coating, providing a means for preparing a robust biomaterial surface that resists protein adsorption.

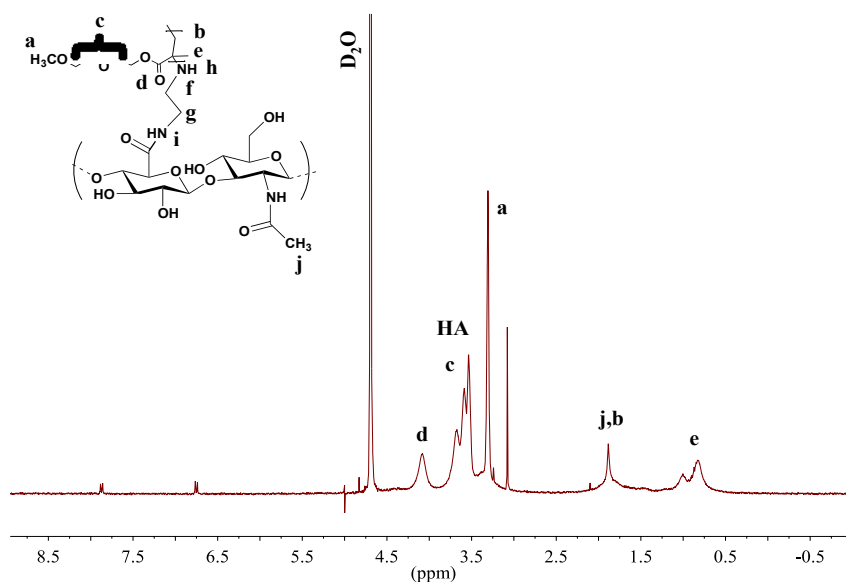


Figure 2.1 ¹H NMR for HA-PMEO₂MA coating material.

2.4.2. Proposed structure of coating. Based on these data, the structure of a single domain is proposed schematically in fig. 2.2. The schematic is depicted assuming that the driving force for adsorption is the change in polymer-graft solubility, but the water contact angle and resistance to protein adsorption appear to be determined largely by the HA so the PMEO₂MA grafts are sequestered at the substrate and within the coating. This mechanism intrinsically leads to a highly hydrophilic surface that resists protein adsorption and adheres tightly to hydrophobic surfaces.

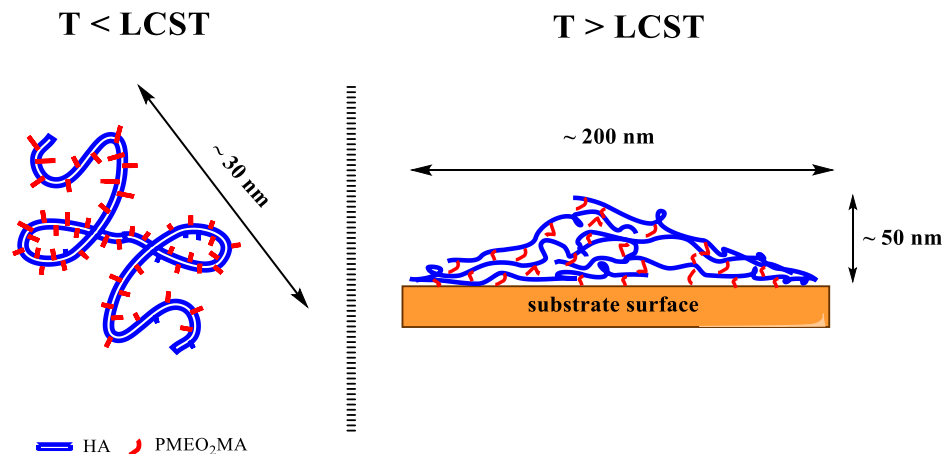


Figure 2.2 Schematic of HA-PMEO₂MA in solution at $T < \text{LCST}$ (left) and the coating ($T > \text{LCST}$). The schematic at $T > \text{LCST}$ illustrates a potential structure that is compatible with the AFM images but is not drawn to scale.

2.4.3. Dynamic Light Scattering. DLS was used to characterize the size of HA-PMEO₂MA in solution. Below the LCST, solutions of HA-PMEO₂MA showed particle sizes not significantly different than unmodified HA solutions, with a mean size of 30 nm, consistent with previous reports.⁴⁶ Above the LCST, HA-PMEO₂MA aggregates showed a particle size approaching 300 nm (Fig. 2.3). This suggests that aggregates form homogenously in solutions and then precipitate onto the surface to form the coating, but further work is required to determine the exact steps of this process.

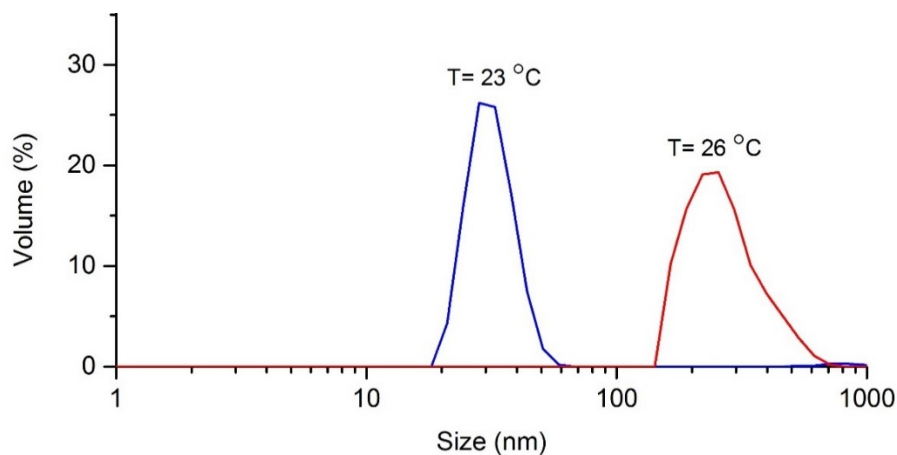
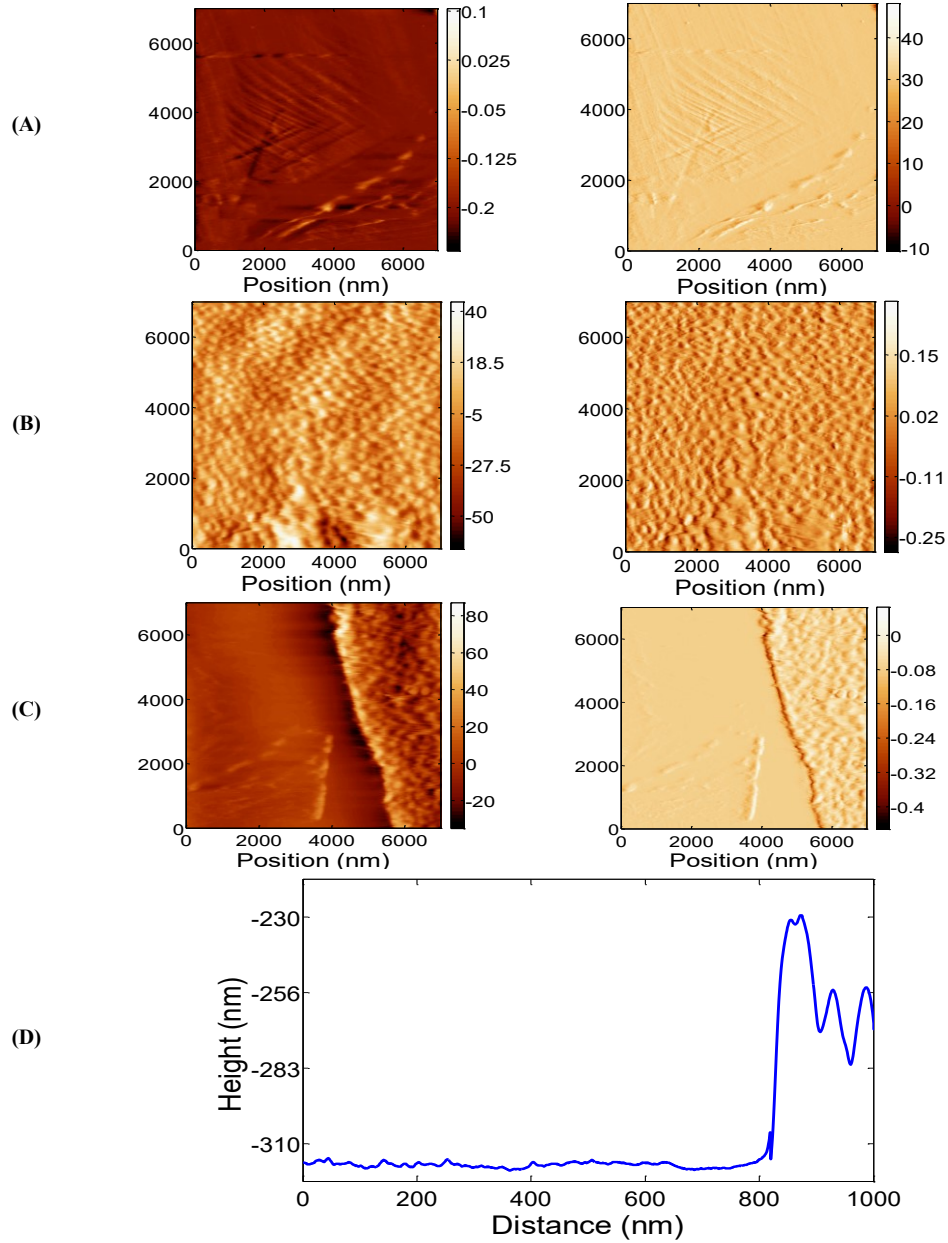


Figure 2.3 DLS data showing the distributions of diameters for HA-PMEO₂MA below LCST and above LCST.

2.4.4. Atomic Force Microscopy (AFM) Analysis. AFM analysis was used to compare the morphology of uncoated SiO₂ surfaces with those exposed to the HA-PMEO₂MA solutions. Moreover, film thickness was assessed employing a scratch test in which a scratch is created on the coated surface, creating a groove of uncoated surface. Results obtained from these experiments are shown in fig. 2.4. In these experiments, HA-PMEO₂MA was deposited on an SiO₂ surface cleaned by sonication in ethanol and blown dry with air. The coating was deposited by drop-casting from an aqueous solution, dried in an incubator, and rinsed with warm water. The thickness of the layer was determined by measuring the film profile following mechanical delamination with a needle. Following the scratch test, a difference in reflectivity was observed with the delaminated region reflecting ambient light much more strongly than the coated region. By comparing the change in film height using AFM, the thickness was determined to be ~50 nm. The scratch clearly exposed the SiO₂ surface, evidenced by the decrease in surface roughness (Fig. 2.4.D) and by the difference of the images taken inside and outside of the scratch (Fig. 2.4.C). When compared to the uncoated SiO₂ surface (delaminated), the coating based on

HA-PMEO₂MA material showed a different morphology (Fig. 2.4.C). AFM analysis revealed the presence of a uniform layer of characteristic granular appearance. The diameter of the rounded asperities was around 230 nm on average, suggesting each is composed of several HA-PMEO₂MA.

Figure 2.4 AFM images HA-PMEO₂MA materials. Images on the left show height (nm) while those on



the right show cantilever deflection (nm). (A) Unmodified silica wafer surface. (B) HA-PMEO₂MA coatings. (C) Scratched HA-PMEO₂MA coatings. (D) Height profile of coating

2.4.5. Water contact angle. The average of 10 measurements on films formed by the drop-casting of HA-PMEO₂MA materials above LCST showed that, although not completely wetting, HA-PMEO₂MA-coated surfaces exhibited a significant increase in hydrophilicity, changing from 98° on uncoated Teflon to 16° on HA-PMEO₂MA films on a Teflon substrate. This effect is believed to be a result of the HA coatings not the hydrophilic ethylene oxide domains in PMEO₂MA because surface-grafted PMEO₂MA brushes have been shown to exhibit water contact angle shifts from 40° to 102° below and above LCST, respectively.⁴⁷ Although the coating domains appeared uniform, as demonstrated by AFM measurements, hydrophobic PMEO₂MA could still be presented from the surface of the coating as opposed to being sequestered in the coating interior or at the Teflon surface. This could explain the less-than-complete-wetting behavior observed on coatings prepared from HA-PMEO₂MA materials (images not shown). However, although not completely wetting, the surface is expected to inhibit protein adsorption.¹⁰⁻¹¹ These results also correlated well with recent theoretical and experimental work dealing with the energy requirements, or the physical chemistry, of the adsorption of blood-proteins to various types of surfaces.¹²

2.4.6. Biolayer Interferometry (BLI) Analysis.

2.4.6.1. Control experiments of protein against the surface of unmodified sensor tips. BLI technology uses interferometric detection of changes in the optical path length at a fiber optic sensor tip to measure binding kinetics. For the current work, a ForteBio Octet Red instrument was used to examine the extent of protein adsorption occurring on a coated material surface. The instrument reports shifts in units of nm, and although this cannot be taken as an absolute thickness measurement, it does provide a highly accurate kinetics

measurement. Control experiments with free protein and an APS sensor tip were performed in which APS tips were reacted with 3-glycidoxypyltrimethoxysilane to functionalize the tip as a moderately hydrophobic surface for interactions with free proteins. By reacting the amine surface with the trimethoxysilane (TMS), we also remove the charge on the sensor surface so that there is no enhancement in affinity between sensor surface and free protein due to electrostatics. Also, more control experiments were performed using PEG-based materials to assess the efficacy of the prepared HA-PMEO₂MA coatings.

Three separate experiments were performed where six sensor tips per experiment were modified with TMS, and introduced to 6 wells of a 96-well plate containing Fbg, BSA, and unmodified HA (all proteins were run in separate experiments). The protein-adsorption experiments were all run at concentrations of 0.2 mg/mL, 0.1 mg/mL, 0.05 mg/mL, 0.025 mg/mL, 0.0125 mg/mL, and 0 mg/mL, while unmodified HA was run at a concentration of 2.5 mg/mL.

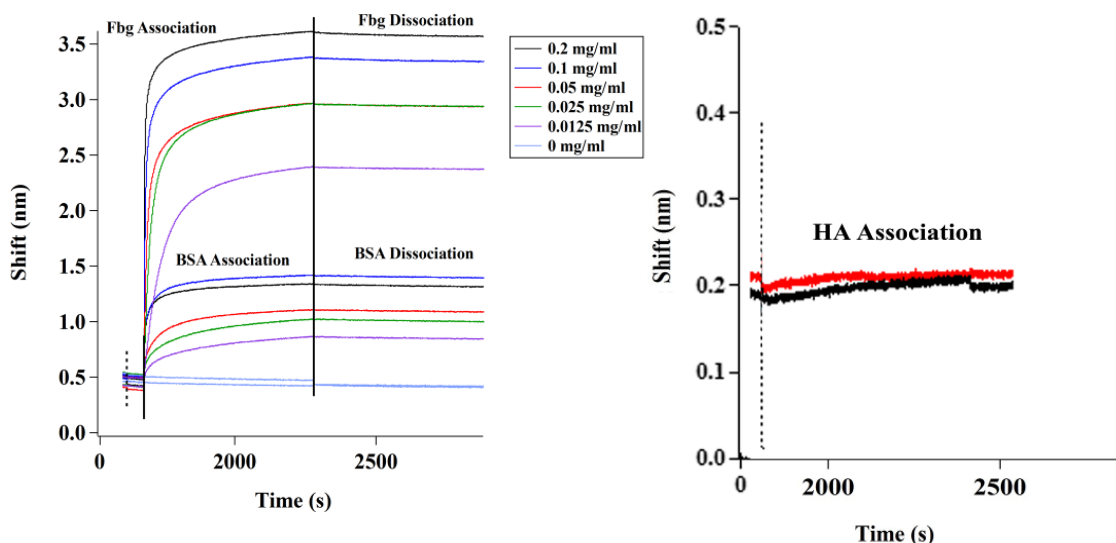


Figure 2.5 Binding behavior of BSA and Fbg proteins (left) and unmodified HA (right) against TMS functionalized sensor tip as measured.

Fig. 2.6 shows representative protein adsorption experiments. The Fbg protein had a change in film thickness characterized by shift values ranging from 1.9 – 3.1 nm, BSA had shift values ranging from 0.4 – 0.9 nm, consistent with relative differences in protein size. The data were fit using the ForteBio analysis software, and an average on-rate, k_{on} , for protein association, was calculated to be $(5.8 \pm 1.3) \times 10^5 \text{ M}^{-1}\text{s}^{-1}$ for Fbg, and $(2.8 \pm 1.9) \times 10^5 \text{ M}^{-1}\text{s}^{-1}$ for BSA. An off-rate was also calculated for this model, for Fbg k_{off} was $(3.0 \pm 1.5) \times 10^{-5} \text{ s}^{-1}$, and for BSA it was $(5.2 \pm 3.6) \times 10^{-5} \text{ s}^{-1}$. The K_D values for Fbg and BSA on the TMS-functionalized surfaces were $5.2 \times 10^{-11} \text{ M}$ and $1.9 \times 10^{-10} \text{ M}$ respectively, suggesting strong binding interactions for both serum proteins on hydrophobically modified sensor surfaces.

2.4.6.2. Effect of free PEG on protein adsorption. A separate control experiment was performed to identify the effect of free PEG on protein adsorption. Here, the amine terminated sensor tips were reacted with an epoxy-terminated 10 kDa methoxyPEG. A 10 kDa molecular weight is estimated, based on the number of active sites on the sensor tips, and the radius of gyration of the 10 kDa PEG, to provide full coverage of the surface area of the sensor tip when the polymer reacted with the free amines.

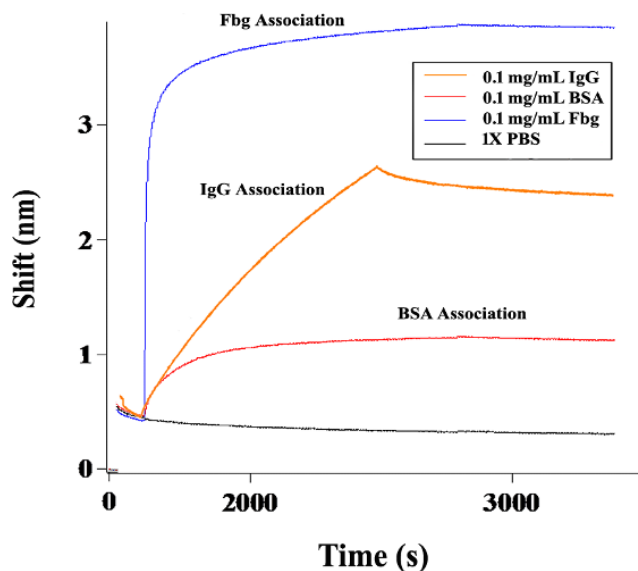


Figure 2.6 Protein adsorption profiles on PEG-modified sensor tips as measured by BLI against BSA, Fbg and IgG.

Fig. 2.7. shows that the Fbg, IgG and BSA deposited with 3.4 nm, 2.5 nm and 0.7 nm change in film thickness, respectively. Despite the presence of a free PEG chain at the surface, proteins were still capable of depositing onto the sensor tip.

2.4.6.3. Modified HA materials. Protein adsorption on the HA-PMEO₂MA coatings was then investigated. Here, the modified sensor tips were introduced to solutions of HA-PMEO₂MA at a concentration of 0.240 mg/mL with an approximate HA modification degree of 10%. The experiments were run at 37 °C to ensure that the experimental temperature exceeded the LCST temperature (26 °C) of the HA-PMEO₂MA materials and to simulate biological temperatures.

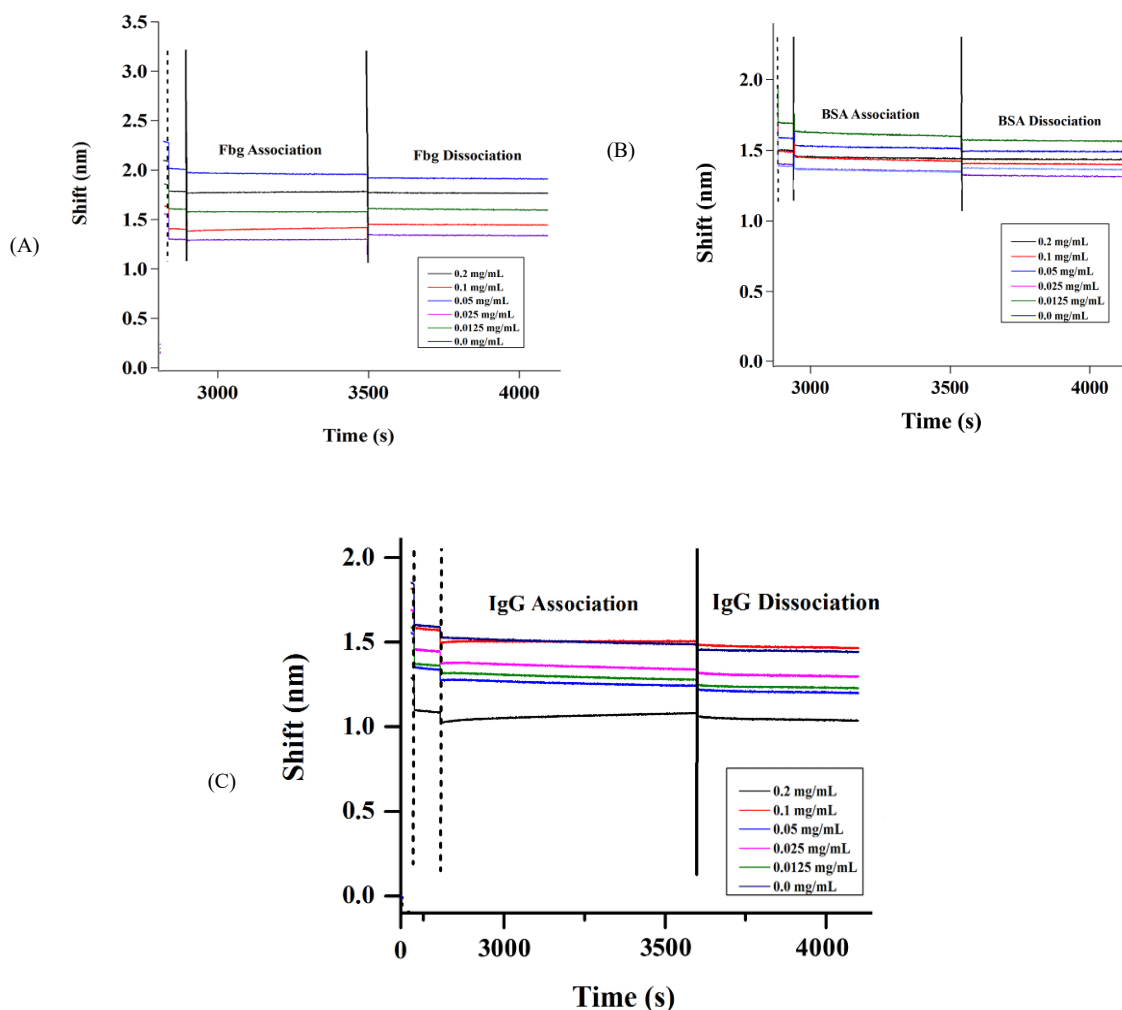


Figure 2.7 Protein adsorption profiles on HA-PMEO₂MA materials as measured using BLI. (A) Fbg. (B) BSA. IgG (C)

HA-PMEO₂MA-functionalized sensor tips were then immersed in solutions of Fbg, BSA and IgG. Fig. 2.7A, 2.7B and 2.7C display the results of protein adsorption to the sensor tips functionalized with the HA-PMEO₂MA material. In the Fbg, BSA and IgG experiments, tips were immersed in the protein solution for 10 min, and showed no measurable association for either Fbg, BSA nor IgG, indicating that the HA-PMEO₂MA polymer prevents protein adsorption to the surface of the functionalized sensor tip.

2.4.7. Quartz Crystal Microbalance with Dissipation Monitoring (QCM-D).

QCM-D measurements were performed to explore the HA-PMEO₂MA coating as antifouling materials. Initial exposure of the silicon dioxide sensors to HA at 15 °C, resulted in a frequency shift of -47.5 ± 1.5 Hz and dissipation shift of 3.8 ± 0.2 for the third overtone ($n=3$). Changing the temperature to 37 °C resulted in *ca.* 250 Hz net decrease of the resonance frequency for the HA coated sensors, whereas the net dissipation decrease was 10^{-6} ($n=3$). Thus, these results indicate a thick enough layer to fully coat the substrate, and highly rigid binding of the HA-PMEO₂MA to the silicon dioxide surfaces. Fig. 2.8 below, shows the frequency shift, Δf , as a function of time upon injection of BSA over HA-coated (HA-PMEO₂MA) silica and plain silica as a positive control.

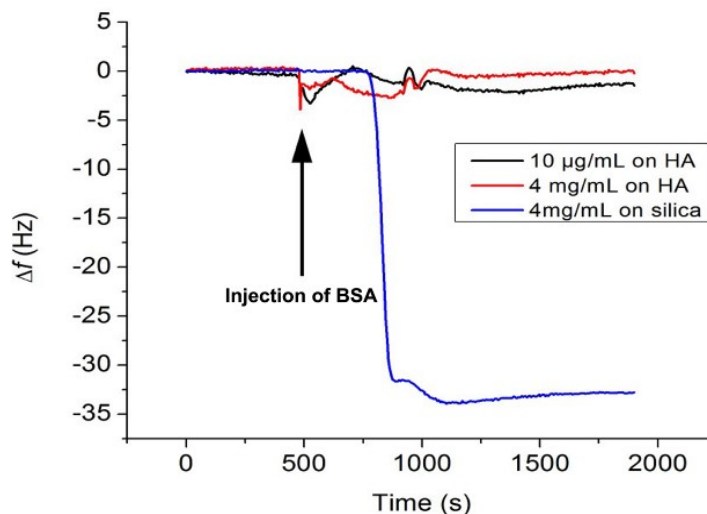


Figure 2.8 Injection of BSA over HA-coated (HA-PMEO₂MA) sensors and plain silicon dioxide as indicated at 37 °C. For injection over HA-PMEO₂MA, the response of the negative control (water injected over HA-PMEO₂MA, not shown) was subtracted.

As can be seen in fig. 2.8, injecting BSA over the HA-coated surfaces results in negligible frequency shifts, whereas injection of BSA over plain silica, results in a

frequency shift of *ca.* 32 Hz. Thus, the data presented in fig.2.8 support the antifouling behavior of the HA coating.

The well-known Sauerbrey relation states that for thin, rigid and homogenous films, Δf is directly proportional to the change in mass,⁴⁸ Δm_f , of the film according to:

$$\frac{\Delta f}{n} = -\frac{f_0}{t_q \rho_q} \Delta m_f \frac{\Delta f}{n} = -\frac{f_0}{t_q \rho_q} \Delta m_f \quad (1)$$

Where f_0 (5 MHz) is the fundamental frequency of the quartz crystal, t_q (3.3×10^{-4} m) the thickness of the quartz plate, ρ_q (2648 kg/m³) the density of quartz and $n = 3, 5, 7 \dots$ the overtone number. However, under viscous damping, energy is lost during the oscillatory motion of the crystals according to

$$D = \frac{E_l}{2\pi E_s} = \frac{1}{\pi f \tau} \quad (2)$$

where E_l and E_s are the lost and stored energies, respectively, and τ is the time constant of the amplitude decay of the oscillating crystal observed as the driving voltage over the crystal is turned off.⁴⁹ In general, thin as well as rigid layers induce low damping, whereas viscoelastic films lead to higher dissipative losses. If water couples hydrodynamically to the film, the dissipation is usually higher, which is observed in a higher $\Delta D/\Delta f$ ratio.⁵⁰⁻⁵² Thus, a net frequency shift of 250 Hz and a dissipation shift of 10^{-6} upon HA binding to the silicon dioxide surfaces indicate highly rigid binding of the HA to the silicon dioxide surfaces.

Lowering the temperature to 15 °C after BSA injection and rinsing with water at 100 μ L/min resulted in the removal of the HA as seen by the large positive frequency shifts. After water injection for 2000 s, the frequency had reversed 90% to the starting value on average for the HA coated surfaces, suggesting the coating can be removed at temperatures below the LCST.

2.4.8. Coatings on complex objects. Fig.2.9 shows micromachined orthogonal PMMA discs incubated at 37 °C with fluorescently labeled HA grafted with PMEO₂MA chains. Excellent coating coverage and stability could be observed, indicating this approach is amenable to coating complex shapes. Further investigations of this are necessary, but good coverage in conformal coating is observed at the higher solution concentrations. fig. 2.9.D shows the same orthogonal discs after 5 minutes incubation in cold water, 4 °C. After incubation, fluorescent signals could not be detected, indicating the complete removal of the labeled HA-PMEO₂MA materials, which further support the reversibility of the coating process.

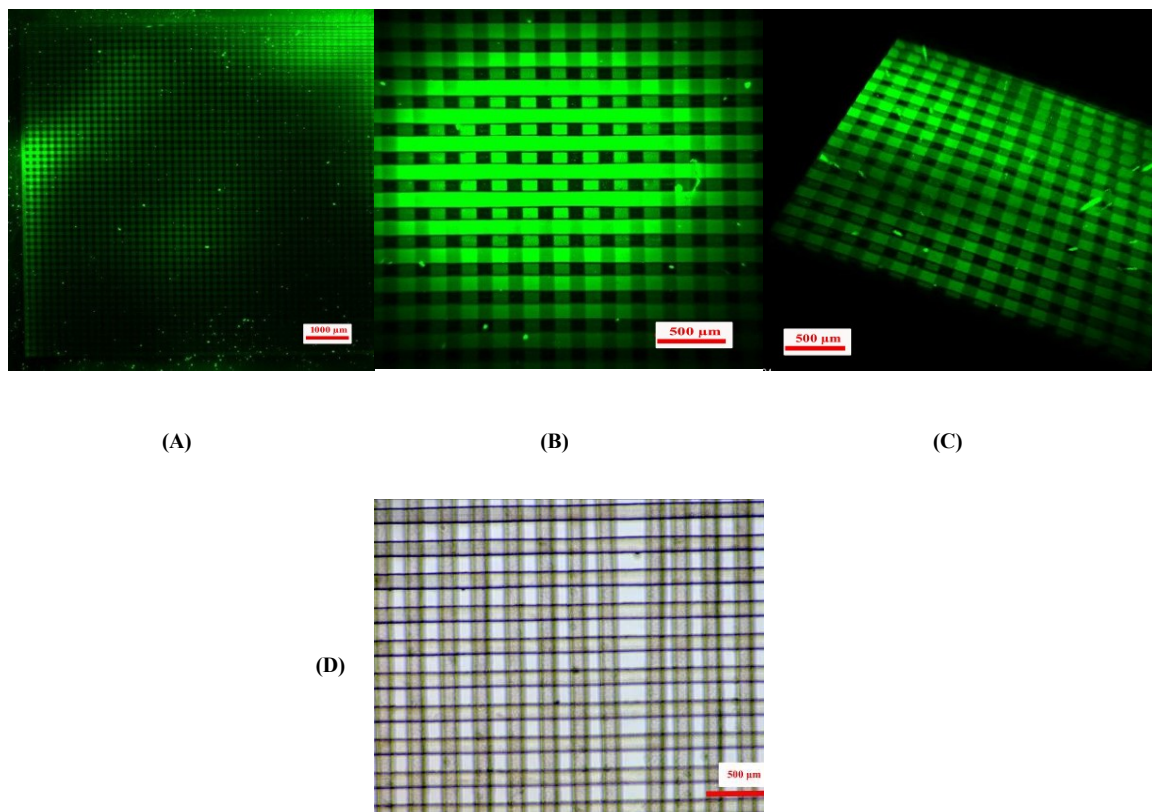


Figure 2.9 Confocal images of HA-PMEO₂MA-coated PMMA discs (A) 1x 2D view (B) 5x 2D, (C) 5x Z-stack view, (D) 4x optical view of PMMA discs after washing with cold water. Grids are 100 x 100 μm.

2.5. Conclusion

We have demonstrated that functionalization of HA with a polymer having an LCST can be used to prepare robust coatings that inhibit protein adsorption. The covalent attachment of PMEO₂MA to HA resulted in a material that became insoluble in aqueous media above 26 °C, forming robust coatings on SiO₂ and Teflon with domains based on a lateral size of *ca.* 230 nm and an average thickness of 50 nm. These coatings had a water contact angle of 16°, making them sufficiently hydrophilic to resist adsorption of BSA, Fbg and IgG as measured using optical interferometry and quartz crystal microbalance. A structural model of the adsorbed coating was proposed in which the PMEO₂MA grafts

segregate to the substrate surface and the interior of the coating domain, presenting the HA to the solution where it imparts resistance to protein adsorption despite the high concentration of hydrophobic grafts. We propose that this approach could be the basis for the facile preparation of robust hydrophilic coatings on a range of hydrophobic surfaces.

ACKNOWLEDGMENT

The authors gratefully acknowledge Prof. Robert Tilton and Prof. Tomek Kowalewski for use of their laboratory facilities and for helpful discussions. NMR instrumentation at CMU was partially supported by NSF (CHE-0130903 and CHE-1039870).

References

- (1)Vroman, L.; Adams, A. L.; Fischer, G. C.; Munoz, P. C., Interaction of high molecular weight kininogen, factor xii, and fibrinogen in plasma at interfaces. *Blood* **1980**, *55* (1), 156-9.
- (2)Garland, A.; Shen, L.; Zhu, X., Mobile precursor mediated protein adsorption on solid surfaces. *Progress in Surface Science* **2012**, *87* (1-4), 1-22.
- (3)Gombotz, W. R.; Guanghai, W.; Horbett, T. A.; Hoffman, A. S., Protein adsorption to poly(ethylene oxide) surfaces. *Journal of Biomedical Materials Research* **1991**, *25* (12), 1547-1562.
- (4)Alcantar, N. A.; Aydil, E. S.; Israelachvili, J. N., Polyethylene glycol-coated biocompatible surfaces. *Journal of Biomedical Materials Research* **2000**, *51* (3), 343-51.
- (5)Geelhood, S. J.; Horbett, T. A.; Ward, W. K.; Wood, M. D.; Quinn, M. J., Passivating protein coatings for implantable glucose sensors: Evaluation of protein retention. *Journal of Biomedical Materials Research. Part B, Applied Biomaterials* **2007**, *81* (1), 251-60.
- (6)Bridges, A. W.; Garcia, A. J., Anti-inflammatory polymeric coatings for implantable biomaterials and devices. *Journal of Diabetes Science and Technology* **2008**, *2* (6), 984-94.
- (7)Lee, J. H.; Lee, H. B.; Andrade, J. D., Blood compatibility of polyethylene oxide surfaces. *Progress in Polymer Science* **1995**, *20* (6), 1043-1079.
- (8)Kennedy, S. B.; Washburn, N. R.; Simon, C. G., Jr.; Amis, E. J., Combinatorial screen of the effect of surface energy on fibronectin-mediated osteoblast adhesion, spreading and proliferation. *Biomaterials* **2006**, *27* (20), 3817-24.

- (9) Dekker, A.; Reitsma, K.; Beugeling, T.; Bantjes, A.; Feijen, J.; van Aken, W. G., Adhesion of endothelial cells and adsorption of serum proteins on gas plasma-treated polytetrafluoroethylene. *Biomaterials* **1991**, *12* (2), 130-8.
- (10) Bumgardner, J. D.; Wiser R Fau - Elder, S. H.; Elder Sh Fau - Jouett, R.; Jouett R Fau - Yang, Y.; Yang Y Fau - Ong, J. L.; Ong, J. L., Contact angle, protein adsorption and osteoblast precursor cell attachment to chitosan coatings bonded to titanium. (0920-5063 (Print)).
- (11) Sigal, G. B.; Mrksich, M.; Whitesides, G. M., Effect of surface wettability on the adsorption of proteins and detergents. *Journal of the American Chemical Society* **1998**, *120* (14), 3464-3473.
- (12) Vogler, E. A., Protein adsorption in three dimensions. *Biomaterials* **2012**, *33* (5), 1201-1237.
- (13) Zhang, M.; Desai, T.; Ferrari, M., Proteins and cells on peg immobilized silicon surfaces. *Biomaterials* **1998**, *19* (10), 953-960.
- (14) Akizawa, T.; Kino, K.; Koshikawa, S.; Ikada, Y.; Kishida, A.; Yamashita, M.; Imamura, K., Efficiency and biocompatibility of a polyethylene glycol grafted cellulosic membrane during hemodialysis. *ASAIO transactions / American Society for Artificial Internal Organs* **1989**, *35* (3), 333-5.
- (15) Churaev, N. V.; Sergeeva, I. P.; Sobolev, V. D., Hydrodynamic thickness and deformation of adsorbed layers of polyethylene oxides. *Journal of Colloid and Interface Science* **1995**, *169* (2), 300-305.

- (16)McPherson, T.; Kidane, A.; Szleifer, I.; Park, K., Prevention of protein adsorption by tethered poly(ethylene oxide) layers: Experiments and single-chain mean-field analysis. *Langmuir : the ACS journal of Surfaces and Colloids* **1998**, *14* (1), 176-186.
- (17)Kenausis, G. L.; Vörös, J.; Elbert, D. L.; Huang, N.; Hofer, R.; Ruiz-Taylor, L.; Textor, M.; Hubbell, J. A.; Spencer, N. D., Poly(l-lysine)-g-poly(ethylene glycol) layers on metal oxide surfaces: Attachment mechanism and effects of polymer architecture on resistance to protein adsorption†. *The Journal of Physical Chemistry B* **2000**, *104* (14), 3298-3309.
- (18)Shi, J.; Xing, M. M. Q.; Zhong, W., Development of hydrogels and biomimetic regulators as tissue engineering scaffolds. *Membranes* **2012**, *2* (4), 70-90.
- (19)Huang, N.-P.; Michel, R.; Voros, J.; Textor, M.; Hofer, R.; Rossi, A.; Elbert, D. L.; Hubbell, J. A.; Spencer, N. D., Poly(l-lysine)-g-poly(ethylene glycol) layers on metal oxide surfaces: Surface-analytical characterization and resistance to serum and fibrinogen adsorption. *Langmuir : the ACS Journal of Surfaces and Colloids* **2000**, *17* (2), 489-498.
- (20)Mauzac, M.; Jozefonvicz, J., Anticoagulant activity of dextran derivatives. Part i: Synthesis and characterization. *Biomaterials* **1984**, *5* (5), 301-4.
- (21)LofAs, S.; Johnsson, B., A novel hydrogel matrix on gold surfaces in surface plasmon resonance sensors for fast and efficient covalent immobilization of ligands. *Journal of the Chemical Society, Chemical Communications* **1990**, 1526-1528.
- (22)Schasfoort, R. B. M.; Tudos, A. J., *Handbook of surface plasmon resonance*. 1 ed.; RSC Publishing: Cambridge, UK, 2008; p 426.
- (23)Cao, B.; Li, L.; Wu, H.; Tang, Q.; Sun, B.; Dong, H.; Zhe, J.; Cheng, G., Zwitteration of dextran: A facile route to integrate antifouling, switchability and optical transparency into natural polymers. *Chemical Communications* **2014**, *50* (24), 3234-3237.

- (24) Dubois, J.; Gaudreault, C.; Vermette, P., Biofouling of dextran-derivative layers investigated by quartz crystal microbalance. *Colloids and Surfaces B: Biointerfaces* **2009**, *71* (2), 293-299.
- (25) Lichty, J. J.; Malecki, J. L.; Agnew, H. D.; Michelson-Horowitz, D. J.; Tan, S., Comparison of affinity tags for protein purification. *Protein Expression and Purification* **2005**, *41* (1), 98-105.
- (26) Tizzotti, M.; Charlot, A.; Fleury, E.; Stenzel, M.; Bernard, J., Modification of polysaccharides through controlled/living radical polymerization grafting—towards the generation of high performance hybrids. *Macromolecular Rapid Communications* **2010**, *31* (20), 1751-1772.
- (27) Thomas, H.; Stephanie, H.; Nico, M.; Katrin, S., Polysaccharide derivatives for the modification of surfaces by self-assembly. In *Model cellulosic surfaces*, American Chemical Society: 2009; Vol. 1019, pp 195-221.
- (28) Segura, T.; Anderson, B. C.; Chung, P. H.; Webber, R. E.; Shull, K. R.; Shea, L. D., Crosslinked hyaluronic acid hydrogels: A strategy to functionalize and pattern. *Biomaterials* **2005**, *26* (4), 359-71.
- (29) Lapcik, L., Jr.; Lapcik, L.; De Smedt, S.; Demeester, J.; Chabreck, P., Hyaluronan: Preparation, structure, properties, and applications. *Chem Rev* **1998**, *98* (8), 2663-2684.
- (30) Kogan, G.; Soltes, L.; Stern, R.; Gemeiner, P., Hyaluronic acid: A natural biopolymer with a broad range of biomedical and industrial applications. *Biotechnology Letters* **2007**, *29* (1), 17-25.
- (31) Stern, R.; Asari, A. A.; Sugahara, K. N., Hyaluronan fragments: An information-rich system. *European Journal of Cell Biology* **2006**, *85* (8), 699-715.

- (32)Schanté, C. E.; Zuber, G.; Herlin, C.; Vandamme, T. F., Chemical modifications of hyaluronic acid for the synthesis of derivatives for a broad range of biomedical applications. *Carbohydrate Polymers* **2011**, 85 (3), 469-489.
- (33)Neumann, A.; Schinzel, R.; Palm, D.; Riederer, P.; Münch, G., High molecular weight hyaluronic acid inhibits advanced glycation endproduct-induced nf- κ b activation and cytokine expression. *FEBS Letters* **1999**, 453 (3), 283-287.
- (34)Bulpitt, P.; Aeschlimann, D., New strategy for chemical modification of hyaluronic acid: Preparation of functionalized derivatives and their use in the formation of novel biocompatible hydrogels. *Journal of Biomedical Materials Research* **1999**, 47 (2), 152-169.
- (35)Kuo, J. W.; Swann, D. A.; Prestwich, G. D., Chemical modification of hyaluronic acid by carbodiimides. *Bioconjugate Chemistry* **1991**, 2 (4), 232-241.
- (36)Tan, H.; Ramirez, C. M.; Miljkovic, N.; Li, H.; Rubin, J. P.; Marra, K. G., Thermosensitive injectable hyaluronic acid hydrogel for adipose tissue engineering. *Biomaterials* **2009**, 30 (36), 6844-53.
- (37)Miura, M.; Cole Ca Fau - Monji, N.; Monji N Fau - Hoffman, A. S.; Hoffman, A. S., Temperature-dependent absorption/desorption behavior of lower critical solution temperature (lcst) polymers on various substrates. (0920-5063 (Print)).
- (38)Yamamoto, S.-I.; Pietrasik, J.; Matyjaszewski, K., The effect of structure on the thermoresponsive nature of well-defined poly(oligo(ethylene oxide) methacrylates) synthesized by atp. *Journal of Polymer Science Part A: Polymer Chemistry* **2008**, 46 (1), 194-202.

- (39)Coessens, V.; Matyjaszewski, K., Synthesis of polymers with hydroxyl end groups by atom transfer radical polymerization. *Macromolecular Rapid Communications* **1999**, *20* (3), 127-134.
- (40)Popova, M. V.; Chernyshev, Y. S., Self-association of potassium nonanoate molecules in aqueous aerosil dispersions: ¹³C nmr data. *Colloid Journal* **2004**, *66* (5), 567-574.
- (41)Penfold, J.; Staples, E.; Tucker, I.; Thomas, R. K., Adsorption of mixed anionic and nonionic surfactants at the hydrophilic silicon surface. *Langmuir : the ACS journal of surfaces and colloids* **2002**, *18* (15), 5755-5760.
- (42)Harewood, K.; Wolff Iii, J. S., A rapid electrophoretic procedure for the detection of sds-released oncornavirus RNA using polyacrylamide-agarose gels. *Analytical Biochemistry* **1973**, *55* (2), 573-581.
- (43)Vig, J. R., UV/ozone cleaning of surfaces. *Journal of Vacuum Science & Technology A* **1985**, *3* (3), 1027-1034.
- (44)Krozer, A.; Rodahl, M., X-ray photoemission spectroscopy study of UV/ozone oxidation of Au under ultrahigh vacuum conditions. *Journal of Vacuum Science & Technology A* **1997**, *15* (3), 1704-1709.
- (45)Lutz, J.-F., Polymerization of oligo(ethylene glycol) (meth)acrylates: Toward new generations of smart biocompatible materials. *Journal of Polymer Science Part A: Polymer Chemistry* **2008**, *46* (11), 3459-3470.
- (46)Grymonpré, K. R.; Staggemeier, B. A.; Dubin, P. L.; Mattison, K. W., Identification by integrated computer modeling and light scattering studies of an electrostatic serum albumin-hyaluronic acid binding site. *Biomacromolecules* **2001**, *2* (2), 422-429.

- (47)Zengin, A.; Yildirim, E.; Caykara, T., Raft-mediated synthesis and temperature-induced responsive properties of poly(2-(2-methoxyethoxy)ethyl methacrylate) brushes. *Journal of Polymer Science Part A: Polymer Chemistry* **2013**, 51 (4), 954-962.
- (48)Sauerbrey, G., The use of quartz oscillators for weighing thin layers and for microweighing. *Zeitschrift fuer Physik* **1959**, 155, 206-22.
- (49)Rodahl, M.; Höök, F.; Krozer, A.; Brzezinski, P.; Kasemo, B., Quartz crystal microbalance setup for frequency and q-factor measurements in gaseous and liquid environments. *Review of Scientific Instruments* **1995**, 66 (7), 3924-30.
- (50)Höök, F.; Kasemo, B., The qcm-d technique for probing biomacromolecular recognition reactions. *Springer Series on Chemical Sensors and Biosensors* **2007**, 5 (Piezoelectric Sensors), 425-447.
- (51)Larsson, C.; Rodahl, M.; Höök, F., Characterization of DNA immobilization and subsequent hybridization on a 2d arrangement of streptavidin on a biotin-modified lipid bilayer supported on sio2. *Analytical Chemistry* **2003**, 75 (19), 5080-5087.
- (52)Reimhult, E.; Larsson, C.; Kasemo, B.; Höök, F., Simultaneous surface plasmon resonance and quartz crystal microbalance with dissipation monitoring measurements of biomolecular adsorption events involving structural transformations and variations in coupled water. *Analytical Chemistry* **2004**, 76 (24), 7211-7220.

Chapter 3 : Polymer-grafted polysaccharide coatings for reduced blood protein adsorption

Polysaccharides have enjoyed a great deal of attention as biomaterials due to their vast abundance, biodegradability, biocompatibility, inertness, and, most importantly, their protein and cell fouling resistance. The use of polysaccharides as biomaterials spans a range of interesting applications, including coatings, biosensors, tissue engineering scaffolds, filtration membranes and drug delivery. A wide selection of biological cargo has been loaded into or onto polymeric vehicles either for the controlled, systemic or local, release of therapeutics owing to better understanding of bioconjugation techniques. Small drug molecules, short and long peptides and proteins as well as many growth factors and signaling molecules have been reported to be better deliverers via polymeric biomaterials.¹

Some of the most commonly investigated synthetic polymer biomaterials include the use of hydrophilic polymers. Poly (ethylene glycol) (PEG) is the most popular hydrophilic polymers in this area due to its relative monodispersity, increased solubility and hydrophilicity. Other hydrophilic polymers used as biomaterials include poly (vinyl alcohol) (PVA) and poly (acrylamide) (PAAm). While the use of hydrophobic polymers as biomaterials is limited by surface properties and degradation profiles, poly (α -esters) are a class of hydrophobic polymers often used as biomaterials due to their hydrolytically susceptible ester bonds. Amphiphilic and responsive materials such as poly (*N*-isopropylacrylamide) (pNIPAAm) and block copolymers offer very progressive and promising solutions for more advanced biomaterial systems.²⁻³ Biocompatibility and biodegradability are still limiting factors facing the full utilization of synthetic polymers as biomaterials. Hence, the need for bioconjugation with biopolymers is amplified.

While hydrophilic synthetic polymers offer some valuable biomaterial solutions, the biocompatibility and clearance of the final polymer formulation often poses a serious problem. In this domain, polysaccharides play an important role as they are often used in conjunction with such polymers in order to address, positively, any biocompatibility issues. Moreover, the bioactivity of some of these polysaccharides makes them especially attractive for *in vivo* applications such as the inclusion of growth factors.

For years, polysaccharides have been used in various applications due to their biocompatibility and solubility. Viewed as inert water-soluble biopolymers, a lot of these applications have been concentrated in the cosmetic and food industries. As such, polysaccharides have been used as fillers, emulsifiers thickening and gelation factors. However, the use of polysaccharides as biomaterials has been and is becoming increasingly common. Owing to the large number of variant chemical and physical properties, polysaccharides are viewed as a very attractive class of biopolymers that are suitable for many biomaterials-based applications such as, tissue engineering scaffolding, drug delivery, film formation and bioactive coatings. Interestingly, polysaccharides are renewable, biocompatible, non-immunogenic and some of their classes exhibit interesting bioactivity. Moreover, the chemical structure of most polysaccharides and the availability of important functionalities allow for functionalization and modification, which, in turn, allows for a wide diversity of biomedical applications.

Two of the most commonly exploited properties of polysaccharides are gel formation, covalent and non-covalent, and film formation. While each different polysaccharide possesses its own unique chemical structure, polysaccharides as a class

share some chemical and physical characteristics that distinguish them from any other class of biopolymers. In general, polysaccharides are hydrophilic, highly functional and stereoregular polymeric materials. Strong fields of intra- and interchain hydrogen bonding is usually observed due to the high presence of –OH groups within the backbone of the biopolymer. This dense network of hydrogen bonding gives rise to rigid helical conformations in solution.⁴ These groups are also responsible for the ability to form physical and chemical gels and films due to the overall ionic charge they add to the polymer. However, while hydrophilic in nature, all polysaccharides share some inherent hydrophobicity due to the presence of CH₃ groups. Additionally, their biological origin makes them easily recognizable by cells and, consequently, enzymatically degradable, which makes them very attractive and suitable for human *in vivo* applications.

As mentioned above, the availability of many functional groups and moieties in the polysaccharide backbone allows for the facile formation of many interesting systems. Polymer-polysaccharide hybrids are one of the most common systems developed to improve the overall biocompatibility and bioactivity of polymeric biomaterials. In addition to biocompatibility, all polysaccharides are derived from biological systems post biosynthesis; extraction and purification of such materials is relatively simple with very large yields, which makes polysaccharides an affordable option as well. Despite the similarity in their basic chemical structure, mammalian and non-mammalian polysaccharides slightly differ in their biological activity, which gives the mammalian-derived polysaccharide the advantage of possessing specific affinity to certain proteins. Table 3.1 shows the most commonly used polysaccharides.

A broad array of bioconjugation methods is available, which allows for the facile modification and functionalization of synthetic polymer, further tailoring them to specific applications. These chemistries include carbodiimide, epoxide, aldehyde, active ester, radical, and hydrazide reactions.⁵⁻⁶ The bioconjugation of natural biopolymers with synthetic once increases biodegradability and allows for the use of high molecular weights, slower clearance of polymers and increased efficacy.⁷ However, some bioconjugation methods, e.g. carbodiimide, aldehyde and epoxide, are not suitable for the *in situ* conjugation due to the production of cytotoxic reaction intermediates that limit cell viability, which leads to the *ex situ* synthesis and extensive purification of bioconjugates.

To address this limitation, a significant amount of work has been dedicated to developing conjugation methods more suitable for *in situ* conjugation and functionalization of polymer biomaterials. For example, addition reactions have also been utilized for *in situ* conjugation of polymers with mild, nontoxic conditions. Such reactions employ nucleophilic substituents, e.g. thiols, primary amines, in fast kinetics reactions for *in situ* and *ex situ* conjugation and crosslinking.^{5, 8} Additionally, Langer et al, reported the use of UV labile materials suitable for *in vivo* polymerization.⁹ Prestwich et al.¹⁰⁻¹¹ reported various systems composed of more than one functionalized polysaccharides and proteins in crosslinked networks with synthetic polymeric biomaterials (fig. 3.1.). Such gels ECM-mimicking structures and afford better integration, neovascularization and growth factor homing and release. The integration of functionalized hyaluronic acid, chitosan, alginate, heparin, gelatin and fibrin is also reported to produce similar results while avoiding batch-to-batch variations compared to ECM-extracted materials.¹⁰⁻¹⁴

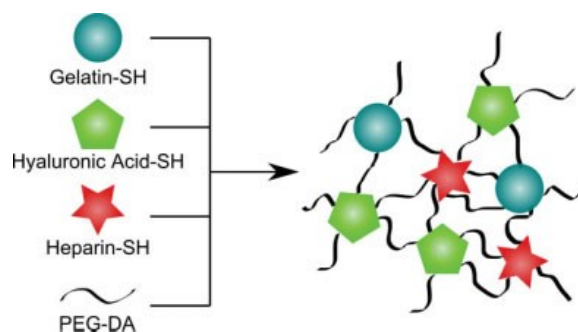


Figure 3.1 Example of multipolysaccharide-polymer hydrogel construct.¹⁵

Alginate: Alginate is a hydrophilic polysaccharide naturally occurring, mostly, in brown algae. Chemically alginate is composed of two blocks of α -L-guluronic acid and β -D-mannuronic acid linked together via a (1 \rightarrow 4) linkage and a carboxylic acid groups at the C5 location.¹⁶ Primarily due to its rapid non-covalent gel formation, alginate has been investigated and used as a biomaterials since the 1940s.¹⁷ Such a property could offer solutions for drug delivery applications where the reversible formation of hydrogels is desirable. For the most part, alginate hydrogels have been used as a sponge-type delivery vehicle, where the dry gel is swelled in a solution containing the biological cargo of interest followed by a subsequent introduction to the host site. Other approaches also include the encapsulation of biologics with the alginate hydrogels *in situ*. Mooney et al. reported modifying alginate with cellular adhesion domain to give alginate non-covalent hydrogels cellular adhesion properties that the unmodified alginate lack.¹⁸

One way polymer-alginate systems are utilized is the context of stabilizing ionic alginate hydrogels. The presence of monovalent cation in solutions containing non-covalent alginate hydrogels leads to destabilization of the gel due to rapid ionic exchange resulting in alteration to both the mechanical properties as well as degradation profile of the hydrogel. Here, carbodiimide conjugation of PEG to the COOH groups on the alginate

chain was reported to stabilize the polymer and control the mechanical properties and swelling behavior of the final hydrogel.¹⁹ Lee et al. reported pH- and temperature-responsive interpenetrating networks (IPN) hydrogels based on the EDC/NHS conjugation of pNIPAAm with alginate prior gelation.²⁰ Moreover, recent work developed by Bencherif et al. introduced the preparation and utilization of injectable and shape memory alginate cryogels which has promising potential when it comes to targeted and minimally invasive drug delivery.²¹

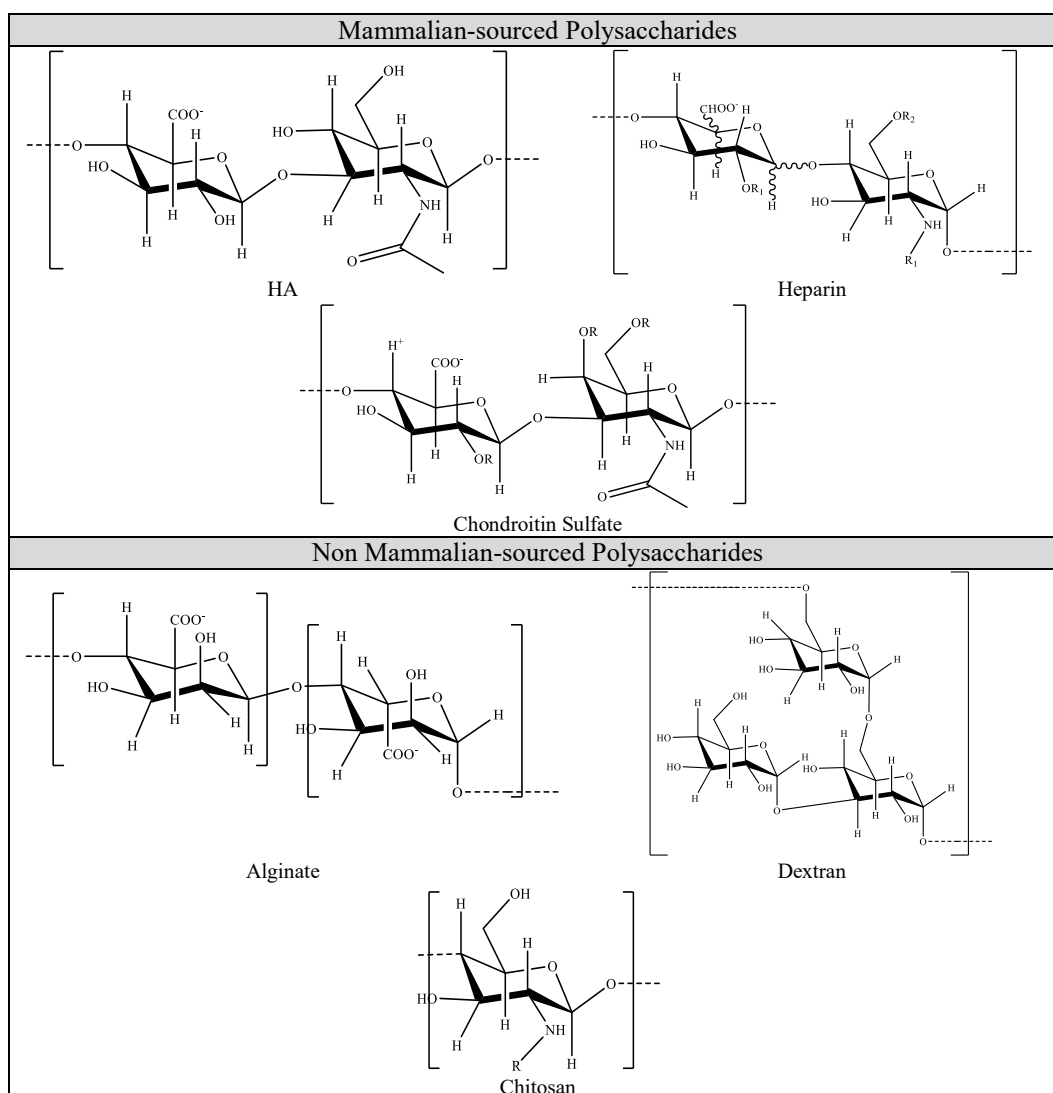


Table 3.1 Common polysaccharide as biomaterials

Alginate-based materials, however, are not the ideal polysaccharide for many application due to clearance and degradation limitations.²² Despite its biocompatibility, the degradation pathway of alginate is not completely understood despite the inconsistent biodegradation results reported, especially at higher molecular weight.²³ Therefore, recent work has been targeted towards explaining the biodegradation and clearance pathways as well as developing strategies that aim to slowly degrade and clear the polymer from the site. For example, Boontheekul et al. reported that partial oxidation of alginate biomaterials to about 1% lead to increase of degradation due rapid acetal hydrolysis.²⁴ Also, Lee et al. used gamma radiations to control, by reduction, the molecular weight of pNIPAAm/alginate IPNs.²⁰

Chitosan: chitosan is an exoskeletal linear hydrophobic polysaccharide. Being one of the most abundant polysaccharides, chitosan consists of (1→4)-β-*N*-acetyl-D-glucosamine and D-glucosamine mixture units. While the acetylated units showed reduced water solubility in neutral pH, deacetylation improves aqueous solubility on the expense of molecular weight and molecular weight distribution.²⁵ The increased use of chitosan in biomedical applications is attributed, mostly, to enhanced solubility post deacetylation, gel forming properties, amine functionality and enzymatic degradation of the β(1→4) link. Taking advantage of these properties as well as other polymer-chitosan systems, chitosan biomaterials have been used as drug delivery vehicles, wound dressings as well as tissue engineering scaffolds.²⁵⁻²⁶

Most applications of chitosan as a biomaterial are based on the unique solubility and hydrophobicity profile of chitosan. For example, Chenite et. al reported the synthesis

of responsive and injectable chitosan hydrogels by dissolving the polymer in acidic pH and gradually raising the pH to 6.2-7, a soft and reversible hydrogel could be obtained without the need for chemical crosslinking.²⁷ Also, polymer-chitosan hydrogel systems have been reported.²⁸ Albertsson et. al reported a poly(lactic acid) (PLA), PLA-chitosan, grafted pH responsive hydrogels.²⁹ More importantly, polymer-chitosan grafted systems exhibit interesting amphiphilic properties that offer valuable solutions for micelles formation and drug delivery. Hydrophobic polyesters such as poly(caprolactone)³⁰ and PLA³¹ have been reported to form unique self-assembled nanoparticles and micellar structures when grafted chitosan. The degree of chitosan modification and grafting density could be tailored towards the desired size and CMC.³² PEGylation of chitosan has also been reported to thermoresponsive hydrogels. Bhattarai et al. synthesized thermoresponsive PEG-chitosan materials that form viscoelastic gels at body temperature, a profile that could be utilized for the controlled release of therapeutic proteins.³³

Overall, chitosan possesses unique chemical and physical properties, namely available amine functionality, water solubility and low cost, which lead to a wide selection of materials and ionic, pH and thermos responsive hydrogels. However, the polysaccharide inherent hydrophobicity limits its use in material interfaces and films.

Dextran: amongst natural polysaccharides, dextran enjoyed a great deal of attention as a biomaterial. One of the earliest applications of dextran came as plasma replacement.³⁴ Dextran is predominantly of bacterial origin. Chemically, dextran is a branched polysaccharide with a linear (1→6)- α -D-glucose backbone and (1→3) branches that forms about 5% grafting density. Dextran is enzymatically degradable and highly

soluble with plenty of –OH groups that also makes suitable target for functionalization and subsequent bioconjugation.³⁵

Dextran hydrogels have been extensively studied for varying applications. Protein and cellular adsorption resistance properties of dextran have been well characterized and utilized over the year giving rise to many commercial applications.³⁶ Also, Cao et al. reported the zwitteration of dextran yielding high preforming dextran non-fouling surfaces.³⁷ Grafting of lactide oligomer have been reported to yield elastic dextran hydrogels.³⁸ Advanced and responsive dextran hydrogels have been described using UV crosslinking of grafted acrylate groups with PLA,³⁹ PEG-diacrylate,⁴⁰ pNIPAAm and other copolymers.⁴¹⁻⁴³ Vinyl sulfone-functionalized dextran have been reported by Hiemstra et al. for *in situ* polymerization with PEG derivatives yielding locally induced hydrogels.⁴⁴ As such, owing its non-fouling behavior, high solubility, functionality and biodegradability, dextran hydrogels have been employed as a biomaterial as a drug delivery vehicles⁴⁵⁻⁴⁶ and non-fouling surfaces in diagnostic and medical devices.^{37, 47-48}

Hyaluronic acid: Hyaluronic acid (HA) is a linear, viscous, naturally occurring, high molecular weight biopolymer composed of glycosaminoglycan (GAG) a copolymer of D-glucuronic acid and N-acetyl-D-glucosamine, through a β -1,4 glycosidic bond, and a β -1,3 bond that links the disaccharides units, as shown in fig.1.⁴⁹⁻⁵³ HA is found in the human body as part of the extracellular matrix (ECM), umbilical cord, synovial fluid, the vitreous humor of the eyes and as a lubricant between the joints. The biopolymer, HA, is synthesized in the cytoplasmic surface of the plasma membrane, which is different than other GAGs and polysaccharides as they are synthesized in the Golgi apparatus.⁵³⁻⁵⁴

One significant difference with PEG is the intrinsic biological activity of HA. HA is known to have anti-inflammatory activities and is recognized by cells through the cell surface receptors that promote a motile phenotype (CD44, RHAMM, ICAM-1), and it is this recognition that has shown to greatly influence some biological processes such as metastasis, morphogenesis, inflammation and wound repair. Another major difference is HA is highly degradable *in vivo* by the enzyme hyaluronidase, and the products of this degradation have been reported to influence and improve the wound healing process.⁵³⁻⁵⁵ The high viscosity of HA offers an advantage for localization and lubrication applications. The final major difference with PEG is that while PEG can be synthesized to be reactive at one or both ends of the molecule using a broad range of reactive groups that do not cross-react with the polyether chain, most chemical functionalization strategies of HA can react at hydroxyl and carboxylic acid groups on every monomer and the residual groups on HA limit options for reactive groups.^{6, 56-57} This provides an advantage in terms of higher reactivity of HA but also a challenge in controlling chemical functionalization, especially since site-specific functionalization of HA is essentially impossible. Soluble HA has been used in clinical applications including ocular surgery, visco-supplementation for arthritis and wound healing. However, the relative rapid degradation and clearance *in vivo* of uncross-linked HA limit many direct clinical applications.⁵⁸

In the current work, a method for polysaccharide modification to obtain hydrophilic nonfouling coatings is described. The polysaccharide alginate (Alg), carboxymethyl dextran (CMD), carboxymethyl cellulose (CMC) and hyaluronic acid (HA) were used to create thermoresponsive antifouling coating materials while preserving biological integrity. This is accomplished by grafting the thermo-responsive polymer,

poly(di(ethylene glycol) methyl ether methacrylate) (PMEO₂MA) to the biopolymer's backbone. By controlling the polymer PMEO₂MA composition, its thermo-responsive behavior can be tuned to a specific temperature known as the low critical solution temperature (LCST), above which the polymer transitions to the hydrophobic domain^{28,29}. This is particularly beneficial when grafting it to the backbone of high molecular weight biopolymers. By keeping the solution temperature above the LCST of PMEO₂MA, the polysaccharide, along with PMEO₂MA, would stay tightly bound to the surface of the substrate by hydrophobic forces.²⁹ Previously, in chapter 2, the ability of these hybrid materials in the context of just hyaluronic acid in preventing blood protein adsorption onto coated surfaces was established. While the anchoring mechanism is the same, insight into coating and antifouling mechanism is needed, and further investigation of the effect of polysaccharide chemistry is to be established.

3.3. Experimental Section

3.3.1. Materials. Di(ethylene glycol) methyl ether methacrylate (M(EO)₂MA), ethyl 2-bromo-2-methylpropionate (EBiB), 2,2'-bipyridine (bpy), Copper(I) bromide (CuBr), anisole, hexanes, ethylenediamine, triethylamine (TEA), 4-(dimethylamino)pyridine (4-DMAP), sodium alginate (Alg) (90 kDa), carboxymethyl cellulose (CMC) (700 kDa), carboxymethyl dextran (CMD) (50 kDa) and hyaluronic acid (HA) derived from *Streptococcus equi* (ca. 1.6 MDa) were purchased from Sigma-Aldrich. Albumin from bovine serum (BSA) (>98%, received as a lyophilized powder) and fibrinogen (Fbg) from human plasma and human (IgG) were purchased from Sigma-Aldrich. Propane phosphonic acid anhydride (T3P) in 50% w/w solution in N,N-dimethylformamide was obtained from Sigma-Aldrich. Monomethoxy poly(ethylene

glycol) epoxide (mPEG-epoxide) of a 10 kDa molecular weight was purchased from Creative PEGWorks and used as received.

3.3.2. Synthesis of the homopolymer of PMEO₂MA by ATRP. Synthesis of PMEO₂MA was performed as reported⁵⁹ with minor modifications. First bpy and CuBr (0.20 mmol and 0.12 mmol, respectively) were added to a dry 25 mL Schlenk flask. The flask was deoxygenated rapidly after adding the solids *via* four consecutive vacuum-nitrogen cycles. Anisole, M(EO)₂MA and EBiB were dried over baked 4 Å molecular sieves and degassed with nitrogen for 30 minutes prior reacting with the catalysts. Using the Schlenk techniques, 3.3 mL anisole, 4.9 mL of the monomer (M(EO)₂MA) (26.6 mmol) and 18.6 µL of EBiB (0.13 mmol) were added to the schlenk flask under nitrogen. The reaction was allowed to proceed at 60 °C using an oil bath for 6 h. The reaction was terminated by exposing it to air. The reaction mixture was then diluted in excess THF and the catalyst was removed from the mixture by passing the sample through a neutral alumina column. The solution was then precipitated in excess hexane and the precipitate was filtered. The solid product was dried under vacuum for 6 h. Polymerization reaction kinetics were monitored by periodically withdrawing samples from the reaction mixture. Composition was validated by ¹H NMR and end group analysis indicated an M_n value of 34,000 g/mol. Gel permeation chromatography (GPC) was used to measure M_n and M_w/M_n.

3.3.3. Modification of PMEO₂MA with amine group. The procedure followed another performed by Coessens et al.⁶⁰ Following drying, PMEO₂MA with a terminal bromide end group was acquired. Then PMEO₂MA was dissolved in ethanol at a

concentration of 50 mg/mL. PMEO₂MA solution was mixed with a 25x molar excess of ethylenediamine (EDA) and 1.2x molar excess of TEA to EDA. The mixture was allowed to react for 48 h in an oil bath at 60 °C then was precipitated into hexanes. The solid polymer was re-dissolved in Milli-Q water and dialyzed against 2,000 MWCO membrane with repeated water changes to remove unreacted reagents. Following dialysis, the sample was frozen at -80 °C and lyophilized on a Labconco Freezeone Plus freeze-dry system. Products were characterized using ¹H NMR.

3.3.4. Synthesis of polysaccharide-PMEO₂MA conjugates. HA, Alg, CMD and CMC were dissolved in Milli-Q water at a concentration of 5 mg/mL. Then 20% of the carboxylic acid groups were activated by 1.5x molar excess T3P. To that 4-DMAP was added to the activated HA as an acylating agent in a 2:1 ratio. To the activated materials, a 1:1 molar ratio of NH₂-PMEO₂MA was added. The reaction mixture was set at room temperature for 24 h. After 24 h the solution was diluted with water and dialyzed against 50,000 and 100,000 MWCO dialysis membrane to remove unreacted PMEO₂MA. Dialyzed samples were frozen at -80 °C and lyophilized. Then ¹H NMR characterization was carried out on the solid product to confirm conjugation.

4.3.5. ¹H NMR characterization. NMR spectra were obtained using a Bruker Avance 300 MHz spectrometer. Deuterated chloroform (CDCl₃) was used as the solvent for PMEO₂MA and its derivatives. Deuterium oxide (D₂O) was used as the solvent for polysaccharides and its derivatives. All samples were prepared at a concentration of 0.5% (wt/wt).

4.3.6. Gel Permeation Chromatography (GPC). A GPC system composed of a Waters 515 HPLC Pump and Waters 2414 Refractive Index Detector using PSS columns (Styrogel 10², 10³, 10⁵ Å) in dimethylformamide (DMF) as an eluent at a flow rate of 1 mL/min at 50 °C was used. Samples were filtered over neutral alumina prior to analysis. The column system was calibrated with 12 poly(methyl methacrylate) (PMMA) standards.

4.3.7. Dynamic light scattering (DLS). Dynamic light scattering (DLS) was measured using a Zetasizer Nano from Malvern Instruments, Ltd. Samples were prepared at a 0.1% (w/w) solution, and diluted in Milli-Q water. Sphere radii were taken from an average of 3 runs.

4.3.8. Tapping mode atomic force microscopy (AFM). Experiments were carried out using a Multimode Nanoscope III system (Veeco 2 Instruments). Measurements were performed in air, using commercial silicon cantilevers with a nominal spring constant and resonance frequency respectively equal to 50 N/m and 290 kHz.

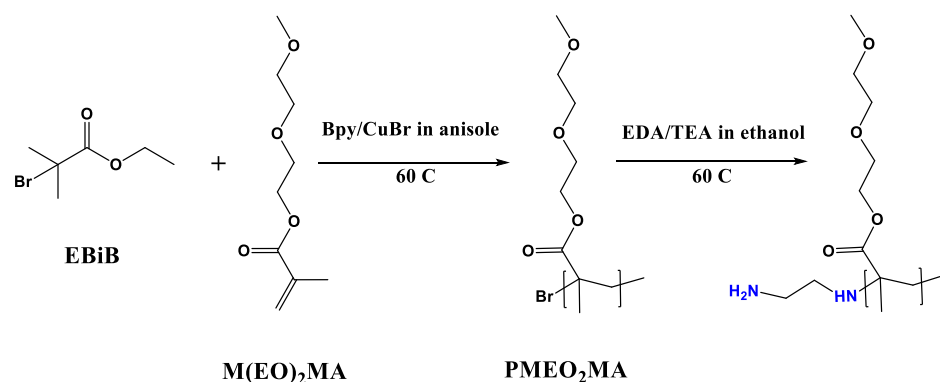
Silicon wafers with native oxide layers were cleaned with a jet of acetone, then with a jet of isopropyl alcohol, before the acetone evaporated, and blown dry with a flow of nitrogen. All samples were drop-casted on the substrates from 1 mg/mL aqueous solutions. Casting above lower-critical solution temperature (LCST) was carried out at 37 °C in a Fisher Scientific low temperature incubator.

The polysaccharide-PMEO₂MA samples were allowed to dry on a substrate at 37 °C. Coated wafers were incubated in a 10% albumin solution for up to 15 days and then imaged to assess protein adsorption on the scratched area.

4.3.9. Water contact angle measurements for modified polysaccharide films.

Water contact angle was measured for films casted on Teflon surfaces using a Ramè-Hart contact angle goniometer. A 4 mg/mL solution of polysaccharide-PMEO₂MA was prepared in pure water. The solution was then drop-cast over Teflon surfaces below the LCST. The discs were then incubated at 37 °C for an hour to ensure transition, uniform and tight coating over the surface. Warm water droplets (2-15 µL) were placed over the cast film and the native substrate; images were taken 30 s post water placement. The process was repeated 10 times for each volume and average measurements are reported.

3.4. Results and discussion



Scheme 3.1 Synthesis of the homopolymer of PMEO₂MA by ATRP

3.4.1. Polysaccharides Modification. PMEO₂MA is a biocompatible thermoresponsive polymer whose lower critical solution temperature (LCST) can be tailored to temperatures in the range of 26-52 °C depending on the number of ethylene oxide repeat units on the side chains.⁵⁹ Once the LCST was exceeded, the polymer precipitated from solution, as the hydrophobic interaction within the polymer chains overcome those of the hydrophilic interactions between the polymer and the solvent, transitions from coil to globule and anchor the polysaccharide to surrounding surfaces.⁶¹

This drove physical adsorption of the polymer to the surface of the substrate, binding the polysaccharide to the surface with it. We hypothesized that this process would result in presentation of the hydrophilic sugar from the surface of the coating, providing a means for preparing a robust biomaterial surface that resists protein adsorption.

3.4.2. Dynamic Light Scattering. DLS was used to characterize the size of polysaccharide-PMEO₂MA in solution. Below the LCST, all measured solutions showed particle sizes not significantly different than unmodified polysaccharide solutions, with a mean size of 30 nm for HA-PMEO₂MA, 20 nm for Alg-PMEO₂MA, 40 nm for CMC-PMEO₂MA and 10 nm for CMD-PMEO₂MA consistent with previous reports.⁶² Above LCST, HA-PMEO₂MA aggregates showed a particle size approaching 300 nm (Fig. 3.2 a-b) while Alg-PMEO₂MA, CMC-PMEO₂MA and CMD-PMEO₂MA showed particle size of 120 nm, 1100 nm and 800 nm respectively. This suggests that aggregates form homogenously in solutions and then precipitate onto the surface to form the coating, but further work is required to determine the exact steps of this process. As shown in fig. 3.2, alginate and dextran-based materials showed a tailing size transition approaching LCST. This is associated with varying degrees of size polydispersity due to polysaccharide aggregation. This is clearer in the CMD-PMEO₂MA material (Fig. 3.2.c). The first transition is observed around particle sizes of 200 nm, which is then increases to approach the average value of 800 nm.

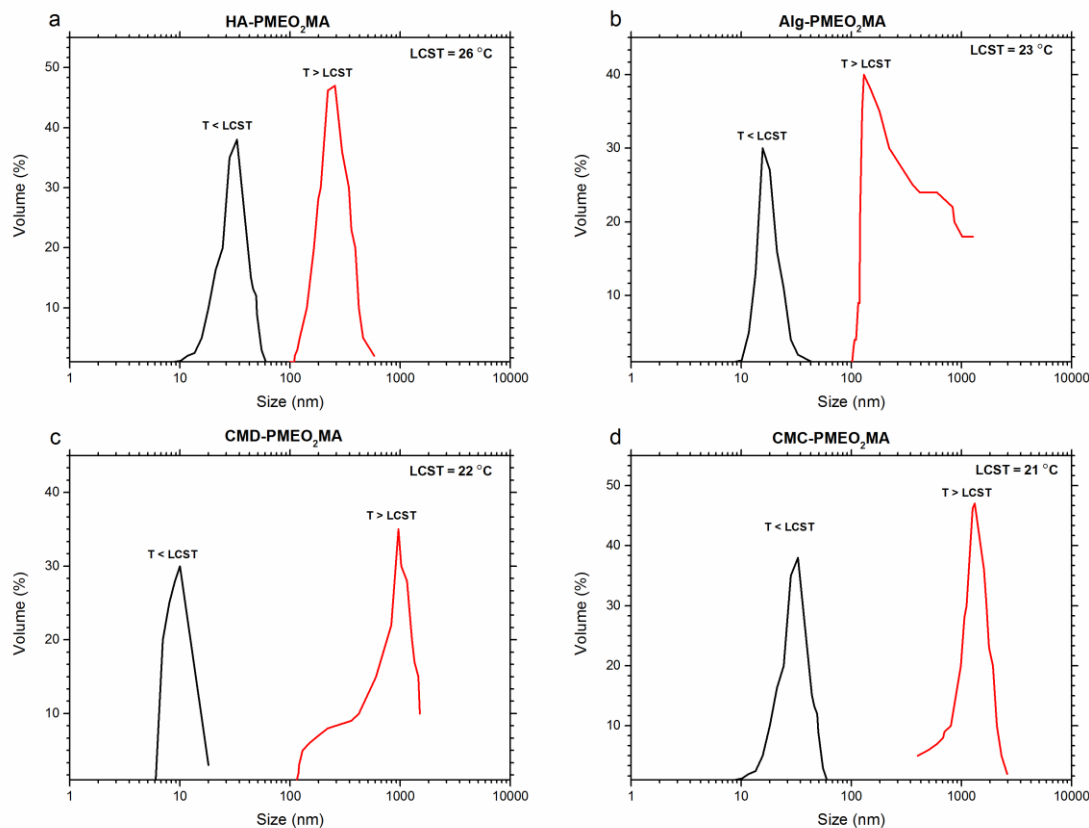


Figure 3.2 DLS data showing the distributions of diameters for (a) HA-PMEO₂MA, (b) Alg-PMEO₂MA, (c) CMD-PMEO₂MA and (d) CMC-PMEO₂MA below LCST and above LCST.

These results also indicate the rapid aggregation or dissolution of the hybrid polymer, especially in the case of CMC-PMEO₂MA. The constant increase in particle size approaching LCST indicates a preferential transition to the hydrophobic domain. Moreover, this also indicates stronger interchain interactions that would lead to more pronounced aggregation. While the difference in temperatures is not very significant, this poses an issue when forming coating materials. The rapid transition of the polysaccharide, strong attraction forces and larger particle size are expected to give rise to the formation of multilayers of coating material on the surface.

The results also show a greater dependence of LCST on the polysaccharide chemistry and molecular weight. This is observed by changes in LCST for the different polymer systems to yield a 23 °C for Alg-PMEO₂MA, 21 °C for CMC-PMEO₂MA and 22 °C for CMD-PMEO₂MA. These value diverge from that observed for the ungrafted polymer of 26 °C. However, the LCST behavior of the polymer is believed to be completely imparted to HA upon grafting. This is indicated by the retention of LCST at 26 °C for HA-PMEO₂MA materials as appose to changes in LCST for the other polysaccharides.

3.4.4. Atomic Force Microscopy (AFM) Analysis. AFM analysis was used to compare the morphology of uncoated SiO₂ surfaces with those exposed to the HA-PMEO₂MA, Alg-PMEO₂MA, CMC-PMEO₂MA and CMD-PMEO₂MA solutions. Moreover, film thickness was assessed employing a scratch test in which a scratch is created on the coated surface, creating a groove of uncoated surface. Results obtained from these experiments are shown in fig. 3.3. In these experiments, coating materials were deposited on an SiO₂ surface cleaned by sonication in ethanol and blown dry with air. The coating was deposited by drop-casting from an aqueous solution, dried in an incubator, and rinsed with warm water. The thickness of the layer was determined by measuring the film profile following mechanical delamination with a needle. Following the scratch test, a difference in reflectivity was observed with the delaminated region reflecting ambient light much more strongly than the coated region. By comparing the change in film height using AFM, the thickness was determined to be ~50 nm for the HA-PEMO₂MA materials. AFM analysis revealed the presence of a uniform layer of characteristic granular appearance. When compared to coatings from CMC-PMEO₂MA, Alg-PMEO₂MA and CMD-PMEO₂MA, the surface profile of the four polysaccharides is significantly different in

nature, thickness and appearance. CMC-PMEO₂MA showed the thickest layers of the four with thickness of > ~240 nm. Alg-PMEO₂MA and CMD-PMEO₂MA recorded ~120 nm and ~80 nm respectively. A similar trend could also be observed when comparing the morphology of the coatings (fig.3.3). CMC-PMEO₂MA showed the smoothest most uniform coating. This could be explained by taking the more favorable interchain interactions amongst the CMC materials into consideration. This is consistent with particle size data obtained with DLS in fig.3.2. Size data suggest increased affinity of CMC particles to aggregate more rapidly and tightly above LCST. This is observed by AFM as thicker more uniform coatings of the substrates above LCST. The trend is maintained for Alg-PMEO₂MA and CMD-PMEO₂MA as there is a good correlation between aggregation and particle size above LCST and film morphology. The AFM phase data also show prominent probe streak patterns on the film which is most associated with high film elasticity. This is also positively correlated with the thickness of the polysaccharide films.

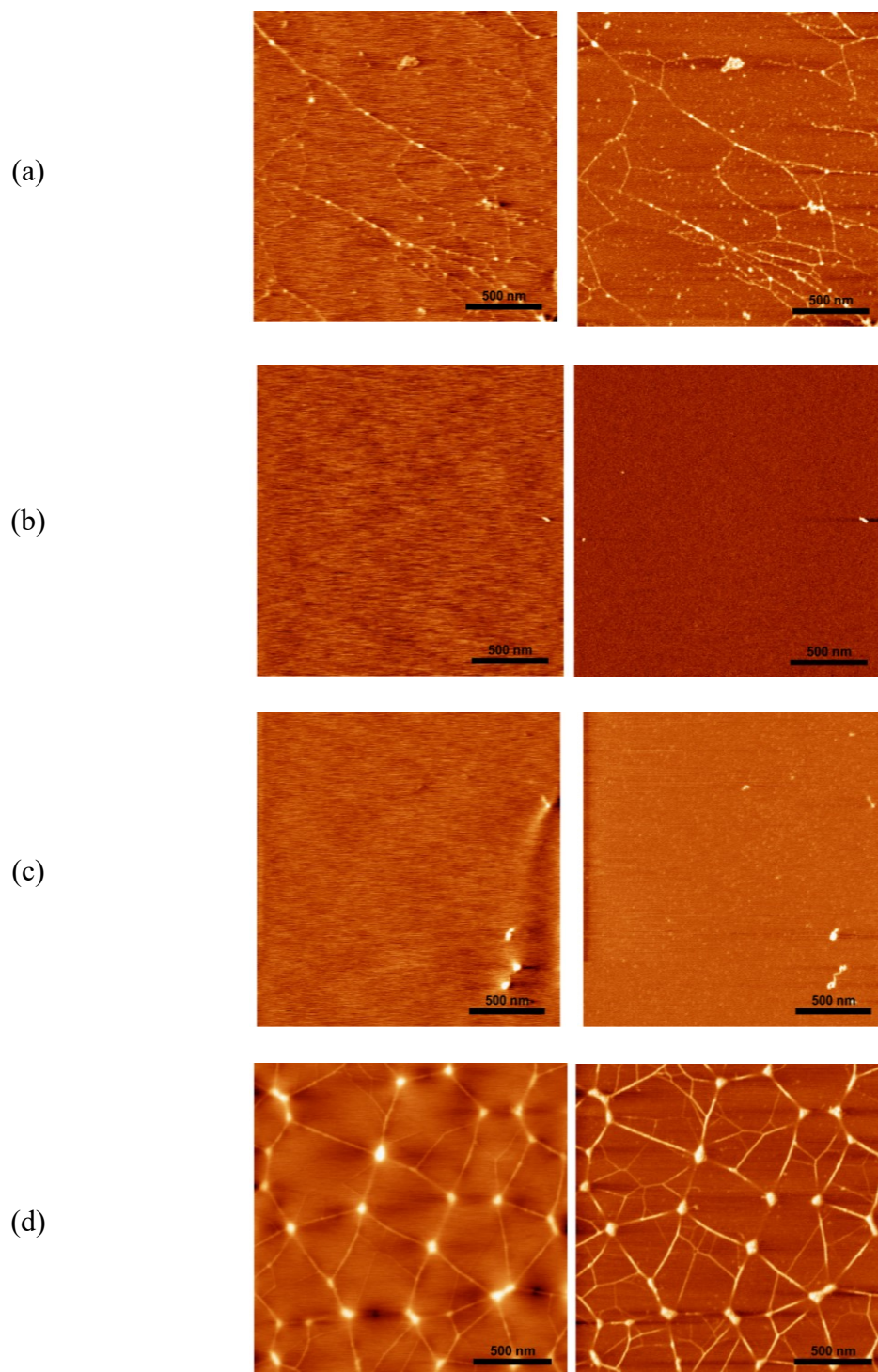


Figure 3.3 AFM images of polysaccharide-PMEO₂MA materials in phase mode (Left) and height (Right).
a) CMD-PMEO₂MA, b) CMC-PMEO₂MA, c) Alg-PMEO₂MA and d) HA-PMEO₂MA

3.4.5. Water contact angle. The average of 10 measurements on films formed by the drop-casting of HA-PMEO₂MA, Alg-PMEO₂MA, CMD-PMEO₂MA and CMC-

PMEO₂MA materials above LCST showed that HA-PMEO₂MA-coated surfaces exhibited most significant increase in hydrophilicity, changing from 98° on uncoated Teflon to 16° on HA-PMEO₂MA films on a Teflon substrate. An increase in hydrophilicity was also observed for the other substrates but with varying degrees with HA giving the lowest water contact angle. CMC-PMEO₂MA recorded the highest water contact angle of 52°, while Alg-PMEO₂MA and CMD-PMEO₂MA recorded 45° and 24° respectively. This effect is believed to be a result of the HA coatings not the hydrophilic ethylene oxide domains in PME₂MA because surface-grafted PME₂MA brushes have been shown to exhibit water contact angle shifts from 40° to 102° below and above LCST, respectively.⁶³ Although the coating domains appeared uniform, as demonstrated by AFM measurements, hydrophobic PME₂MA could still be presented from the surface of the coating as opposed to being sequestered in the coating interior or at the Teflon surface. The drop in hydrophilicity could be correlated to two factors. As the molecular weight of the polysaccharide increase, the hydrophilic interactions as well as the hydrogen bonding between the chains in solution are expected to overcome the hydrophobicity of the PEMO₂MA domains. However, this is not the case for the CMC materials as the degree of substitution plays a big role as well. CMC materials with higher substitution ratio is intrinsically more hydrophobic.

Coating materials	Polysaccharide MW	Water contact angle
CMC-PMEO ₂ MA	700 kDa	52°
Alg-PMEO ₂ MA	120 kDa	45°
CMD-PMEO ₂ MA	50 kDa	25°
HA-PMEO ₂ MA	1.64 MDa	16°

Table 3.2 Water contact angle measurements of polysaccharide-PEMO₂MA-coated surfaces

It is, therefore, suggested that intrinsic HA properties are responsible for the increased hydrophilicity of the coated substrates as reflected by the near-wetting water contact angles measured on the modified substrates.

3.4.6. Biolayer Interferometry (BLI) Analysis.

2.4.6.1. Control experiments of protein against the surface of unmodified sensor tips. BLI

Three separate experiments were performed where six sensor tips per experiment were modified with TMS, and introduced to 6 wells of a 96-well plate containing BSA, and unmodified HA (proteins was run in a separate experiment). The protein-adsorption experiments were all run at concentrations of 0.2 mg/mL, 0.1 mg/mL, 0.05 mg/mL, 0.025 mg/mL, 0.0125 mg/mL, and 0 mg/mL, while unmodified HA was run at a concentration of 2.5 mg/mL.

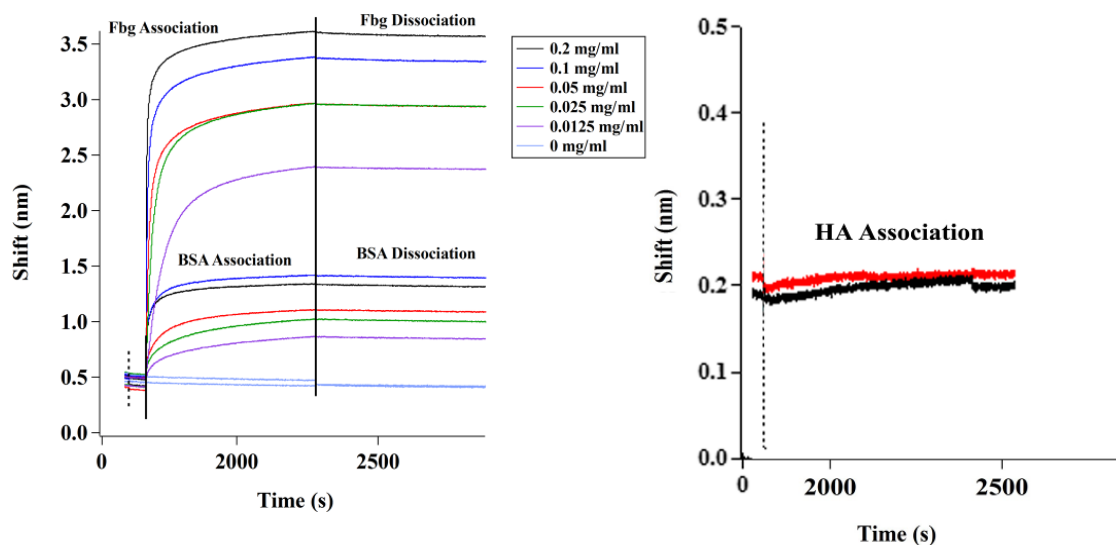


Figure 3.4 Binding behavior of BSA and Fbg proteins (left) and unmodified HA (right) against TMS functionalized sensor tip as measured.

Fig. 3.5. shows representative protein adsorption experiments. The Fbg protein had a change in film thickness characterized by shift values ranging from 1.9 – 3.1 nm, BSA

had shift values ranging from 0.4 – 0.9 nm, consistent with relative differences in protein size. The data were fit using the ForteBio analysis software, and an average on-rate, k_{on} , for protein association, was calculated to be $(5.8 \pm 1.3) \times 10^5 \text{ M}^{-1}\text{s}^{-1}$ for Fbg, and $(2.8 \pm 1.9) \times 10^5 \text{ M}^{-1}\text{s}^{-1}$ for BSA. An off-rate was also calculated for this model, for Fbg k_{off} was $(3.0 \pm 1.5) \times 10^{-5} \text{ s}^{-1}$, and for BSA it was $(5.2 \pm 3.6) \times 10^{-5} \text{ s}^{-1}$. The K_D values for Fbg and BSA on the TMS-functionalized surfaces were $5.2 \times 10^{-11} \text{ M}$ and $1.9 \times 10^{-10} \text{ M}$ respectively, suggesting strong binding interactions for both serum proteins on hydrophobically modified sensor surfaces.

2.4.6.2. Effect of free PEG on protein adsorption. A separate control experiment was performed to identify the effect of free PEG on protein adsorption. Here, the amine terminated sensor tips were reacted with an epoxy-terminated 10 kDa methoxyPEG. A 10 kDa molecular weight is estimated, based on the number of active sites on the sensor tips, and the radius of gyration of the 10 kDa PEG, to provide full coverage of the surface area of the sensor tip when the polymer reacted with the free amines.

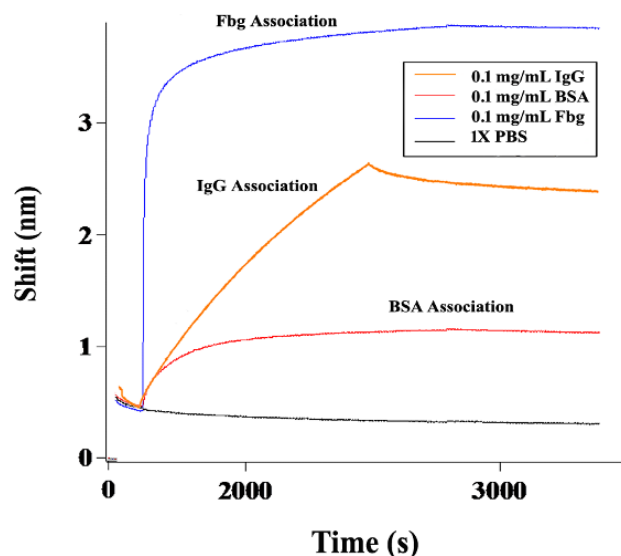


Figure 3.5 Protein adsorption profiles on PEG-modified sensor tips as measured by BLI against BSA, Fbg and IgG.

Fig. 3.6. shows that the Fbg, IgG and BSA deposited with 3.4 nm, 2.5 nm and 0.7 nm change in film thickness, respectively. Despite the presence of a free PEG chain at the surface, proteins were still capable of depositing onto the sensor tip.

2.4.6.3. Modified polysaccharide materials. Protein adsorption on the HA-PMEO₂MA, Alg-PMEO₂MA, CMC-PMEO₂MA and CMD-PMEO₂MA coatings was then investigated. Here, the modified sensor tips were introduced to solutions of coating materials at a concentration of 0.240 mg/mL with an approximate polysaccharide modification degree of 10%. The experiments were run at 37 °C to ensure that the experimental temperature exceeded the LCST temperature of all the hybrid materials and to simulate biological temperatures.

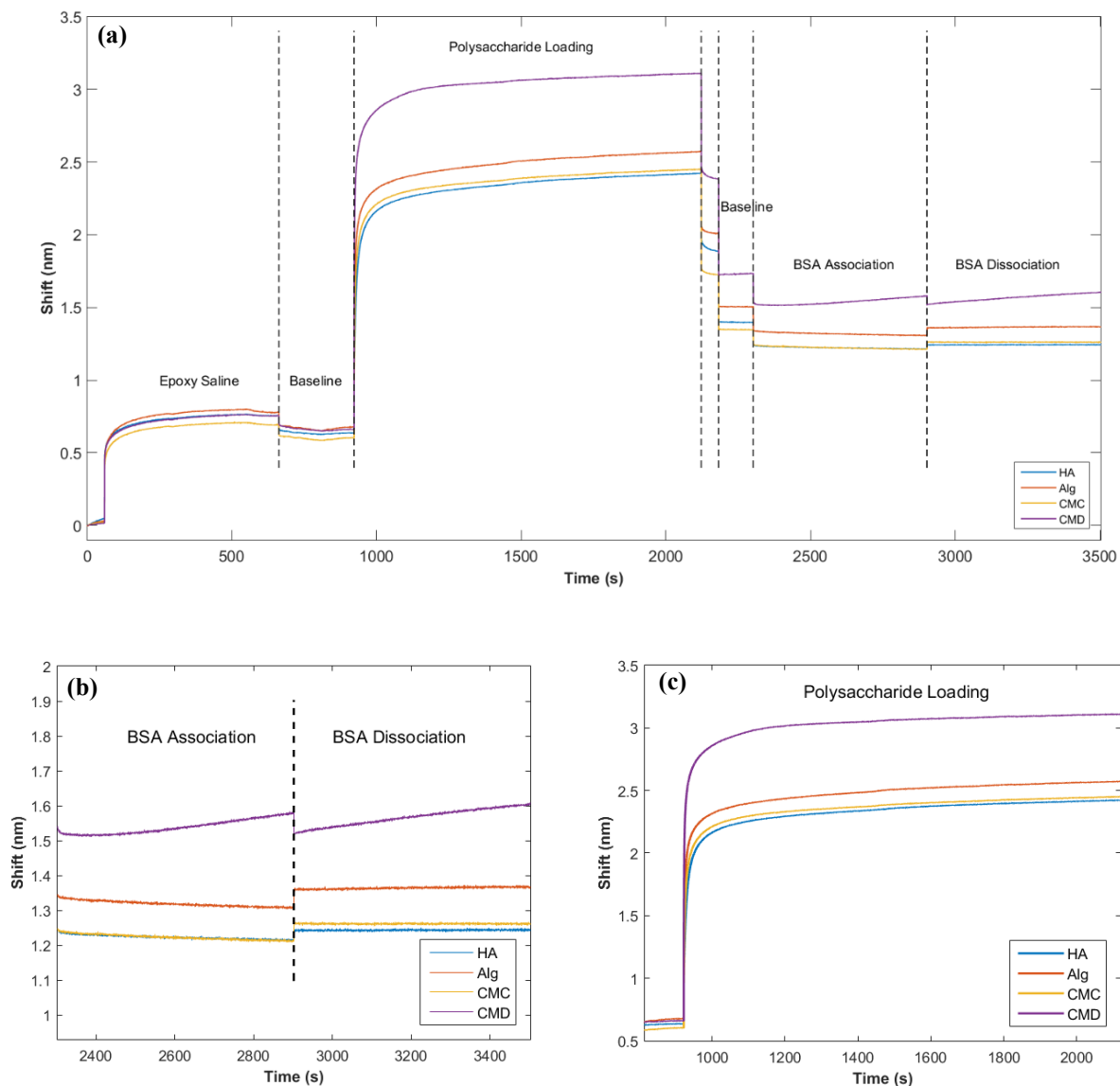


Figure 3.6 Protein adsorption profiles on HA-PMEO₂MA, Alg-PMEO₂MA, CMC-PMEO₂MA and CMD-PMEO₂MA materials as measured using BLI: (a) overall steps, (b) BSA association and dissociation curves and (c) polysaccharide loading curves

The functionalized sensor tips were then immersed in solutions of BSA. Fig. 3.7.a, b and c display the results of protein adsorption to the sensor tips functionalized with the HA-PMEO₂MA, Alg-PMEO₂MA, CMC-PMEO₂MA and CMD-PMEO₂MA material. In the BSA experiments, tips were immersed in the protein solution for 30 min, and showed

no measurable association for BSA, indicating that the polysaccharide-PMEO₂MA polymer prevents protein adsorption to the surface of the functionalized sensor tip.

It is interesting, however, to point out to the gradual increase of film thickness in the case of the CMD-PMEO₂MA material after 10 minutes of protein submersion. This increase is gradual and very slight (fig. 3.7.a). Consistent with the DLS data, this could be explained in lights of the increased particle aggregation. Further examination (fig. 3.7.c) of the CMD-PMEO₂MA profile reveals the greater degree of loading onto the sensor tip. CMD-PMEO₂MA material gave a chemical shift of 3 nm, as appose to just 2 nm for the rest of the polysaccharides studied in this context. Moreover, the shift profile observed is not very consistent with that associated with protein adsorption, which further supports the aggregation hypothesis.

3.5. Conclusions

In conclusion, these results establish the fact that the PMEO₂MA-grafted hybrid system is suitable for polysaccharide application to yield versatile thermo responsive coatings materials. While the degree of hydrophilicity appeared to be greatly dependent on the molecular weight of the used polysaccharide, the intrinsic interactions of the polysaccharide also affects the final properties of the hybrid system. Combined results from BLI, DLS, AFM and water contact angle also show that HA-PMEO₂MA materials show the most promising material tested for antifouling coatings. The combination of near-wetting profile of the coatings, uniform consists coatings and biological activity makes HA the material of choice for further applications. While the other tested polysaccharides showed increased hydrophilicity, the final properties of the coatings remain greatly

dependent on the degree of substitution and favorable interchain interactions that would limit the applicability of some of these systems, namely in microfluidic and diagnostic applications. More studies are needed to assess the protein adsorption profile on the polysaccharide hybrids as well as to establish a more clear correlation of film formation with molecular weight and degree of substitution.

References

- (1)Langer, R., New methods of drug delivery. *Science* **1990**, 249 (4976), 1527-1533.
- (2)Peppas, N. A.; Langer, R., New challenges in biomaterials. *Science* **1994**, 263 (5154), 1715-1720.
- (3)Duncan, R., The dawning era of polymer therapeutics. *Nature Reviews Drug Discovery* **2003**, 2 (5), 347-360.
- (4)Rinaudo, M., Main properties and current applications of some polysaccharides as biomaterials. *Polymer International* **2008**, 57 (3), 397-430.
- (5)Hermanson, B. T.; Mallia, A.; Smith, P., Academic press. *San Diego, Calif* **1996**.
- (6)Prestwich, G. D.; Marecak, D. M.; Marecek, J. F.; Vercruysse, K. P.; Ziebell, M. R., Controlled chemical modification of hyaluronic acid: Synthesis, applications, and biodegradation of hydrazide derivatives. *Journal of Controlled Release* **1998**, 53 (1), 93-103.
- (7)Hamidi, M.; Azadi, A.; Rafiei, P., Pharmacokinetic consequences of pegylation. *Drug Delivery* **2006**, 13 (6), 399-409.
- (8)Hennink, W.; Van Nostrum, C., Novel crosslinking methods to design hydrogels. *Advanced Drug Delivery Reviews* **2012**, 64, 223-236.
- (9)Elisseeff, J.; Anseth, K.; Sims, D.; McIntosh, W.; Randolph, M.; Langer, R., Transdermal photopolymerization for minimally invasive implantation. *Proceedings of the National Academy of Sciences* **1999**, 96 (6), 3104-3107.

- (10) Kirker, K. R.; Luo, Y.; Nielson, J. H.; Shelby, J.; Prestwich, G. D., Glycosaminoglycan hydrogel films as bio-interactive dressings for wound healing. *Biomaterials* **2002**, *23* (17), 3661-3671.
- (11) Riley, C. M.; Fuegy, P. W.; Firpo, M. A.; Zheng Shu, X.; Prestwich, G. D.; Peattie, R. A., Stimulation of in vivo angiogenesis using dual growth factor-loaded crosslinked glycosaminoglycan hydrogels. *Biomaterials* **2006**, *27* (35), 5935-5943.
- (12) Serban, M. A.; Liu, Y.; Prestwich, G. D., Effects of extracellular matrix analogues on primary human fibroblast behavior. *Acta Biomaterialia* **2008**, *4* (1), 67-75.
- (13) Hosack, L. W.; Firpo, M. A.; Scott, J. A.; Prestwich, G. D.; Peattie, R. A., Microvascular maturity elicited in tissue treated with cytokine-loaded hyaluronan-based hydrogels. *Biomaterials* **2008**, *29* (15), 2336-2347.
- (14) Pike, D. B.; Cai, S.; Pomraning, K. R.; Firpo, M. A.; Fisher, R. J.; Shu, X. Z.; Prestwich, G. D.; Peattie, R. A., Heparin-regulated release of growth factors in vitro and angiogenic response in vivo to implanted hyaluronan hydrogels containing vegf and bfgf. *Biomaterials* **2006**, *27* (30), 5242-5251.
- (15) Baldwin, A. D.; Kiick, K. L., Polysaccharide-modified synthetic polymeric biomaterials. *Peptide Science* **2010**, *94* (1), 128-140.
- (16) Draget, K.; Bræk, G. S.; Smidsrød, O., Alginic acid gels: The effect of alginate chemical composition and molecular weight. *Carbohydrate Polymers* **1994**, *25* (1), 31-38.
- (17) Blaine, G., Experimental observations on absorbable alginate products in surgery: Gel, film, gauze and foam. *Annals of Surgery* **1947**, *125* (1), 102.
- (18) Rowley, J. A.; Madlambayan, G.; Mooney, D. J., Alginate hydrogels as synthetic extracellular matrix materials. *Biomaterials* **1999**, *20* (1), 45-53.

- (19) Lee, K. Y.; Rowley, J. A.; Eiselt, P.; Moy, E. M.; Bouhadir, K. H.; Mooney, D. J., Controlling mechanical and swelling properties of alginate hydrogels independently by cross-linker type and cross-linking density. *Macromolecules* **2000**, *33* (11), 4291-4294.
- (20) Lee, S. B.; Park, E. K.; Lim, Y. M.; Cho, S. K.; Kim, S. Y.; Lee, Y. M.; Nho, Y. C., Preparation of alginate/poly (n-isopropylacrylamide) semi-interpenetrating and fully interpenetrating polymer network hydrogels with γ -ray irradiation and their swelling behaviors. *Journal of Applied Polymer Science* **2006**, *100* (6), 4439-4446.
- (21) Bencherif, S. A.; Sands, R. W.; Bhatta, D.; Arany, P.; Verbeke, C. S.; Edwards, D. A.; Mooney, D. J., Injectable preformed scaffolds with shape-memory properties. *Proceedings of the National Academy of Sciences* **2012**, *109* (48), 19590-19595.
- (22) Sawabe, T.; Oda, Y.; Shiomi, Y.; Ezura, Y., Alginate degradation by bacteria isolated from the gut of sea urchins and abalones. *Microbial Ecology* **1995**, *30* (2), 193-202.
- (23) Gilchrist, T.; Martin, A., Wound treatment with sorbsan—an alginate fibre dressing. *Biomaterials* **1983**, *4* (4), 317-320.
- (24) Boontheekul, T.; Kong, H.-J.; Mooney, D. J., Controlling alginate gel degradation utilizing partial oxidation and bimodal molecular weight distribution. *Biomaterials* **2005**, *26* (15), 2455-2465.
- (25) Kumar, M. R.; Muzzarelli, R. A.; Muzzarelli, C.; Sashiwa, H.; Domb, A., Chitosan chemistry and pharmaceutical perspectives. *Chemical Reviews* **2004**, *104* (12), 6017-6084.
- (26) Khor, E.; Lim, L. Y., Implantable applications of chitin and chitosan. *Biomaterials* **2003**, *24* (13), 2339-2349.

- (27)Chenite, A.; Chaput, C.; Wang, D.; Combes, C.; Buschmann, M.; Hoemann, C.; Leroux, J.; Atkinson, B.; Binette, F.; Selmani, A., Novel injectable neutral solutions of chitosan form biodegradable gels in situ. *Biomaterials* **2000**, *21* (21), 2155-2161.
- (28)Qu, X.; Wirsén, A.; Albertsson, A. C., Synthesis and characterization of ph-sensitive hydrogels based on chitosan and d, l-lactic acid. *Journal of Applied Polymer Science* **1999**, *74* (13), 3193-3202.
- (29)Qu, X.; Wirsén, A.; Albertsson, A.-C., Novel ph-sensitive chitosan hydrogels: Swelling behavior and states of water. *Polymer* **2000**, *41* (12), 4589-4598.
- (30)Yu, H.; Wang, W.; Chen, X.; Deng, C.; Jing, X., Synthesis and characterization of the biodegradable polycaprolactone-graft-chitosan amphiphilic copolymers. *Biopolymers* **2006**, *83* (3), 233-242.
- (31)Feng, H.; Dong, C.-M., Preparation, characterization, and self-assembled properties of biodegradable chitosan-poly (l-lactide) hybrid amphiphiles. *Biomacromolecules* **2006**, *7* (11), 3069-3075.
- (32)Hu, F.-Q.; Ren, G.-F.; Yuan, H.; Du, Y.-Z.; Zeng, S., Shell cross-linked stearic acid grafted chitosan oligosaccharide self-aggregated micelles for controlled release of paclitaxel. *Colloids and Surfaces B: Biointerfaces* **2006**, *50* (2), 97-103.
- (33)Bhattarai, N.; Ramay, H. R.; Gunn, J.; Matsen, F. A.; Zhang, M., Peg-grafted chitosan as an injectable thermosensitive hydrogel for sustained protein release. *Journal of Controlled Release* **2005**, *103* (3), 609-624.
- (34)Harrison, J. H., Dextran as a plasma substitute with plasma volume and excretion studies on control patients. *Annals of Surgery* **1954**, *139* (2), 137.

- (35)Rosenfeld, E.; Lukomskaya, I., The splitting of dextran and isomaltose by animal tissues. *Clinica Chimica Acta* **1957**, *2* (2), 105-114.
- (36)Massia, S. P.; Stark, J.; Letbetter, D. S., Surface-immobilized dextran limits cell adhesion and spreading. *Biomaterials* **2000**, *21* (22), 2253-2261.
- (37)Cao, B.; Li, L.; Wu, H.; Tang, Q.; Sun, B.; Dong, H.; Zhe, J.; Cheng, G., Zwitteration of dextran: A facile route to integrate antifouling, switchability and optical transparency into natural polymers. *Chem. Commun.* **2014**, *50* (24), 3234-3237.
- (38)Hennink, W.; De Jong, S.; Bos, G.; Veldhuis, T.; Van Nostrum, C., Biodegradable dextran hydrogels crosslinked by stereocomplex formation for the controlled release of pharmaceutical proteins. *International Journal of Pharmaceutics* **2004**, *277* (1), 99-104.
- (39)Zhang, Y.; Won, C. Y.; Chu, C. C., Synthesis and characterization of biodegradable hydrophobic–hydrophilic hydrogel networks with a controlled swelling property. *Journal of Polymer Science Part A: Polymer Chemistry* **2000**, *38* (13), 2392-2404.
- (40)Sun, G.; Chu, C.-C., Synthesis, characterization of biodegradable dextran–allyl isocyanate–ethylamine/polyethylene glycol–diacrylate hydrogels and their in vitro release of albumin. *Carbohydrate Polymers* **2006**, *65* (3), 273-287.
- (41)Zhang, X.; Wu, D.; Chu, C.-C., Synthesis and characterization of partially biodegradable, temperature and ph sensitive dex–ma/pnipaam hydrogels. *Biomaterials* **2004**, *25* (19), 4719-4730.
- (42)Huang, X.; Zhang, Y.; Donahue, H. J.; Lowe, T. L., Porous thermoresponsive-co-biodegradable hydrogels as tissue-engineering scaffolds for 3-dimensional in vitro culture of chondrocytes. *Tissue Engineering* **2007**, *13* (11), 2645-2652.

- (43) Kumashiro, Y.; Huh, K. M.; Ooya, T.; Yui, N., Modulatory factors on temperature-synchronized degradation of dextran grafted with thermoresponsive polymers and their hydrogels. *Biomacromolecules* **2001**, *2* (3), 874-879.
- (44) Hiemstra, C.; van der Aa, L. J.; Zhong, Z.; Dijkstra, P. J.; Feijen, J., Novel in situ forming, degradable dextran hydrogels by michael addition chemistry: Synthesis, rheology, and degradation. *Macromolecules* **2007**, *40* (4), 1165-1173.
- (45) Jeong, B.; Bae, Y. H.; Lee, D. S.; Kim, S. W., Biodegradable block copolymers as injectable drug-delivery systems. *Nature* **1997**, *388* (6645), 860-862.
- (46) Hiemstra, C.; Zhong, Z.; van Steenberg, M. J.; Hennink, W. E.; Feijen, J., Release of model proteins and basic fibroblast growth factor from in situ forming degradable dextran hydrogels. *Journal of Controlled Release* **2007**, *122* (1), 71-78.
- (47) Karmali, P. P.; Chao, Y.; Park, J.-H.; Sailor, M. J.; Ruoslahti, E.; Esener, S. C.; Simberg, D., Different effect of hydrogelation on antifouling and circulation properties of dextran-iron oxide nanoparticles. *Molecular Pharmaceutics* **2012**, *9* (3), 539-545.
- (48) Yu, H.; Zhang, Y.; Sun, X.; Liu, J.; Zhang, H., Improving the antifouling property of polyethersulfone ultrafiltration membrane by incorporation of dextran grafted halloysite nanotubes. *Chemical Engineering Journal* **2014**, *237*, 322-328.
- (49) Sun, L. T.; Bencherif, S. A.; Gilbert, T. W.; Lotze, M. T.; Washburn, N. R., Design principles for cytokine-neutralizing gels: Cross-linking effects. *Acta Biomaterialia* **2010**, *6* (12), 4708-4715.
- (50) Garland, A.; Shen, L.; Zhu, X., Mobile precursor mediated protein adsorption on solid surfaces. *Progress in Surface Science* **2012**, *87* (1), 1-22.

- (51)Dhandayuthapani, B.; Yoshida, Y.; Maekawa, T.; Kumar, D. S., Polymeric scaffolds in tissue engineering application: A review. *International Journal of Polymer Science* **2011**, *2011*.
- (52)Shi, J.; Xing, M. M.; Zhong, W., Development of hydrogels and biomimetic regulators as tissue engineering scaffolds. *Membranes* **2012**, *2* (1), 70-90.
- (53)Meyer, K.; Palmer, J. W., The polysaccharide of the vitreous humor. *Journal of Biological Chemistry* **1934**, *107* (3), 629-634.
- (54)Lapčák, L.; Lapcik, L.; De Smedt, S.; Demeester, J.; Chabreck, P., Hyaluronan: Preparation, structure, properties, and applications. *Chemical Reviews* **1998**, *98* (8), 2663-2684.
- (55)Stern, R.; Asari, A. A.; Sugahara, K. N., Hyaluronan fragments: An information-rich system. *European Journal of Cell Biology* **2006**, *85* (8), 699-715.
- (56)Kogan, G.; Šoltés, L.; Stern, R.; Gemeiner, P., Hyaluronic acid: A natural biopolymer with a broad range of biomedical and industrial applications. *Biotechnology Letters* **2007**, *29* (1), 17-25.
- (57)Schanté, C. E.; Zuber, G.; Herlin, C.; Vandamme, T. F., Chemical modifications of hyaluronic acid for the synthesis of derivatives for a broad range of biomedical applications. *Carbohydrate Polymers* **2011**, *85* (3), 469-489.
- (58)Burdick, J. A.; Prestwich, G. D., Hyaluronic acid hydrogels for biomedical applications. *Advanced Materials* **2011**, *23* (12), H41-H56.
- (59)Yamamoto, S.-I.; Pietrasik, J.; Matyjaszewski, K., The effect of structure on the thermoresponsive nature of well-defined poly(oligo(ethylene oxide) methacrylates)

synthesized by atp. *Journal of Polymer Science Part A: Polymer Chemistry* **2008**, 46 (1), 194-202.

(60)Coessens, V.; Matyjaszewski, K., Synthesis of polymers with hydroxyl end groups by atom transfer radical polymerization. *Macromolecular Rapid Communications* **1999**, 20 (3), 127-134.

(61)Lutz, J.-F., Polymerization of oligo(ethylene glycol) (meth)acrylates: Toward new generations of smart biocompatible materials. *Journal of Polymer Science Part A: Polymer Chemistry* **2008**, 46 (11), 3459-3470.

(62)Grymonpré, K. R.; Staggemeier, B. A.; Dubin, P. L.; Mattison, K. W., Identification by integrated computer modeling and light scattering studies of an electrostatic serum albumin-hyaluronic acid binding site. *Biomacromolecules* **2001**, 2 (2), 422-429.

(63)Zengin, A.; Yildirim, E.; Caykara, T., Raft-mediated synthesis and temperature-induced responsive properties of poly(2-(2-methoxyethoxy)ethyl methacrylate) brushes. *Journal of Polymer Science Part A: Polymer Chemistry* **2013**, 51 (4), 954-962.

Chapter 4 : Non-Fouling Hyaluronic Acid Coatings for Improved Sandwich ELISA Measurements in Plasma Mixtures

4.1. Abstract: Nonspecific protein adsorption can interfere with blood diagnostics, especially in point-of-care tests for which minimal sample processing is required. Here we report a non-fouling coating material for presenting capture antibodies in ELISA that significantly increased precision and accuracy compared to a commercial ELISA microplates in human plasma and model solutions containing plasma proteins. The coating was prepared by functionalizing the hydrophilic polysaccharide hyaluronic acid (HA) with a thermoresponsive polymer, poly(di(ethylene glycol)) methyl ether methacrylate (PMEO₂MA). Previous studies demonstrated that these coatings were resistant to adsorption of major blood proteins, and we demonstrate that functionalization of the coatings with a monoclonal antibody against tumor necrosis factor- α (TNF- α) provided enhanced detection accuracy for this pro-inflammatory cytokine in ELISA. Three plasma-type solutions were explored in this work based either on buffer containing known concentrations of albumin, fibrinogen and immunoglobulin at sub-physiological and physiological concentrations, and non-diluted human plasma. In model solutions of plasma, even sub-physiological concentrations of plasma proteins resulted in a 20% overestimate of TNF- α concentration in the commercial ELISA kit but a 4% overestimate in HA-coated microwells. However, in human plasma, the commercial ELISA kit underestimated the analyte concentration by up to 95% while the HA-coated microwells did so by only 15% at an analyte concentration of 12.5 pg/mL. The improvements in precision and accuracy provided by HA coatings suggests they could be used to enhance ELISA measurements in a broad range of complex biological media.

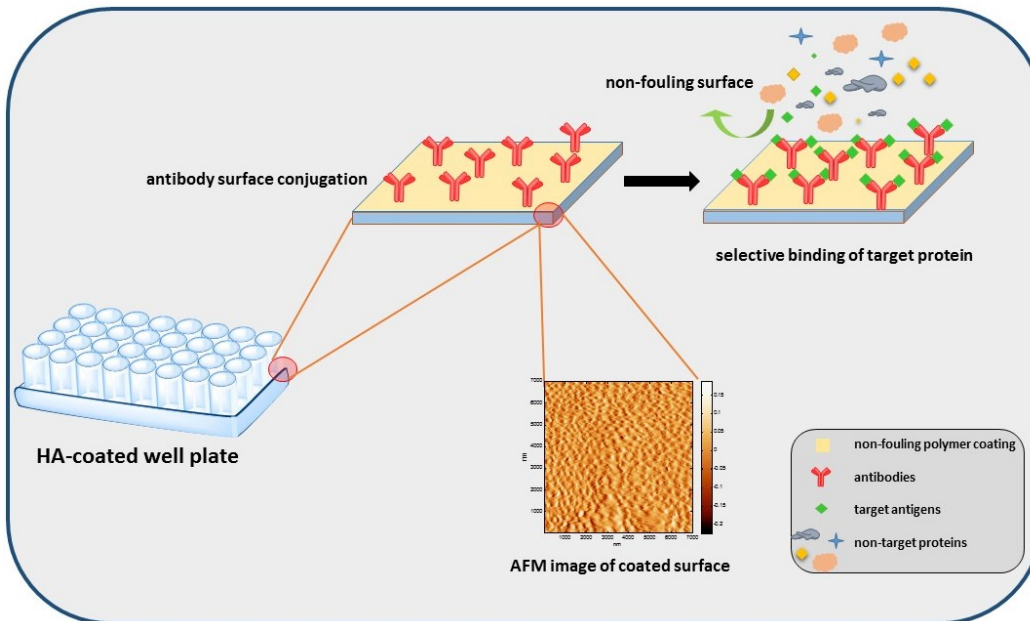


Figure 4.1 Non-Fouling Hyaluronic Acid Coatings for Improved Sandwich ELISA Measurements in Plasma Mixtures

4.2. Introduction

Enzyme-linked immuno assay (ELISA) is the most commonly used quantitative protein measurement. In the sandwich ELISA format, a primary or capture antibody is physisorbed¹ or covalently immobilized²⁻³ on a solid surface, which is then exposed to the analyte solution. After binding the immobilized antibody, the analyte is sandwiched by a second antibody, and detection is performed via a secondary antibody linked to a reporter enzyme that produces a colorimetric readout that amplifies the original signal via a reaction with an enzyme substrate. ELISA assays have become the gold standard in analysis of blood proteins with reports ranging from inflammatory markers and monocytes⁴ to early detection of various cancers⁵ and viral infections⁶⁻⁷. However, non-specific binding (NSB) of serum proteins often results in overestimation of analyte concentrations,⁸⁻¹² which can be attributed to adsorption of the secondary antibody. While other detection methods are

developed to address this issue,¹³ sample dilution is still the most common option to mitigate the background sample interference effect which, as a result, maximizes signal/noise ratios but with a concomitant decrease in sensitivity. Furthermore, this approach becomes less useful for point-of-care diagnostics due to inherently low signals and the need for minimal sample processing.¹⁴⁻¹⁵

A critical variable in performing sensitive, accurate ELISA measurements is the primary-antibody surface concentration and the method used to immobilize it on the surface. While greater sensitivity is theoretically achieved at high antibody concentrations, there are upper limits based on antibody orientation,¹⁶⁻¹⁷ and denaturation¹⁸⁻¹⁹ or deactivation.²⁰ In particular, physisorption of capture antibodies onto hydrophobic supports, such as polystyrene, can result in up to 90% loss of activity.²¹ However, reducing antibody loading on the surface requires blocking open sites to prevent non-specific protein adsorption that reduces accuracy.²² For example, non-specific adsorption of the second “sandwich” antibody or the secondary detection antibody is one mechanism for the overestimation of analyte concentration.²³ Common blocking agents include denatured proteins, such as albumin,²⁴ or detergents²⁵⁻²⁶, but these can still promote antibody or serum-protein adsorption, often through incomplete coverage of the blocking agent. One strategy to avoid this is to change the surface chemistry in order to drive strong adsorption of blocking agents. Sung et al. coated the substrate with cationic poly(ethylene imine) in a polyelectrolyte multilayer,²⁷ while Shen et al. used poly(allylamine),²⁸ both of which bind anionic albumin strongly. Moreover, the relatively large size of some common blocking agents and their ability to carry charges that would interact with both the activity of the antibody and surface coverage efficiency offers a challenge that eventually would limit the

assay sensitivity.¹⁶ In other approaches, Sung et al. presented the capture antibody via protein G coupled to an albumin antibody,²⁷ making fabrication significantly more complicated, while Shen et al.²⁸ only reported assays down to 20 ng/mL, 100-fold greater than commercial ELISA kits, and this reduced sensitivity might be due to strong interactions between the capture antibody and the cationic coating. Nagasaki et al. demonstrated the use of tandem electrostatic and covalent grafting of a hexamine-functionalized poly(ethylene glycol) (PEG) on carboxylated magnetic beads, which offer advantages in sensitivity using covalently grafted capture antibodies.²⁹ However, this strategy was based on a two-step coupling process starting with covalent linking of the antibody to the substrate presenting reactive sites for amide bond formation, which can make the subsequent functionalization difficult given the rapid hydrolysis of the active ester groups used in this work.²⁹ In general, blocking strategies can be challenging to realize in practice, which ultimately limits the effectiveness of this approach.

An alternate strategy is to immobilize capture antibodies on a non-fouling substrate. Numerous biomaterial approaches have been developed to prevent non-specific protein adsorption³⁰⁻³⁵ that can be adapted to improving the accuracy of ELISA.³⁶⁻⁴¹ In the general context of non-fouling surfaces, covalent grafting of poly(ethylene glycol) (PEG) has been investigated in depth, but previous studies indicated these formulations may be susceptible to immunoglobulin adsorption,^{31, 33, 35} which would make them particularly unsuited for ELISA. One strategy to address this involves crosslinking dextran onto gold substrates as gel substrates for surface plasmon resonance assays in serum using conjugated antibody capture of analytes,⁴²⁻⁴⁴ and preliminary results suggest this approach also improves ELISA detection as well.⁴¹ Indeed, polysaccharides may offer superior resistance to NSB of serum

proteins, making interfaces based on these appealing for blood and serum diagnostics. However, these gel interfaces are not suitable for all techniques, and there exists a need for approaches to prepare non-fouling coatings on a broad range of substrates. Previously, we demonstrated that hyaluronic acid (HA) grafted with the thermoresponsive polymer poly(di(ethylene glycol)) methyl ether methacrylate (PMEO₂MA) readily forms stable hydrophilic coatings with water contact angles of 16° sufficient to prevent protein adsorption at physiological concentrations of serum proteins.⁴⁵ Here we explore the use of HA coatings as the basis for improving the accuracy of ELISA in analyte solutions containing serum proteins. The pro-inflammatory cytokine TNF- α was used as an analyte, and monoclonal antibodies were covalently attached to the HA coating to produce high-affinity sites for these assays. Model serum solutions were prepared using albumin, fibrinogen, and immunoglobulin at sub-physiological and physiological concentrations to explore the dependence of ELISA accuracy on the presence of serum proteins.

4.3. Methods

1. Synthesis of HA-PMEO₂MA: the hybrid polymer was synthesis as previously reported.⁴⁵ Briefly, the homopolymer was synthesized by atom transfer radical polymerization (ATRP) at a molecular weight of 34 kDa. The purified polymer was then grafted onto HA using T3P chemistry at a final grafting density of ~20%. The lyophilized product was then dissolved in filtered PBS to a final concentration of (4 mg/mL).
2. Plate preparation: A standard flat bottom 96 wells polystyrene plate was incubated with 150 μ L of HA-PMEO₂MA at 37 °C for 5 hours. Excess solution was aspirated out of the wells and the wells were gently washed with warm water. Anti-TNF- α

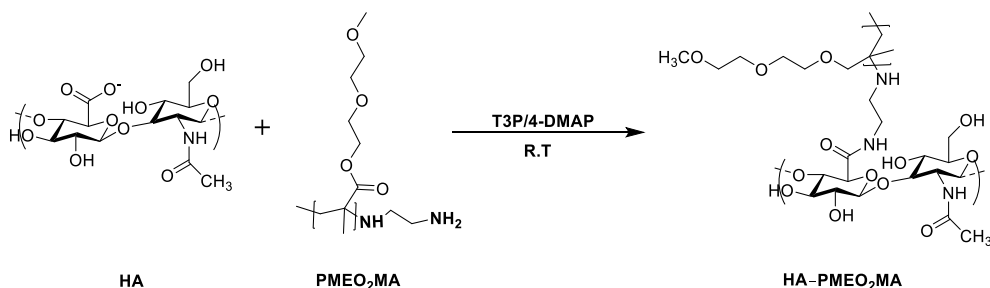
was conjugated to HA using T3P chemistry. Briefly, 150 μ L of 15 μ g/mL anti-TNF- α solution was added to wells percolated with HA. To that, mmol of T3P and mmol of 4-DMAP were added to the wells. The plate was then very carefully agitated to assure proper mixing of the reagents. The well plate was incubated for 4 hours at 37 $^{\circ}$ C to allow for antibody conjugation.

3. Anti-TNF- α conjugation efficiency: the amount of antibody immobilized on the well surface was quantified by difference using a ForteBio Octet Red (Pall Life Sciences) system. The supernatant from the conjugation step was collected, homogenized and run against a series of standard concentrations of anti-TNF- α using protein A and protein L sensor tips. Assay details could be found in the supplementary section. For further validation, the supernatants were also assayed for total protein concentrations using the Pierce BCA Protein Assay kit (Thermo Scientific, Rockford, IL). The assay was carried out according to the kit procedure and was analyzed by SAFIRE microplate reader (SAFIRE, San Jose, CA) with absorbance set at 562 nm.
4. Enzyme-linked immunosorbent assay ELISA procedure: an ELISA assay Quantikine Rat TNF- α ELISA kit (R&D Systems, Minneapolis, MN), was used for TNF- α quantitation in samples containing known concentrations of serum proteins BSA, Fbg and IgG. A head-to-head comparison between the standard commercially available ELISA kit and the polymer-coated polystyrene well plate is established for all studied serum protein concentrations. After preparing the plate by coating it with the hybrid polymer and functionalizing the surface with anti-TNF- α antibodies, the steps of a standard ELISA assay is followed as recommended by the

manufacturer and analyzed using a SAFIRE microplate reader with absorbance 450 nm and 540 nm correction. Briefly, the coated wells are gently washed with warm washing solutions while maintain a steady temperature of 37 °C. The standards and samples are then added to the well plates and incubated as a sealed system for 3 hours. A washing step preceded the final detection antibody binding to the surface. Curve fitting to the standard concentrations was used to express TNF- α concentration in pg/mL of solution.

4.4. Results and Discussion

The coatings were prepared by grafting PMEO₂MA homopolymer, which has a lower critical solution temperature (LCST) of 26 °C, *onto* HA as shown in Scheme 4.1. This results in a hybrid biopolymer having temperature-dependent solubility, which can be used to form stable coatings by warming buffer solutions above the LCST.



Scheme 4.1 Chemical modification of HA yielding non-fouling HA-PMEO₂MA coatings

A standard 96-well polystyrene flat bottom microplate was coated with polymer-grafted HA by incubating the plate for 5 hours at 37 °C. Excess solution was then aspirated and the wells were gently washed with warm water. Anti-TNF- α was immobilized to the HA surface using T3P conjugation chemistry while maintaining elevated temperature. The amount of the immobilized antibody was determined by difference after measuring the

concentration of the remaining antibodies using a ForteBio Octet Red and Protein A and Protein L sensor tips as well as total protein concentration analysis using a Pierce BCA protein assay kit. A schematic of the coating formation process is shown in fig. 4.2.

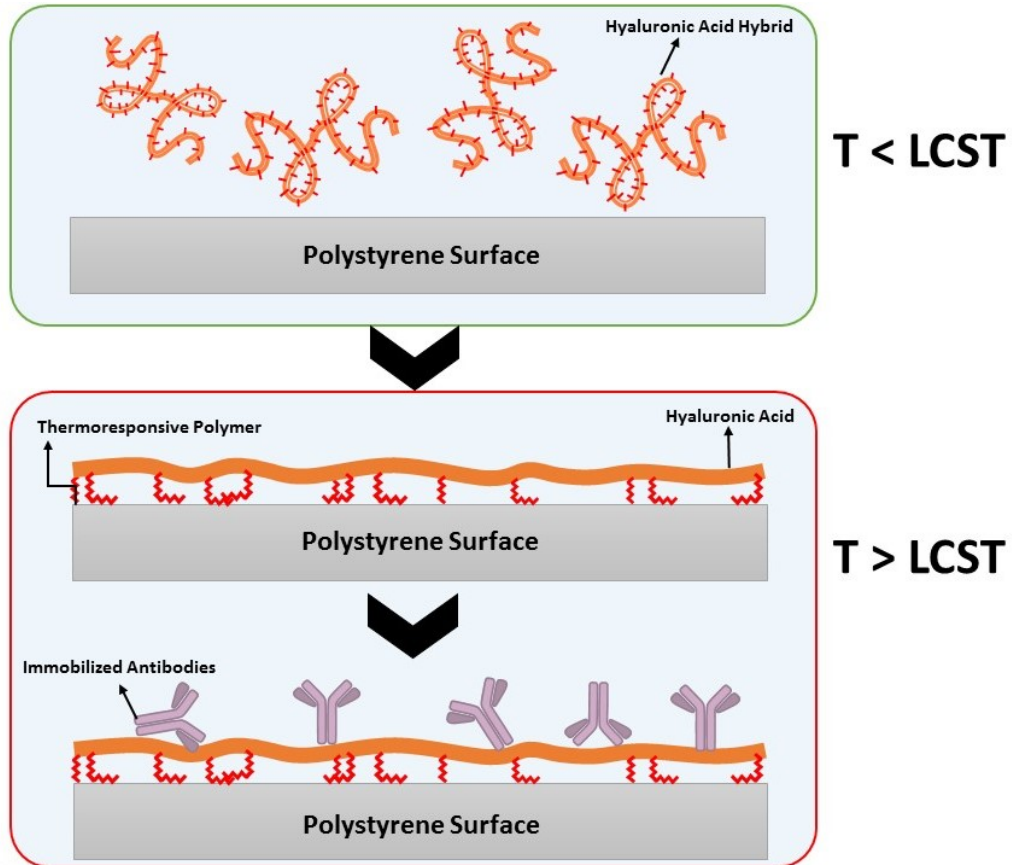


Figure 4.2 Schematic of the coating and antibody immobilization process. Figure not drawn to scale.

The antibody coverage for a microwell containing 100 μL of solution may be estimated assuming an antibody hydrodynamic radius of 5 nm,⁴⁶⁻⁴⁷ and the theoretical maximum possible number of antibodies on the surface was 1.30×10^{12} antibodies/well. The results from both methods shown in fig. 4.3 indicate a total of 7.53×10^{11} (1.25×10^{-12} moles) anti-TNF- α was immobilized on the surface of the wells. Similar to the reported values from commercial ELISA kits, these antibody values lead to antibody densities on the well

plate surface of 7.32×10^{11} antibody/cm² corresponding to approximately 60% surface coverage.

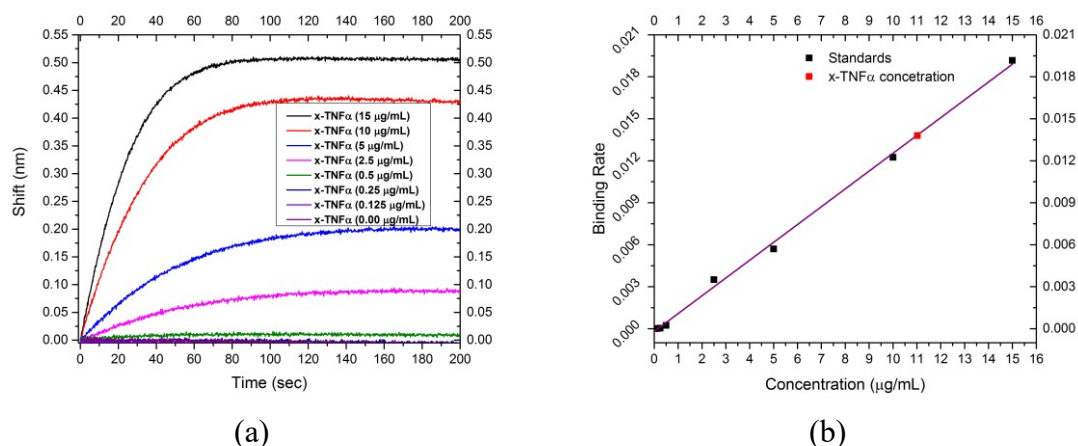


Figure 4.3 Residual anti-TNF- α quantification using BLI on ForteBio: (a) real-time association vs. time for anti-TNF- α standards and (b) anti-TNF- α standards and samples binding rate vs concentration. (N=40, $r^2=0.999$, $SD \pm 0.002411$)

A direct comparison was then performed between the HA-coated microplate and a commercial TNF- α ELISA kit using the manufacturer-provided well plates and reagents. Both kits were subjected to the same assay procedures and conditions, including analyte concentrations, number of replicates and assay temperature. The detection efficiency was assessed in measuring four concentration of rat TNF- α in four different samples: TNF- α in buffer (control), TNF- α in a solution containing sub-physiological concentrations of three blood proteins albumin, IgG and FbG (1:1 mass ratios relative to the analyte), TNF- α in a solution containing physiological concentrations of the same proteins and finally TNF- α in human plasma. Protein concentrations under these four conditions are listed in Table 4.1.

Sample ID	TNF- α Concentration (pM)	Serum Albumin Concentration (pM)	Fibrinogen Concentration (pM)	IgG Concentration (pM)
Control	45.72	0	0	0
	11.43			
	2.86			
	0.72			
Sub-physiological	45.72	0.151	0.118	0.267
	11.43			
	2.86			
	0.72			
Physiological	45.72	1.21×10^8	1.76×10^6	2.00×10^6
	11.43			
	2.86			
	0.72			
Plasma	45.72	-	-	-
	11.43			
	2.86			
	0.72			

Table 4.1 Protein and TNF- α concentrations in the analyzed samples.

The TNF- α concentrations tested were chosen to fall within the range of detection of the commercial assay (12.5-800 pg/mL). The plates were then analyzed using a SAFIRE microplate reader with absorbance 450 nm and 540 nm correction. The calibration curves of TNF- α standards measured on both ELISA microplates are shown in fig. 4.4(a), (b) and a summary of the data are numerically shown in Table 4.2.

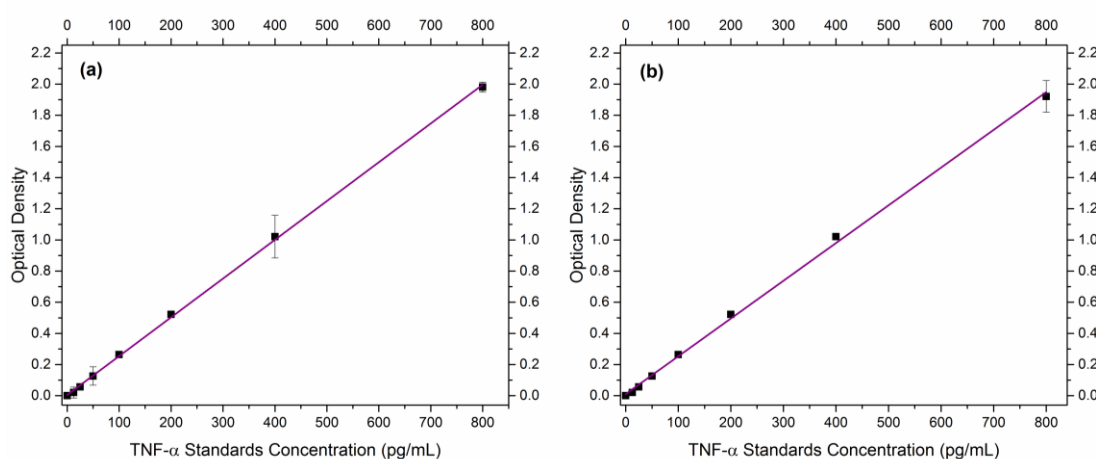


Figure 4.4 ELISA detection of TNF α : calibration curves of TNF- α standards for (a) commercial, non-coated microwells and (b) HA-coated microwells

In control solutions containing TNF- α at all tested nominal concentration (800, 200, 50 and 12.5 pg/mL) but no blood proteins, the commercial ELISA microplates measured 799.96 \pm 1.77, 202.19 \pm 2.46, 51.10 \pm 1.66, 12.64 \pm 0.99 pg/mL respectively while the HA-coated wells measured, respectively, 801.36 \pm 0.68, 201.57 \pm 1.28, 49.98 \pm 0.89, 12.64 \pm 0.65 pg/mL, demonstrating that the HA coatings did not interfere with ELISA measurements and antibody activity was preserved at this surface concentration. Conformational changes in the antibody molecular structure are known to be a result of passive adsorption onto hydrophobic surfaces,⁴⁸ and we hypothesize that the HA coating may have contributed to retention of antibody activity. The density of anti-TNF- α on the surface is also confirmed to be adequate and comparable to the commercially available ELISA kits/microplates consistent with other cited work.¹⁷ These results also establish the ability to use the HA-coated plates as ELISA interfaces as indicated by the accurate measurements of pure TNF- α concentrations with high precision (coefficient of variation (CV) below 1% across all samples measured in the absence of blood proteins). Consequently, an arbitrary accuracy percentage of 95% is deemed acceptable for all sample measured. Fig. 4.5 (a)-(d) shows a visual summary of the results.

		TNF- α Concentration (800/pg/mL)	\pm SD	TNF- α Concentration (200/pg/mL)	\pm SD	TNF- α Concentration (50/pg/mL)	\pm SD	TNF- α Concentration (12.5/pg/mL)	\pm SD
Control	Non coated	799.96	1.77	202.19	2.46	51.10	1.66	12.64	0.99
	coated	801.36	0.69	201.57	1.28	49.98	0.89	12.64	0.65
Sub-physiological	Non coated	883.76	5.99	227.77	13.52	55.33	2.75	13.94	0.22
	coated	828.66	1.69	207.79	1.91	51.19	1.69	12.89	0.20
Physiological	Non coated	957.15	2.49	243.37	6.01	61.11	3.11	15.66	0.06
	coated	835.94	5.85	213.28	1.22	54.39	0.48	13.18	0.36
Plasma	Non coated	1104.14	127.87	253.24	4.62	33.47	10.04	0.69	1.96
	coated	1021.5	68.92	235.39	3.46	47.67	4.41	10.33	2.05

Table 4.2 Summary of Measured TNF- α concentration under the tested conditions and concentrations

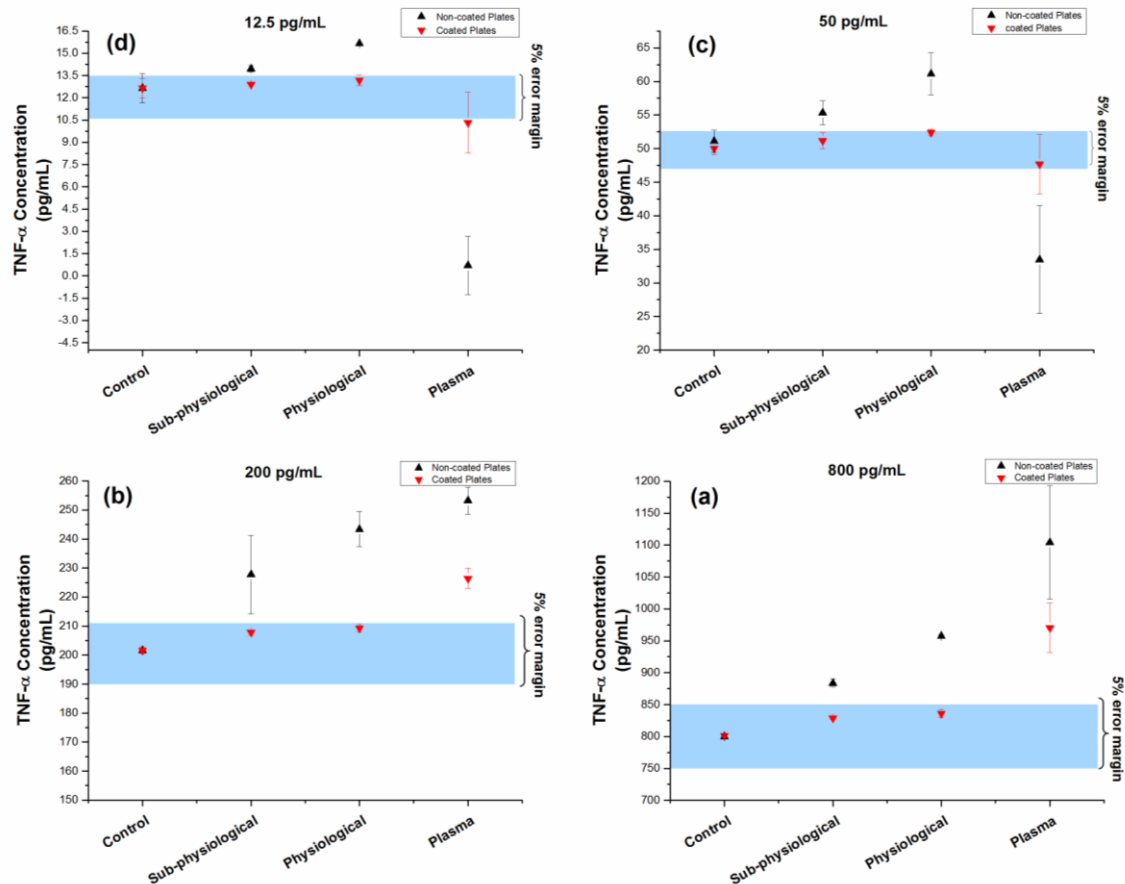
As shown in fig. 4.5, at sub-physiological concentrations of blood proteins, the measured TNF- α concentrations were higher for both microplates tested. The commercial ELISA microplate recorded values of 883.36 \pm 5.99, 227.77 \pm 13.52, 55.33 \pm 2.75 and 13.94 \pm 0.22 pg/mL compared to 828.66 \pm 1.69, 207.79 \pm 1.91, 51.19 \pm 1.69 and 12.89 \pm 0.20 pg/mL for the HA-coated microplates of TNF- α respective to the nominal concentrations of 800, 200, 50 and 12.5 pg/mL, respectively. The decrease in accuracy of measurements for both plates could be due to NSB of blood proteins present in the samples at relative ratios compared to those of the TNF- α target antigen. While both microplates exhibited some degree of variance due to NSB, the HA-coated microplates showed higher accuracy with just 3.01% error compared to 20.2% of errors obtained from the non-coated microplates. Additionally, the precision afforded by the HA-coated microplates (CV 2.6%) was improved compared to the non-coated microplates (CV 4.5%).

At physiological concentrations of blood proteins, the effect of NSB is greater. The measured TNF- α concentration on the non-coated microplates and the HA-coated microplates were 957.15 \pm 2.49, 243.37 \pm 6.01, 61.11 \pm 3.11, 15.66 \pm 0.06 pg/mL and 835.94 \pm 5.85, 213.28 \pm 1.22, 54.39 \pm 0.48, 13.18 \pm 0.36 pg/mL respectively. Here, both the accuracy and precision of measurements afforded by the HA-coated microplates, 5.3% error and CV of 1.5%, was also greater compared to that of the commercial ELISA microplates with 22.1% error and CV of 5.2%.

The TNF- α concentrations measured in plasma samples diverted significantly from the control values of 800, 200, 50 and 12.5 pg/mL on commercial non-coated ELISA microplates with recorded concentrations of 1104.14 \pm 127.87, 253.24 \pm 4.62, 33.47 \pm

10.04 and 0.69 \pm 1.96 pg/mL, respectively. Conversely, the results obtained from the HA-coated microplates were as follows 1021.5 \pm 68.92 pg/mL for the 800 pg/mL TNF- α concentration, 235.39 \pm 3.46 pg/mL for the 200 pg/mL TNF- α concentration, 47.67 \pm 4.41 pg/mL for the 50 pg/mL TNF- α concentration and 10.33 \pm 2.05 pg/mL for the 12.5 pg/mL TNF- α concentration. While plasma components were hypothesized to be non-specifically crowding or absorbing onto the non-coated microplates surfaces, which is indicated by the significant underestimation of the analyte concentration at low TNF- α concentration and the substantial overestimation of TNF- α at higher concentrations, this effect is relatively mitigated on the HA-coated microplates as indicated by the improvement in detection accuracy across all concentrations measured compared to the non-coated commercial ELISA microplates. In such cases the accuracy was consistently approaching the acceptable 5% error margin.

While the HA-coated microplates showed an increase in detection accuracy compared to the commercial non-coated microplates, the error was still significant and blocking of the non-coated surfaces by plasma proteins was evident.



*results not significantly different ($p < 0.001$)

Figure 4.5 ELISA detection of TNF- α in solutions consistent of pure TNF- α , protein mixtures of subphysiological and physiological concentrations of BSA, IgG and FbG and plasma samples (a) results from TNF- α concentration of 800 pg/mL (b) results from TNF- α concentration of 200 pg/mL (c) Results from TNF- α concentration of 50 pg/mL (d) results from TNF- α concentration of 12.5 pg/mL. All data are presented as mean \pm SD. ($p < 0.001$)

It is interesting to note that in the commercial ELISA microplates, a similar overestimation of TNF- α concentration was measured at the two levels of blood proteins but the precision appeared to decrease significantly at physiological concentrations. (In comparing the results at physiological concentration of blood proteins, one-way ANOVA and Tukey tests were performed on all tested samples ($n=5$), and at the level of 0.001, the means of all the populations were found to be significantly different.) This indicates that even small concentrations of serum proteins are sufficient to interfere with traditional

ELISA measurements despite the effort to block the surface, resulting in a consistent error in estimation of analyte concentration.

This overestimation, as opposed to underestimation, is attributed to avid binding of plasma proteins that leads to adsorption of secondary “sandwich” or enzyme-linked antibodies on surfaces that are nominally blocked since interference with the capture antibody would presumably lead to underestimates of analyte concentrations. Given the concentration-independent accuracy of the commercial ELISA kit at the levels measured, this behavior suggests that a small number of high-affinity sites are saturated at low blood-protein concentrations. If these sites have a stoichiometric correspondence to the overestimation of analyte concentration, then they present a fundamental limit to detection sensitivity in the presence of plasma. Further study is necessary to test this prediction, but clearly improved strategies for antibody-based diagnostics in blood and plasma need to be developed.

Acknowledgments

Prof. Phil Campbell for providing fresh human plasma samples. NMR instrumentation at CMU was partially supported by NSF (CHE-0130903 and CHE-1039870).

References

- (1)Nygren, H.; Stenberg, M., Immunochemistry at interfaces. *Immunology* **1989**, *66* (3), 321-327.
- (2)Nakanishi, K.; Muguruma, H.; Karube, I., A novel method of immobilizing antibodies on a quartz crystal microbalance using plasma-polymerized films for immunosensors. *Analytical Chemistry* **1996**, *68* (10), 1695-1700.
- (3)Bhatia, S. K.; Shriver-Lake Lc Fau - Prior, K. J.; Prior Kj Fau - Georger, J. H.; Georger Jh Fau - Calvert, J. M.; Calvert Jm Fau - Bredehorst, R.; Bredehorst R Fau - Ligler, F. S.; Ligler, F. S., Use of thiol-terminal silanes and heterobifunctional crosslinkers for immobilization of antibodies on silica surfaces. *Analytical Biochemistry* **1989**, *178* (2), 408-413.
- (4)Evanoff, H. L.; Burdick, M. D.; Moore, S. A.; Kunkel, S. L.; Strieter, R. M., A sensitive elisa for the detection of human monocyte chemoattractant protein-1 (mcp-1). *Immunological Investigations* **1992**, *21* (1), 39-45.
- (5)Wulfkuhle, J. D.; Liotta, L. A.; Petricoin, E. F., Proteomic applications for the early detection of cancer. *Nat Rev Cancer* **2003**, *3* (4), 267-275.
- (6)Grandien, M.; Pettersson, C. A.; Gardner, P. S.; Linde, A.; Stanton, A., Rapid viral diagnosis of acute respiratory infections: Comparison of enzyme-linked immunosorbent assay and the immunofluorescence technique for detection of viral antigens in nasopharyngeal secretions. *Journal of Clinical Microbiology* **1985**, *22* (5), 757-760.
- (7)Rowe, T.; Abernathy, R. A.; Hu-Primmer, J.; Thompson, W. W.; Lu, X.; Lim, W.; Fukuda, K.; Cox, N. J.; Katz, J. M., Detection of antibody to avian influenza a (h5n1) virus

in human serum by using a combination of serologic assays. *Journal of Clinical Microbiology* **1999**, 37 (4), 937-943.

(8)Boscato, L. M.; Stuart, M. C., Heterophilic antibodies: A problem for all immunoassays. *Clinical Chemistry* **1988**, 34 (1), 27-33.

(9)Levinson, S. S., Antibody multispecificity in immunoassay interference. *Clinical Biochemistry* **1992**, 25 (2), 77-87.

(10)Rotmensch, S.; Cole, L. A., False diagnosis and needless therapy of presumed malignant disease in women with false-positive human chorionic gonadotropin concentrations. *The Lancet* **2000**, 355 (9205), 712-715.

(11)Martins, T. B.; Pasi, B. M.; Litwin, C. M.; Hill, H. R., Heterophile antibody interference in a multiplexed fluorescent microsphere immunoassay for quantitation of cytokines in human serum. *Clinical and Diagnostic Laboratory Immunology* **2004**, 11 (2), 325-329.

(12)Zweig, M. H.; Csako, G.; Benson, C. C.; Weintraub, B. D.; Kahn, B. B., Interference by anti-immunoglobulin g antibodies in immunoradiometric assays of thyrotropin involving mouse monoclonal antibodies. *Clinical Chemistry* **1987**, 33 (6), 840-844.

(13)Waterboer, T.; Sehr, P.; Pawlita, M., Suppression of non-specific binding in serological luminex assays. *Journal of Immunological Methods* **2006**, 309 (1-2), 200-204.

(14)Tudos, A. J.; Besselink, G. A. J.; Schasfoort, R. B. M., Trends in miniaturized total analysis systems for point-of-care testing in clinical chemistry. *Lab on a chip* **2001**, 1 (2), 83-95.

(15)Wang, J., Electrochemical biosensors: Towards point-of-care cancer diagnostics. *Biosensors and Bioelectronics* **2006**, 21 (10), 1887-1892.

- (16) Wiseman, M. E.; Frank, C. W., Antibody adsorption and orientation on hydrophobic surfaces. *Langmuir : the ACS journal of surfaces and colloids* **2011**, *28* (3), 1765-1774.
- (17) Xu, H.; Lu, J. R.; Williams, D. E., Effect of surface packing density of interfacially adsorbed monoclonal antibody on the binding of hormonal antigen human chorionic gonadotrophin. *The Journal of Physical Chemistry B* **2006**, *110* (4), 1907-1914.
- (18) YoungáJeong, J.; HyunáChung, B., Recent advances in immobilization methods of antibodies on solid supports. *Analyst* **2008**, *133* (6), 697-701.
- (19) Conradie, J. D.; Govender, M.; Visser, L., Elisa solid phase: Partial denaturation of coating antibody yields a more efficient solid phase. *Journal of Immunological Methods* **1983**, *59* (3), 289-299.
- (20) Turková, J., Oriented immobilization of biologically active proteins as a tool for revealing protein interactions and function. *Journal of Chromatography B: Biomedical Sciences and Applications* **1999**, *722* (1–2), 11-31.
- (21) Butler, J. E.; Ni, L.; Nessler, R.; Joshi, K. S.; Suter, M.; Rosenberg, B.; Chang, J.; Brown, W. R.; Cantarero, L. A., The physical and functional behavior of capture antibodies adsorbed on polystyrene. *Journal of Immunological Methods* **1992**, *150* (1–2), 77-90.
- (22) Reimhult, K.; Petersson, K.; Krozer, A., Qcm-d analysis of the performance of blocking agents on gold and polystyrene surfaces. *Langmuir : the ACS journal of surfaces and colloids* **2008**, *24* (16), 8695-8700.
- (23) Yolken Rh Fau - Stopa, P. J.; Stopa, P. J., Analysis of nonspecific reactions in enzyme-linked immunosorbent assay testing for human rotavirus. *Journal of Clinical Microbiology* **1979**, *10* (5), 703-707.

- (24)Vogt Rf Jr Fau - Phillips, D. L.; Phillips DI Fau - Henderson, L. O.; Henderson Lo Fau - Whitfield, W.; Whitfield W Fau - Spierto, F. W.; Spierto, F. W., Quantitative differences among various proteins as blocking agents for elisa microtiter plates. *Journal of Immunological Methods* **1987**, *101* (1), 43-50.
- (25)Gardas, A.; Lewartowska, A., Coating of proteins to polystyrene elisa plates in the presence of detergents. *Journal of Immunological Methods* **1988**, *106* (2), 251-255.
- (26)Kenny, G. E.; Dunsmoor, C. L., Effectiveness of detergents in blocking nonspecific binding of igg in the enzyme-linked immunosorbent assay (elisa) depends upon the type of polystyrene used. *Isr J Med Sci* **1987**, *23* (6), 732-734.
- (27)Sung, W.-C.; Chang, C.-C.; Makamba, H.; Chen, S.-H., Long-term affinity modification on poly (dimethylsiloxane) substrate and its application for elisa analysis. *Analytical Chemistry* **2008**, *80* (5), 1529-1535.
- (28)Shen, H.; Watanabe, J.; Akashi, M., Polyelectrolyte multilayers-modified membrane filter for rapid immunoassay: Protein condensation by centrifugal permeation. *Polymer Journal* **2010**, *43* (1), 35-40.
- (29)Nagasaki, Y.; Kobayashi, H.; Katsuyama, Y.; Jomura, T.; Sakura, T., Enhanced immunoresponse of antibody/mixed-peg co-immobilized surface construction of high-performance immunomagnetic elisa system. *Journal of Colloid and Interface Science* **2007**, *309* (2), 524-530.
- (30)Garland, A.; Shen, L.; Zhu, X., Mobile precursor mediated protein adsorption on solid surfaces. *Progress in Surface Science* **2012**, *87* (1-4), 1-22.

- (31)Gombotz, W. R.; Guanghai, W.; Horbett, T. A.; Hoffman, A. S., Protein adsorption to poly(ethylene oxide) surfaces. *Journal of Biomedical Materials Research* **1991**, *25* (12), 1547-1562.
- (32)Alcantar, N. A.; Aydil, E. S.; Israelachvili, J. N., Polyethylene glycol-coated biocompatible surfaces. *Journal of Biomedical Materials Research* **2000**, *51* (3), 343-51.
- (33)Geelhood, S. J.; Horbett, T. A.; Ward, W. K.; Wood, M. D.; Quinn, M. J., Passivating protein coatings for implantable glucose sensors: Evaluation of protein retention. *Journal of Biomedical Materials Research. Part B, Applied Biomaterials* **2007**, *81* (1), 251-60.
- (34)Bridges, A. W.; Garcia, A. J., Anti-inflammatory polymeric coatings for implantable biomaterials and devices. *Journal of Diabetes Science and Technology* **2008**, *2* (6), 984-94.
- (35)Lee, J. H.; Lee, H. B.; Andrade, J. D., Blood compatibility of polyethylene oxide surfaces. *Progress in Polymer Science* **1995**, *20* (6), 1043-1079.
- (36)Sadik, O. A.; Van Emon, J. M., Applications of electrochemical immunosensors to environmental monitoring. *Biosensors & Bioelectronics* **1996**, *11* (8), i-xi.
- (37)Sergeyeva, T. A.; Lavrik, N. V.; Rachkov, A. E.; Kazantseva, Z. I.; El'skaya, A. V., An approach to conductometric immunosensor based on phthalocyanine thin film. *Biosensors and Bioelectronics* **1998**, *13* (3-4), 359-369.
- (38)Parellada, J.; Narváez, A.; López, M. A.; Domínguez, E.; Fernández, J. J.; Pavlov, V.; Katakis, I., Amperometric immunosensors and enzyme electrodes for environmental applications. *Analytica Chimica Acta* **1998**, *362* (1), 47-57.
- (39)Skládal, P., Advances in electrochemical immunosensors. *Electroanalysis* **1997**, *9* (10), 737-745.

- (40)Wang, J.; Pamidi, P. V. A.; Rogers, K. R., Sol-gel-derived thick-film amperometric immunosensors. *Analytical Chemistry* **1998**, *70* (6), 1171-1175.
- (41)Liberelle, B.; Merzouki, A.; Crescenzo, G. D., Immobilized carboxymethylated dextran coatings for enhanced elisa. *Journal of Immunological Methods* **2013**, *389* (1-2), 38-44.
- (42)Dubois, J.; Gaudreault, C.; Vermette, P., Biofouling of dextran-derivative layers investigated by quartz crystal microbalance. *Colloids and Surfaces B: Biointerfaces* **2009**, *71* (2), 293-299.
- (43)Zhou, Y.; Andersson, O.; Lindberg, P.; Liedberg, B., Protein microarrays on carboxymethylated dextran hydrogels: Immobilization, characterization and application. *Microchimica Acta* **2004**, *147* (1-2).
- (44)Johnsson, B.; LofAs, S.; Lindquist, G., Immobilization of proteins to a carboxymethylated dextran-modified gold surface for biospecific interaction analysis in surface plasmon resonance sensors. *Analytical Biochemistry* **1991**, *198*, 268-277.
- (45)Ramadan, M. H.; Prata, J. E.; Karacsony, O.; Dunér, G.; Washburn, N. R., Reducing protein adsorption with polymer-grafted hyaluronic acid coatings. *Langmuir : the ACS Journal of Surfaces and Colloids* **2014**.
- (46)Jøssang, T.; Feder, J.; Rosenqvist, E., Photon correlation spectroscopy of human igg. *J Protein Chem* **1988**, *7* (2), 165-171.
- (47)Zhang, S.; Garcia-D'Angeli, A.; Brennan, J. P.; Huo, Q., Predicting detection limits of enzyme-linked immunosorbent assay (elisa) and bioanalytical techniques in general. *Analyst* **2014**, *139* (2), 439-445.

(48)Butler, J. E., The behavior of antigens and antibodies immobilized on a solid-phase. In *Structure of antigens*, Regenmortel, M. H. V. V., Ed. CRC: 1992; Vol. I, pp 209-259.

Chapter 5 : Microfabricated and Nanofabricated Hyaluronic Acid Constructs: Design and Applications

5.1. Introduction

Recent advances in microfabrication techniques have allowed for a wide range of opportunities. Combining successes in basic material design, chemical and physical properties with elaborate control over the underlying microarchitecture, enabling obtaining highly organized constructs able to mimic, treat and eventually replace diseased and damaged tissue organs. While utilized by many researchers to obtain deliberate 3D microarchitectures, these methods often face serious common challenges that limit their universal applicability to tissue engineering. In general, such challenges are related to interfacial cell-biomaterial interactions, porosity and efficient inter-scaffold biological mass transport, adequate vascularization, and, eventually functionality of the newly forming tissue.

The basic principle that most rapid prototyping methods builds upon is the use of computer-aided design (CAD) models. These designs are created individually for each construct and then fed to a computer that controls a material creator that, in turn, creates the material in a layer-by-layer fashion. The major advantage of these methods is the ability to go to very small feature sizes while maintaining precise control over the 3D geometry. This is possible because the CAD design is sliced into very thin cross-sectional layers of the print. The material is created either via 1) layer-by-layer deposition of polymerizable material through an extruder, such is the case in printer-based methods; 2) layer-by-layer polymerization from a material reservoir, such is the case laser-based methods; 3) layer-by-layer deposition of polymer melts, such is the case in nozzle-based methods.¹

In the past 10 years the prospects of using such precise control for the designing and creating tissue replacement constructs or even live tissue sample and organs motivated a lot of interesting research focused on optimizing the process. Such research was to enhance extrusion mechanisms, slicing patterns and material curing methods. As such, the three main rapid prototyping could be classified according to the curing method employed. In a very general manner, these classifications are photofabrication (photopolymerizable polymer constructs), thermofabrication (curing using heat) and powder fabrication (curing of deposited powders).²⁻³ These methods have been reported to be able to print biomaterials scaffold of various feature sizes and resolution of many materials types such as hydrogels, PEG scaffolds, PLLA, PCL. Yeong, et al. provides a valuable review of these materials.⁴

The prevailing route for delivering stimulating therapeutics to damaged tissue is parenteral routes using hypodermic needles⁵. At the same time that this route presents a simple approach that offers direct access to the injury site, certain complications are also associated with such methods. Some of these complications include requiring highly trained personnel, tissue damage following needle insertion, potential transmission of infectious diseases through needle reuse, poor patient compliance due to pain, and, most importantly, the reduced bioavailability of the delivered therapeutics due to rapid degradation of agents which leads to the necessity of increased doses to obtain affective administration⁶. In light of the aforementioned disadvantages of hypodermal needles, cutaneous routes of delivery of therapeutics present an attractive alternative⁵. Conversely, an important limitation is the need to overcome the physical barrier of the outer layer of the tissue. This layer consists of tightly arranged layers of cells that, unbreached, prevent

molecules larger than 500 Da from penetrating the tissue, thus, significantly limiting the type of biologics used for such routes and necessitating the need for specific design strategies to overcome the tissue barrier and successfully deliver the needed agents to the site of injury⁷.

Work published in the last decade shows the feasibility of microneedle arrays (MNAs) in providing sustained highly controlled delivery of wide range therapeutics via the cutaneous route⁶. MNAs are engineered arrays of high aspect-ratio features that range from 100 to 1000 μm in width and up to 1 mm in length⁷. The tips of the MNAs enable the penetration of the tissue and allow for the delivery of biologics to the desired site. Following the same principles, many types of MNAs have been reported, illustrated in fig. 5.1, with limitations and advantages to each one. Solid MNAs involves a solid microneedle that acts as a passive drug carrier. This type of MNAs does not include any therapeutics; rather it serves solely as an aid tool. The tips of this type of MNAs create micro piercings in the patch site, which enhance the delivery and penetration of the topically applied therapeutics. However, this type of MNAs offers little to no control over dosage and release profile of the target therapeutic. Coated MNAs employ solid micro needles that are coated with the target therapeutics. Upon patching, the tips of the MNAs penetrate the site and deliver the therapeutic to the targeted site. This approach offers some control over dosage as the concentration of the coating layers could be tuned. However, the control over rate of release is minimal. Hollow MNAs consists of solid; hollow micro needles attached to a solid therapeutic reservoir. At the same time that this offers more control over dosage and release rate, it also remains a technologically challenging approach that requires complex fabrication and application methods, which limits its potential. Of special interest is a more

advanced type of MNAs, which is the bioresorbable MNAs. This last type of MNAs employs biocompatible degradable materials to prepare solid MNAs capable of penetrating the target tissue, and dissolve only after penetrating the tissue ⁵⁻⁶. Each MNA type is suitable for some applications and biologic agents, which makes using MNAs a very versatile approach that could prove helpful for a wide range of applications. Designing bioresorbable MNAs using mechanically robust IPNs would then be a desired outcome.

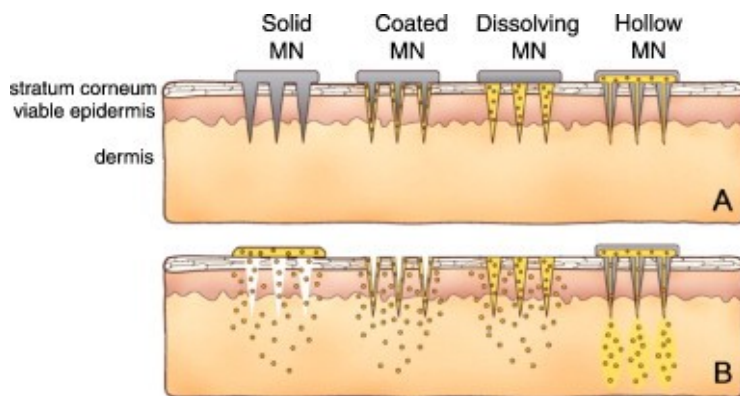


Figure 5.1 Illustration of the four types of microneedles.⁸

Alternatively, many attempts have also been made using biomaterials to help regenerate muscle tissue⁹. Biodegradable scaffolds or constructs prepared from either natural or synthetic materials have been reported and possess a high potential in this field, of special interest are hydrogels.

Hydrogels are naturally or synthetically derived cross-linked polymers that are characterized with very high water content. Reaching 95%-99%, the high water content of hydrogels makes it a very viable choice for tissue engineering approaches of many organs and conditions¹⁰. The mechanical properties of hydrogels are another key attractive feature that give the hydrogels the upper hand in any applications. Although very similar to biological tissues, the mechanical properties of hydrogels could be tuned by controlling

few parameters, such as the chemistry and density of crosslinks, concentration and the molecular weight of the precursors used to prepare the hydrogel. Controlling the mechanical properties of the prepared hydrogel is not only important to the successful implantation of the gel, but it is also vital to the survival of the used cells. The importance of the mechanical properties of hydrogels has been reported and demonstrated ¹¹⁻¹². It has been shown that seeded cells differentiate to the tissue precursor most similar to the underlying construct ¹³. While this is not the only design criterion, it remains a very important one to keep in mind.

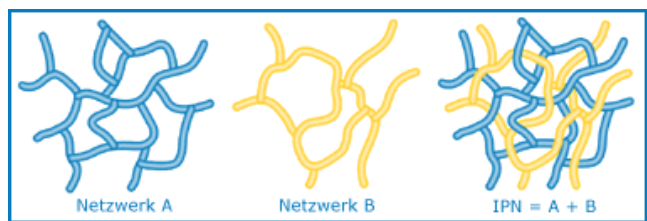


Figure 5.2 Interpenetrating polymer networks IPNs

Interpenetrating polymer networks (IPN), represent a method for combining the desired properties from two or more polymers into the same network. An IPN could be obtained by mixing two or more polymer networks at the molecular level and inducing a crosslinking mechanism that would lead to either a full-IPN or semi-IPN, where only one component is cross-linked while the other remains linear¹⁴. However, the methods described here could be tuned to accommodate changes in the polymers used according to desired applications with the limitation, beside all previously mentioned criteria, of processability of the chosen polymers. Preparing IPNs from biocompatible and biodegradable polymers serves to improve the mechanical properties of the prepared network, i.e. the mechanical properties of the prepared IPN is significantly better than those of the individual polymer components¹⁵. Moreover, these enhancements in strength,

stiffness and failure stress of IPN hydrogels have been shown to be achieved while preserving the elasticity of the hydrogel.^{14, 16}

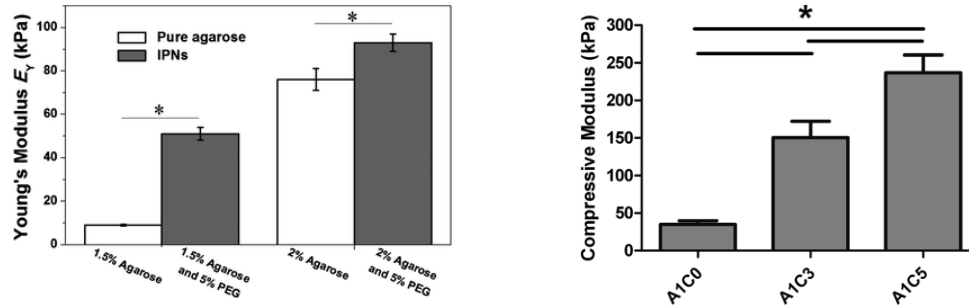


Figure 5.3 Mechanical properties of IPNs compared to individual networks.^{14, 16}

In this chapter, two methods for microfabrication of hyaluronic acid (HA) constructs are introduced. First, HA tissue engineering scaffolds are prepared using methacrylated hyaluronic acid using a novel 3D printing method. Second, MNAs prepared from HA-TNF- α hydrogels are prepared using a modified micromolding technique.

5.1. 3D Printing of Complex Biological Structures by Freeform Reversible Embedding of Suspended Hydrogels

Over the past decade, the additive manufacturing (AM) of biomaterials has gone from a rapid prototyping tool used in research and development and transitioned into a viable approach for the manufacturing of patient-specific medical devices. Key to this is the ability to precisely control structure and material properties in 3D and tailor these to unique anatomical and physiological criteria based on CT and MRI medical imaging data. First-in-human applications include customized polyetherketoneketone bone plates for the repair of large cranial defects¹⁷⁻¹⁸ and polycaprolactone bioresorbable tracheal splints for pediatric applications¹⁹. The enabling 3D printing technologies are based primarily on selective laser sintering (SLS) of metal, ceramic or thermoplastic microparticles, fused

deposition modeling (FDM) of thermoplastics or photopolymerization of photosensitive polymer resins²⁰⁻²¹ and have tremendous growth potential for surgical and medical devices^{20, 22} and scaffolds for tissue repair²³⁻²⁴. However, these approaches are limited in their ability to 3D print very soft materials such as elastomers, gels, and hydrogels that are integral components of many medical devices and are required for most future applications in tissue engineering and regenerative medicine²⁵⁻²⁶. Specifically, biological hydrogels composed of polysaccharides and/or proteins are a class of materials that are challenging to 3D print because they must be gelled *in situ* during the fabrication process and then supported so they do not collapse or deform under their own weight. While the need for support materials is common across many AM techniques, it is particularly difficult for these soft biological hydrogels, where the elastic modulus is <100 kPa, and there is a narrow range of thermal, mechanical, and chemical conditions that must be met to prevent damage to the materials and potentially integrated cells.

Current approaches for the 3D printing of biological hydrogels have achieved important advances, but are still in need of significant improvement^{25, 27}. For example, syringe-based extrusion has been used to 3D print polydimethylsiloxane (PDMS) elastomer and alginate hydrogel into multiple biological structures including the ear²⁸ and aortic heart valve²⁹⁻³⁰. Other research teams have demonstrated the direct bioprinting of fibrin³¹⁻³², gelatin³³ and mixtures of proteins derived from decellularized tissues³⁴ or cast ECM gels around dissolvable templates³⁵. These results have expanded the range of materials that can be used and demonstrated the ability to incorporate and print live cells. There are also commercially available bioprinters from Organovo³⁶⁻³⁸ and EnvisionTEC^{23, 39} that have expanded the accessibility of bioprinters beyond the groups that custom build

their own systems. However, the complexity of microstructure and 3D anisotropy that can be created are still limited; often the structures printed are simple square lattices, similar to stacked Lincoln logs, which does not recapitulate the microstructure of real tissues.

As a field, significant improvements are still needed in terms of the ability to directly manufacture using biologically relevant hydrogels, controlling microstructure and anisotropy in 3D, and expanding biological AM research by driving down the cost of entry while increasing quality and fidelity of the printing process. Our goal was to specifically address five major challenges, including (i) deposition and crosslinking of soft biomaterials and viscous fluids with elastic moduli of <100 kPa, (ii) supporting these soft structures as they are printed so they do not collapse or deform, (iii) depositing the material anisotropically to match the microstructure of real tissue, (iv) removing any support material that is used, and (v) keeping cells alive during this whole process using aqueous environments that are pH, ionic, temperature and sterility controlled within tight tolerances 40-42.

Natural biopolymers are modified to be used as 3D printing ink, including sodium alginate, CMC and HA. HA could be chemically modified so it could be cross-linked to form mechanically robust hydrogels. These modifications are ideally directed towards the carboxyl or hydroxyl groups on the polymer backbone, as they are the most reactive functional groups present in the polymer structure. Chemical crosslinking is possible through the modification of the backbone and reacting with bifunctional, low molecular weight cross-linkers. One way of doing that is via the esterification of the carboxylic acid groups followed by crosslinking by dihydrazide, dialdehyde, or disulfide cross-linkers, whereas hydroxyl groups are modified using divinyl sulfone and diglycidyl ethers. In this

work we are describing the photocrosslinking of HA via modifying it with glycidyl methacrylate (GM) to get the photopolymerizable glycidyl methacrylate (HAGM) material. Polymerization takes place using UV light in the presence of a photoinitiator, Irgacure I2959, to obtain a cross-linked hydrogel of HA. The mechanical properties and degradation rate are directly related to the degree of modification that would be measured and determined by ^1H NMR.

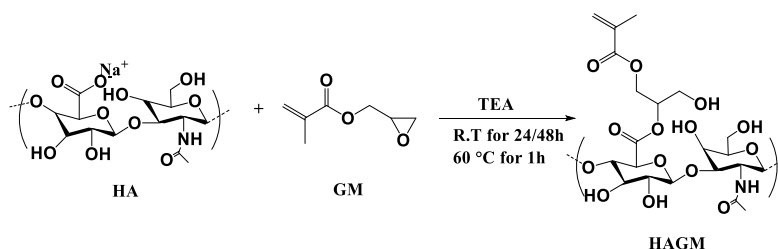


Figure 5.4 Synthesis of HAGM

5.1.1. Materials and Methods

5.1.1.1. Preparation and Analysis of Gelatin Slurry Support Bath

To create the gelatin slurry support bath, 150 mL of 4.5% w/v gelatin (Type A, Thermo Fisher Scientific) in 11 mM CaCl₂ (Sigma-Aldrich) was mixed into a solution and then gelled for 12 hrs at 4 °C in a 500 mL mason jar (Ball Inc.). Next, 350 mL of 11 mM CaCl₂ at 4 °C was added to the jar and its contents were blended (at “pulse” speed) for a period of 30 to 120 s on a consumer-grade blender (Osterizer MFG) (fig. S2A). Then, the blended gelatin slurry was loaded into 50 mL conical tubes (fig. S2B) and centrifuged at 4,200 RPM for 2 min, causing slurry particles to settle out of suspension (fig. S2C). Supernatant was removed and replaced with 11 mM CaCl₂ at 4 °C. The slurry was vortexed back into suspension and centrifuged again. This process was repeated until no bubbles were observed at the top of the supernatant, which

indicated most of the soluble gelatin was removed. At this point, gelatin slurries could be stored at 4 °C. For FRESH printing, the slurry was poured into a Petri dish or container large enough to hold the object to be printed (fig. S2D). Any excess fluid was removed from the gelatin slurry support bath using Kimwipes (Kimberly-Clark), which produced a slurry material that behaved as a Bingham plastic. All 3D printing was performed using gelatin blended for 120 s.

To measure the effect of blend time on gelatin particle size, the gelatin was blended for periods of time of 30, 45, 60, 75, 90, 105, 120 s. Blend times of greater than 120 s were not used because the gelatin particles began to dissolve entirely into solution. For each blend time analyzed, 500 μ L of slurry was removed and diluted to 10 mL with 11 mM CaCl_2 and 0.1% w/v black food coloring (McCormick & Co.). Then, 140 μ L of each diluted sample was mounted on a coverslip and imaged with a digital camera (D7000 SLR, Nikon) mounted on a stereomicroscope with oblique illumination (SMZ1000, Nikon). For each image, ImageJ (National Institutes of Health)⁴³ was used to enhance contrast, convert to LAB color space, and apply a lightness threshold. ImageJ was then used to count particles and measure their Feret diameters, areas, and circumferences using the “analyze particle” function. Linear regression of particle diameter as a function of time was performed using SigmaPlot 11 (Systat Software, Inc.).

To measure the rheological properties of the gelatin slurry support bath, the gelatin was blended for 120 s and then prepared as described for the FRESH 3D printing process. The slurry was loaded onto a Gemini 200 Rheometer with a 40 mm, 4° cone (Malvern) and analyzed in frequency sweep from 0.001 to 100 Hz at 150 μ m separation

and 25 °C. The storage (G') and loss (G'') moduli were measured and recorded in Microsoft Excel and plotted using SigmaPlot 11.

5.1.1.2. Preparation of Hydrogel Inks for 3D Printing

To prepare fluorescently-labeled alginate for 3D printing, a solution of 2.0% w/v sodium alginate (FMC Biopolymer), 0.02% w/v 6-aminofluorescein (FITC, Sigma), 0.022% w/v 1-ethyl-3-(3dimethylaminopropyl)carbodiimide (EDC, Sigma) and 0.025% w/v sulfo-N-hydroxysuccinimide (NHS, Sigma) in distilled water was prepared and stirred for 48 hrs at 20 °C. Unreacted FITC was removed from FITC-labeled alginate by five consecutive 12 hrs dialysis shifts against 2% w/v sodium alginate at 4 °C in dialysis cassettes (Slide-A-Lyzer 3.5k MWCO, Thermo Fisher). After dialysis, 100 μ L of FITC-labeled alginate was added to 10 mL solution of 4% w/v sodium alginate, 0.4% w/v hyaluronic acid (Sigma), and 0.1% w/v black food coloring (for visualization during printing) to create a fluorescently labeled alginate ink. Fluorescent alginate prints were imaged using a Leica SP5 multiphoton microscope with a 10x (NA = 0.4) objective and a 25x (NA=0.95) water immersion objective. Higher magnification images were obtained using a Zeiss LSM700 confocal microscope with a 63x (NA = 1.4) oil immersion objective. Bi-material prints and arterial tree prints were imaged using a Nikon AZ-C2 macro confocal microscope with a 1x (NA = 0.1) objective. 3D image stacks were deconvolved with AutoQuant X3 and processed with Imaris 7.5 (Bitplane Inc.).

To prepare fibrinogen for 3D printing of fibrin constructs, a solution of 10 mg/mL fibrinogen (VWR), 0.5% w/v hyaluronic acid (Sigma), 1% w/v bovine serum albumin (Sigma), 10 mM sodium-HEPES (Sigma), and PBS (VWR) was prepared and loaded

into a syringe for printing. To ensure crosslinking of the fibrinogen into fibrin once printed in the support bath, the baths were supplemented with 0.1 U/mL thrombin (VWR). Fibrinogen prints were released from bath material by incubation at 37 °C for at least 1 hour (fig. S3C).

For 3D printing of collagen, rat tail collagen type I (BD Biosciences) at concentrations ranging from 8.94 to 9.64 mg/mL in 0.02 N acetic acid was used as received without further modification. To ensure crosslinking of collagen into a gel following extrusion, the support bath was supplemented with 10 mM HEPES to maintain a pH of ~7.4 and neutralize the acetic acid. After printing, scaffolds were incubated at 37 °C for at least 1 hour to further crosslink the collagen (fig. S3D) and melt the support bath.

For 3D printing of cellularized constructs, components of a multi-component ECM ink were prepared at 4 °C under sterile conditions in a biosafety cabinet. The ECM ink consisted of a solution of 2 mg/mL collagen type I (BD Biosciences), 0.25 mg/mL Matrigel (BD Biosciences), 10 mg/mL fibrinogen (VWR), 0.5% w/v hyaluronic acid, 1% w/v bovine serum albumin (Sigma), 10 mM sodium-HEPES (Sigma), and PBS (VWR) which was prepared and thoroughly mixed at 4 °C. This specific protein and polysaccharide mixture was experimentally determined to gel quickly while maintaining viability of printed cells. C2C12 myoblasts or MC3T3-E1.4 cells were suspended in media at a concentration of 8×10^6 cells/mL and diluted 1:4 with the ECM mixture to create a final concentration of 2×10^6 cells/mL. The cellularized ink was then loaded into a sterile syringe used in the 3D printer. To ensure crosslinking of the ECM-

based ink once printed, the support bath was supplemented with 10 mM HEPES and 0.1 U/mL Thrombin.

5.1.1.3. The FRESH 3D Printing Process

Digital 3D models for FRESH prints were created using 3D imaging data or designed using SolidWorks software (Dassault Systèmes). The files for the human femur and coronary artery tree were downloaded from the BodyParts3D database ⁴⁴. The model of the human brain was provided under creative commons licensing by Andy Millns (Initiation Co). The 3D digital models were opened in MeshLab (<http://meshlab.sourceforge.net/>) to be exported in the STL file format. For the 3D model of the coronary artery tree, only the outer surface was provided by the BodyParts3D database, so the arterial tree was resampled to create a smaller daughter surface with inverted normals. When both surfaces were combined, a hollow model with internal and external surfaces with a wall thickness of ~1 mm resulted, which was exported as an STL file for printing. All STL files were processed by Skeinforge (<http://fabmetheus.crsndoo.com/>) or KISSlicer (<http://www.kisslicer.com/>) software and sliced into 80 µm thick layers to generate G-code instructions for the 3D printer. G-code instruction sets were sent to the printer using ReplicatorG (<http://replicat.org/>), an open source 3D printer host program.

To perform FRESH printing, hydrogel precursor inks were first drawn into a 2.5 mL syringe (model 1001 Gastight Syringe, Hamilton Company) with a 150 µm-ID 0.5” stainless steel deposition tip needle (McMaster-Carr) used as the nozzle. The syringe was then mounted into the syringe pump extruder on the 3D printer (fig. S1B and S1C). A petri dish or similar container large enough to hold the part to be printed was filled

with the gelatin slurry support bath and manually placed on the build platform, and the container was held in place using a thin layer of silicone grease. The tip of the syringe needle was positioned at the center of the support bath in X and Y and near the bottom of the bath in Z before executing the G-code instructions. Scaffolds were printed at 20 °C over a period of 1 min to 4 hours depending on the size and complexity of the printed construct as well as the ink used. For cellularized constructs, sterility was maintained by printing in a biosafety cabinet. In order to liquefy the support bath and release a print after FRESH, embedded constructs were heated to 37 °C directly on the printer's platform, placed on a dry bath, or placed inside an incubator. Once the gelatin was melted, alginate prints were rinsed with 11mM CaCl₂ and stored at 4 °C. Once the gelatin was melted for collagen and fibrin prints, the objects were rinsed with PBS and stored at 4 °C. For multi-component ECM prints containing cells, scaffolds were rinsed with the appropriate culture medium based on the incorporated cell types and incubated at 37 °C.

5.1.1.4. Cell Culture and Fluorescent Staining

All reagents were purchased from Life Technologies unless otherwise specified. The MC3T3-E1.4 fibroblast cell line and prints containing MC3T3 cells (CRL-2593, ATCC) were cultured in α -MEM supplemented with 10% fetal bovine serum (FBS, Gibco Labs), penicillin (100 units/mL), and streptomycin (100 μ g/mL). The C2C12 myoblast cell line and prints containing C2C12 cells (CRL-1722, ATCC) were cultured at 37 °C under 5% CO₂ in Dulbecco's Modified Eagle Medium supplemented with 10% v/v FBS, 1% v/v L-glutamine (200 mM), penicillin (100 units/mL), and streptomycin (100 μ g/mL), based on published methods ⁴⁵.

Cell viability after FRESH printing was assessed by performing a LIVE/DEAD assay (Life Technologies) on prints containing C2C12 cells (fig. S5A, B). Each print was first washed with Opti-MEM media containing 2% FBS and 2% 10,000-unit penicillin-streptomycin solution and incubated at 37 °C under 5% CO₂ for 30 min. The prints were then removed from the incubator, rinsed with PBS, incubated in 2 mL of PBS with 2 µL of calcein AM and 4 µL of ethidium homodimer per sample for 30 min and then imaged on a Zeiss LSM 700 confocal microscope. The number of live and dead cells in each of 5 images per 3 independent samples were counted and the percent viability was calculated by dividing the number of live cells by the number of total cells per image.

Prints containing cells were cultured for up to 7 days and analyzed at 1 and 7 day time points to verify cell survival and growth. After 1 and 7 days of culture, printed sheets were rinsed with PBS (supplemented with 0.625 mM MgCl₂ and 0.109 mM CaCl₂) at 37 °C, fixed in 4% w/v formaldehyde (Polysciences, Inc.) for 15 min, and then washed 3 times in PBS. Fixed prints were incubated for 12 hrs in a 1:200 dilution of DAPI (Life Technologies) and 3:200 dilution of Phalloidin conjugated to Alexa-Fluor 488 (Life Technologies). Prints were then washed three times in PBS and mounted with Prolong Gold antifade reagent (Life Technologies) between a microscope glass slide and a N1.5 glass cover slip. The mounted samples were stored at room temperature and protected from light for 12 hrs to allow the Prolong reagent to cure. Prints were imaged using a Leica SP5 multiphoton microscope with a 10x (NA = 0.4) objective and a 25x (NA=0.95) water immersion objective. 3D image stacks were deconvolved with AutoQuant X3 and processed with Imaris 7.5.

5.1.1.5. Perfusion of 3D printed Coronary Arterial Tree

In order to evaluate whether the 3D printed arterial tree was manifold, it was mounted in a custom-made 3D printed perfusion fixture (fig. S4A and S4B). A solution of 11 mM CaCl₂ (Sigma) and 0.1 % w/v black food coloring was injected into the root of the tree using a standard 3 mL syringe (BD Biosciences) with a 150 μ m-ID 0.5 in needle and the tip at the end of each branch was cut off to permit outflow. Perfusion was captured with a digital camera (D7000 SLR, Nikon) mounted on a stereomicroscope with oblique illumination (SMZ1000, Nikon).

5.1.1.6. Creation of a 3D Model of the Heart of a 5-day-old Chick Embryo

The 3D model of the embryonic chick heart was generated from 3D optical imaging data of a fluorescently labeled 5-day-old heart. To do this, White Leghorn chicken fertilized eggs were incubated at 37 °C and 50% humidity for 5 days. Then the embryo (Hamburger-Hamilton Stage 27-28 ⁴⁶) was explanted and the heart (ventricles, atria and outflow tract) was dissected and fixed for 15 min in PBS with calcium, magnesium and 4% formaldehyde. After washing in PBS, the heart was blocked and permeabilized for 2 hrs at 37 °C in PBS with 0.1% Triton X-100 and 5% goat serum. Two steps of immunostaining were carried out overnight at 4 °C. The first stain used dilutions of 1:200 DAPI, 3:100 Phalloidin conjugated to Alexa Fluor 633 (Life Technologies) and 1:100 anti-fibronectin primary antibody (mouse, Sigma-Aldrich). After extensive washing in PBS, the samples were stained with a 1:100 dilution of goat anti-mouse secondary antibody conjugated to Alexa Fluor 546 (Life Technologies). Samples were then washed and dehydrated by immersion in successive solutions of PBS with an increasing concentration of isopropyl alcohol as described previously ⁴⁷. Finally, the

samples were cleared by transferring to a solution of 1:2 benzyl alcohol to benzyl benzoate (BABB) to match the refractive index of the tissue. The transparent sample was mounted in BABB and imaged with a Nikon AZ-C2 macro confocal microscope with a 5x objective (0.45 NA).

The 3D image stack was deconvolved using AutoQuant X3 and processed with Imaris 7.5, MATLAB (MathWorks), and ImageJ. The DAPI (fig. S6A), actin (fig. S6B) and fibronectin (fig. S6C) channels were merged to obtain an image with simultaneously well-defined trabeculae and outer wall of the heart (fig. S6D). A detailed mask of the heart showing the trabeculae was created by segmenting the averaged signals using a high-pass threshold (fig. S6E). A rough mask showing the bulk of the heart was obtained using a low-pass threshold (fig. S6F). Next, the Imaris “Distance Transform” XTension was used on the bulk mask to create a closed shell of the outer wall of the heart. The high detail mask and the mask of the closed shell were combined to get a complex model of the heart with detailed trabeculae and a completely closed outer wall (fig. S6G). The final model was smoothed and segmented using Imaris to preserve a level of detail adequate for 3D printing (fig. S6H). A 3D solid object was created by exporting the smoothed model as an STL file using the Imaris XT module and the “Surfaces to STL” Xtension for MATLAB (fig. S6I and S6J).

5.1.2. Results and Discussion

Here we report development of a 3D bioprinting technique termed Freeform Reversible Embedding of Suspended Hydrogels (FRESH). FRESH uses a thermo-reversible support bath to enable deposition of hydrogels in complex, 3D biological structures and is implemented using open-source tools, serving as a highly adaptable and

cost-effective biological AM platform. The key innovation in FRESH is deposition and embedding of the hydrogel(s) being printed within a second hydrogel support bath that maintains the intended structure during the print process and significantly improves print fidelity (Fig 5.5 A and B). The support bath is composed of gelatin microparticles that act as a Bingham plastic during the print process, behaving as a rigid body at low shear stresses but flowing as a viscous fluid at higher shear stresses. This means that as a needle-like nozzle moves through the bath, there is little mechanical resistance, yet the hydrogel being extruded out of the nozzle and deposited within the bath is held in place. Thus, soft materials that would collapse if printed in air are easily maintained in the intended 3D geometry. This is all done in a sterile, aqueous, buffered environment compatible with cells, which means cells can be extruded out of the printer nozzle with the hydrogel and maintain viability. Once the entire 3D structure is FRESH printed, the temperature is raised to a cell-friendly 37 °C, causing the gelatin support bath to melt in a non-destructive manner.

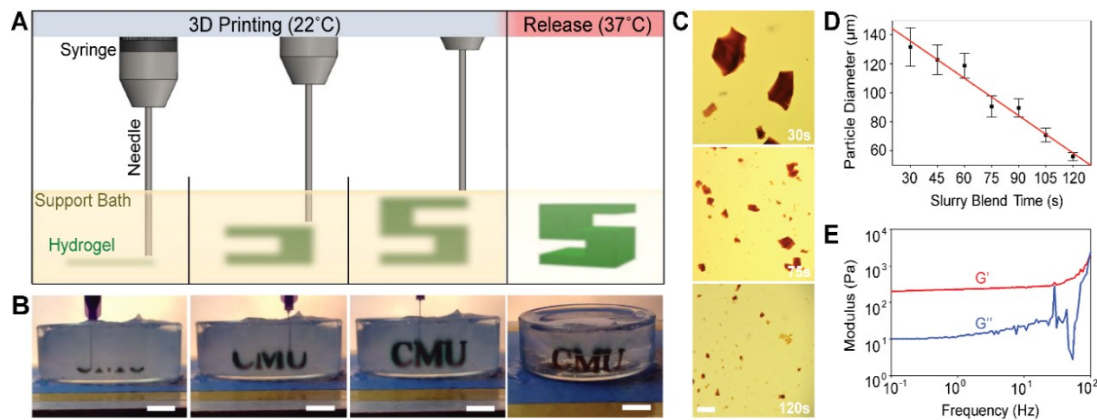


Figure 5.5 FRESH printing is performed by depositing a hydrogel precursor ink within thermoreversible support bath consisting of gelatin microparticles and initiating gelling *in situ* through one of multiple crosslinking mechanisms. (A) A schematic of the FRESH process showing the hydrogel (green) being extruded and crosslinked within the gelatin slurry support bath (yellow). The 3D object is built layer-by-layer and when completed is released by heating to 37 °C and melting the gelatin. (B) Images of the letters “CMU” FRESH printed in alginate in Times New Roman font (black) and released by melting the gelatin support

(grey material in the Petri dish). (C) Representative images of gelatin particles produced by blending for 30, 75 or 120 s. (D) The mean Feret diameter of gelatin particles as a function of blending time from 30 to 120 s ($N > 1000$ per time point, red line is a linear fit, error bars indicate standard deviation). (E) Rheological analysis of storage (G') and loss (G'') modulus for gelatin support bath showing Bingham plastic behavior. Scale bars, (B) 1cm and (C) 1mm.

FRESH is implemented on a MakerBot Replicator modified with a custom syringe-based extruder designed for precision hydrogel deposition. All plastic parts to convert the MakerBot into a bioprinter are printed in PLA using the stock thermoplastic extruder, which is then replaced with the custom syringe-based. Our syringe-based extruder uses the stepper motor, taken from the original extruder, to move the plunger of a 3 mL syringe via a direct gear drive. Overall size and mass is comparable to the original extruder and, once mounted, integrates seamlessly with the MakerBot hardware and software, requiring only calibration of the number of motor steps that extrudes a given volume of fluid. Typically we use a 150 μm diameter stainless steel needle on the end of the syringe, but a range of needle diameters can be selected to control the volume of material being extruded.

The FRESH support bath consists of a slurry of gelatin microparticles processed to have a Bingham plastic rheology. To do this, a solid block of gelatin hydrogel is blended to break up the material into microparticles and then centrifuged to remove the supernatant and produce the final slurry. Increasing the blending time decreases microparticle size (Fig 5.6. C), with a blending time of 120 s producing microparticles with a mean Feret diameter of $55.3 \pm 2 \mu\text{m}$ (Fig. 5.5.D). Rheometry confirmed that the 120 s blended gelatin slurry behaved as a Bingham plastic (Fig. 5.5.E), not yielding until a threshold shear force is reached. Maintaining the gelatin slurry at room temperature ($\sim 22^\circ\text{C}$) preserves these rheological properties. For FRESH, the gelatin support slurry is loaded into a container of sufficient size to hold the part to be printed.

FRESH works by extruding the liquid phase material from the syringe into the support bath, where the material must rapidly gel into a filament without diffusing away. This gelation process occurs via rapid crosslinking of the polymer molecules into a network, and the crosslinking mechanism depends on the hydrogel being 3D printed. We have validated this process using fluorescently-labeled alginate crosslinked by divalent cations (0.16% CaCl_2) added to the support bath. A representative alginate filament embedded in the support bath illustrates that the gelatin microparticles are moved out of the way, but still influence the surface morphology of the filament (Fig. 5.6.A). As the alginate gels, there are visible “spurs” that form in-between microparticles, but these are not necessarily a problem in the context of a larger 3D printed structure. According to the print settings used, the diameter of the extrusion was $199 \pm 41 \text{ }\mu\text{m}$ (Fig. 5.6.B). However, the diameter of the extruded hydrogel filament depends on a large number of factors including the hydrogel being printed and its crosslinking kinetics, gelatin microparticle size, nozzle diameter, extruder translation speed, and flow rate. Thus, like 3D printing of most materials, the resolution and morphology of a print depends on a number of machine settings and requires optimization for each material used.

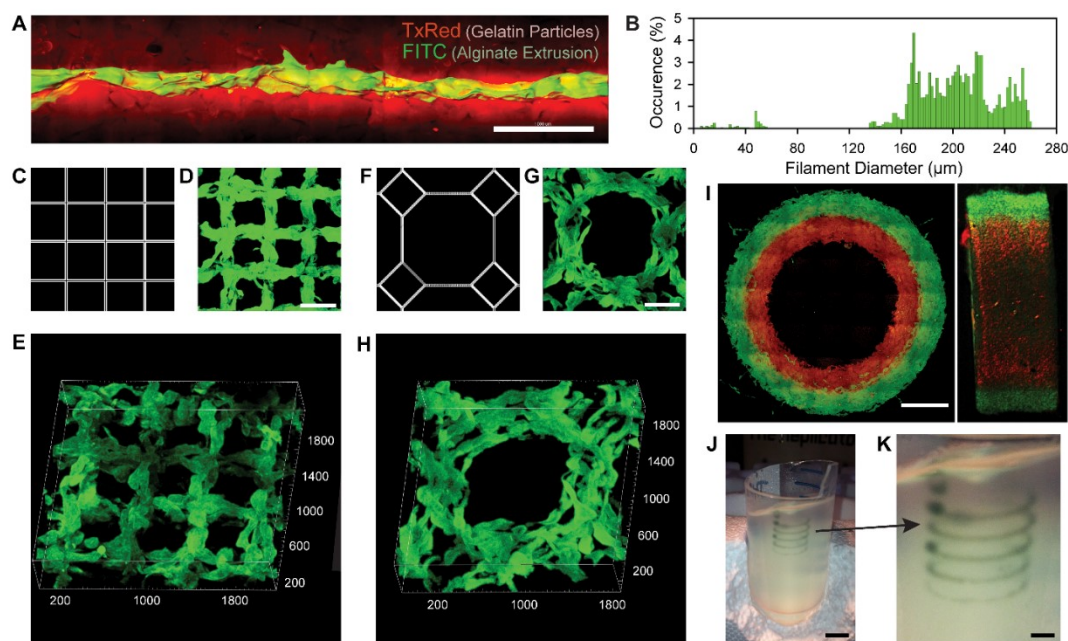


Figure 5.6 Analysis of the hydrogel filaments and structures fabricated using FRESH. (A) A representative alginate filament (green) embedded within the gelatin slurry support bath (red). (B) Histogram of the diameter of isolated alginate filaments within the gelatin support bath showing a range from 160 to 260 μm . (C) A standard square lattice pattern commonly used for infill in 3D printing FRESH printed in fluorescent alginate (green) and viewed (D) top down and (E) in 3D. (F) An octagonal infill pattern FRESH printed in fluorescent alginate (green) and viewed (G) top down and (H) in 3D. (I) Example of a two material print of coaxial cylinders in red and green fluorescently labeled alginate with a continuous interface shown in top down and lateral cross-sections. (J) An example of a freeform, non-planar FRESH print of a helix shown embedded in the gelatin support bath. (K) A zoom in of the helix demonstrating that FRESH can print in true freeform and is not limited to standard layer-by-layer planar fabrication. Scale bars, (A) 1 mm, (D, G) 500 μm , (I) 2 mm, (J) 10 mm, and (K) 2.5 mm.

While the properties of single filaments are important, it is the ability of filaments to fuse into larger scale structures that is required for 3D printing. Metal and plastic 3D printing typically produces parts that are <100% solid, creating an external skin that is infilled using a repeating geometric structure with a defined porosity. For FRESH, we used rectilinear and octagonal infill algorithms to generate patterns of interconnected alginate filaments (Fig. 5.6 C to H). The rectilinear infill is a simple square lattice structure (Fig. 5.6.C) that we FRESH printed at a 500 μm pitch (Fig. 5.6.D). Confocal imaging and 3D rendering clearly demonstrates that there is interconnectivity between filaments in the X, Y and Z axes (Fig. 5.6.E). The octagonal infill is a more complex pattern of squares and

octagons (Fig. 5.6.F) that we FRESH printed at a 750 μm pitch (Fig. 5.6.G). A 3D rendering again demonstrates the interconnectivity between filaments in the X, Y and Z axes (Fig. 5.6.H). It should be noted that the fidelity of these infill patterns is comparable to that achieved using the stock thermoplastic extruder to print the same geometries in PLA, and further improvements are anticipated by performing FRESH on better hardware with optimized print parameters.

FRESH can also be used to 3D print complex, multi-material parts and in non-planar geometries. Dual syringe-based extruders can be mounted onto the MakerBot and directly leverage the dual extruder printing capability built into the software to alternate between extruders. To demonstrate dual material printing, two different fluorescently-labeled alginates were printed in concentric cylinders. Multiphoton imaging clearly shows distinct layers, each 1 mm wide, integrated together throughout a 3 mm thickness (Fig. 5.6.I). Uniquely, FRESH is also not limited to standard layer-by-layer 3D printing, and can freeform deposit material in 3D space with high fidelity as long as the extruder does not pass through previously deposited material. This is demonstrated by printing a single filament along a helical path (Fig. 5.6.J and 5.6.K).

FRESH was next used to print complex biological structures based on medical imaging data to demonstrate the capability to fabricate complex geometries. Further, we wanted to validate that prints were mechanically robust and could be formed from multiple types of protein and polysaccharide hydrogels. First, a human femur from CT data (Fig. 5.7.A) was scaled down to a length of ~ 35 mm and a minimum diameter of ~ 2 mm and FRESH printed in alginate (Fig. 5.7.B). Applying uniaxial strain showed that the femur could undergo $\sim 40\%$ strain and recover elastically (Fig. 5.7.C), validating there was

mechanical fusion between the printed alginate layers. Further, the femur could be bent in half and elastically recover, and when strained to failure fractured at an oblique angle to the long-axis of the bone, confirming that failure was not due to layer delamination. Next, we created a simple bifurcated tube in CAD to demonstrate the ability to FRESH print a hollow structure (fig. S3). We used both the femur and bifurcated tube to show that other ECM hydrogels including collagen type I and fibrin can be FRESH printed with comparable fidelity to alginate (fig. S3). Further, sheets of C2C12 myoblasts suspended in a mixture of fibrinogen, collagen type I, and Matrigel were printed at 20 °C under sterile conditions and showed 99.7% viability by LIVE/DEAD staining (fig. S5A and S5B). Multiday studies using C2C12 myoblasts and MC3T3 fibroblasts showed that cells were well distributed in 3D (fig. S5C and S5E, respectively), and over a 7 day culture period formed a high-density cellular network (fig. S5D and S5F, respectively). These examples demonstrate that FRESH can 3D print mechanically robust parts with high fidelity, high repeatability (fig. S4C), from a range of ECM hydrogels including collagen, fibrin, and Matrigel (fig. S4D) and with embedded cells (fig. S5A and S5B).

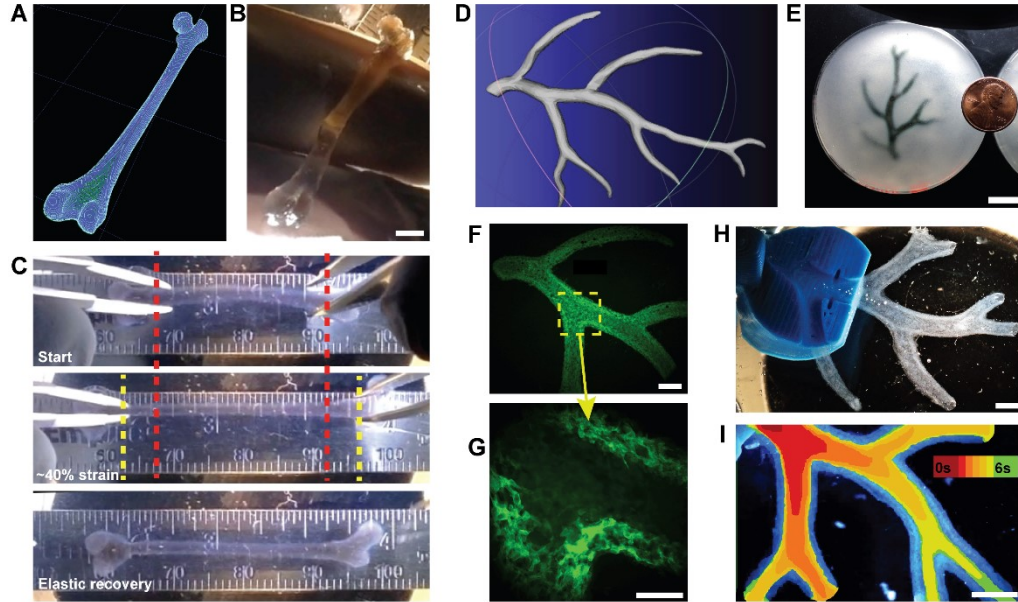


Figure 5.7 FRESH printing of biological structures based on 3D imaging data and functional analysis of the printed parts. (A) A model of a human femur from 3D CT imaging data is scaled down and processed into machine code for FRESH printing. (B) The femur is FRESH printed in alginate and after removal from the support bath closely resembles the model and is easily handled. (C) Uniaxial tensile testing of the printed femur demonstrates the ability to be strained up to 40% and elastically recover. (D) A model of a section of a human right coronary arterial tree from 3D MRI imaging is processed at full scale into machine code for FRESH printing. (E) An example of the arterial tree printed in alginate (black) and embedded in the gelatin slurry support bath. (F) A section of the arterial tree printed in fluorescent alginate (green) and imaged in 3D to show the hollow lumen and multiple bifurcations. (G) A zoom in of the arterial tree shows the clearly defined vessel wall <1 mm thick and well-formed lumen. (H) A darkfield image of the arterial tree mounted in a perfusion fixture to position a syringe in the root of the tree. (I) A time-lapse image of black dye perfused through the arterial tree false-colored at time points of 0 to 6 s to show flow through the lumen and not through the vessel wall. Scale bars, (B) 4 mm, (E) 10 mm, (F) 500 μm , (G) 250 μm , and (H, I) 500 μm .

Next, we evaluated the ability to fabricate a more complex, perfusable structure using MRI data of part of the right coronary artery vascular tree and creating a hollow lumen with a wall thickness of <1 mm (Fig. 5.7.D)⁴⁸. This was FRESH printed to scale with an overall length from trunk to tip of 5 cm and contained multiple bifurcations with 3D tortuosity (Fig. 5.7.E). Arterial trees printed using fluorescent alginate confirmed that the internal lumens and bifurcations were well formed (Fig. 5.7.F) and that a wall thickness of <1 mm and lumen diameters of 1 to 3 mm were achieved (Fig. 5.7.G). A custom fixture to hold the arterial tree was 3D printed in PLA (Fig. 5.7.H and fig. S4) and used to perfuse

the print. Black dye pumped through the arterial tree confirmed it was patent, manifold, and that hydrogel density was sufficient to prevent diffusion through the wall (Fig. 5.7.I). Similar to the mechanical testing of the femur (Fig. 5.7.C), the minimal diffusion through the arterial wall confirmed that the alginate layers were well fused together forming a solid structure.

Finally, we evaluated the ability to FRESH print 3D biological structures with complex internal and external architectures that would be extremely challenging or impossible to create using traditional fabrication techniques. First, we selected a day 5 embryonic chick heart (Fig. 5.8.A) because of the complex internal trabeculations. We fixed and stained the heart for cell nuclei, F-actin and fibronectin and generated a 3D optical image using confocal microscopy (Fig. 5.9.B). The 3D optical image was then thresholded, segmented and converted into a solid model for 3D printing (Fig. 5.9.C and fig. S5). The diameter of the actual embryonic heart (~1 mm) was scaled up by an order-of-magnitude (~1 cm) in order to better match the resolution of the printer and FRESH printed using fluorescently labeled alginate. The printed heart was then imaged using a multiphoton microscope to generate a cross-section through the structure (Fig. 5.9.D) showing internal trabeculation comparable to that in the model (Fig. 5.9.C). A darkfield image of the whole heart provided further validation of print fidelity and the ability to fabricate complex internal structures on the sub-millimeter length scale (Fig. 5.9.E).

To create complex surface structures, we used an MRI image of the human brain (Fig. 5.9.F) because of the intricate folds in the cortical tissues. A high-resolution view of the 3D brain model shows the surface in detail (Fig. 5.9.G). While the embryonic heart was scaled up in size, the human brain was scaled down to 3 cm in length in order to evaluate

the resolution limits of the printer and reduce print times. The human brain was 3D printed using alginate and different regions including the frontal and temporal lobes of the cortex and the cerebellum were clearly defined (Fig. 5.9.H). Visualization of the brain surface was enhanced with black dye and revealed structures that matched in detail the major white matter folds in the 3D model (Fig. 5.9.I). Both the 3D printed embryonic heart and brain clearly demonstrate the unique ability of FRESH to print hydrogels with complex internal and external structures at high fidelity.

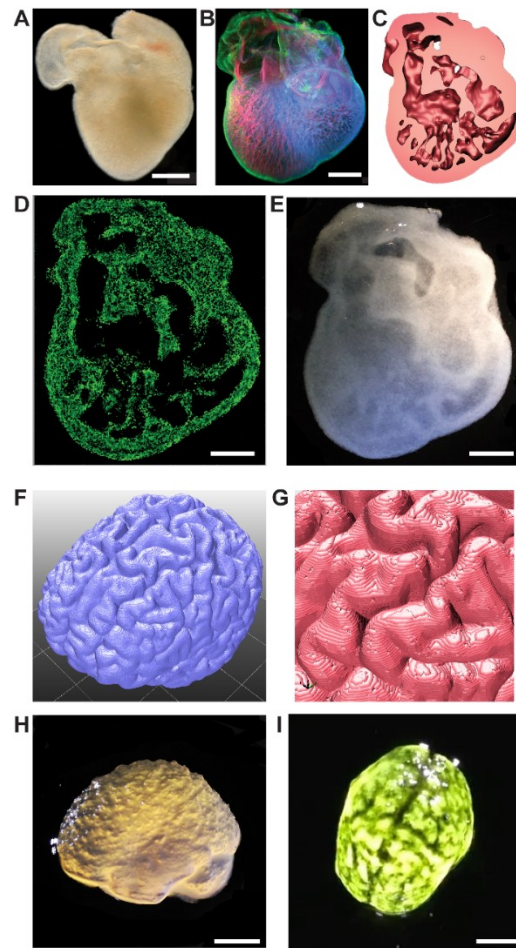
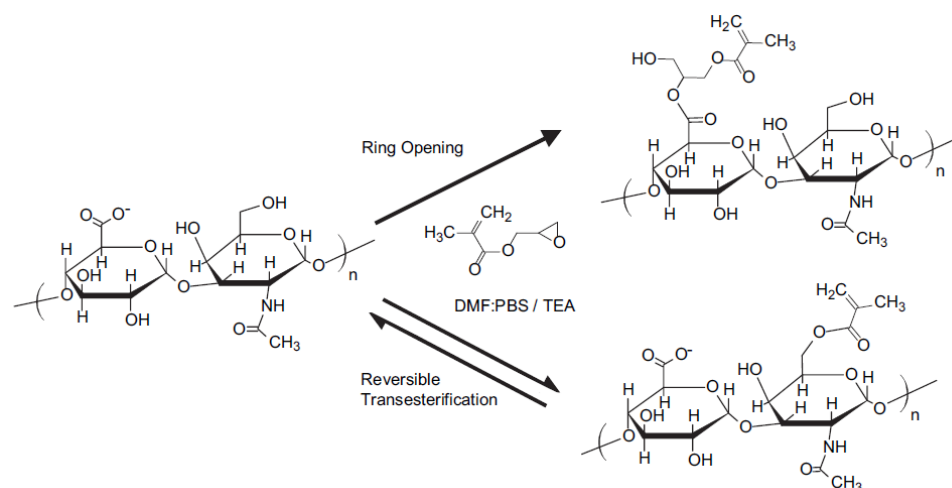


Figure 5.8 FRESH printed scaffolds with complex internal and external architectures based on 3D imaging data from whole organs. (A) A darkfield image of an explanted embryonic chick heart. (B) A 3D image of the 5-day-old embryonic chick heart stained for fibronectin (green), nuclei (blue), and F-actin (red) and imaged with a confocal microscope. (C) A cross-section of the 3D CAD model of the embryonic heart with complex internal trabeculation, based on the confocal imaging data. (D) A cross-section of the 3D printed heart in fluorescent alginate (green) showing recreation of the internal trabecular structure from the CAD

model. The heart has been scaled up by a factor of 10 to match the resolution of the printer. (E) A darkfield image of the 3D printed heart with internal structure visible through the translucent heart wall. (F) A 3D rendering of a human brain from MRI imaging data processed for FRESH printing. (G) A zoom in of the 3D brain model showing the complex, external architecture of the white matter folds. (H) A lateral view of the brain 3D printed in alginate showing major anatomical features including the cortex and cerebellum. The brain has been scaled down to ~3 mm in length to reduce printing time and test the resolution limits of the printer. (I) A top down view of the 3D printed brain with black dye dripped on top to help visualize the white matter folds printed in high fidelity. Scale bars, (A, B) 1 mm, (D, E, H, I) 1 cm.

HA was modified with methacrylate groups at the carboxylic acid group moiety of its structure by reacting with glycidyl methacrylate in the presence of TEA as a catalyst. The mechanism of this reaction is explained by the ring opening reaction of the epoxide moiety of glycidyl methacrylate following the nucleophilic attack of the carboxyl group. However, due to the existence of the nucleophilic hydroxyl groups on the HA molecule, transesterification reaction between glycidyl methacrylate and the hydroxyl group of HA is possible as well. Van Dijk-Wolthuis et al.⁴⁹ proved such mechanism for dextran modification with methacrylates. On the other hand, the reversibility of the transesterification reaction yields a mixture of both reactions products, i.e. ring opening and transesterification products. Bencherif et al.⁵⁰ showed that the ring opening products are more stable and abundant in the reaction and their yield could be increased by increasing the reaction time. In the same time, the separation of one product over the other is beyond the scope of this study as the desired end result is a cross-linked hydrogels between the newly introduced acrylates to HA regardless of its position.



Scheme 5.1 HA methacrylation mechanism⁵⁰

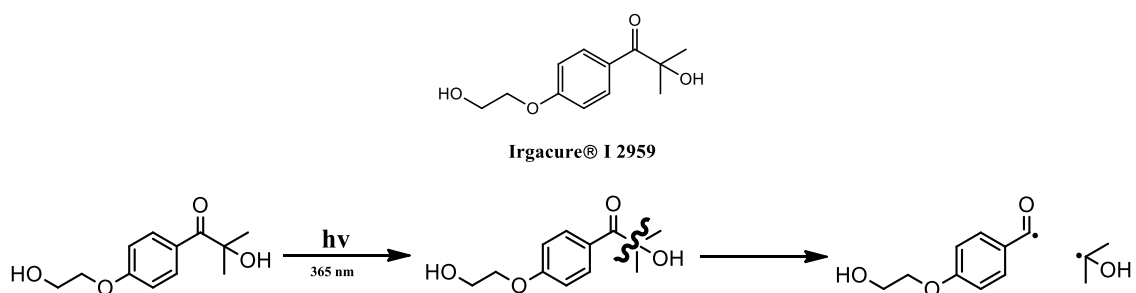
¹HNMR spectroscopy was used to confirm the occurrence of the reaction and acrylate peaks ~5.6 and ~6.1 ppm were detected in the resulting product. The same peaks were used as a guide to estimate the DM as percent methacrylation. Such percent is calculated by comparing the integration values of both acrylate peaks with HA's methyl peak at ~1.9 ppm. Using this method, a summary of reaction conditions leading to varying DMs is established and HAGM materials with 17, 20 and 50% modification were prepared, table 5.1. This is important as previous studies have showed the dependence of hydrogel properties on DM.⁵¹

Degree of modification (DM)	Molar Excess GM	DMF Volume	Reaction Time
17 %	20	---	24 h
20 %	30	---	24 h
50 %	50	50 %	48 h

Table 5.1 Summary of modification conditions

HAGM hydrogels were prepared by exposing a solution of HAGM and the photoinitiator 1-[4-(2-hydroxyethoxy)-phenyl]-2-hydroxy-2-methyl-1-propanone,

Irgacure I2959, fig. 4, to UV light with a wavelength of 365 nm for 10 minutes. Irgacure I2959 is a type I initiator that monolithically cleaves upon UV illumination to generate free radicals that are capable of initiating the cross-linking of the acrylate groups on the HAGM structure. It is the most commonly used initiator for cellular encapsulation into hydrogels applications, due to its relatively high water solubility compared to other initiators. Degree of modification, HA concentration and I2959 concentration affect the properties of the resultant hydrogel.⁵²



Scheme 5.2 Photo initiator Irgacure I2959 mechanism of action

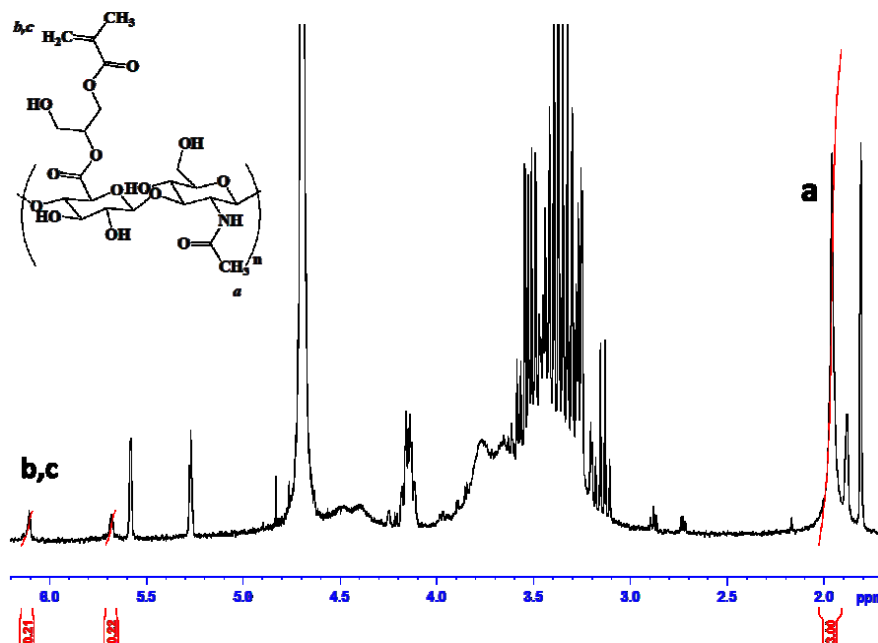


Figure 5.9 ¹H NMR 20% DM HAGM

HAGM with 20% DM was chosen as the 3D printing material (ink). At the time the support material offers a tremendous support to the printed structure by preserving the integrity of the structure and increasing the quality of the print, HAGM cross-linking to form hydrogels is not instantaneous which gives time to the ink to diffuse in between the support material particles. The diffused individual threads also lead to swelling, which compromises print fidelity as well and construct features. Fig. 5.10 shows a printed HAGM construct and a zoomed in view of the swollen individual threads.

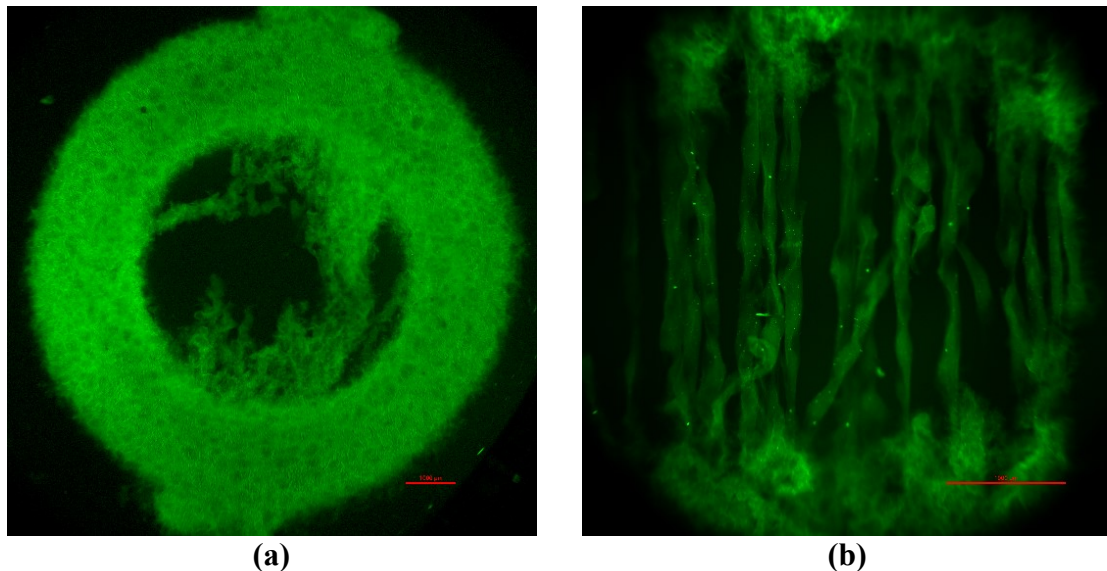


Figure 5.10 Printed HAGM circle-threads. a) Swelling of the printed constructs leads to brittle hydrogel. b) Swollen individual threads increases feature size. Scale bar 1000 μm

This diffusion was limited by increasing the concentration of the HAGM in ink. However, the diffusion still occurred and the integrity of the structure was compromised, to varying degrees, upon UV illumination. Sodium alginate is a natural biopolymer that has received attention lately due to its bio compatibility and biodegradability. Alginates are linear copolymers of β -D-manuronic acid (M) and α -L-guluronic acid (G) units. M and G units are linked 1 \rightarrow 4 glycosidic bonds. In the presence of polyvalent cations, such as Ca^{+2} , they act as cross-linkers between the anionic polymer chains forming a hydrogel, fig. 5.11.

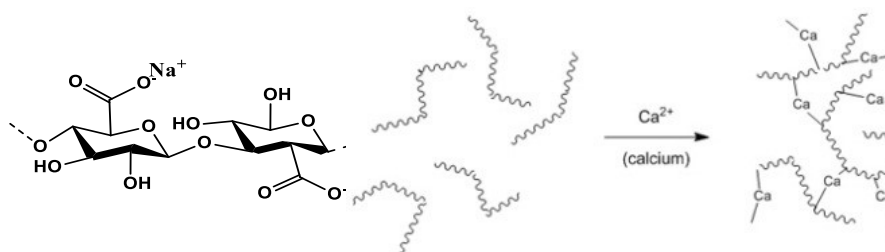
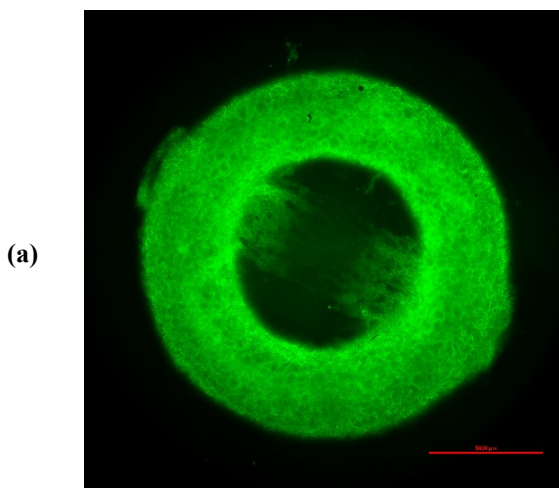


Figure 5.11 Sodium alginate crosslinks

Using a mixture of 3% HAGM and 10% sodium alginate (10:1 ratio) in the ink improved the quality of the print. Introducing Ca^{+2} in the support material to the ink leads to rapid cross-linking of sodium alginate. The formed alginate layer acts as a protective barrier that prevents the diffusion of HAGM gel into the support material which, as a result, protects the printed structure and maintain the required design criteria. HA was fluorescently labeled using a hydrazide label through the carboxyl group of the HA. Printed HAGM hydrogels were imaged using a laser scanning Nikon confocal microscope with a 488 nm laser at an excitation wave length of 493 nm.



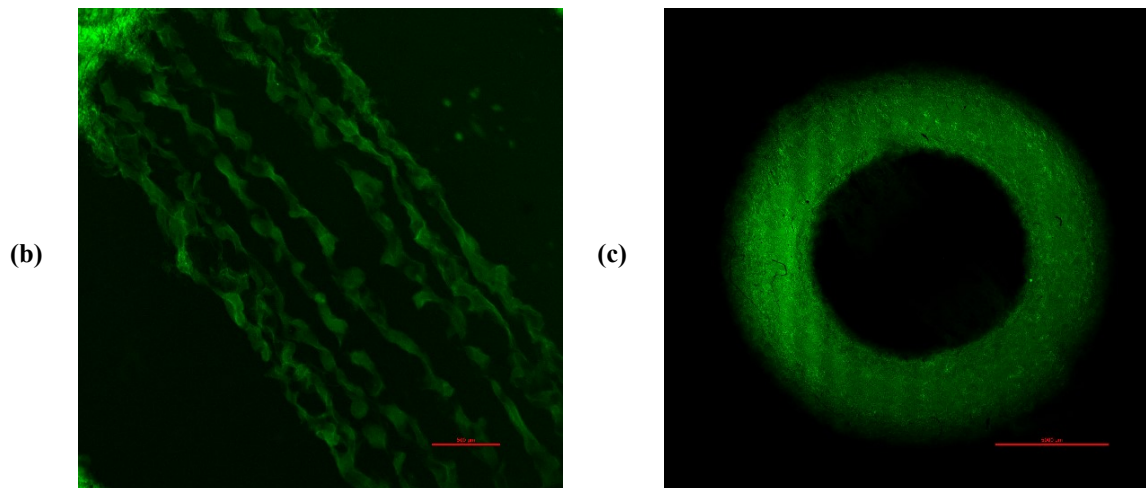


Figure 5.12 Confocal images of printed HAGM/alginate constructs (a) circle thread view shows improved print fidelity and feature size. (b) Sharp individual non-swollen threads. (c) A printed circle shows sharp-edged hydrogel constructs. Scale bar 500 μm

5.1.2. Conclusions:

We demonstrate the additive manufacturing of complex 3D biological structures using soft, protein and polysaccharide hydrogels that are challenging or impossible to create using traditional fabrication approaches. These structures are built by embedding the printed hydrogel within a secondary hydrogel that serves as a temporary, thermoreversible and biocompatible support. This process, termed freeform reversible embedding of suspended hydrogels (FRESH), enables 3D printing of hydrated materials with an elastic modulus <200 kPa including alginate, collagen, and fibrin, based on CAD models of 3D optical, CT and MRI imaging data at a resolution of ~ 200 μm . Proof-of-concept structures including femurs, branched coronary arteries, trabeculated embryonic hearts and human brains that are anatomically accurate, mechanically robust and recreate complex 3D internal and external architectures with high-fidelity and at low cost.

Looking forward, can we leverage these FRESH bioprinting capabilities to engineer soft hydrogel scaffolds for advanced tissue engineering applications? In terms of complex scaffold design, our results clearly demonstrate the ability to fabricate a wide

range of 3D biological structures based on 3D imaging data with spatial resolution and fidelity that matches or exceeds previous results. Further, this is done directly with natural biopolymers such as alginate, fibrin and collagen type I, which are crosslinked by ionic, enzymatic and pH/thermally driven mechanisms, respectively. This flexibility in materials used and architectures printed define a new level of capability for soft materials additive manufacturing. In fact, the square and octagonal infill patterns (Fig. 5.6.C to H) show results comparable to those achieved with thermoplastics (e.g., PLA) printed on the stock MakerBot Replicator printer we used, suggesting we may in fact be limited by the hardware. We anticipate that higher resolution is possible using higher precision printers, smaller diameter needles and gelatin slurries with smaller particle diameter. Cost is also an important consideration for the future expansion of 3D bioprinting as a tissue biofabrication platform, as commercially available and custom-built printers are currently >\$100,000 and/or require specialized expertise to operate^{23, 33, 36-39, 53}.

In contrast, FRESH is built on open source hardware and software and the gelatin slurry is low cost and readily processed using consumer blenders. To emphasize the accessibility of the technology, we implemented FRESH on a \$400 3D printer and include the STL file to 3D print the custom syringe-based extruder as supplemental material. It should be acknowledged that the direct bioprinting of functional tissues and organs requires further research and development to become fully realized, and a number of companies and academic laboratories are actively working towards this goal. The low-cost of FRESH and ability to 3D print a range of hydrogels should enable expansion of bioprinting into many academic and commercial laboratory settings and accelerate important

breakthroughs in tissue engineering for a wide range of applications, from pharmaceutical testing to regenerative therapies.

5.2. Therapeutic intradermal delivery of tumor necrosis factor- α antibodies using tip-loaded dissolvable microneedle arrays

5.2.1. Abstract

Tumor necrosis factor- α (TNF- α) specific antibodies (anti-TNF- α) have been shown to be potent TNF inhibitors and effective therapeutics for a range of inflammatory diseases. Typically, these drugs are administered systemically, but systemic dosing sufficient to achieve locally effective concentrations in peripheral tissues has been associated with systemic immunosuppression and related adverse events. Here, we evaluated the use of tip-loaded dissolvable microneedle arrays (MNAs) for localized intradermal delivery of anti-TNF- α . MNAs with obelisk shape microneedles that incorporate the antibody cargo in the needle tips were created from carboxymethylcellulose (CMC) using a micromilling/spin-casting fabrication method. We found that Anti-TNF- α integrated into MNAs using this room temperature fabrication process maintained conformationally dependent TNF- α binding activity. Further, these MNAs efficiently delivered anti-TNF- α to the dermis of human skin with clinically applicable release profiles. To evaluate MNA delivered anti-TNF- α function, we applied anti-TNF- α containing MNAs to established psoriasiform lesions on the skin of mice. MNA anti-TNF- α treatment reduced key biomarkers of psoriasiform inflammation including epidermal thickness and IL-1 β expression. Taken together, these results demonstrate efficient and biologically effective MNA delivery of anti-TNF- α to the intradermal microenvironment

of the skin in mice and humans, and support the development of MNA mediated antibody delivery for clinical applications.

5.2.2. Introduction

A variety of autoimmune mechanisms result in localized inflammatory skin disease characterized by dysregulated cytokine expression in the cutaneous microenvironment. In particular, localized overexpression of tumor necrosis factor- α (TNF- α), a central mediator of inflammation, has been associated with a broad range of autoinflammatory dermatosis and is a rational target for therapeutic inhibition.⁵⁴⁻⁵⁷ TNF- α specific neutralizing antibodies have been particularly effective in treating inflammatory diseases by selectively binding to soluble TNF- α and thereby reducing TNF- α receptor activation. While subcutaneous and intramuscular injection of TNF- α -blockers have been shown to effectively mitigate skin inflammation, administration of TNF- α inhibitors by these systemic routes requires relatively high doses to achieve locally effective concentrations in the skin.⁵⁸⁻⁶² These relatively high systemic doses of TNF- α inhibitors can result in non-specific immune suppression that has been associated with increased infection rates and a variety of adverse events.⁶³⁻⁶⁴ This trade off in efficacy versus off-target immunosuppression limits both efficacy and the broader applicability of TNF- α inhibitors.⁶⁵

Topical administration of immunosuppressive agents has considerable advantages over systemic delivery. However, effective topical administration requires penetration of the stratum corneum, the thick outer barrier of the skin, and localization of the therapeutic agent in the intradermal region. Topically applied corticosteroids can be used to effectively

treat inflammatory skin diseases. With molecular weights between 200–500 Da, corticosteroids penetrate the stratum corneum which is generally considered to be permissive to molecules of less than 500 Da.⁶⁶ However, due to their low molecular weight, corticosteroids have a short residence time in the skin and quickly diffuse into the blood stream. This necessitates repeated applications and frequently long-term use that can lead to undesirable sequelae including loss of skin tone, deterioration of skin cells, and increased risk of infection. On the other hand, antibody therapeutics, typically in the 150 kDa range, are not effective when administered topically as skin penetration is poor due to their high molecular weight. Interestingly, results from topical application of anti-TNF- α in the setting of an already breached skin barrier demonstrate their potential effectiveness if penetration limitations can be overcome. For example, topical application of infliximab was shown to be a promising strategy to improve healing in diabetic skin ulcers.⁶⁷

Over the last decade, a number of approaches have been developed for transdermal delivery of therapeutics.⁶⁸⁻⁷² Most are being developed for transdermal delivery for systemic dosing and are geared towards small molecule drugs and macromolecules smaller than an antibody. Of these techniques, thermal ablation and microneedles have been most successful in the delivery of larger macromolecules. Thermal ablation is a technique in which the skin is heated up to or above 100 °C for microseconds to milliseconds to selectively disrupt the stratum corneum. Thus far, although this technique has demonstrated some success in animal models, general variability in skin thickness and integrity will likely limit the broad application of this technique.⁷⁰

Dissolvable microneedle arrays (MNAs) are transdermal delivery systems designed to mechanically penetrate the stratum corneum.⁷³ A number of micro-fabrication techniques has been developed to create polymer MNAs that can incorporate drug and fully dissolve in skin to deliver therapeutics in a minimally invasive manner.⁷⁴⁻⁷⁵ *In vivo* and *in vitro* studies of MNAs loaded with biologics greater than 500 Da supported effectiveness and safety for intradermal drug delivery.⁷⁶⁻⁷⁷ Several laboratories, including our own, have demonstrated the use of dissolvable MNAs to deliver vaccines with improved efficiencies, enabling far lower required antigen doses compared to traditional intradermal needle injections.⁷⁸⁻⁸⁰ We have previously described the use of micromilling/spin-casting technique to develop microneedle arrays with unique microneedle and array geometries designed for precise and specific drug delivery to human skin.⁸⁰ The unique advantages of dissolvable polymer MNAs suggest that they could be used to effectively deliver anti-TNF- α intradermally for localized treatment of inflammatory skin disease.

In this paper, we describe the fabrication of MNAs with anti-TNF- α integrated into obelisk-shaped microneedles designed for optimal human skin penetration. Importantly, different from our earlier work where the entire microneedle body and the backing layer was filled with the cargo, in the present work, the fabrication process is modified to integrate the cargo only in the apex (tip) of the obelisk microneedles, enabling efficient, more controlled, and cost effective drug delivery. These MNAs delivered anti-TNF- α antibodies to the dermis of human skin with clinically applicable release profiles, and anti-TNF- α MNA treatment reduced key indicators of inflammation in a murine model of psoriasiform dermatitis. Taken together, our results support the clinical development of MNA delivered TNF inhibitors for the treatment of localized inflammatory skin diseases.

5.2.3. Materials and Methods

5.2.3.1. Fabrication of tip-loaded dissolvable microneedle arrays

Our previous study demonstrated that dissolvable MNAs with obelisk shape microneedles have considerably better insertion and cargo delivery characteristics than those with traditional microneedle geometries, such as pyramidal microneedles.⁸⁰ In this work, the MNA design utilized obelisk microneedle geometry to deliver TNF- α inhibitors. A critical departure from previously demonstrated fabrication approach is that the microneedles of MNAs used in this study are tip loaded with the bioactive cargo (anti-TNF- α) for delivering them to the targeted skin sites. The overall approach used for fabrication of tip-loaded dissolvable MNAs is graphically presented in Fig 5.13. The approach involves three steps: (a) creation of mastermolds from a wear resistant and easily machinable polymer using the mechanical micromilling process; (b) fabrication of production molds using mastermolds through elastomer molding; and (c) fabrication of tip loaded dissolvable MNAs from production molds using two-step spin-casting technique: (c.1) the sufficient amount of bioactive cargo is loaded into the elastomer mold, and centrifuged at the appropriate temperature and speed into the microneedles. After removal of excess cargo, centrifuging was continued until (only) the tip portions of the microneedles of production molds contain the dry antibody cargo. Next, (c.2) the structural material of MNAs in hydrogel form is loaded into the elastomer molds, and centrifuged at prescribed temperature and speed until the full density, dry, tip-loaded MNAs are obtained. Currently in our laboratories we are scaled to fabricate 500+ microneedle arrays in a 6 hour day. The fabrication process is readily scalable using industrial grade equipment and automation to

dramatically increase output for clinic applications. The fabrication process facilitates easy and rapid changes in geometric and material parameters so that application-specific optimized microneedle array designs can be achieved.

5.2.3.1.1. Fabrication of mastermolds and elastomer production molds

The mastermold geometry, shown in Fig.1, includes four 10x10 MNAs with obelisk geometry microneedles as well as channels that surround each array. The channels are intended to become raised pockets in the production molds to serve as a reservoir for both bioactive cargo and the structural material during the spin-casting process. The width, height, and apex angle of the obelisk shape microneedles were selected to be 210 μm , 700 μm , and 30°, respectively. The tip-to-tip distance of microneedles within an array of 10x10 was 650 μm . A fillet with radius of 35 μm was created at the base of each microneedle, since our previous study has shown that fillets considerably increase the effective strength of the microneedles during insertion.⁸⁰ The mastermolds were created from poly (methylmethacrylate) (PMMA, 8560K274, McMaster Carr) using the mechanical micromilling technique performed within a precision miniature machining tool (MMT) using micro-scale cutting tools. The production molds were then fabricated from a two component clear curable elastomer SYLGARD® 184 polydimethylsiloxane (PDMS, Dow Corning) through elastomer molding enabled by the polymer mastermolds. The elastomer molding is a well-established method presented in the literature for accurate replication.^{74, 80} Briefly, the uncured material was mixed with a catalyst at 10:1 SYLGARD®-to-curing agent ratio. Subsequently, the mixture was degassed for 10 min in a vacuum chamber and

poured over the mastermold to form an approximately 8 mm layer. This was followed by another step of degassing in the vacuum chamber for 10 min. Next, the mastermold loaded with degassed mixture was placed in an oven, and elastomer was cured at 75 °C for 1 h. The cured PDMS was cooled to room temperature and then separated from the mastermold.

5.2.3.1.2. Preparation of anti-TNF- α formulations

Rat anti-mouse TNF-alpha antibody was purchased from AbD serotec. Antibody was labeled with Cy3 fluorescent dye and purified through extensive dialysis against phosphate-buffered saline (PBS). Final product used for MNAs contained 0.5 mg/mL of anti-TNF- α . Penetration enhancer used for comparative study was dimethyl sulfoxide (DMSO). Treatments were prepared by mixing 50% of DMSO with antibody in PBS. Final product used for topical application with penetration enhancer again contained 0.5 mg/mL of anti-TNF- α .

5.2.3.1.3. Preparation of dissolvable materials for tip-loaded MNAs

To serve as the structural material of the MNAs, a biocompatible and dissolvable polymer, low viscosity sodium carboxymethyl cellulose (CMC, cat# C5678, Sigma-Aldrich, St Louis, MO) was used. The dry powdered form of CMC was dissolved in deionized (DI) water until the CMC-hydrogel with 20 wt% mass concentration was obtained. The CMC-hydrogel was refrigerated at 4 °C for 24 h to equilibrate, and subsequently centrifuged at 2000g for 30 min to remove the occasional bubbles from the hydrogel prior to creating the CMC-MNAs.

5.2.3.1.4. Spin-Casting

Tip-loaded CMC-MNAs with obelisk shape microneedles were fabricated through two-step spin-casting technique using a centrifuge (ThermoFisher Scientific – Heraeus Multifuge X3R with Swinging Bucket Rotor TX 750). First, the tip loading was performed. To this end, 15 μL of antibody cargo was dispensed over each of the PDMS production molds and the production molds were centrifuged for 3 min at 10 $^{\circ}\text{C}$ and at 3500g to fill the obelisk-shaped cavities. Once the production molds were filled completely, the excessive antibody cargo within the reservoir of the production molds was recovered. The production molds were again centrifuged for 30 min at 10 $^{\circ}\text{C}$ and at 3500g to ensure that the dry bioactive cargo is located at the tip portion of the obelisk-shaped cavities in the production molds. After tip loading was successfully achieved, considering the geometry of the production molds, sufficient amount of CMC-hydrogel was loaded over the production molds to fill the obelisk-shaped geometries in the production molds and to form the backing layer of the MNAs. For each tip-loaded MNA, 50 μL of CMC-hydrogel was placed over the each of the production molds. The CMC-hydrogel loaded production molds were then placed in the centrifuge, and centrifuged for 6 h at 10 $^{\circ}\text{C}$ and at 3500g to obtain tip-loaded dissolvable MNAs with above 95% dryness ratio.

5.2.3.1.5. Geometric characterization of fabricated MNAs

The geometries of the fabricated mastermolds and tip-loaded CMC-MNAs were observed from environmental scanning electron microscope (ESEM-Quanta 600) and bright light field microscope images. Furthermore, the production molds

were imaged using a bright field microscope to investigate tip loading. To better demonstrate the presence of Cy3-labeled-anti-TNF- α at the tip portion of the CMC-MNAs, MNAs were imaged using a Nikon inverted fluorescence microscope equipped with a charge-coupled device (CCD) camera and a Nikon transmission fluorescent microscope.

5.2.3.2. The integrity and activity of anti-TNF- α

5.2.3.2.1. Anti-TNF- α amount in tip-loaded CMC-MNAs

To determine the amount of anti-TNF- α in tip-loaded CMC-MNAs, Rat IgG ELISA kit was purchased from Abcam (Cambridge, England) and used according to the kit instructions. MNAs were dissolved in 0.1 M sodium bicarbonate for 15 s at 0.05 mL/patch and diluted 10x for the assay in assay diluent.

5.2.3.2.2. Binding affinity measurements

To test the activity of anti-TNF- α in tip-loaded CMC-MNAs, binding affinity was determined based on methods previously described by our laboratory using the ForteBio Octet QK system, which measures optical thickness of a streptavidin-functionalized sensor tip.⁸¹⁻⁸² Recombinant mouse TNF-alpha (R&D systems Inc, Minneapolis, MN) was biotinylated using EZ link sulfo-NHS-LC-LC-biotin (Thermo Fischer Scientific, Rockville, IL), which binds strongly to the streptavidin tip. Streptavidin sensor tips were hydrated in PBS for at least 5 minutes prior to starting the experiment. The experimental parameters consisted of the following dipping sequence: PBS baseline, 1 min; TNF- α loading, 2 min; biocytin quench (10 μ g/mL), 3 min; PBS wash, 3 min; PBS baseline 2, 3 min; antibody

association (as fresh antibody or dissolved MNA), 15 min; PBS dissociation, 15 min. The association step used a series of at least 3 dilutions of dissolved MNAs. The association rate constants, dissociation rate constants, and equilibrium dissociation constants were determined by using the Fortebio data analysis program, which calculated these values by generating a line of best-fit for the binding isotherm.

5.2.3.3. Topical and MNA-directed intradermal delivery of TNF- α -inhibitors to ex vivo human skin

5.2.3.3.1. Preparation of ex vivo human skin explants

Human skin explants used in this study were prepared based on the standard methods previously described.⁸³ Briefly, *ex vivo* human skin samples were obtained as freshly excised plastic surgery residuals under IRB approval and used according to University of Pittsburgh Medical Center guidelines. Human skin samples were prepared using dermatome to a thickness of approximately 2 mm. The resulting human skin samples were comprised of unaltered epidermis and a thin layer of underlying dermis, and maintained as explants in normal physiological state by culture at an air-fluid interface.

5.2.3.3.2. Image analysis of topical and MNA-directed intradermal delivery of TNF- α -inhibitors to human skin explants

To image the intradermal delivery of anti-TNF- α from tip-loaded, obelisk-shaped dissolvable MNAs to human skin explants, tip-loaded CMC-MNAs encapsulating Cy3-labeled anti-TNF- α were fabricated through the spin-casting

technique as described above. Prior to application of MNAs to the human skin explants, they were imaged using ESEM. Subsequently, MNAs were applied to human skin explants using a custom-made spring-loaded applicator. Considering the thickness of the skin samples, the travel distance of the impact head of the applicator was limited to 1.5 mm. After 30 min, MNAs were removed and the final shapes of the dissolved MNAs were imaged by ESEM. The targeted human skin samples were then excised and imaged using a Nikon inverted fluorescence microscope fitted with a CCD camera, at 4x optical magnification to show the pattern of the fluorescent Cy3-labeled deposited microneedle materials into the human skin samples.

For qualitative histological assessment of intradermal delivery of anti-TNF- α from tip-loaded CMC-MNAs to human skin, tip-loaded CMC-MNAs were embedded with Cy3-labeled anti-TNF- α and applied to human skin explants as described above. Similarly, Cy3-labeled anti-TNF- α with DMSO solvent was applied to human skin explants topically to demonstrate that even potent solvents do not help penetrate stratum corneum. Subsequently, the targeted human skin samples were fixed in 2% paraformaldehyde followed by immersion in sucrose solution, with 3 changes of solution over 24 hours. Tissue sections were then flash frozen in optimum cutting temperature (OCT) histology compound, and cryo-sectioned into approximately 10 μ m thick cross-sections. The sectioned human skin samples were counter-stained using nuclear DAPI fluorescent dye. The stained sections were then imaged using a Nikon transmission fluorescent microscope to detect the fluorescent microneedle-materials (Cy3-labeled-anti-TNF- α) into the

cross-sections of the human skin explants and fluorescent topical-materials at the surface of the stratum corneum.

5.2.3.3.3. Quantitative assessment of MNA-directed delivery of TNF- α - inhibitors to ex vivo human skin

To quantitatively evaluate the intradermal delivery of anti-TNF- α and kinetics of the intradermal delivery from tip-loaded CMC-MNAs to *ex vivo* human skin, tip-loaded CMC-MNAs with embedded Cy3-labeled anti-TNF- α were prepared through the spin-casting technique as described above. Subsequently, MNAs were applied to human skin explants in six replicates for each treatment of 5, 10, 20, and 40 min using a spring-loaded applicator and then removed. The targeted skin areas were sampled using an 8 mm biopsy punch. The deposited Cy3 fluorescence dye was released from the skin samples by ProteaseK digest at 37 °C overnight. The cleared samples were dispensed into 96-well plates in quadruplicates and quantitated by spectro-fluorometry at 540/570 nm excitation and emission wavelength. The kinetics of the intradermal delivery of anti-TNF- α from tip-loaded CMC-MNAs to human skin explants was expressed as the percentage of Cy3-labeled-anti-TNF- α content of the MNAs.

5.2.3.4. Animal studies

Female Balb/c mice were purchased from The Jackson Laboratories (Bar Harbor, Maine) and used between the ages of 6 and 12 weeks. Mice were housed under specific-pathogen-free conditions and treated according to the University of Pittsburgh's institutional animal care guidelines. To induce a psoriasiform inflammatory response 62.5

mg of Aldara™ cream (3M pharmaceuticals) containing 5% imiquimod (wt/wt) was applied to the shaved backs of mice daily for 4 days. On day 1 and 3 mice were treated with CMC-MNAs delivering anti-TNF- α . On day 5 mice were sacrificed and cutaneous tissues were collected for histological analysis and qRT-PCR.

5.2.3.5. Real-time quantitative RT-PCR

Total RNA was extracted from ears utilizing TRI-reagent (Molecular Research Center; Cincinnati, OH) and reverse transcribed using the QuantiTect Reverse Transcription Kit (Qiagen; Hilden, Germany) according to manufacturers' instructions. Quantitative real-time PCR was performed utilizing the Taqman Gene Expression Master Mix (Life Technologies) according to manufacturer's instructions with IDT PrimeTime qPCR assays (IDT; Coralville, IA) specific for GusB (endogenous control) and IL-1 β . Reactions were run and analyzed on a Step One Plus sequence detection system (Applied Biosystems). Expression levels were normalized based on the 2- $\Delta\Delta C_t$ method.

5.2.3.6. Cutaneous microscopy

To assess cutaneous histology, cross-sections of mouse ears were prepared and stained as previously described.⁸⁴ Briefly, frozen cross-sections were embedded in Tissue-Tek OCT (Miles Laboratories; Elkhart, IN) and snap frozen in pre-chilled methyl-butane (Sigma Aldrich). Cryostat sections (8 μ m) were mounted onto slides pre-treated with Vectabond (Vector Laboratories; Burlingame, CA), air-dried, and fixed in 96% EtOH and used for H&E staining. Images were acquired using an Olympus Provis AX-70 microscope system (Olympus; Center Valley, PA) with FluoView 500 software.

5.2.3.7. Statistical analysis

Comparison of 2 groups was performed by a 2-tailed Student's t-test. A p-value of < 0.05 was considered statistically significant.

5.2.4. Results and Discussions

5.2.4.1. Fabrication of MNAs with tip-loaded cargo.

Critical parameters influencing the feasibility of MNA delivery include penetration and delivery efficiency. The obelisk needle shape we utilize maximizes the proportion of the needle body that enters the skin. This results in an increase in needle volume delivered to the skin and a higher delivery capacity per unit surface area. For example we have shown that MNAs with obelisk needle geometries deliver 4 times more cargo for the same array configuration and microneedle height than pyramidal needle geometries.⁸⁰ We reasoned that further efficiencies could be achieved by optimizing the proportion of drug integrated in the skin penetrating portion of the needle body. Thus, a fabrication method that results in drug localized in the needle apex (or tip) would result in a higher proportion of drug delivery. This efficiency of drug delivery is particularly important when the therapeutic approach requires delivery of a bioactive agent that is rare or expensive, such as an antibody.

Dissolvable MNAs that integrate the antibody cargo primarily in the tip portion of the needles (referred to as “tip-loaded”) were fabricated using a three-stage fabrication technique through mastermold (positive) to production mold (negative) to final dissolvable MNAs (positive). This is schematically depicted in Fig 5.13. The mastermolds were

created from a PMMA workpiece using the mechanical micromilling process to circumvent the expensive, equipment sensitive, and geometrically limited SU-8 based lithography and laser etching techniques.⁸⁰ PMMA was chosen as the mastermold material since it is easy to machine and provides good wear resistance during fabrication of production molds through elastomer molding (Fig. 5.13.A). An ESEM image of an entire fabricated mastermold and a high magnification insert of individual obelisk-shaped microneedles are shown in Fig 5.14.A. The PMMA mastermolds were then used to fabricate several flexible production molds from PDMS through elastomer molding (Fig. 5.13.B). PDMS was selected as the production mold material due to its flexibility and low cost.

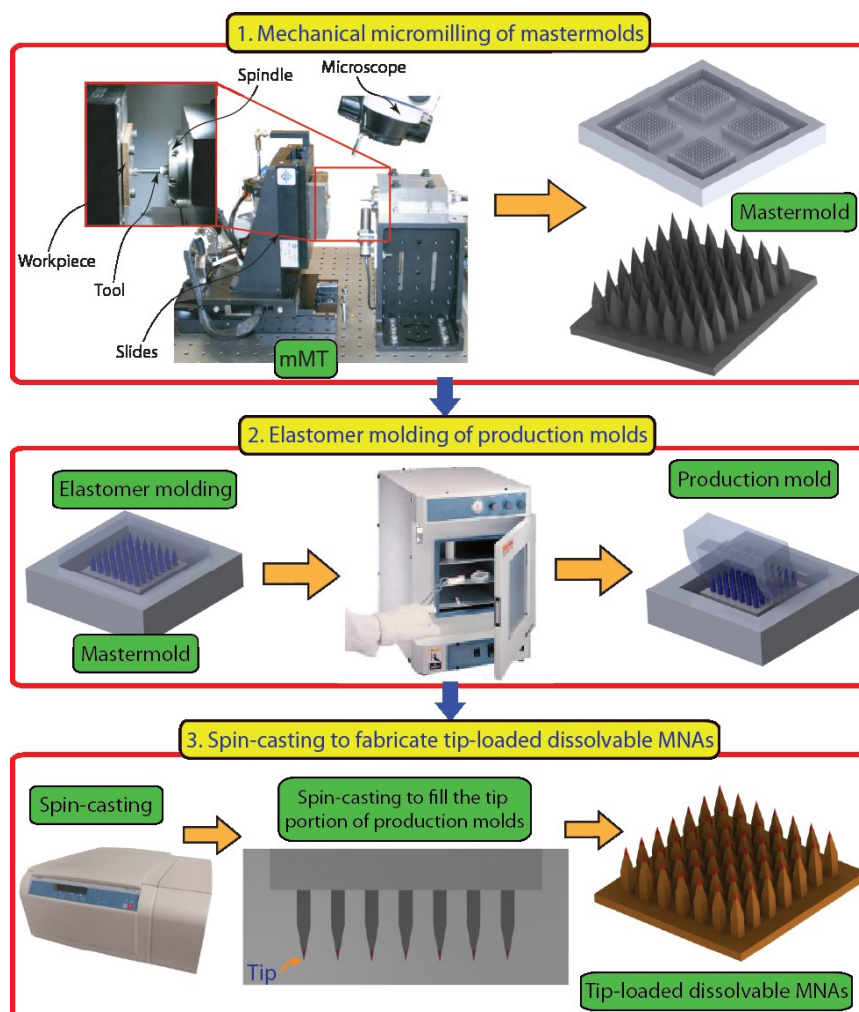


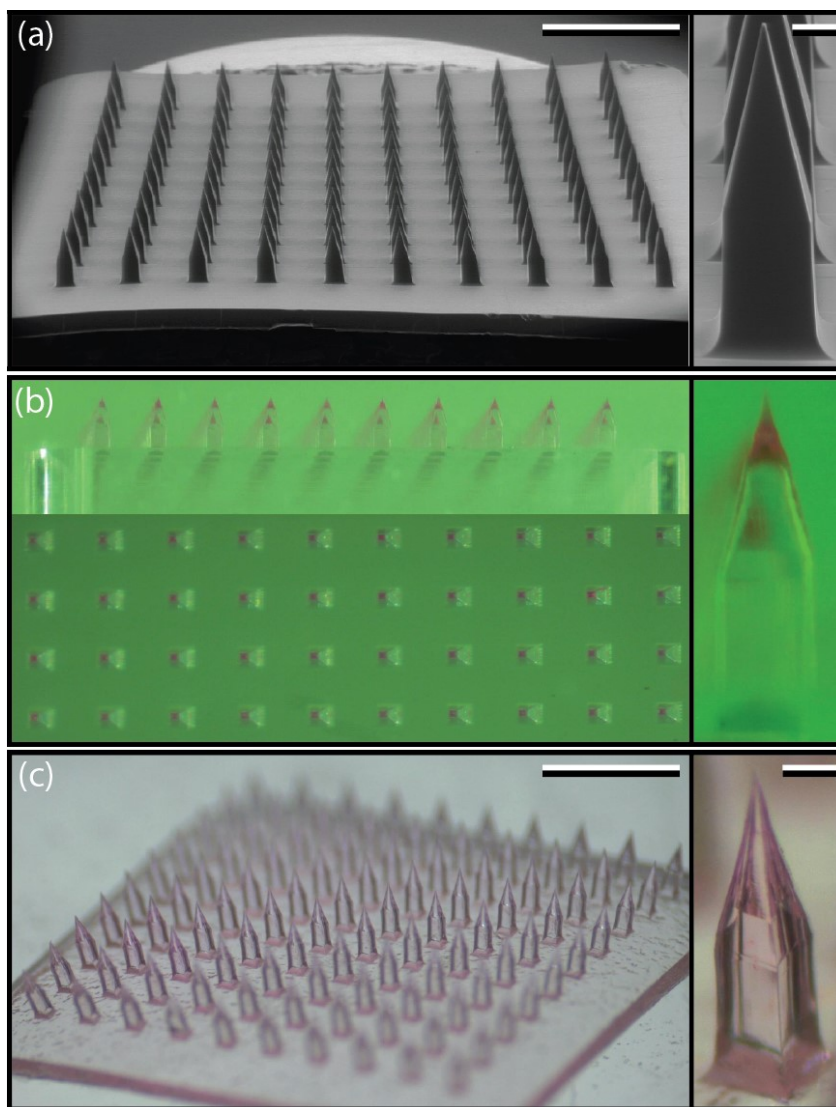
Figure 5.13 Description of the micromilling/spin-casting based fabrication approach used for creating tip-loaded dissolvable microneedle arrays. Three-steps: (a) Mechanical micromilling of mastermolds. (b) Elastomer molding of production molds. (c) Spin-casting to localize anti-TNF- α in the apex of obelisk microneedles and fabricate tip-loaded dissolvable MNAs.

MNAs with tip-loaded anti-TNF- α were fabricated from low viscosity sodium carboxymethyl cellulose (CMC) using PDMS production molds through a two-step spin-casting technique (Fig. 5.13.C). This fabrication process enables room temperature processing throughout, increasing the likelihood that the conformationally dependent bioactivity of the integrated anti-TNF- α would be preserved. Further, CMC was chosen as the structural material for the MNAs because it is a biodissolvable, mechanically strong, and water soluble polymer.^{80, 84} Further, it can be intradermally injected with no toxic or

inflammatory effects, which facilitates repetitive treatments for autoinflammatory diseases with relapsing-remitting nature.⁸⁵ Furthermore, the general characteristics of the CMC based-MNAs shown by us and other laboratories support drug stability within the device for a broad range of bioactive cargos, a feature particularly useful for applications to populations with limited resources or disadvantaged socio-economic conditions.^{8, 86-88} In the first step, the bioactive cargo was loaded into the elastomer mold and forced into the tips of the microneedle wells by centrifugation. Then, CMC hydrogel was layered into the elastomer molds that were centrifuged again to form an anti-TNF- α integrated CMC tip. Fig. 5.14.B shows top-view (en face) and front-view bright light microscope images of the production mold after tip loading, and an image of an individual tip-loaded microneedle cavity. In this image, fluorescent labeling of anti-TNF- α with Cy3 enables visualization of the antibody during the fabrication process, and reveals uniform tip loading visible within the production mold (Fig. 5.14.B). After tip loading, production molds were loaded with 20 wt% CMC hydrogel to both fill the obelisk-shaped microneedle cavities, and to form the backing layer of the MNAs. To avoid formation of voids between layers in the microneedles that could potentially decrease their mechanical strength, low viscosity CMC was used during this portion of the fabrication process.

Bright field microscope images of the final tip-loaded MNA demonstrate localization of Cy3-labeled anti-TNF- α in the needle tips, as further demonstrated by the insert showing a single needle from the MNA at high magnification (Fig. 5.14.C). Tip localization of Cy3-labeled anti-TNF- α was confirmed by fluorescence microscopy analysis. MNAs with embedded Cy3-labeled anti-TNF- α were imaged using a Nikon inverted fluorescence microscope fitted with a CCD camera and a Nikon transmission

fluorescent microscope. En face views of an intact MNA (Fig. 5.14.D), and high magnification images of individual obelisk-shaped microneedles demonstrate the presence and uniformity of Cy3-labeled anti-TNF- α cargo in the needle tips (Fig. 5.14.E,F).



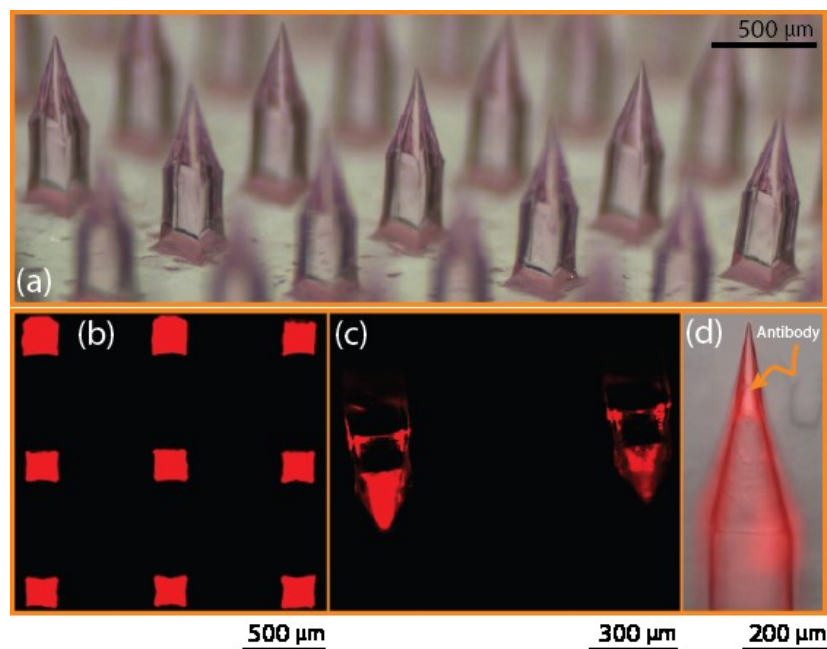


Figure 5.14 Tip-loaded dissolvable MNAs created using the micromilling/spin-casting technique for intradermal delivery of anti-TNF- α . (a) ESEM images of the PMMA mastermold. Scale bars on the image of array and individual microneedle correspond to 1 mm and 100 μm , respectively. (b) Optical microscope images of the production mold after tip loading with bioactive cargo. (c) Bright field microscope images of the tip-loaded MNAs. Scale bars on the image of array and individual microneedle correspond to 1 mm and 100 μm , respectively. (d) Inverted fluorescence microscope image of a dissolvable MNA tip-loaded with Cy3-labeled anti-TNF- α . (e) Inverted fluorescence microscope image of the individual tip-loaded dissolvable MNAs. (f) Merged bright field and fluorescence microscope image of the tip portion of the individual microneedle.

5.2.4.2. Binding affinity of MNA integrated anti-TNF- α

The ability of anti-TNF- α to specifically bind their TNF- α ligand depends on the integrity of their conformationally dependent antibody binding sites. This tertiary protein structure is relatively unstable and susceptible to changes in temperature, pH, mechanical stress, and other factors. We designed the fabrication process with these limitations in mind, utilizing compatible materials and room temperature processing throughout. To evaluate the specific binding capacity of the MNA integrated anti-TNF- α , MNA microneedles were dissolved in 0.1 M sodium bicarbonate solution and anti-TNF- α quantitated by IgG ELISA. Anti-TNF- α recovered from MNAs and quantified with an IgG

ELISA was $1.93 \pm .11$ μg of the 2 μg loaded per MNA. The purchased ELISA kit was validated to determine if it detected fully intact IgG or if it could also detect denatured and reduced IgG. Less than 1% of the reduced and denatured antibody was detected, which means that 99% of the antibody detected using this ELISA kit is intact, which is important to both MNA loading quantification and proper calibration of binding affinity measurements. Binding affinity of the MNA recovered anti-TNF- α was determined by measuring the optical thickness of a streptavidin-functionalized sensor tip using the ForteBio Octet QK system,^{79,82} using fresh anti-TNF- α (not MNA integrated) as a positive control. Characteristic association and dissociation curves of TNF- α with anti-TNF- α from anti-TNF- α loaded MNA vs. fresh anti-TNF- α show similar binding characteristics, with differences in apparent thickness attributed to slight differences in antibody concentrations extracted from the MNAs (Fig 5.15.A). Data were normalized to the amount of antibody in each MNA, measured by IgG ELISA. Curves were fit using the ForteBio Octet analysis software and K_D values were averaged for each MNA tested, with a total of 3 MNAs tested per group (Fig 5.15.B). MNA integrated anti-TNF- α demonstrated a similar though marginally decreased binding affinity compared to fresh unintegrated, which had an average K_D of 9.33 ± 3.18 pM, as indicated by the higher average K_D of 50.6 ± 5.84 pM. Our observation that MNA integrated anti-TNF- α maintained picomolar binding affinities supports our hypothesis that these MNAs can deliver functionally active and biologically effective and the feasibility of MNA mediated antibody delivery for clinical applications.

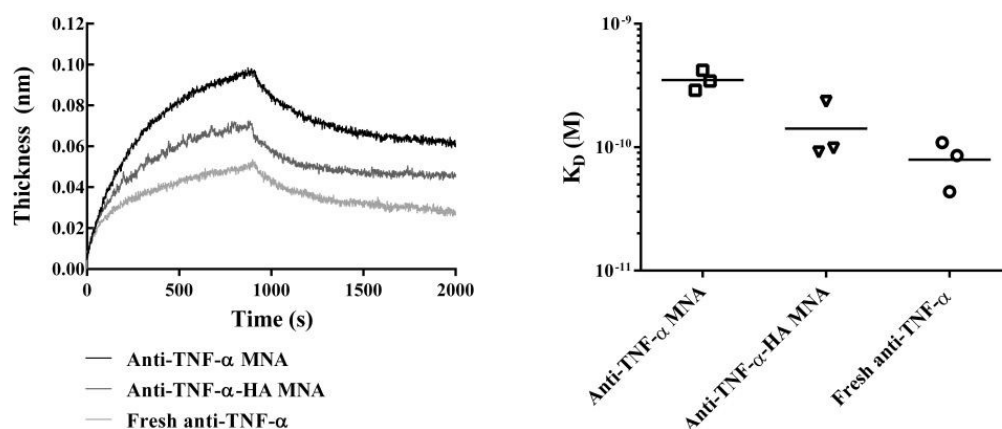


Figure 5.15 TNF- α binding affinity for anti-TNF- α using biolayer interferometry. Biolayer interferometry was used to measure binding affinity of fresh or previously encapsulated anti-TNF- α with TNF- α immobilized on the sensor tip to characterize the effects of processing on antibody binding affinity. (a) Characteristic binding curves of fresh and previously encapsulated anti-TNF- α show similar binding kinetics in real time. (b) K_D values extracted from binding curves using a 1:1 binding isotherm model show slight increases in K_D for anti-TNF- α previously encapsulated in MNA ($K_D = 50.6 \pm 5.84$ pM) compared to fresh anti-TNF- α ($K_D = 9.33 \pm 3.18$ pM), corresponding to a slight decrease in binding affinity.

5.2.4.3. MNA-directed delivery of anti-TNF- α to human skin.

To investigate delivery characteristics, tip-loaded MNAs carrying integrated Cy3-labeled anti-TNF- α were fabricated as described above. Human skin explants were prepared from freshly excised human skin by methods we previously described.⁸³ These MNAs were applied to living human skin explants using a spring-loaded applicator, and removed 30 min later. Images of these MNAs before application (Fig 5.16.A) and after removal (Fig 5.16.B) from human skin demonstrate the nearly complete dissolution of the obelisk microneedles extending to the base, and corresponding deposits of Cy3-labeled anti-TNF- α in the targeted skin (Fig 5.16.C). The nearly complete insertion of these microneedles is enabled by the obelisk design that minimizes insertion forces and skin resistance, and improves dissolution characteristics compared to more commonly used alternative needle geometries, thereby enabling increased delivery efficiencies.⁸⁰

For skin therapeutics, drug delivery through the stratum corneum and into the epidermal and dermal microenvironments is essential for biologic function. In the case of the MNAs we have developed, the mechanism of delivery is mechanical penetration of the top layers of the skin, followed by dissolution of the needles in the aqueous environment of the skin. The MNAs are fabricated from biodissolvable (water-soluble) materials (polymers) with drug within the microneedle matrix. These needles are strong enough in their dry-state to penetrate the stratum corneum and epidermis, and then rapidly dissolve in the fluid environment of the skin, thereby releasing embedded drug payload.

To anatomically evaluate the delivery of Cy3-labeled anti-TNF- α into human skin, MNAs with integrated Cy3-labeled anti-TNF- α were fabricated and applied to human skin explants as described previously. The targeted human skin was cryosectioned and imaged using a Nikon transmission fluorescent microscope. Histology demonstrates microneedle cavities penetrating through the epidermis into the dermis, and Cy3-labeled anti-TNF- α colocalized throughout the periphery of the microneedle cavity and the cavity base (Fig 5.16.D-F, DAPI nuclear stain, Cy3-labeled anti-TNF- α , and overlay, respectively). In contrast and as expected, Cy3-labeled anti-TNF- α applied with DMSO as a solvent was restricted to the skin surface (Fig 5.16.G-I). These results demonstrate MNA delivery of anti-TNF- α to the epidermis and dermis of human skin.

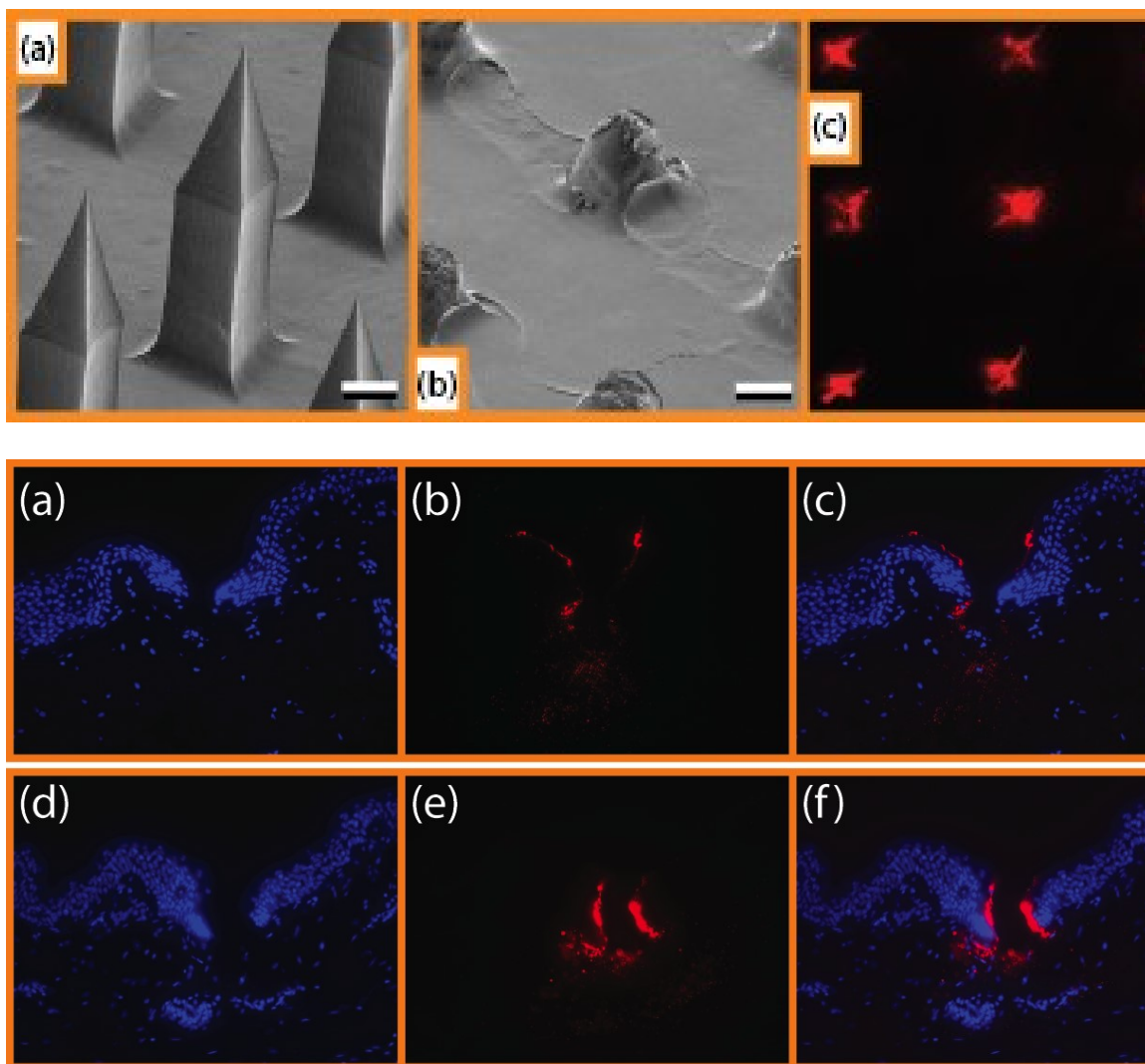


Figure 5.16 Microneedle penetration, deposition of cargo and intradermal delivery of anti-TNF- α from tip-loaded CMC-MNAs. (a) ESEM image of the microneedle arrays before application. Scale bars correspond to 100 μ m. (b) ESEM image of the microneedle arrays after 30 min of application. Scale bars correspond to 100 μ m. (c) Inverted fluorescence microscope image of Cy-3 labeled microneedle traces on living human skin explants. 4 x optical magnification. (d, e, f) Intradermal delivery of anti-TNF- α from tip-loaded CMC MNAs. 20x optical magnification. (g, h, i) Intradermal delivery of anti-TNF- α from topical application with DMSO. 20x optical magnification. (d, g) Fluorescence microscope image of the DAPI stained human skin insertion sites. (e, h) Fluorescence microscope images of the Cy3-labeled antibody cargo. (f, i) Fluorescence microscope composite images that demonstrate delivery cavities penetrating the epidermis and upper dermis, and delivery of fluorescent cargo of the microneedles.

5.2.4.4. Kinetics of MNA-directed anti-TNF- α delivery to human skin.

To evaluate the time-dependent intradermal delivery profile of anti-TNF- α from tip-loaded anti-TNF- α MNAs, MNAs were fabricated with Cy3-labeled anti-TNF- α and

applied to human skin as described previously, and then removed after the indicated time periods. MNA targeted skin sites were biopsied and transfer efficiency and kinetics of Cy3-labeled anti-TNF- α were determined by measuring Cy3 fluorescence in the target skin samples. The release profile of Cy3-labeled anti-TNF- α from tip-loaded dissolvable MNAs is shown in Fig. 5.17. Within 5 minutes, greater than 50% of the integrated antibody was delivered to the skin. Delivery peaked between 10 and 20 min, with greater than 75% of the MNA integrated antibody delivered to the skin microenvironment.

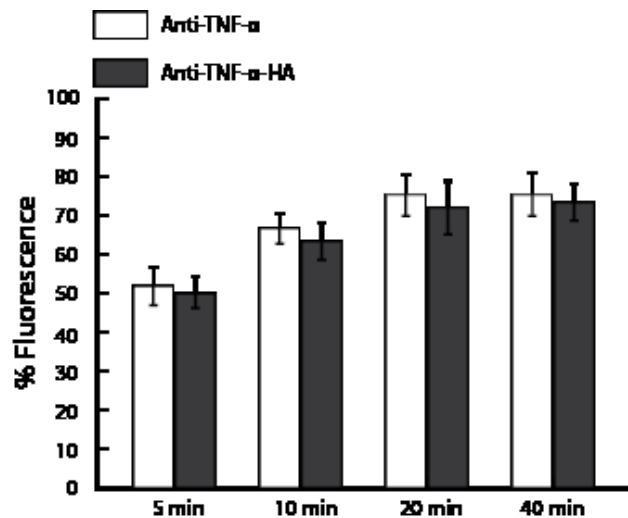


Figure 5.17 Intradermal release profiles of anti-TNF- α from tip-loaded CMC-MNAs. Tip-loaded MNAs created as described above were applied to living human skin for the indicated time intervals and then removed. Targeted skin was excised and assayed for Cy3-fluorescence content by spectrofluorometry. Standard deviation values were from 6 replicates.

5.2.4.5. MNA-directed anti-TNF- α treatment of psoriasiform dermatitis.

To evaluate the therapeutic potential of MNA delivered anti-TNF- α , we utilized an established murine model of psoriasiform dermatitis.⁸⁹⁻⁹¹ In this model, repeated delivery of the TLR7 agonist Aldera induces inflammation that results in immune cell infiltration, KC proliferation and enhanced dermal vascularity.⁹² This results in a red, scaly skin phenotype clinically similar to human psoriasis, and shared histologic features including

epidermal hyperplasia, inflammatory infiltrates, and increased expression of the proinflammatory mediator IL-1 β .⁸⁹ Mechanistically, Aldara induces a local shift in the immunoregulatory balance of the skin toward a proinflammatory environment that is associated with psoriatic disease. Localized delivery of immune modifiers has the potential to directly treat autoimmune disease, and to tip the immunoregulatory balance away from a pro-inflammatory environment and toward a more “tolerant” environment. In this way, a locally delivered immune modifier can have direct immediate effects on disease symptoms, in the context of the potential for longer term therapeutic restoration of immune imbalance.

Potent clinical treatments have been developed based on inhibitors of tumor necrosis factor- α (TNF- α), a central mediator of pro-inflammatory responses. Regrettably, efficacy can be limited by off-target side effects of systemically administered TNF- α inhibitors and have included side effects including increased rates of tuberculosis, fungal infections, and lymphoma. By delivering the TNF- α inhibitors locally, it may be possible to decrease the total dose administered to the patient, and systemic exposure. This in turn could reduce side effects while, at the same time, increasing the amount of active therapeutic at the site of interest. As such, our approach could potentially provide the basis for effective treatment of many inflammatory diseases by targeting local immune dysfunction.

Briefly, to induce a psoriasiform inflammatory response AldaraTM cream (3M pharmaceuticals) containing 5% imiquimod was applied to the shaved backs of mice daily for 4 days. First, it was confirmed that application of empty MNAs without anti-TNF- α does not have any effect on the Aldara response (data not shown). Next, on day 1 and 3

mice were treated with anti-TNF- α integrated MNAs. Notably in this application the maximum systemic exposure, which would assume that all delivered drug reached the blood, would be approximately 10 fold less than systemic concentrations commonly reached in humans, and another 5,000 fold less in human circulation. On day 5 mice were sacrificed and cutaneous tissues were collected for histological analysis and qRT-PCR. On day 5 a pronounced decrease in psoriasiform inflammation was observed that was characterized by a significant decrease in cellular infiltrates and epidermal thickness at treated sites compared to un-treated control sites. (Fig 5.18.A-C). Moreover, following treatment there was a significant decrease in IL-1 β mRNA expression in treated skin compared to untreated skin (Fig 5.18.D). Taken together, these data demonstrate that MNA delivered anti-TNF- α are biologically active and have a therapeutic effect in an animal model of psoriasiform dermatitis.

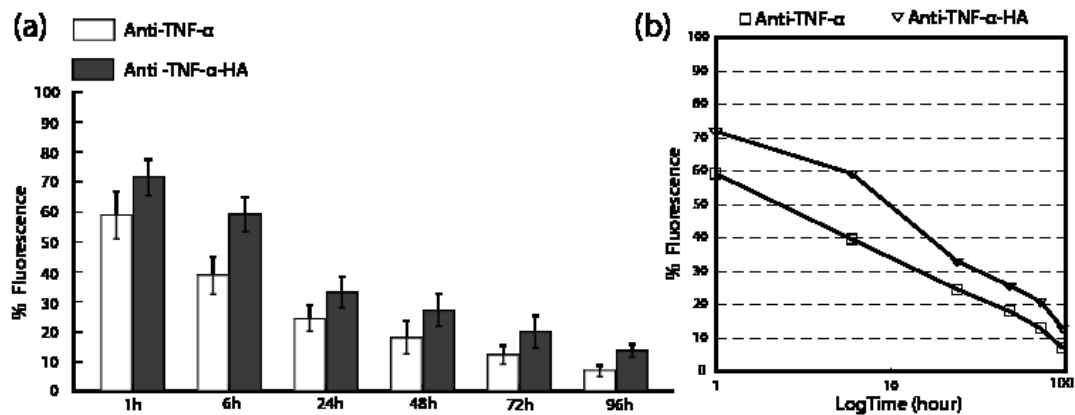


Fig.6. MNAs delivering TNF- α antibodies abrogate the development of psoriasiform dermatitis. Balb/c mice were treated with Aldara for 4 days. On day 1 and 3 mice were treated with MNA patches delivering TNF- α antibody or Aldara alone as a negative control. **(a)** H&E staining of cutaneous cross-sections collected on day 5. **(b)** Quantitation of cellular infiltrate. Each symbol represents an individual mouse with 10 high-powered fields averaged per mouse. The bar represents the mean of three mice. Asterisks designate a significant difference between indicated treatment groups, *** $p < 0.001$, ** $p < 0.01$. **(c)** Quantitation of epidermal thickness, bars represent the mean thickness of the epidermis from 15 high-powered fields \pm S.D. **(d)** Fold-change in IL-1 β mRNA expression detected on day 5 by qRT-PCR. Fold-change was determined using the $2^{-\Delta\Delta C_t}$ method in which samples were normalized to GusB endogenous

control. Each symbol represents an individual mouse with each sample ran in triplicate. The bar represents the mean of three mice.

5.2.4. Conclusion

Therapeutic antibodies are being widely developed for the treatment of a broad spectrum of human diseases. Typically these antibodies are administered systemically, requiring high systemic doses to achieve locally effective concentrations. Therapeutically effective systemic dosing can result in off target effects and adverse events that reduce safety and limit optimal dosing/effectiveness and broader applicability. Development of locally targeted delivery strategies has the potential to overcome these limitations, resulting in safer and more effective therapies. This is particularly true for inflammatory skin diseases. The skin has proven to be a formidable barrier to topical antibody delivery.

Here we demonstrate a dissolvable MNA delivery strategy for therapeutic antibodies. Using a unique fabrication process that integrates the antibody cargo into the MNA scaffold while preserving the tertiary protein structure necessary for antibody ligand binding, we show that MNA integrated antibodies have similar binding affinities as non-integrated control antibodies. Further, using MNAs with obelisk-shaped microneedles with optimized insertion and delivery characteristics, and a tip loading strategy that concentrates the antibody cargo in the needle tips to increase delivery efficiency and eliminate waste, we demonstrate efficient delivery of anti-TNF- α to the dermis of human skin with clinically applicable release profiles. To evaluate the feasibility of MNA antibody delivery for the treatment of inflammatory skin diseases, we sought to intervene in the localized overexpression of tumor necrosis factor-alpha (TNF- α), a central mediator of

inflammation that has been associated with a broad range of autoinflammatory skin diseases including psoriasis. Using a mouse model of psoriasiform dermatitis, we demonstrate that MNA delivered anti-TNF- α treatment reduced key biomarkers of psoriasiform inflammation including epidermal thickness and IL-1 β expression. Taken together, these results demonstrate efficient and biologically effective MNA delivery of anti-TNF- α to the intradermal microenvironment of the skin in mice and humans, and support the development of MNA mediated antibody delivery for clinical applications.

5.2.5. Acknowledgments

This work was supported by the National Institute of Health Grant R01EB012776. NRW gratefully acknowledges support from the Heinz Endowments (C1747).

References

- (1)Billiet, T.; Vandenhaute, M.; Schelfhout, J.; Van Vlierberghe, S.; Dubruel, P., A review of trends and limitations in hydrogel-rapid prototyping for tissue engineering. *Biomaterials* **2012**, 33 (26), 6020-6041.
- (2)Peltola, S. M.; Melchels, F. P.; Grijpma, D. W.; Kellomäki, M., A review of rapid prototyping techniques for tissue engineering purposes. *Annals of medicine* **2008**, 40 (4), 268-280.
- (3)Zorlutuna, P.; Annabi, N.; Camci-Unal, G.; Nikkhah, M.; Cha, J. M.; Nichol, J. W.; Manbachi, A.; Bae, H.; Chen, S.; Khademhosseini, A., Microfabricated biomaterials for engineering 3d tissues. *Adv Mater* **2012**, 24 (14), 1782-804.
- (4)Yeong, W.-Y.; Chua, C.-K.; Leong, K.-F.; Chandrasekaran, M., Rapid prototyping in tissue engineering: Challenges and potential. *Trends in biotechnology* **2004**, 22 (12), 643-652.
- (5)Giudice, E. L.; Campbell, J. D., Needle-free vaccine delivery. *Advanced drug delivery reviews* **2006**, 58 (1), 68-89.
- (6)Kim, Y. C.; Park, J. H.; Prausnitz, M. R., Microneedles for drug and vaccine delivery. *Advanced drug delivery reviews* **2012**, 64 (14), 1547-68.
- (7)Bediz, B.; Korkmaz, E.; Khilwani, R.; Donahue, C.; Erdos, G.; Falo, L. D., Jr.; Ozdoganlar, O. B., Dissolvable microneedle arrays for intradermal delivery of biologics: Fabrication and application. *Pharmaceutical research* **2013**.

- (8)Kim, Y.-C.; Park, J.-H.; Prausnitz, M. R., Microneedles for drug and vaccine delivery. *Advanced drug delivery reviews* **2012**, *64* (14), 1547-1568.
- (9)Segers, V. F.; Lee, R. T., Biomaterials to enhance stem cell function in the heart. *Circulation research* **2011**, *109* (8), 910-22.
- (10)Kuen Yong Lee, K. Y.; Mooney, D. J., Hydrogels for tissue engineering. *Chemical Reviews* **2001**, *101* (7).
- (11)Zimmermann, W. H., Tissue engineering of a differentiated cardiac muscle construct. *Circulation research* **2001**, *90* (2), 223-230.
- (12)Fink, C.; Ergun, S.; Kralisch, D.; Remmers, U.; Weil, J.; Eschenhagen, T., Chronic stretch of engineered heart tissue induces hypertrophy and functional improvement. *The Journal of the Federation of American Societies for Experimental Biology* **2000**, *14*, 669-679.
- (13)Engler, A. J.; Sen, S.; Sweeney, H. L.; Discher, D. E., Matrix elasticity directs stem cell lineage specification. *Cell* **2006**, *126* (4), 677-89.
- (14)Gursel, I.; Balcik, C.; Arica, Y.; Akkus, O.; Akkas, N.; Hasirco, V., Synthesis and mechanical properties of interpenetrating networks of polyhydroxybutyrate-co-hydroxyvalerate and polyhydroxyethyl methacrylate. *Biomaterials* **1998**, *19*, 1137—1143.
- (15)Sun, J.; Xiao, W.; Tang, Y.; Li, K.; Fan, H., Biomimetic interpenetrating polymer network hydrogels based on methacrylated alginate and collagen for 3d pre-osteoblast spreading and osteogenic differentiation. *Soft Matter* **2012**, *8* (8), 2398.
- (16)Brigham, M. D.; Bick, A.; Edward Lo, E.; Bendali, A.; Burdick, J. A.; Khademhosseini, A., Mechanically robust and bioadhesive collagen and

photocrosslinkable hyaluronic acid semi-interpenetrating networks. *Tissue Eng Part A* **2009**, *15*, 1645-1653.

(17)Shah, A. M.; Jung, H.; Skirboll, S., Materials used in cranioplasty: A history and analysis. *Neurosurgical Focus* **2014**, *36* (4), E19.

(18)510(k) summary statement for osteofab patient specific cranial device. Health, C. f. D. a. R., Ed. 2013.

(19)Zopf, D. A.; Hollister, S. J.; Nelson, M. E.; Ohye, R. G.; Green, G. E., Bioresorbable airway splint created with a three-dimensional printer. *New England Journal of Medicine* **2013**, *368* (21), 2043-2045.

(20)Bhatia, S.; Sharma, S., 3d-printed prosthetics roll off the presses. *Chemical Engineering Progress* **2014**, (May), 28-33.

(21)Tumbleston, J. R.; Shirvanyants, D.; Ermoshkin, N.; Januszewicz, R.; Johnson, A. R.; Kelly, D.; Chen, K.; Pinschmidt, R.; Rolland, J. P.; Ermoshkin, A.; Samulski, E. T.; DeSimone, J. M., Continuous liquid interface production of 3d objects. *Science* **2015**, *347* (6228), 1349-1352.

(22)Fullerton, J. N.; Frodsham, G. C. M.; Day, R. M., 3d printing for the many, not the few. *Nature Biotechnology* **2014**, *32* (11), 1086-1087.

(23)Lee, C. H.; Rodeo, S. A.; Fortier, L. A.; Lu, C.; Eriskien, C.; Mao, J. J., Protein-releasing polymeric scaffolds induce fibrochondrocytic differentiation of endogenous cells for knee meniscus regeneration in sheep. *Science Translational Medicine* **2014**, *6* (266), 266ra171.

(24)Derby, B., Printing and prototyping of tissues and scaffolds. *Science* **2012**, *338* (6109), 921-926.

- (25)Murphy, S. V.; Atala, A., 3d bioprinting of tissues and organs. *Nature Biotechnology* **2014**, 32 (8), 773-785.
- (26)Martin, I.; Simmons, P. J.; Williams, D. F., Manufacturing challenges in regenerative medicine. *Science Translational Medicine* **2014**, 6 (232), 232fs16.
- (27)Sinha, G., Cell presses. *Nature Biotechnology* **2014**, 32 (8), 716-719.
- (28)Mannoor, M. S.; Jiang, Z.; James, T.; Kong, Y. L.; Malatesta, K. A.; Soboyejo, W. O.; Verma, N.; Gracias, D. H.; McAlpine, M. C., 3d printed bionic ears. *Nano Letters* **2013**, 13 (6), 2634-2639.
- (29)Hockaday, L. A.; Kang, K. H.; Colangelo, N. W.; Cheung, P. Y. C.; Duan, B.; Malone, E.; Wu, J.; Girardi, L. N.; Bonassar, L. J.; Lipson, H.; Chu, C. C.; Butcher, J. T., Rapid 3d printing of anatomically accurate and mechanically heterogeneous aortic valve hydrogel scaffolds. *Biofabrication* **2012**, 4 (3).
- (30)Duan, B.; Hockaday, L. A.; Kang, K. H.; Butcher, J. T., 3d bioprinting of heterogeneous aortic valve conduits with alginate/gelatin hydrogels. *Journal of biomedical materials research. Part A* **2013**, 101 (5), 1255-64.
- (31)Cui, X.; Boland, T., Human microvasculature fabrication using thermal inkjet printing technology. *Biomaterials* **2009**, 30 (31), 6221-7.
- (32)Xu, T.; Gregory, C. A.; Molnar, P.; Cui, X.; Jalota, S.; Bhaduri, S. B.; Boland, T., Viability and electrophysiology of neural cell structures generated by the inkjet printing method. *Biomaterials* **2006**, 27 (19), 3580-8.
- (33)Kolesky, D. B.; Truby, R. L.; Gladman, A. S.; Busbee, T. A.; Homan, K. A.; Lewis, J. A., 3d bioprinting of vascularized, heterogeneous cell-laden tissue constructs. *Advanced Materials* **2014**, 26 (19), 3124-3130.

- (34)Pati, F.; Jang, J.; Ha, D.-H.; Won Kim, S.; Rhie, J.-W.; Shim, J.-H.; Kim, D.-H.; Cho, D.-W., Printing three-dimensional tissue analogues with decellularized extracellular matrix bioink. *Nature Communications* **2014**, *5*.
- (35)Miller, J. S.; Stevens, K. R.; Yang, M. T.; Baker, B. M.; Nguyen, D.-H. T.; Cohen, D. M.; Toro, E.; Chen, A. A.; Galie, P. A.; Yu, X.; Chaturvedi, R.; Bhatia, S. N.; Chen, C. S., Rapid casting of patterned vascular networks for perfusable engineered three-dimensional tissues. *Nature Materials* **2012**, *11* (9), 768-774.
- (36)Marga, F.; Jakab, K.; Khatiwala, C.; Shepherd, B.; Dorfman, S.; Hubbard, B.; Colbert, S.; Gabor, F., Toward engineering functional organ modules by additive manufacturing. *Biofabrication* **2012**, *4* (2).
- (37)Jakab, K.; Norotte, C.; Marga, F.; Murphy, K.; Vunjak-Novakovic, G.; Forgacs, G., Tissue engineering by self-assembly and bio-printing of living cells. *Biofabrication* **2010**, *2* (2).
- (38)Norotte, C.; Marga, F. S.; Niklason, L. E.; Forgacs, G., Scaffold-free vascular tissue engineering using bioprinting. *Biomaterials* **2009**, *30* (30), 5910-5917.
- (39)Lantada, A., Biofabrication: Main advances and challenges. In *Handbook on advanced design and manufacturing technologies for biomedical devices*, Lantada, A. D., Ed. Springer US: 2013; pp 261-275.
- (40)Melchels, F. P. W.; Domingos, M. A. N.; Klein, T. J.; Malda, J.; Bartolo, P. J.; Hutmacher, D. W., Additive manufacturing of tissues and organs. *Progress in Polymer Science* **2012**, *37* (8), 1079-1104.
- (41)Tasoglu, S.; Demirci, U., Bioprinting for stem cell research. *Trends in Biotechnology* **2013**, *31* (1), 10-19.

- (42)Ozbolat, I. T.; Yu, Y., Bioprinting toward organ fabrication: Challenges and future trends. *IEEE Transactions On Biomedical Engineering* **2013**, *60* (3), 691-699.
- (43)Schneider, C. A.; Rasband, W. S.; Eliceiri, K. W., Nih image to imagej: 25 years of image analysis. *Nat Meth* **2012**, *9* (7), 671-675.
- (44)Mitsuhashi, N.; Fujieda, K.; Tamura, T.; Kawamoto, S.; Takagi, T.; Okubo, K., Bodyparts3d: 3d structure database for anatomical concepts. *Nucleic acids research* **2009**, *37* (Database issue), D782-5.
- (45)Sun, Y.; Duffy, R.; Lee, A.; Feinberg, A. W., Optimizing the structure and contractility of engineered skeletal muscle thin films. *Acta biomaterialia* **2013**, *9* (8), 7885-7894.
- (46)Hamburger, V.; Hamilton, H. L., A series of normal stages in the development of the chick embryo. *Journal of morphology* **1951**, *88* (1), 49-92.
- (47)Kim, H. Y.; Davidson, L. A., Punctuated actin contractions during convergent extension and their permissive regulation by the non-canonical wnt-signaling pathway. *J Cell Sci* **2011**, *124* (Pt 4), 635-46.
- (48)Mitsuhashi, N.; Fujieda, K.; Tamura, T.; Kawamoto, S.; Takagi, T.; Okubo, K., Bodyparts3d: 3d structure database for anatomical concepts. *Nucleic Acids Research* **2009**, *37* (suppl 1), D782-D785.
- (49)Zhang, F.; Kang, E.; Neoh, K.; Wang, P.; Tan, K., Modification of si (100) surface by the grafting of poly (ethylene glycol) for reduction in protein adsorption and platelet adhesion. *Journal of biomedical materials research* **2001**, *56* (3), 324-332.
- (50)Bencherif, S. A.; Srinivasan, A.; Horkay, F.; Hollinger, J. O.; Matyjaszewski, K.; Washburn, N. R., Influence of the degree of methacrylation on hyaluronic acid hydrogels properties. *Biomaterials* **2008**, *29* (12), 1739-1749.

- (51)Leach, J. B.; Schmidt, C. E., Characterization of protein release from photocrosslinkable hyaluronic acid-polyethylene glycol hydrogel tissue engineering scaffolds. *Biomaterials* **2005**, *26* (2), 125-135.
- (52)Fairbanks, B. D.; Schwartz, M. P.; Bowman, C. N.; Anseth, K. S., Photoinitiated polymerization of peg-diacrylate with lithium phenyl-2, 4, 6-trimethylbenzoylphosphinate: Polymerization rate and cytocompatibility. *Biomaterials* **2009**, *30* (35), 6702-6707.
- (53)Wu, W.; DeConinck, A.; Lewis, J. A., Omnidirectional printing of 3d microvascular networks. *Advanced Materials* **2011**, *23* (24), H178-H183.
- (54)O'Shea, J. J.; Ma, A.; Lipsky, P., Cytokines and autoimmunity. *Nature Reviews Immunology* **2002**, *2* (1), 37-45.
- (55)Hirano, T.; Kishimoto, T., Interleukin-6: Possible implications in human diseases. *Research in Clinic and Laboratory* **1989**, *19* (1), 1-10.
- (56)Piguet, P. F.; Grau, G. E.; Vassalli, P., Tumor necrosis factor and immunopathology. *Immunologic research* **1991**, *10* (2), 122-140.
- (57)Clark, I. A., How tn timer was recognized as a key mechanism of disease. *Cytokine & growth factor reviews* **2007**, *18* (3), 335-343.
- (58)Gottlieb, A. B.; Antoni, C. E., Treating psoriatic arthritis: How effective are tn timer antagonists? *ARTHRITIS RESEARCH AND THERAPY* **2004**, *6*, S31-S35.
- (59)Sfikakis, P. P., The first decade of biologic tn timer antagonists in clinical practice: Lessons learned, unresolved issues and future directions. *Curr Dir Autoimmun* **2010**, *11* (3), 180-210.
- (60)Rozenblit, M.; Lebwohl, M., New biologics for psoriasis and psoriatic arthritis. *Dermatologic therapy* **2009**, *22* (1), 56-60.

- (61)Gupta, A. K.; Skinner, A. R., A review of the use of infliximab to manage cutaneous dermatoses. *Journal of Cutaneous Medicine and Surgery: Incorporating Medical and Surgical Dermatology* **2004**, *8* (2), 77-89.
- (62)Paudel, K. S.; Milewski, M.; Swadley, C. L.; Brogden, N. K.; Ghosh, P.; Stinchcomb, A. L., Challenges and opportunities in dermal/transdermal delivery. *Therapeutic delivery* **2010**, *1* (1), 109-131.
- (63)Scheinfeld, N., A comprehensive review and evaluation of the side effects of the tumor necrosis factor alpha blockers etanercept, infliximab and adalimumab. *Journal of dermatological treatment* **2004**, *15* (5), 280-294.
- (64)Wolfe, F.; Michaud, K., Biologic treatment of rheumatoid arthritis and the risk of malignancy: Analyses from a large us observational study. *Arthritis & Rheumatism* **2007**, *56* (9), 2886-2895.
- (65)Daugherty, A. L.; Mersny, R. J., Formulation and delivery issues for monoclonal antibody therapeutics. *Advanced drug delivery reviews* **2006**, *58* (5), 686-706.
- (66)Yang, J.-A.; Kim, E.-S.; Kwon, J. H.; Kim, H.; Shin, J. H.; Yun, S. H.; Choi, K. Y.; Hahn, S. K., Transdermal delivery of hyaluronic acid–human growth hormone conjugate. *Biomaterials* **2012**, *33* (25), 5947-5954.
- (67)Streit, M.; Beleznay, Z.; Braathen, L. R., Topical application of the tumour necrosis factor- α antibody infliximab improves healing of chronic wounds. *International wound journal* **2006**, *3* (3), 171-179.
- (68)Brown, M. B.; Martin, G. P.; Jones, S. A.; Akomeah, F. K., Dermal and transdermal drug delivery systems: Current and future prospects. *Drug delivery* **2006**, *13* (3), 175-187.

- (69)Ranade, V. V., Drug delivery systems. 6. Transdermal drug delivery. *The Journal of Clinical Pharmacology* **1991**, 31 (5), 401-418.
- (70)Levin, G.; Gershonowitz, A.; Sacks, H.; Stern, M.; Sherman, A.; Rudaev, S.; Zivin, I.; Phillip, M., Transdermal delivery of human growth hormone through rf-microchannels. *Pharmaceutical research* **2005**, 22 (4), 550-555.
- (71)Prausnitz, M. R.; Langer, R., Transdermal drug delivery. *Nature biotechnology* **2008**, 26 (11), 1261-1268.
- (72)Durand, C.; Alhammad, A.; Willett, K. C., Practical considerations for optimal transdermal drug delivery. *American Journal of Health-System Pharmacy* **2012**, 69 (2), 116-124.
- (73)Arora, A.; Prausnitz, M. R.; Mitragotri, S., Micro-scale devices for transdermal drug delivery. *International Journal of pharmaceutics* **2008**, 364 (2), 227-236.
- (74)Lee, J. W.; Park, J.-H.; Prausnitz, M. R., Dissolving microneedles for transdermal drug delivery. *Biomaterials* **2008**, 29 (13), 2113-2124.
- (75)Donnelly, R. F.; Majithiya, R.; Singh, T. R. R.; Morrow, D. I.; Garland, M. J.; Demir, Y. K.; Migalska, K.; Ryan, E.; Gillen, D.; Scott, C. J., Design, optimization and characterisation of polymeric microneedle arrays prepared by a novel laser-based micromoulding technique. *Pharmaceutical research* **2011**, 28 (1), 41-57.
- (76)Liu, S.; Jin, M.-n.; Quan, Y.-s.; Kamiyama, F.; Kusamori, K.; Katsumi, H.; Sakane, T.; Yamamoto, A., Transdermal delivery of relatively high molecular weight drugs using novel self-dissolving microneedle arrays fabricated from hyaluronic acid and their characteristics and safety after application to the skin. *European Journal of Pharmaceutics and Biopharmaceutics* **2014**, 86 (2), 267-276.

- (77)Donnelly, R. F.; Singh, T. R. R.; Woolfson, A. D., Microneedle-based drug delivery systems: Microfabrication, drug delivery, and safety. *Drug delivery* **2010**, *17* (4), 187-207.
- (78)Hegde, N. R.; Kaveri, S. V.; Bayry, J., Recent advances in the administration of vaccines for infectious diseases: Microneedles as painless delivery devices for mass vaccination. *Drug discovery today* **2011**, *16* (23), 1061-1068.
- (79)Alarcon, J. B.; Hartley, A. W.; Harvey, N. G.; Mikszta, J. A., Preclinical evaluation of microneedle technology for intradermal delivery of influenza vaccines. *Clinical and Vaccine Immunology* **2007**, *14* (4), 375-381.
- (80)Bediz, B.; Korkmaz, E.; Khilwani, R.; Donahue, C.; Erdos, G.; Falo Jr, L. D.; Ozdoganlar, O. B., Dissolvable microneedle arrays for intradermal delivery of biologics: Fabrication and application. *Pharmaceutical research* **2014**, *31* (1), 117-135.
- (81)Sun, L. T.; Bencherif, S. A.; Gilbert, T. W.; Farkas, A. M.; Lotze, M. T.; Washburn, N. R., Biological activities of cytokine-neutralizing hyaluronic acid–antibody conjugates. *Wound repair and regeneration* **2010**, *18* (3), 302-310.
- (82)Sun, L. T.; Buchholz, K. S.; Lotze, M. T.; Washburn, N. R., Cytokine binding by polysaccharide– antibody conjugates. *Molecular pharmaceuticals* **2010**, *7* (5), 1769-1777.
- (83)Morelli, A. E.; Rubin, J. P.; Erdos, G.; Tkacheva, O. A.; Mathers, A. R.; Zahorchak, A. F.; Thomson, A. W.; Falo, L. D.; Larregina, A. T., Cd4+ t cell responses elicited by different subsets of human skin migratory dendritic cells. *The Journal of Immunology* **2005**, *175* (12), 7905-7915.
- (84)Nair, L. S.; Laurencin, C. T., Polymers as biomaterials for tissue engineering and controlled drug delivery. In *Tissue engineering i*, Springer: 2006; pp 47-90.

- (85)FALCONE, S. J.; DOERFLER, A. M.; BERG, R. A., Novel synthetic dermal fillers based on sodium carboxymethylcellulose: Comparison with crosslinked hyaluronic acid–based dermal fillers. *Dermatologic Surgery* **2007**, *33* (s2), S136-S143.
- (86)Erdos, G.; Donahue, C.; Zhang, J.; Gambotto, A.; Ozdoganlar, B.; Falo, L. In *Dissolvable microneedle arrays enable delivery of live adenovectors to the skin for cutaneous transduction and genetic immunization*, Journal of Investigative Dermatology, Nature publishing group 75 varick st, 9th flr, new york, ny 10013-1917 USA: 2012; pp S105-S105.
- (87)Erdos, G.; Donahue, C.; Williams, M.; Ozdoganlar, B.; Falo, L., Biodegradable dissolving microneedle arrays effectively deliver antigens and adjuvants to skin dcs for the induction of antigen specific immune responses. *The Journal of Immunology* **2010**, *184* (Meeting Abstracts 1), 48.12.
- (88)Sullivan, S. P.; Koutsonanos, D. G.; del Pilar Martin, M.; Lee, J. W.; Zarnitsyn, V.; Choi, S.-O.; Murthy, N.; Compans, R. W.; Skountzou, I.; Prausnitz, M. R., Dissolving polymer microneedle patches for influenza vaccination. *Nature Medicine* **2010**, *16* (8), 915-920.
- (89)Flutter, B.; Nestle, F. O., Tlrs to cytokines: Mechanistic insights from the imiquimod mouse model of psoriasis. *European journal of immunology* **2013**, *43* (12), 3138-3146.
- (90)Sweeney, C. M.; Tobin, A.-M.; Kirby, B., Innate immunity in the pathogenesis of psoriasis. *Archives of Dermatological Research* **2011**, *303* (10), 691-705.
- (91)van der Fits, L.; Mourits, S.; Voerman, J. S.; Kant, M.; Boon, L.; Laman, J. D.; Cornelissen, F.; Mus, A.-M.; Floencia, E.; Prens, E. P., Imiquimod-induced psoriasis-like

skin inflammation in mice is mediated via the il-23/il-17 axis. *The Journal of Immunology* **2009**, *182* (9), 5836-5845.

(92)Swindell, W. R.; Johnston, A.; Carbajal, S.; Han, G.; Wohn, C.; Lu, J.; Xing, X.; Nair, R. P.; Voorhees, J. J.; Elder, J. T., Genome-wide expression profiling of five mouse models identifies similarities and differences with human psoriasis. *PloS One* **2011**, *6* (4), e18266.

5.3. Supporting Figures

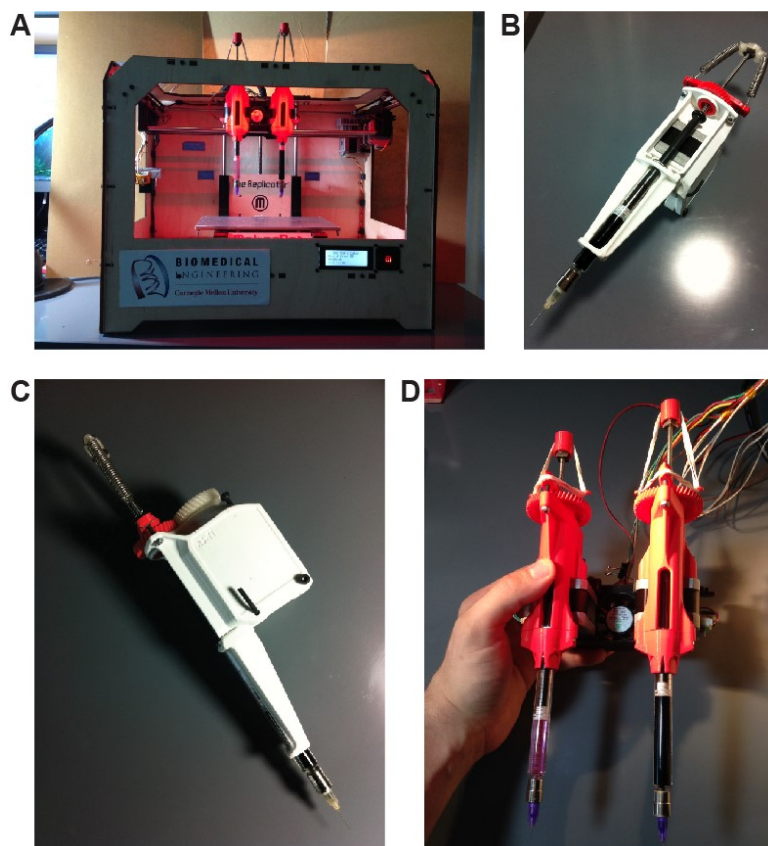


Fig. S1. Modification of an open source 3D printer for FRESH printing (A) MakerBot Replicator showing stock thermoplastic extruder replaced with the dual syringe pump extruder and glass syringes. (B) Example of a syringe pump extruder 3D printed from ABS using a non-modified MakerBot. (C) Side view of syringe pump extruder. (D) Example of the dual syringe pump extruder capable of printing two materials at one time.

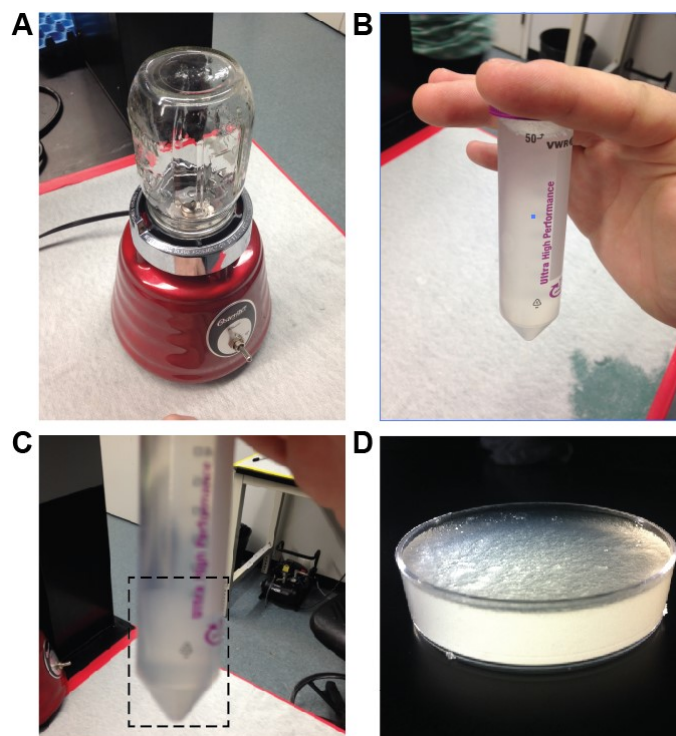


Fig. S2. Preparation of the gelatin slurry support bath. (A) The blender with a 500 mL mason jar attached, which is used to create the microparticulate slurries from solid gelatin blocks. (B) A 50 mL centrifuge filled with the blended gelatin slurry before suspended particles are separated from the supernatant by centrifugation. (C) The blended gelatin solution after centrifugation showing settled gelatin slurry at bottom and supernatant on top. (D) A 35 mm petri dish filled with the gelatin slurry for use in FRESH printing, showing the bath after the supernatant has been removed and excess water has been wicked off using Kim wipes.

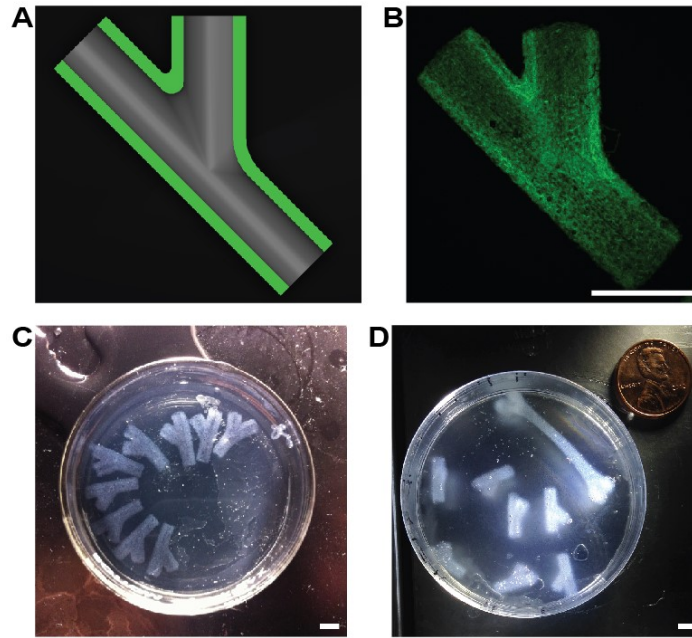


Fig. S3. Examples of 3D printed bifurcated tubes using alginate, fibrin and collagen. (A) A 3D CAD model of a bifurcated tube used to calibrate and benchmark the performance of various gel inks for FRESH printing. (B) Example of a 3D printed bifurcated tube using FITC-labeled alginate imaged using the confocal microscope to show the cross-section and sub-millimeter wall thickness. (C) An example of 9 identical 3D printed bifurcated tubes using fibrinogen ink (cross-linked to fibrin once printed in the Thrombin supplemented bath) to show the repeatability of the technique using ECM protein hydrogels. (D) An example of 7 identical 3D printed bifurcated tubes (and 1 femur) using collagen ink (cross-linked using a support bath with pH = 7.4) to show the repeatability using additional ECM protein hydrogels. Scale bars are 5 mm.

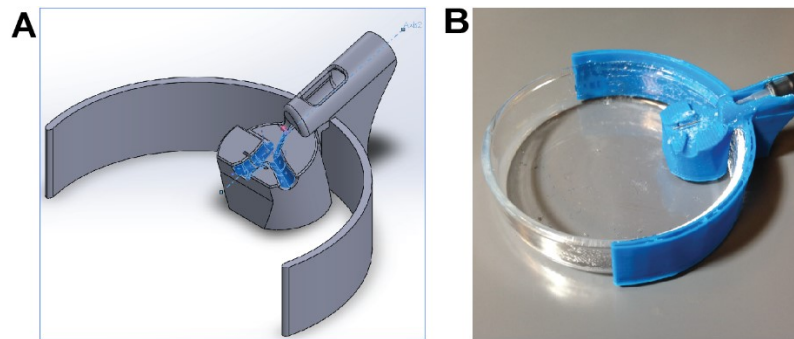


Fig. S4. A 3D printed perfusion fixture for the right coronary arterial tree. (A) A 3D CAD model of the perfusion fixture with the arterial saddle (recessed grooves) shown in blue. (B) An example of the perfusion fixture 3D printed using PLA and positioned on a Petri dish. The syringe tip used for perfusion into the trunk of the arterial tree is visible on the right.

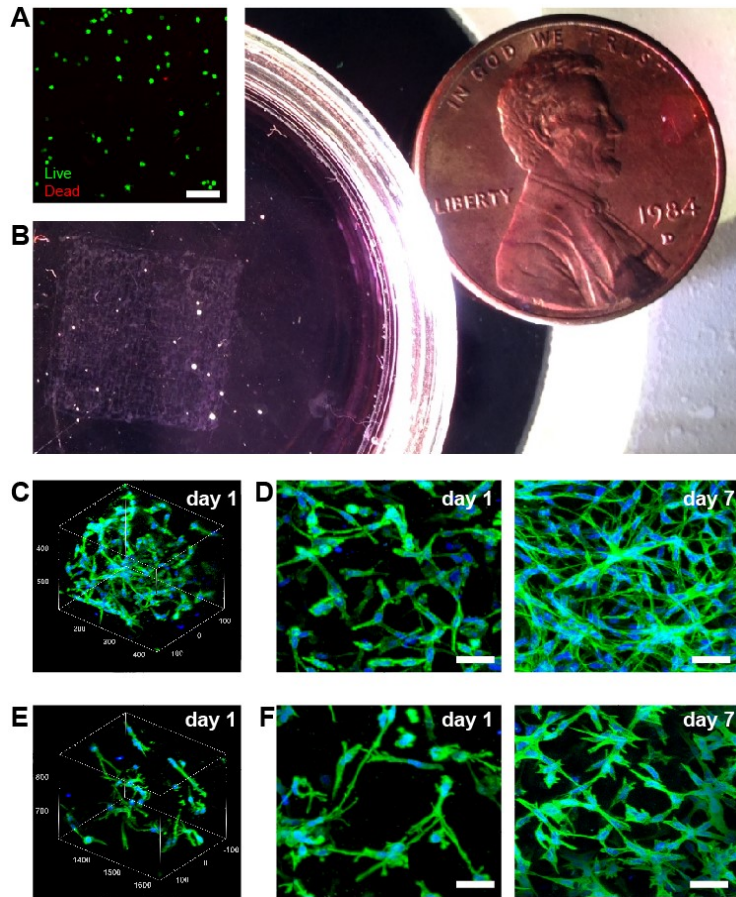


Fig. S5. 3D printed sheets of cells and ECM. (A) Representative live (green) and dead (red) staining of C2C12 cells in 3D printed sheets of multi-component ECM gel 2 hours post fabrication. Scale bar is 100 μm . (B) Brightfield image of a printed cell sheet with dimensions of 1 cm square and approximately 200 μm thick. (C) 3D image of C2C12 myoblasts and (E) MC3T3 fibroblasts in printed sheets after 24 hrs incubation demonstrating homogenous distribution of cells throughout. (D) Maximum intensity projections of confocal microscope images of MC3T3 fibroblasts and (F) C2C12 myoblasts in FRESH printed constructs at 1 and 7 day time points demonstrating that cells spread and proliferate in 3D. Scale bars are 50 μm .

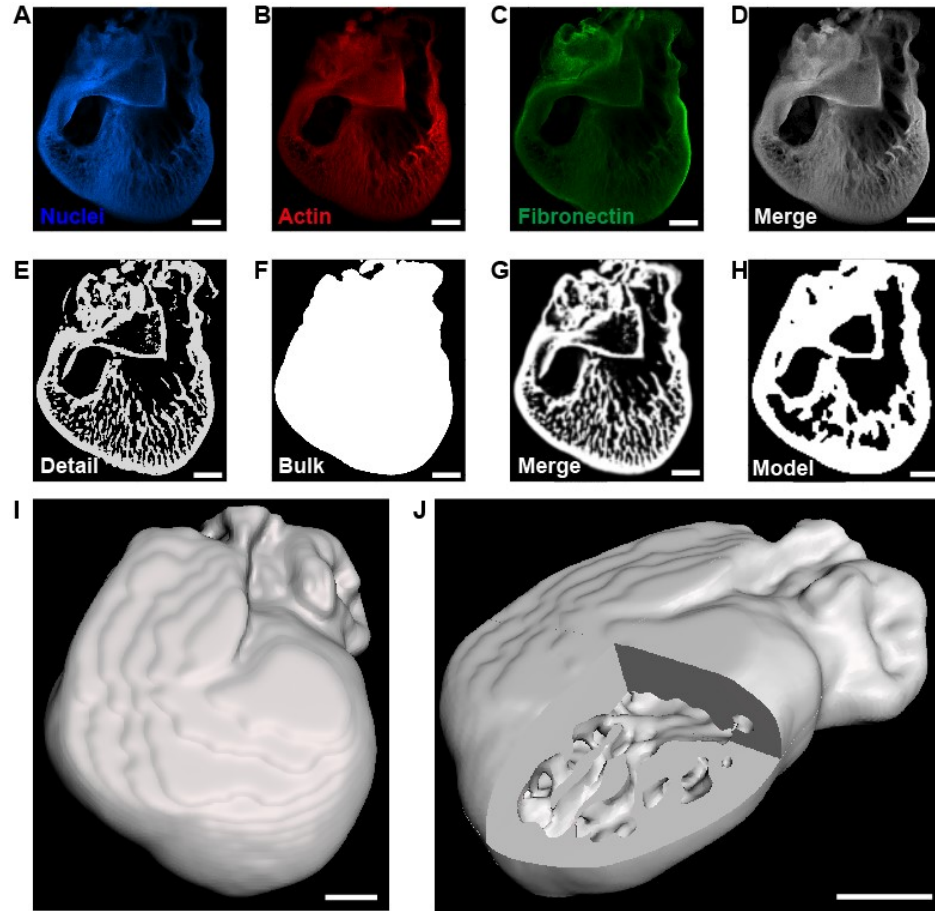


Fig. S6. Generation of a 3D model of the embryonic heart from confocal microscopy. A 5-day-old embryonic chick heart was dissected, fixed and stained to for the nuclei (blue), F-actin (red) and fibronectin (green). (A-C) Individual slices from confocal Z-stacks showing the wall of the heart as well as internal trabeculae. (D) The three channels were merged to create a complete image of the heart. A high and a low threshold were used to create binary images to preserve detailed trabeculae (E) or the outer wall (envelope) of the heart (F), respectively. (G) A combined image was created by combining the trabeculae visible in (E) with the envelope obtained from (F) to create a binary image with maximum detail. (H) The binary image in (G) was dilated to decrease resolution and smoothed to create a final binary Z-stack, which was segmented into a solid model using Imaris 7.5. (I) 3D representation of the STL file created from (H). (J) A cutaway view of (I) shows the trabeculated left ventricle that recapitulates some of the internal trabecular architecture of the embryonic heart. Scale bars are 200 μm .

Chapter 6 : Microfabricated Gecko-inspired Fibers for Enhanced Wet Tissue Adhesion

6.1. Abstract

Dopamine methacrylamide (DMA) copolymers are interesting materials due to their strong and reversible adhesive properties under both wet and dry conditions. It is being used as a component in a growing number of applications, particularly as a novel biomedical adhesive. Combining the wet adhesive properties of DMA copolymers with the strong revisable adhesion of gecko-microfibers is investigated here in the context of animal tissue samples. Adhesion on non-processed porcine skin under water was tested. Below 3 mN or preload values, a maximum adhesion values of 4 mN was observed. Work of adhesion, however, showed a direct dependence on both the elasticity of the substrate and contact time. Moreover, in investigating this material, a sharp reduction in adhesive characteristics over the course of days was observed.

Here, we quantified the physical changes observed in the copolymer using adhesion and compression tests. Additionally, we used NMR, gel permeation chromatography (GPC), electrospray ionization mass spectrometry (ESI-MS) and UV-vis spectroscopy (UV-Vis) to assess chemical changes that underlie the material changes. The adhesion and compression tests demonstrated a significant decrease in adhesion and increase in stiffness in the first 24 hours followed by more gradual but continuous changes. In contrast, the data from NMR and GPC experiments did not appear to change with time, suggesting the physical changes may be limited to side groups on the polymers without inter-chain crosslinking. However, UV-Vis and ESI-MS measurements indicated that aromatic functional groups from the DMA copolymer were extracted from the samples over time, which may suggest an unusual auto-degradation mechanism. While these changes may not

impact long-term bonding performance if used soon after preparation, they significantly reduce reversible adhesion, which could result in variability of material properties reported. These studies point to a need for investigations into strategies for inhibiting these degradation processes without interfering with the variety of mechanisms involved in the adhesion of catechol-based copolymers to surfaces.

6.2. Introduction

The deteriorating effect of water on the adhesion properties of polymers have been a long standing problem. While there are multiple mechanisms by which this effect could be magnified, most explanations have to deal with water-induced plasticization, polymer hydrolysis, erosion and swelling.¹ Marine organisms such as mussels and polychaetes are known for their robust ability to adhere to surfaces in a broad range of conditions including varying temperature, salinity, surface types, and wet vs. dry environments.²⁻⁴

Marine mussels live on rocky shallow shores, where waves are strong, taking advantage of the abundance of nutrients and sunlight.⁵ With the aid of specialized holdfasts, called the byssus, that are actively fabricated and maintained by mussels, consuming about 12% of the total metabolic capacity of marine mussels, they are able to stick firmly onto rocky surfaces while submerged underwater. This phenomenon has inspired a lot of research and solutions for the development of underwater adhesives.^{1, 6-12}

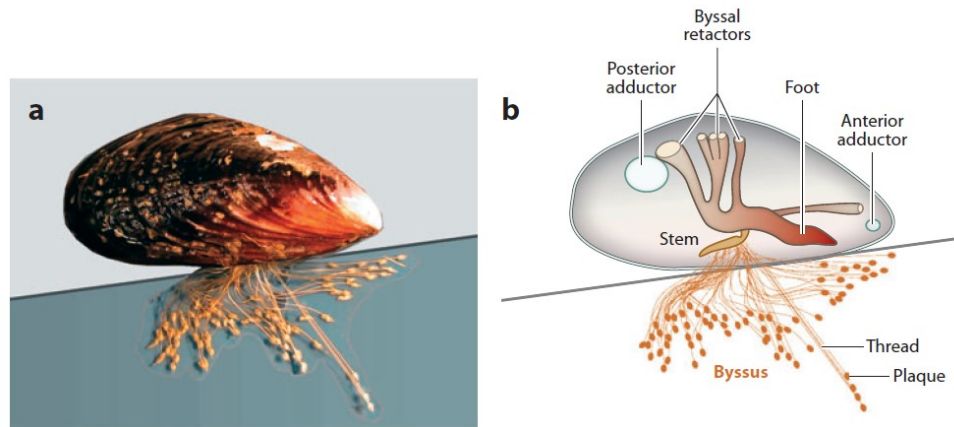


Figure 6.1 A view of marine mussels structure.¹

The byssus is a protein-based structure comprised of a very elegant and strict hierarchy of threads, plaques, retractor muscles, beads, stems and a root.^{1, 7} While the structure, fabrication mechanism and the attachment to the living retractor muscle parts of the mussels are important aspects to the survival of mussels, and the under-water adhesion sensing mechanism, the byssal plaques are solely responsible for the mussels' tenacity to various solid surfaces underwater.⁶⁻⁷ The microstructure of the plaques is precisely engineered with a very fine porous and hierarchical order. This microporous structure accommodates the distal thread core of the byssus, which consists of dense bundles of microfibers insulated by a granular matrix, and exhibits a precise pore diameter gradient ranging from 200 nm to 3 μm , near the solid surface and the thread interface respectively. This porous network, about 40% porosity, is highly interconnected and lubricated with the aids of very smooth walls and fluids and is extended to trabeculae with pore diameters of 50-500 nm and only 50 nm wall thickness.¹³ This highly porous microstructure of the plaques, not only permits a better distributions of the microfibers bundles, but also creates a cup-like structure able to maintain an attachment angle to the solid surface and an effect

similar to that of suction cups. This elegant micro organization helps adhesion protein, in the tips of the microfibers, find suitable spots of solid surfaces for strong adhesion.

On the molecular level, the plaque is packed with a group of 7-8 proteins that match the diversity of the microfibrillar threads. At the time the bysuss is made exclusively of about 25-30 types of specialized proteins, 5 proteins exclusive to the plaque are, mussel foot protein (mfp): mfp-2, mfp-3, mfp-4, mfp-5, mfp-6.¹ While the individual protein sequences for these proteins are distinctively different, one common component among all of them is the posttranslational modified amino acid 3,4-dihydroxyphenyl-L-alanine (Dopa). The molecular weights of these proteins as well as the Dopa content varies reaching almost 40% Dopa content.^{1, 11} This unique adhesion have inspired scientists for decades to study and use these Dopa-containing polymers for various applications such as, coatings,¹⁴⁻¹⁵ synthetic medical adhesives¹⁶ and sealants.¹⁷⁻¹⁸

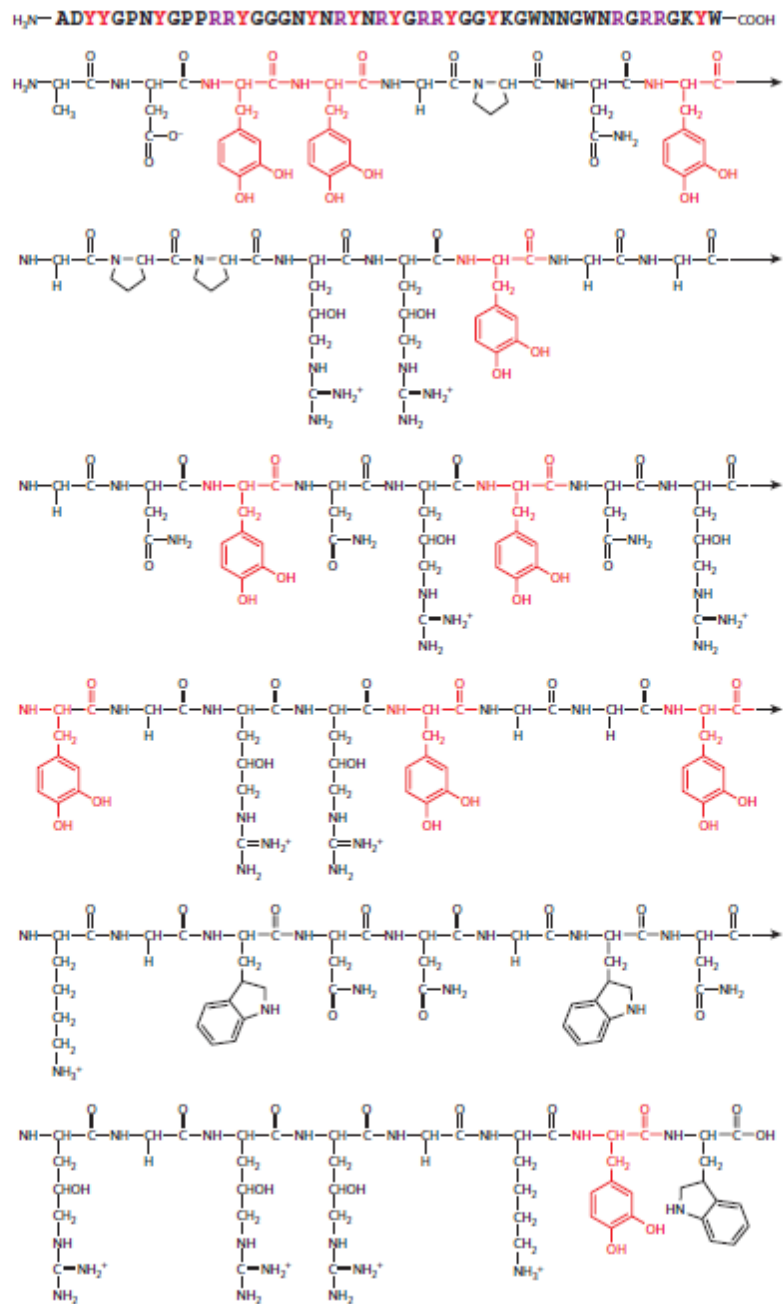


Figure 6.2 mfp-3 chemical structure as an example of the Dopa content (highlighted in red) in the mfp family

Investigations on the reactivity of the catechol group on Dopa have revealed that Dopa is able to interact with a variety of surface types through a number of mechanisms. For metals and metal oxides, the catechol group has been shown to chelate the metal or to

adsorb to the surface through exchange of the hydroxyl groups on the Dopa molecule with the water and hydroxyl groups bound to the metal in aqueous solution.¹⁹⁻²⁰ In these adhesion modes, the *ortho*-dihydroxy configuration of the molecule is the driving force behind this adsorption because similar *meta* and *para* compounds failed to display significant adsorption capabilities.²¹ For non-metal organic surfaces, both suggested adhesion mechanisms arise through oxidation of the catechol moiety to a quinone. The quinone can then crosslink with itself via formation of bisquinones or participate in Michael-type addition reactions with amines found in proteins or other materials.^{19, 22}

In previous work, research has also been focused on the development and characterization of novel Dopa-based copolymers materials due to its unique properties. Copolymers of Dopa and L-lysine exhibited moisture-resistant adhesion after polymer oxidation⁴ while Dopa based adhesive hydrogels for biomedical applications have been synthesized by photopolymerization of dopamine methacrylamide (DMA) with poly(ethylene glycol) diacid.²³ Improved crosslinking chemistries may also broaden the range of applications for which DMA copolymers are used.²⁴ In another study, a first generation copolymer adhesive for bone fixation was synthesized by free radical polymerization of monoacryloxyethyl phosphate (MAEP), DMA, and acrylamide. However, further optimization of the polymer is necessary for improved adhesion performance.¹⁷ Additional studies have focused on the synthesis of DMA-co-methoxyethyl acrylate (MEA) polymers as tip coatings for gecko-inspired pillar structures with reversible adhesion.^{15, 25-26}

Although there have been a number of studies relating to the mechanism of adhesion of Dopa and the synthesis of promising adhesive copolymers, there has been little research on how the properties of these polymers change over time. Because of the high reactivity of the catechol group, questions arise over the stability of Dopa-based materials. In our work with DMA-co-MEA polymers, we have observed that while these polymers initially have excellent mechanical properties that contribute to the work of adhesion,²⁶ they rapidly become less sticky and more rigid over time. In this paper, we have used a variety of different analytical techniques to follow and characterize the physical changes seen with the DMA-co-MEA polymer over time in an attempt to explain the mechanism behind these changes, which could eventually help increase the viability and operative life of the polymer for reversible adhesive applications.

6.3. Experimental

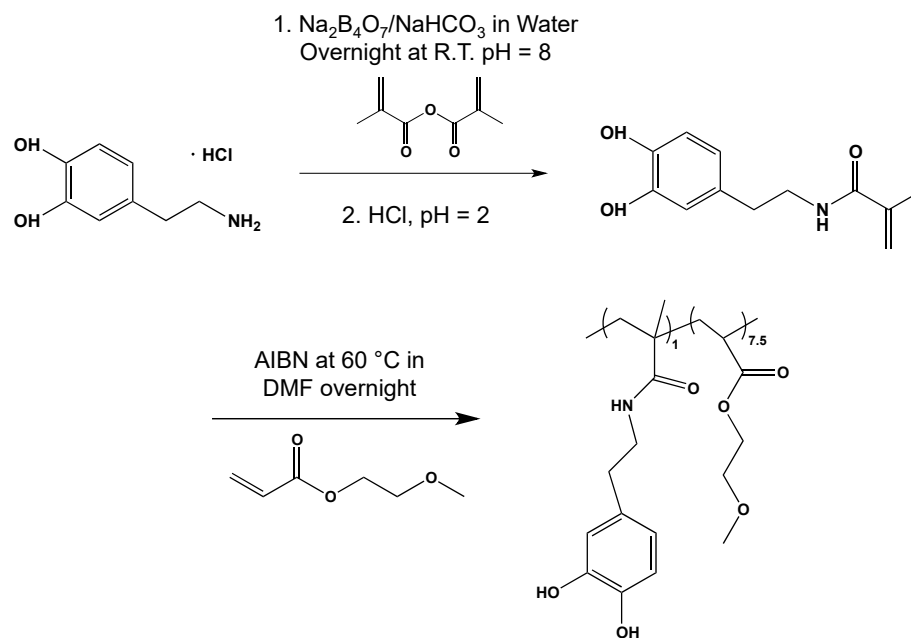
6.3.1. Materials

Dopamine hydrochloride, 2-methoxyethyl acrylate (MEA), azobisisobutyronitrile (AIBN) were purchased from Sigma Aldrich. Methacrylic anhydride was purchased from Alfa Aesar and polyurethane precursors ST1060A and ST1060B were purchased from BJB Enterprises. AIBN was purified by recrystallization twice in methanol at 75 °C, otherwise all materials were used as received.

6.3.2. Synthesis of DMA Monomer

Distilled water (200 mL) was added to a 500 mL round bottom flask and then sodium tetraborate decahydrate (20.25 g, 53.1 mmol) and sodium bicarbonate (8.03 g, 95.6 mmol) were added. The solution was stirred with a stir bar to help dissolve the solid. The solution was bubbled with nitrogen gas for 20 minutes. Dopamine hydrochloride (10 g, 53

mmol) was added to a round bottom flask. Methacrylate anhydride (9.70 mL, 65.1 mmol) in tetrahydrofuran (50 mL) was added dropwise over 15 minutes. The pH was kept above 8 with addition of 6 M sodium hydroxide solution. The reaction was stirred overnight for 14 hours with nitrogen gas bubbling. The solution was filtered using a glass frit filter and washed with ethyl acetate (150 mL) twice. About 2-3 hours were allowed between each wash and the solution was kept in a nitrogen atmosphere. The pH of the aqueous solution was reduced to lower than 2 with concentrated hydrochloric acid. The solution was filtered with a glass frit filter to remove gray solids. The solid was washed on the filter with ethyl acetate. The aqueous solution was then extracted with ethyl acetate (100 mL) three times. The combined ethyl acetate layers were dried over anhydrous magnesium sulfate and the volume was reduced to 100 mL using rotary evaporation. The solution was added dropwise to cold hexane (800 mL) in a 1000 mL beaker. The solid product was then recrystallized with ethyl acetate and hexane and dried in a vacuum oven. A total of 3.426 g (15.5 mmol, 29% yield) of DMA monomer was obtained. ¹H NMR (dDMSO): 6.60 ppm (m, 2H), 6.42 ppm (d, 1H), 5.61 ppm (s, 1H), 5.30 ppm (s, 1H), 3.20 ppm (m, 2H), 2.50 (m, 2H), 1.80 ppm (s, 3H).



Scheme 6.1 Reaction scheme for the synthesis of DMA and DMA-co-MEA.

6.3.3. Synthesis of DMA Copolymer

MEA (3.1 mL, 24.1 mmol), DMA monomer (1.0 g, 4.5 mmol), and AIBN (0.0631 g, 0.384 mmol) were added to a 50 mL round bottom flask with N,N-dimethylformamide (12 mL). The solution was stirred with a stir bar and bubbled with nitrogen gas for 30 min. The solution was then heated in an oil bath at 60 °C with stirring and a nitrogen atmosphere overnight. The flask was removed from the heating apparatus and allowed to cool. The polymer was dissolved in a minimal amount of methanol and was added dropwise to diethyl ether (500 mL). The ether was decanted from the resulting shiny light brown solid, which was dried with a gentle air stream and then dissolved in methylene chloride. The methylene chloride solid mixture was added dropwise to diethyl ether (500 mL) and the cream solid was dried for 3 hours in the vacuum oven. The copolymer was stored at standard temperature and pressure following synthesis and for the remainder of the study, unless otherwise noted. ^1H NMR (CDCl_3): 8.03ppm (1H), 6.60-6.83ppm (3H), 4.21ppm

(2H), 3.58ppm (2H), 3.37ppm (3H), 2.71ppm (2H), 2.40ppm (1H), 1.94ppm (2H), 1.70ppm (4H), 1.00ppm (3H). Integration and comparison of the peaks from the catechol group at 6.60-6.83 ppm and the methoxy peak 3.37 ppm gave a DMA to MEA ratio of 1:7.5 in the copolymer. A summary of the DMA-co-MEA synthesis procedure is shown below in Scheme 6.1.

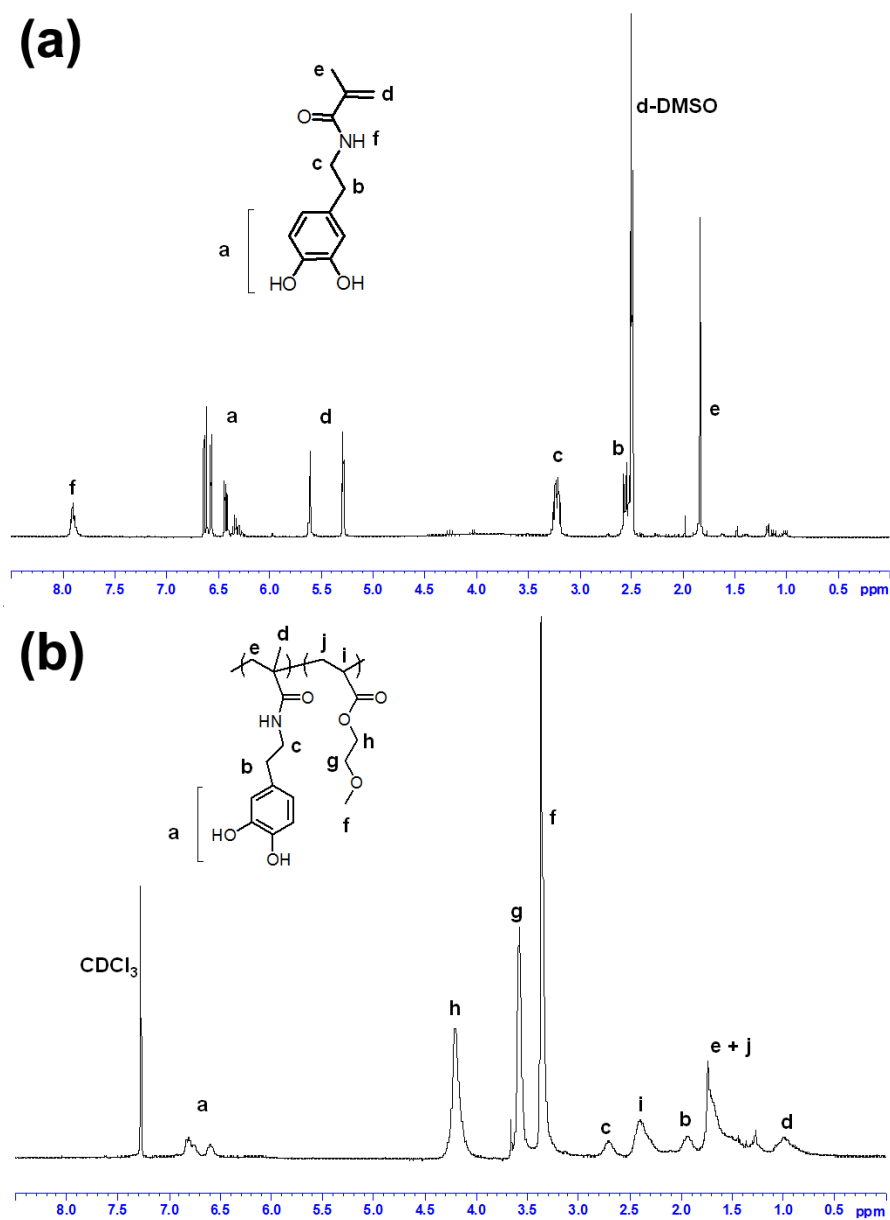


Figure 6.3 ^1H NMR spectra for DMA monomer (a) and DMA-co-MEA copolymer (b)

6.3.4. Coatings of gecko-microfibers

Mushroom-tip elastomer gecko-fibers were cleaned with ethanol and degassed for 2 hours. DMA-co-MEA solutions in DMF were prepared right before use. The DMA-co-MEA solutions were spin-coated onto clean SiO₂ wafer for 3 minutes at 3000 rpm. Upon spin coating, the microfibers were stamped onto the wafer under a load of 200 mg. Unidirectional peeling of the microfiber stamps followed. For the crosslinked formulations, EGDMA was added as a crosslinker and UV illumination at 365 nm followed the stamping step.

6.3.5. Indentation adhesion test

A uniaxial indentation test was performed using a 6 mm hemispherical glass probe. The setup was modified to include a water bath to assure full water submersion. Testing was performed on fresh, smooth, non-treated porcine skin tissue samples. The samples were fixed to the bottom of a 2 cm deep tank on a glass slide mounted to an inverted optical microscope (TE200, Nikon). A 6 mm diameter glass hemisphere was attached to the stem of a load cell (GSO-50, Transducer Techniques), which was controlled by a linear stage (MFA-CC, Newport Corporation). Custom software was written to control the motion of the glass hemisphere while collecting data from the load cell. For testing under aqueous conditions, the shallow tank was filled with deionized water, entirely submerging the sample. For each sample in both wet and dry conditions, the samples were indented with the glass hemisphere at 0.1 mm/s speed until a predefined preload force was reached. The glass hemisphere was then retracted at the same speed, while the adhesion force at the material interface was measured. The maximum contact area²⁷ was calculated from the indentation depth of the hemisphere, which was computed from the distance between the

position of the hemisphere when contact with the test surface was initiated and the position of the hemisphere at the moment when the maximum preload was reached. Contact areas were obtained for each individual adhesion test, and varied from $1-8 \times 10^{-6} \text{ m}^2$, depending on the preload force and sample properties. Two-tailed t tests were used to demonstrate statistical significance between each group of adhesion tests.

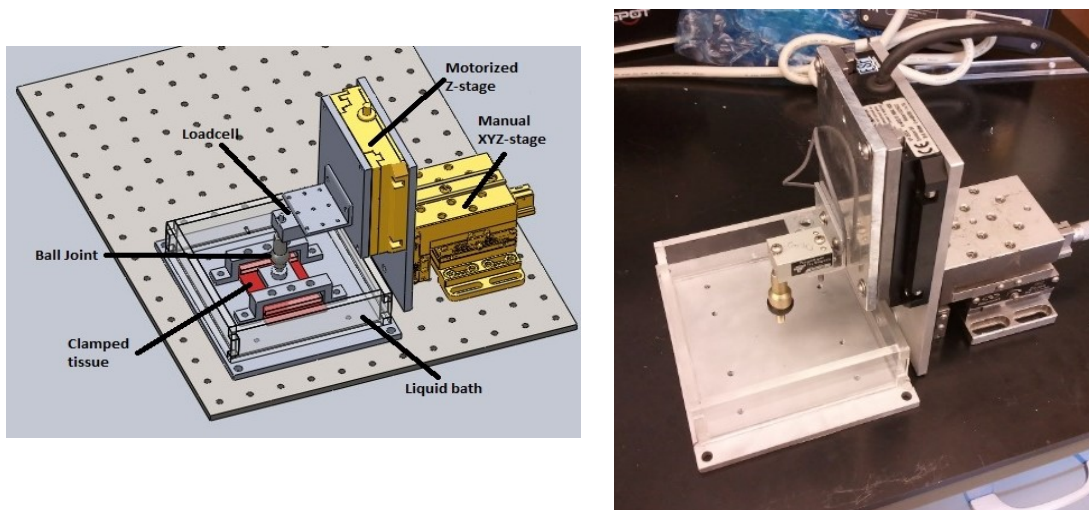


Figure 6.4 Customized underwater indentation adhesion test setup.

6.3.6. Extraction of DMA Copolymer and Analysis by UV-Vis

DMA copolymer (0.1544 g) was added to a 100 mL round bottom flask with phosphate buffered saline (PBS) solution (3 mL). Each extraction was stirred for 24 hours with a stir bar and heating at 37 °C. The liquid portion of the extraction was then removed and analyzed using a Cary 300 UV-Vis Spectrophotometer. Fresh PBS solution was added to the flask every 24 hours for a period of 5 days. The peak absorbance values were taken at 279 nm corresponding to the DMA catechol group¹⁷ and DMA monomer solutions of 0.2 mM, 2.0 mM, 3.0 mM, and 4.0 mM were used to construct a calibration curve. Solid residue (0.1325 g), or 86% of the starting material, remained in the extraction flask after all extraction experiments were complete.

6.3.7. Adhesion and Compression Tests

Adhesion and compression tests were carried out in triplicate the day the polymer was synthesized (day 0) as well as at 1 day, 3 days, 6 days, 14 days, and 30 days after the polymer was synthesized. For adhesion testing, the sample consisted of the DMA copolymer on a polyurethane substrate mounted on a glass slide. The substrate was formed in 24 hours by mixing polyurethane precursors ST1060A and ST1060B in a 6:3.3 ratio. Then, 11 drops of 0.200 g copolymer dissolved in 0.1 mL methylene chloride were spin-coated onto the substrate and residual methylene chloride was removed by drying in a vacuum oven at 25 °C. The adhesion tests were carried out as described previously.⁹ Samples for the compression tests were made by shaping the polymer into circular disk-like samples using non-stick aluminum foil molds. In order to do this, it was necessary to heat the polymer inside the mold on a hotplate to slightly melt it and shape it with a spatula. For each sample, 3 diameter and 3 height measurements were taken using calipers and averaged in order to determine the dimensions of the sample accurately. The samples were then analyzed using an Intron 5943 Electromechanical System with a 50 N load cell and a compression rate of 0.5 mm/min. The software for the system was Blue Hill (version 3). The compressive moduli of the samples were calculated using the formula given in Equation 1.¹⁹

$$\frac{F}{A} = G_e (\lambda - \lambda^{-2}) \quad [1]$$

In this equation, F is the force acting on the material, A is the area of the sample, G_e is the compressive (also elastic) modulus of the sample, and $\lambda = l/l_0$ where l is the thickness of the polymer during compression and l_0 is the initial polymer thickness. By

plotting $\frac{F}{A}$ versus $(\lambda - \lambda^{-2})$, the slope of the linear region taken between $\lambda = 0.85$ and $\lambda = 0.65$ gave the compressive modulus of the sample.

6.3.8. GPC, ESI-MS, and NMR

After extraction of the DMA copolymer for UV-Vis, additional extraction solution was analyzed by ESI-MS and the remaining solid was analyzed by GPC and NMR. For ESI-MS, 2.5 mL of extraction solution from day 0 was added to Spectrum Labs SpectraPor CE Dialysis Membrane 100 Da MWCO tubing and dialyzed in 1000 mL of water with stirring for 2 days. The water was changed 3 times per day. After dialysis, the sample (2.1 mL) was mixed with 0.9 mL of methanol and analyzed by ESI-MS along with a blank, which consisted of 2.1 mL of water and 0.9 mL of methanol. ESI-MS was conducted using a Thermo-Fisher LCQ ESI-APCI Ion Trap in positive ion mode.

NMR measurements were carried out using a Bruker Advance 300 MHz NMR Instrument in CDCl_3 . GPC measurements were taken using a Waters GPC (Polymer Standards Services (PSS) columns (guard, 105, 103, and 102 Å)) using DMF as an eluent (flow rate 1.00 mL/min, 50 °C) with differential refractive index (RI) detector. The DMA copolymer (0.009 g) was dissolved in 3 mL of DMF containing 1 drop of toluene and syringe filtered before injection. The apparent molecular weights (M_n) were determined with a calibration based on linear poly(methyl methacrylate) standards using WinGPC 7.0 software from PSS.

6.4. Results and Discussion

6.4.1. Adhesion and Compression Tests

The coated microfibers were tested in the better-coated sections. Plots of the work of adhesion and compressive modulus as a function of time are shown below in fig. 6.5. Work of adhesion was calculated as a measure of the adhesive property of the copolymer and normalized using the sample (copolymer and polyurethane substrate) thickness. As shown in the graph, the copolymer undergoes a rapid drop in the work of adhesion within the first day following synthesis. This was consistent with the rapid change in adhesiveness of the copolymer previously observed. Reversible adhesion continues to decrease in subsequent days, however not as dramatically as in the first 24 hours. This indicates that the copolymer also undergoes some sort of chemical change rapidly after being made, possibly due to degradation. After the first 24 hours, the polymer properties continue to change, but the majority of the physical and therefore chemical changes to the polymer occur within the first day under ambient conditions.

For comparison, the compressive moduli of DMA-co-MEA samples were also measured at the same time points as the adhesion samples. As shown in fig. 1, the compressive modulus increases significantly after 24 hours demonstrating an increase in the stiffness of the polymer. The modulus continues to increase with time, but not as significantly as after the first 24 hours. This trend is anticorrelated with the trend observed for the change in the work of adhesion over time and further demonstrates the proposed rapid initial degradation and loss of function of the polymer.

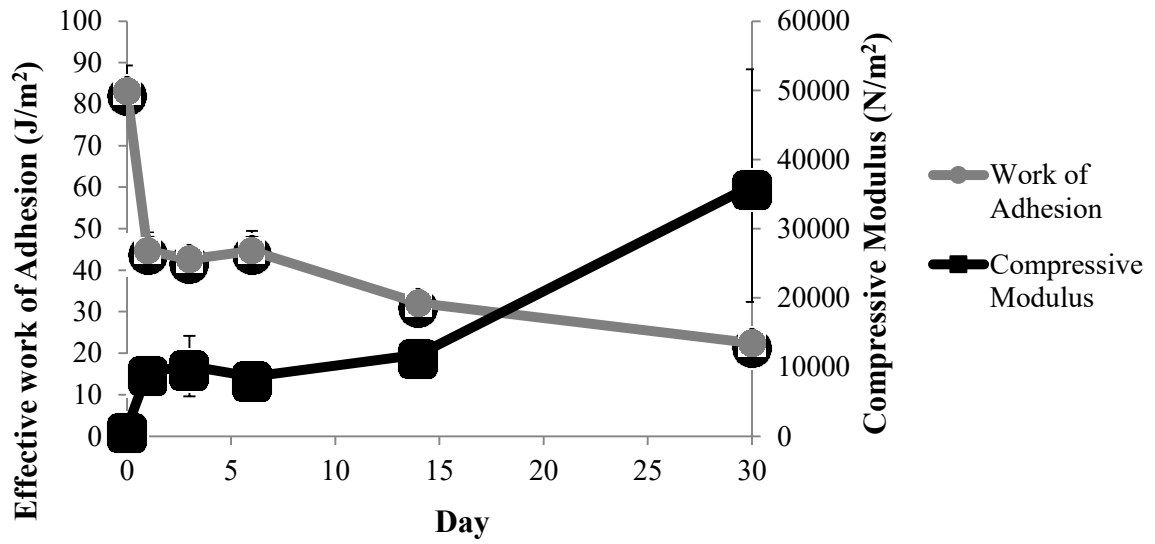


Figure 6.5 Work of adhesion and compressive modulus as a function of time.

For tissue samples, the relationship between preload and adhesion was observed to be linear below preloads of 3 mN (fig. 6.6.). Beyond this preload values, adhesion values varied a lot with a decreasing trend. This could be explained in the context of the mechanical properties of the elastomeric microfibers. Above 3 mN preload values, the microfibers are entangled and the glass indenter is believed to be in contact with the bulk of the backing layer. This means that the applied force, due to increased preloads, is dissipated within that layer and stored due to its high elasticity. It is interesting, however, to note that maximum adhesion values of 4 mN were read within the linear range.

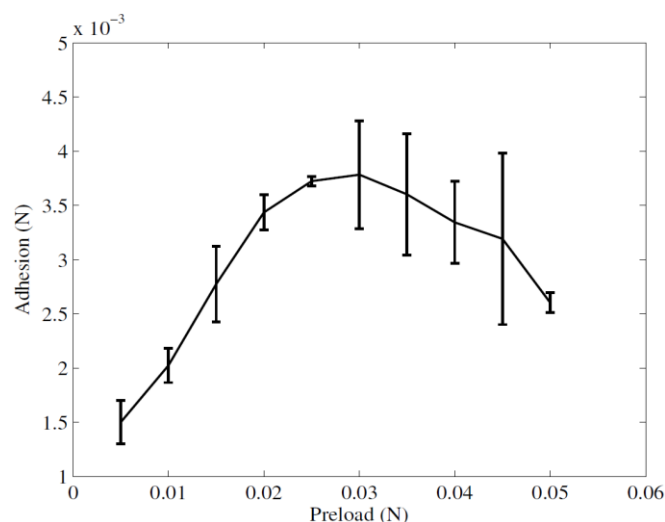


Figure 6.6 Underwater maximum adhesion plot of DMA-co-MEA-coated microfibers on porcine skin tissue sample as a function of preload.

Such effect could also be observed when measuring work of adhesion. Fig. 6.7. shows a summary for work of adhesion measurements of skin tissue samples with varying contact times. These work of adhesion measurements did not correlate to the maximum adhesion values obtained within the linear range. Conversely, these values seemed to increase with increasing contact time. This also supports that the elasticity of the microfiber substrates leads to enhanced adhesion. This further adds to the energy requirements of the system. In other words, the energy consumed is not only that needed to break the adhesion force at the interface, but also to overcome the elasticity of the substrate. The increased work of adhesion with increased contact times suggests that surface reorganization takes place upon contact. This reorganization could be in the form of more catechol groups that are in contact of the surface or as a result of increased oxidation of the same groups.

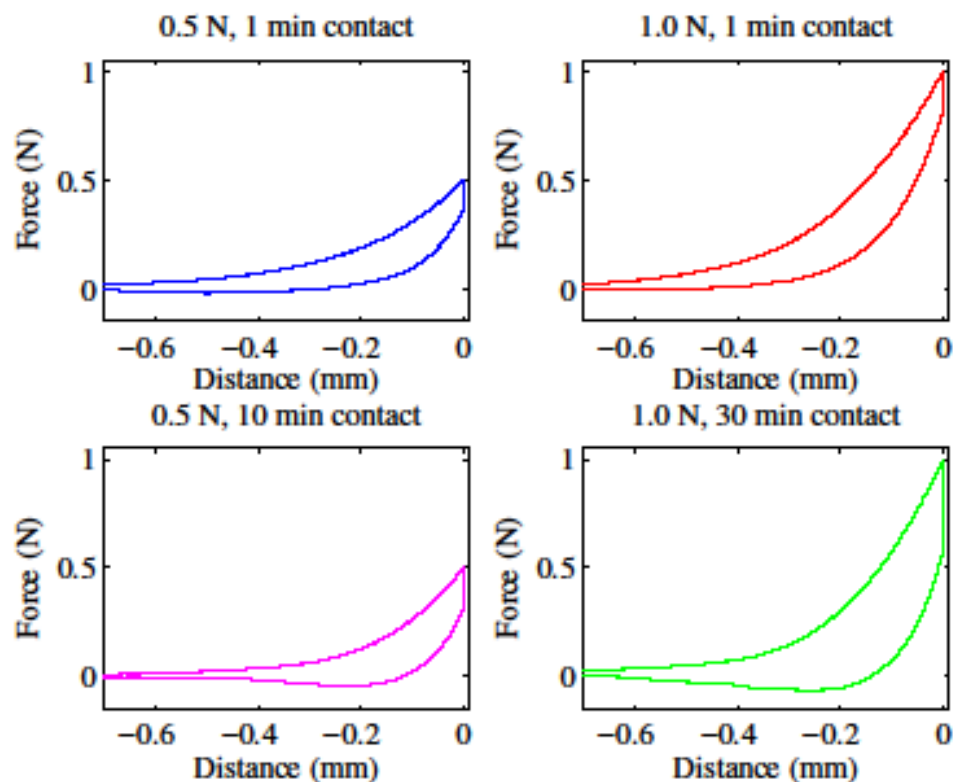


Figure 6.7 Underwater work of adhesion plots for DMA-co-MEA-coated microfibers as a function of contact time

6.4.2. Mass Spectrometry and UV-Vis Absorbance

The DMA copolymer was extracted using PBS in which the dopamine group is soluble but the MEA is not. UV-Vis analysis of the extraction solution resulted in a peak at 279 nm, which overlaps with the absorbance range for Dopa.¹⁷ No other peaks were observed in the 250-600 nm range. Mass spectrometry was used to provide preliminary determination of the extract. The ESI-MS data from the extraction supernatant, shown in fig. 6.8., displays two strong peaks with corresponding to ions with molecular weights of 163 g/mol and 185 g/mol. These molecular weight values are than that of the DMA monomer (221 g/mol) but could be derived from the catechol groups in the DMA copolymer.

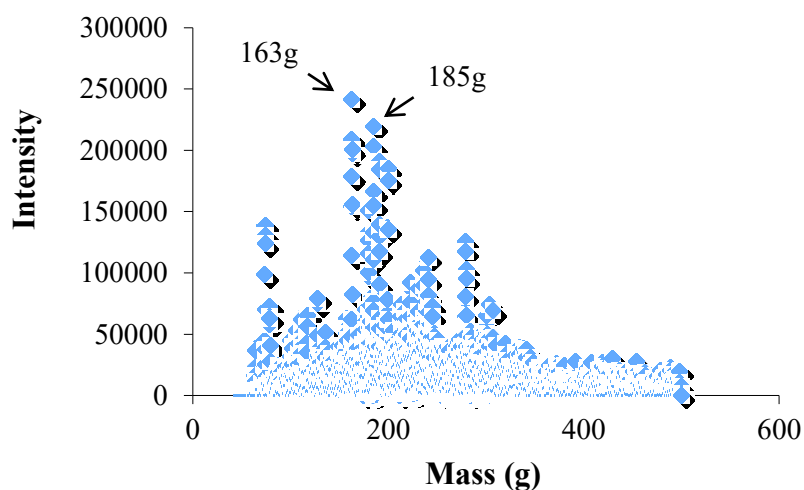


Figure 6.8 ESI-MS of Day 0 DMA copolymer extraction.

The concentration of DMA extracted per day for a period of 5 days was determined by comparing the absorbance of the extraction solutions to a calibration curve. A graph of the concentration versus time is shown in fig. 6.9. As shown in the graph, the highest concentration was extracted in the first 24 hours following synthesis, with decreasing concentrations recovered until the end of the experiment. This finding is consistent with the data from the adhesion and compression tests, which both also demonstrated the largest changes in adhesion and compression after 24 hours.

To further support the polymer degradation argument, the concentration values were used to determine the total percent of material extracted over time using the molar absorptivity of the DMA monomer for calibration. Basing concentration calculations on the DMA monomer likely introduces error into the measurements but can be used to obtain an estimate. From these values, it was determined that 8.8% of the DMA monomer came off in the first 24 hours, with a total of 15.3% fragmenting in the 5-day period. Given the

large degree of polymerization, it is unlikely that the extracted material is due to non-polymerized starting material. In addition, the significant change in material properties suggests that in fact a greater fraction of the DMA monomer may have been cleaved than was measured based on the extract solution. This is consistent with the 14% decrease in sample mass following extraction, suggesting that DMA copolymers are quite reactive. The UV-Vis, adhesion, and compression data indicate that the first 24 hours after synthesis of the polymer appears to be the critical period where the majority of the physical and chemical changes occur. Additionally, since the UV-Vis data indicate that the Dopa groups are fragmenting from the polymer, the loss of dopamine groups is likely the reason for the drop in adhesion and increase in compressive modulus since the remaining polymer chain is more similar to glassy polyacrylates.

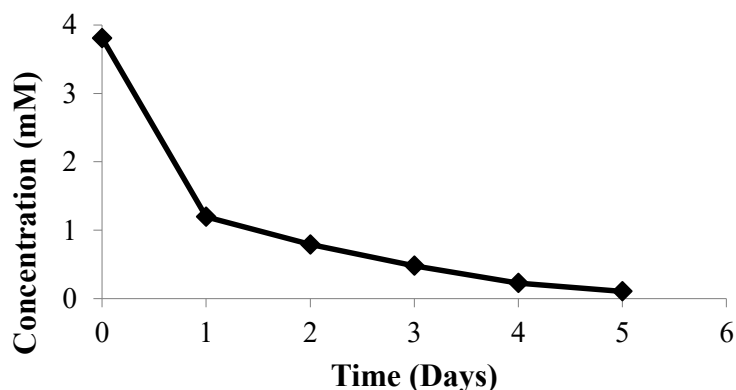


Figure 6.9 UV-Vis analysis of extraction experiments from the DMA copolymer.

6.4.3. GPC and NMR

GPC and NMR were also used to investigate the physical changes in the DMA copolymer over time. The GPC traces for days 0, 1, 3, and 16 are shown in fig. 6.10. These GPC traces establish that there were no major shifts in the molecular weight distribution over time, suggesting that the polymer must be degrading in a way that does not

significantly affect the molecular weight of the polymer. Specifically, oxidation of the catechol groups to a quinone would result in crosslinking via formation of bisquinones, as demonstrated by Deming and co-workers.²⁸ This would result in a significant increase in the molecular weight of the polymer, which was not observed. Conversely, the lack of molecular weight decrease supports the side-chain fragmentation hypothesis because the degree of polymerization does not appear to be affected at the resolution level of our GPC instrument.

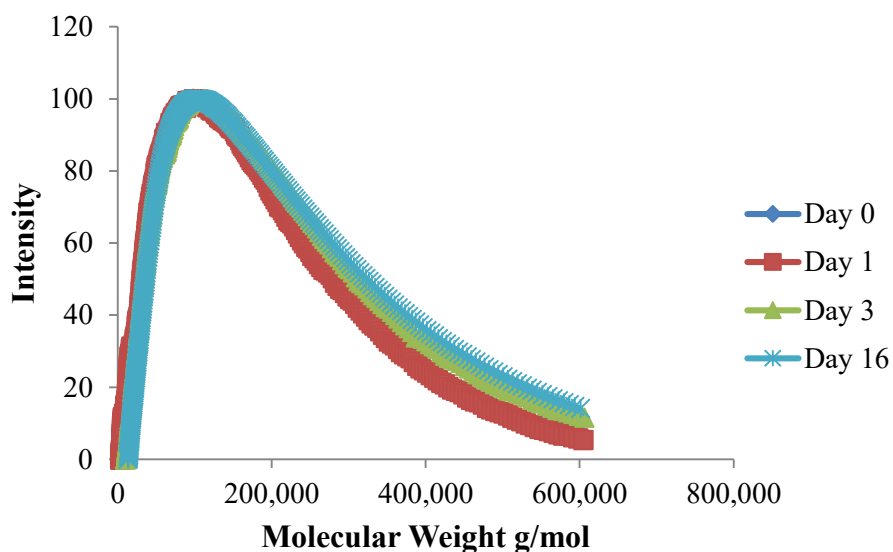


Figure 6.10 GPC traces for days 0, 1, 3, and 16.

The NMR spectra from multiple time points were also compared, however there were no significant changes in peak positions or intensities, although the resolution of the aromatic protons on the DMA monomers was low. Additionally, the absence of the vinyl group protons demonstrates that the UV-Vis data were not simply a result of residual unreacted monomer. We suggest that the mechanism of copolymer degradation is thought to be radical-based fragmentation of the Dopa group because other suitable explanations

such as quinone oxidation or chain degradation would cause shifts in both the NMR and GPC data.

Our data indicate that a novel degradation mechanism involving loss of pendant catechol groups may be responsible for the changes in material properties observed in DMA copolymer adhesives. Previous reports on the mechanism of photooxidative degradation of acrylates demonstrate that acrylates can degrade by radical fragmentation of the side chain at the carbonyl group.²⁹ Possibly, the DMA side chain could be fragmenting in a similar mechanism, however, additional studies are necessary to fully investigate this hypothesis. Further studies regarding the addition of radical scavengers may also be beneficial in extending the functional lifetime of these materials, although inhibition of auto degradation may also inhibit particular adhesion mechanisms for the substrates.

6.5. Conclusions

The physical changes that the DMA copolymer undergoes as it ages using adhesion and compression tests were characterized. It was found that the largest drop in adhesion and increase in modulus occur in the first day after the copolymer was synthesized. These changes in material properties were correlated with extraction of aromatic groups from the sample, which we attributed to cleavage of the catechol groups from the DMA monomers. Concentrations of extracted material, measured through UV-Vis spectroscopy, decreased monotonically with time and tracked with the changes in the material properties. GPC results confirmed that no significant changes in degree of polymerization were occurring during degradation, consistent with the proposed mechanism of catechol group cleavage.

These rapidly changing physical properties present a challenge to the reproducible study and technological applications of this unique class of adhesive polymer.

When it comes to wet tissue samples, the DMA-co-MEA-coated microfibers showed good, linear adhesion properties underwater. These properties are found to directly proportional to both the elasticity and aspect ratio of the elastomeric microfibers as well as contact time. Future work is needed for microfabrication optimization. The wetting properties the DMA copolymers onto the microfibers needs to be carefully studied and optimized. While the process was, for the most part, optimized for to yield effective coating of the microfibers, batch-to-batch variations and well as fiber-to-fiber variations continue to be a serious issue (fig. 6.11.). Here, attempts to overcome difficulties in wetting were made by increasing and modifying the applied weight. However, there is an upper limit to amount of load the microfibers could withstand. Therefore, any serious consideration for this system for other applications must take these properties into consideration and surface properties must be optimized.

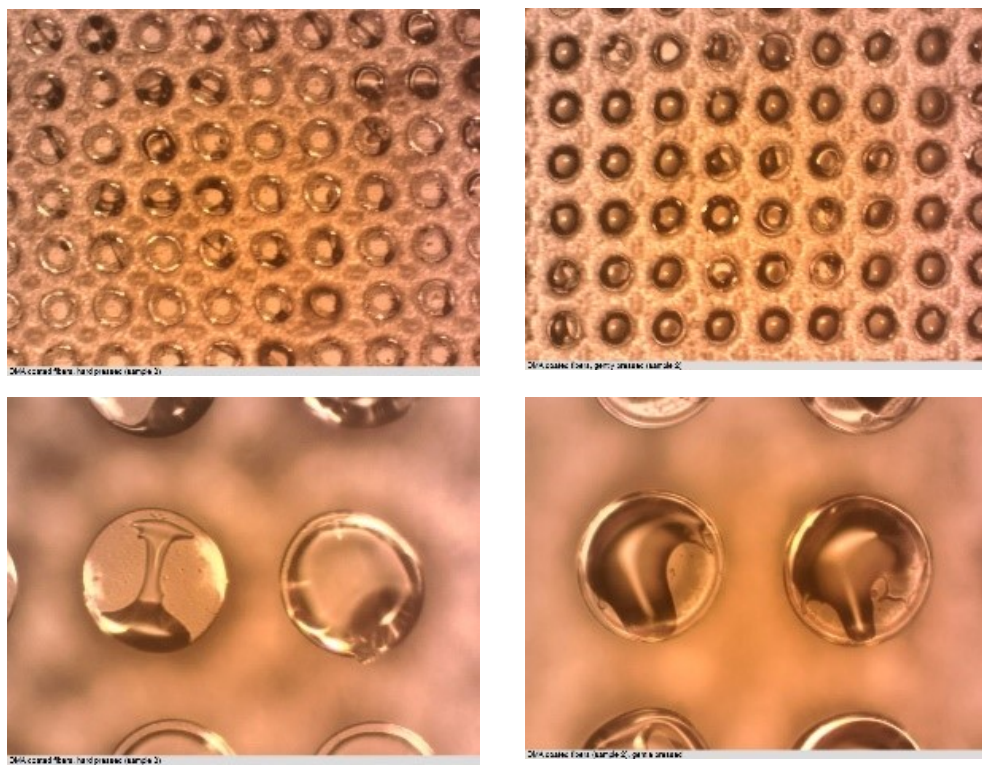


Figure 6.11 Optical microscopy images of the poorly coated mushroom tip gecko microfibers

Acknowledgements

The authors acknowledge the NMR facility at Carnegie Mellon University (NMR instrumentation partially supported by NSF CHE-0130903).

References

- (1) Lee, B. P.; Messersmith, P. B.; Israelachvili, J. N.; Waite, J. H., Mussel-Inspired Adhesives and Coatings. *Annual review of materials research* **2011**, *41*, 99-132.
- (2) Stewart, R. J.; Ransom, T. C.; Hlady, V., Natural underwater adhesives. *Journal of Polymer Science Part B: Polymer Physics* **2011**, *49* (11), 757-771.
- (3) WAITE, J. H., Adhesion in byssally attached bivalves. *Biological Reviews* **1983**, *58* (2), 209-231.
- (4) Yu, M.; Deming, T. J., Synthetic polypeptide mimics of marine adhesives. *Macromolecules* **1998**, *31* (15), 4739-4745.
- (5) Hawkins, A. J. S.; Bayne, B. L., Seasonal variation in the relative utilization of carbon and nitrogen by the mussel *Mytilus edulis*: budgets, conversion efficiencies and maintenance requirements. *Mar. Ecol. Prog. Ser.* **25**:181–88. *Marine Ecology - Progress Series* **1985**, *25*, 181–188.
- (6) Waite, J. H., Mussel power. *nature materials* **2008**, *7*, 8-10.
- (7) Deming, T. J., Mussel byssus and biomolecular materials. *Curr. Opin. Chem. Biol.* **1999**, *3*, 100-105.
- (8) Lee, H.; Dellatore, S. M.; Miller, W. M.; Messersmith, P. B., Mussel-inspired surface chemistry for multifunctional coatings. *Science* **2007**, *318* (5849), 426-30.
- (9) Lee, H.; Lee, B. P.; Messersmith, P. B., A reversible wet/dry adhesive inspired by mussels and geckos. *Nature* **2007**, *448*, 338.

- (10)Guvendiren, M.; Messersmith, P. B.; Shull, K. R., Self-Assembly and Adhesion of DOPA-Modified Methacrylic Triblock Hydrogels. *Biomacromolecules* **2008**, *9*, 122-128.
- (11)Lee, H.; Scherer, N. F.; Messersmith, P. B., Single-molecule mechanics of mussel adhesion. *Proc. Natl. Acad. Sci. U.S.A* **2006**, *103* (35), 12999-13003.
- (12)Yang, F.; Zhao, B., Adhesion Properties of Self-Polymerized Dopamine Thin Film. *The Open Surface Science Journal* **2011**, *3*, 115-122.
- (13)Tamarin A Fau - Lewis, P.; Lewis P Fau - Askey, J.; Askey, J., The structure and formation of the byssus attachment plaque in *Mytilus*. **1976**, (0362-2525 (Print)).
- (14)Glass, P.; Chung, H.; Washburn, N. R.; Sitti, M., Enhanced reversible adhesion of dopamine methacrylamide-coated elastomer microfibrillar structures under wet conditions. *Langmuir : the ACS journal of surfaces and colloids* **2009**, *25* (12), 6607-6612.
- (16)Brubaker, C. E.; Kissler, H.; Wang, L.-J.; Kaufman, D. B.; Messersmith, P. B., Biological performance of mussel-inspired adhesive in extrahepatic islet transplantation. *Biomaterials* **2010**, *31* (3), 420-427.
- (17)Shao, H.; Bachus, K. N.; Stewart, R. J., A Water-Borne Adhesive Modeled after the Sandcastle Glue of *P. californica*. *Macromolecular bioscience* **2009**, *9* (5), 464-471.
- (18)Bilic, G.; Brubaker, C.; Messersmith, P. B.; Mallik, A. S.; Quinn, T. M.; Haller, C.; Done, E.; Gucciardo, L.; Zeisberger, S. M.; Zimmermann, R., Injectable candidate sealants for fetal membrane repair: bonding and toxicity in vitro. *American journal of obstetrics and gynecology* **2010**, *202* (1), 85. e1-85. e9.
- (19)Connor, P. A.; Dobson, K. D.; McQuillan, A. J., New sol-gel attenuated total reflection infrared spectroscopic method for analysis of adsorption at metal oxide surfaces in aqueous solutions. Chelation of TiO₂, ZrO₂, and Al₂O₃ surfaces by catechol, 8-quinolinol, and

acetylacetone. *Langmuir : the ACS journal of surfaces and colloids* **1995**, *11* (11), 4193-4195.

(20)McBride, M. B.; Wesselink, L. G., Chemisorption of catechol on gibbsite, boehmite, and noncrystalline alumina surfaces. *Environmental science & technology* **1988**, *22* (6), 703-708.

(21)Vasudevan, D.; Stone, A. T., Adsorption of catechols, 2-aminophenols, and 1, 2-phenylenediamines at the metal (hydr) oxide/water interface: effect of ring substituents on the adsorption onto TiO₂. *Environmental science & technology* **1996**, *30* (5), 1604-1613.

(22)Yamamoto, H.; Kuno, S.; Nagai, A.; Nishida, A.; Yamauchi, S.; Ikeda, K., Insolubilizing and adhesive studies of water-soluble synthetic model proteins. *International journal of biological macromolecules* **1990**, *12* (5), 305-310.

(23)Lee, B. P.; Huang, K.; Nunalee, F. N.; Shull, K. R.; Messersmith, P. B., Synthesis of 3, 4-dihydroxyphenylalanine (DOPA) containing monomers and their co-polymerization with PEG-diacrylate to form hydrogels. *Journal of Biomaterials Science, Polymer Edition* **2004**, *15* (4), 449-464.

(24)Chung, H.; Grubbs, R. H., Rapidly cross-linkable DOPA containing terpolymer adhesives and PEG-based cross-linkers for biomedical applications. *Macromolecules* **2012**, *45* (24), 9666-9673.

(25)Glass, P.; Chung, H.; Washburn, N. R.; Sitti, M., Enhanced Wet Adhesion and Shear of Elastomeric Micro-Fiber Arrays with Mushroom Tip Geometry and a Photopolymerized p(DMA-co-MEA) Tip Coating. *Langmuir : the ACS journal of surfaces and colloids* **2010**, *26* (22), 17357-17362.

- (26) Chung, H.; Glass, P.; Pothen, J. M.; Sitti, M.; Washburn, N. R., Enhanced Adhesion of Dopamine Methacrylamide Elastomers via Viscoelasticity Tuning. *Biomacromolecules* **2010**, *12* (2), 342-347.
- (27) Flanigan, C. M.; Shull, K. R., Adhesive and elastic properties of thin gel layers. *Langmuir : the ACS journal of surfaces and colloids* **1999**, *15* (15), 4966-4974.
- (28) Yu, M.; Hwang, J.; Deming, T. J., Role of L-3, 4-dihydroxyphenylalanine in mussel adhesive proteins. *Journal of the American Chemical Society* **1999**, *121* (24), 5825-5826.
- (29) Singh, B.; Sharma, N., Mechanistic implications of plastic degradation. *Polymer Degradation and Stability* **2008**, *93* (3), 561-584.